REFERENCE ONLY

UNIVERSITY OF LONDON THESIS

Degree PhD Year 2005 Name of Author KOU GOULOS, E

COPYRIGHT

This is a thesis accepted for a Higher Degree of the University of London. It is an unpublished typescript and the copyright is held by the author. All persons consulting the thesis must read and abide by the Copyright Declaration below.

COPYRIGHT DECLARATION

I recognise that the copyright of the above-described thesis rests with the author and that no quotation from it or information derived from it may be published without the prior written consent of the author.

LOANS

Theses may not be lent to individuals, but the Senate House Library may lend a copy to approved libraries within the United Kingdom, for consultation solely on the premises of those libraries. Application should be made to: Inter-Library Loans, Senate House Library, Senate House, Malet Street, London WC1E 7HU.

REPRODUCTION

University of London theses may not be reproduced without explicit written permission from the Senate House Library. Enquiries should be addressed to the Theses Section of the Library. Regulations concerning reproduction vary according to the date of acceptance of the thesis and are listed below as guidelines.

A. Before 1962. Permission granted only upon the prior written consent of the author. (The Senate House Library will provide addresses where possible).

B. 1962 - 1974. In many cases the author has agreed to permit copying upon completion of a Copyright Declaration.

C. 1975 - 1988. Most theses may be copied upon completion of a Copyright Declaration.

D. 1989 onwards. Most theses may be copied.

This thesis comes within category D.

☑ This copy has been deposited in the Library of UCL

☐ This copy has been deposited in the Senate House Library, Senate House, Malet Street, London WC1E 7HU.

UNIVERSITY COLLEGE LONDON
Department of Chemical Engineering

PREDICTIVE MODELLING OF ORGANIC CRYSTALLIZATION PROCESSES

Eleftherios Kougoulos AMIChEME

M.Eng (Hons) in Chemical with Biochemical Engineering

A Thesis Submitted to the University of London for the Degree of Doctorate of Philosophy

2005

ProQuest LLC
789 East Eisenhower Parkway
P.O. Box 1346
Ann Arbor, MI 48106-1346

CONTENTS

CONTENTS

CONTENTS

CONTENTS

CONTENTS

Abstract

This thesis is concerned with the development of a predictive model for batch cooling suspension pharmaceutical crystallizations, with a focus on product performance. A major challenge involved in the design of industrial pilot plant pharmaceutical crystallizers, is to predict the influence of crystallizer geometry, scale and operating conditions on the process behaviour and crystal size distribution (CSD). The design of industrial crystallizers is hindered by the lack of scale-up rules due to the absence of reliable predictive process models. Currently no reliable predictive or 'dial up a particle size' tool exists for scale-up predictions.

The research involves the development of a novel predictive compartmental modelling framework for the scale-up of an organic fine chemical. A new approach of using compartments is developed in order to facilitate scale-up design and process modelling by separating crystallization kinetic and hydrodynamic phenomena. Application of this technique involves determining key process engineering information on a laboratory scale, which is critical for technology transfer, and combining this data with hydrodynamic information on transfer to large scale for predictive scale-up purposes. The key process engineering information required for predictive modelling includes the determination of solubility characteristics, thermodynamic properties and crystallization kinetics of the organic fine chemical. Attenuated Total Reflectance Ultra-Violet (ATR-UV) spectroscopy is used as an *'in-situ'* measurement technique to measure solute concentration. A modified continuous Mixed Suspension Mixed Product Removal (MSMPR) crystallizer is designed specifically for innovative drug candidates available in limited quantities to derive steady state crystallization kinetics with minimal influence from hydrodynamic phenomena. Batch attrition experiments were carried out to determine the effects of specific power input on the CSD using Lasentec Focussed Beam Reflectance Monitoring (FBRM) to monitor the process on-line and to develop an attrition rate model.

Computational Fluid Dynamics (CFD) is a simulation tool that is also introduced to provide valuable insight into mixing, heat transfer and hydrodynamic phenomena within agitated batch cooling suspension crystallization

vessels including investigating the effects of scale-up. CFD is used to aid the development of the compartmental modelling framework. The design of the compartmental structure is based on high spatial resolution CFD simulations of internal flow, mixing and heat transfer within crystallizers upon scale-up. The great advantage of using a compartmental modelling framework is that the spatial resolution is reduced and the full population balance with kinetic models can be implemented. The detailed compartmental framework is based on the overall flow pattern, local energy dissipation rate, solids concentration and temperature distribution obtained from CFD. The number, location, cross-sectional area and volume of compartments are determined from CFD results based on the physical crystallizer dimensions. The compartments are selected such that they have approximately uniform temperature, local energy dissipation and solids concentration. Each dynamic compartment has a mass, concentration, enthalpy and population balance combined with MSMPR crystallization kinetic models. The compartments are therefore well mixed and physically connected via interconnecting flows determined from CFD. A general process modelling tool, gPROMS (Process Systems Enterprises) that supports both steady state and dynamics simulations is used to solve sets of ordinary differential and algebraic equations in each compartment.

A single compartmental modelling approach is used initially as a first approach without taking into account local variations in process conditions. Predictions on a laboratory scale for an MSMPR and batch cooling crystallizer were satisfactory but upon scale-up the effects of mixing and hydrodynamics is not taken into account and therefore the predictions become less reliable. A compartmentalization approach can be introduced into gPROMS whereby the compartments are modelled as individual units with input and output streams using CFD hydrodynamic information.

Chapter 1

INTRODUCTION

Crystallization is a process that involves the formation of an ordered solid phase from a gas, liquid or amorphous phase. Industrial pharmaceutical crystallization is a chemical engineering process. It is a critical step in the separation and purification of pharmaceutical products. Pharmaceuticals are characterised by purity, crystal habit, morphology, crystal size distribution and polymorphism. The main advantages of crystallization are as follows:

I. *A high purity in one process step.* The rigid structure of the crystalline material results in a low tendency to incorporate foreign substances or solvent molecules. Hence high purity substances can be produced in crystallization.

II. *Low level of energy consumption.* If cooling crystallization is used instead of distillation, a significant energy reduction is achieved.

III. *Relatively mild process conditions.* Crystallization is a favourable unit operation for temperature sensitive or even temperature labile substances.

The production of particles from solution is one of the oldest unit operations in the chemical industries. This involves, mass, energy, momentum and population transfer including the crystallization process. Crystallization process rates are dependent on the scale of operation and the crystallization behaviour varies according to the scale of operation. Therefore there is a need to develop predictive models by taking information from small scales (laboratory) to develop and design large-scale (pilot plant) processes. This is known as process *'scale-up'*.

This research focuses on the scale-up of a batch cooling suspension crystallization process for an organic fine chemical produced by GlaxoSmithKline pharmaceuticals and the development of a novel predictive modelling framework based on a compartmental modelling technique. Thus far, conventional,

geometrically lumped models of physical processes occurring within crystallization vessels are used. These models, however, are not suitable for scale-up purposes and poor predictions are obtained. The reason for this is that upon scale-up hydrodynamic phenomena produce variations in the local process parameters, which are not taken into account. The degree of supersaturation, energy dissipation, temperature and suspension density are all factors that influence batch cooling crystallization processes and affect the product quality and performance. The hydrodynamic conditions are such that the process variables are non-uniformly distributed throughout the agitated crystallization vessels. The organic fine chemical considered, is crystallized from an isopropyl-alcohol-water solvent system on a pilot plant scale and constitutes the fifth stage of the industrial manufacturing process. A major problem associated with the pilot plant crystallization process is that a number of batches fail to comply with the standards imposed by the food and drugs agency (FDA). There is also a stringent requirement for the crystal size distribution to be between 20-200 μm. The current Good Manufacturing Practice campaign (cGMP) using a batch suspension crystallization process results in the production of wide particle size distributions and therefore drying and milling are process unit operations are necessary in order to reduce the particle size. However, drying and milling may have the effect of damaging the particles and physically altering the morphology. Table 1.1 shows the particle size (μm) from pre-drying, pre-milling and post-milling stages for a typical batch cooling crystallization on the pilot plant scale from the GMP campaign (Wood-Kaczmar, 2003). The development of a generic predictive modelling tool could allow companies to save time, money and resource. The need to perform costly trial and error scale-up experiments including optimisation to obtain the required CSD can be significantly reduced.

Operation	D_{10}	D_{50}	D_{90}	% <19.3 μm
Pre-Drying	64	185	412	2.8
Pre-Milling	41	133	272	5
Post-Milling	6	59	164	21

Table.1.1: *Particle size (μm) percentiles from pre-drying, pre-milling and post-milling (Wood-Kaczmar, 2003).*

Furthermore, the number of batches that fail to meet the narrow CSD requirements for important pharmaceutical candidates could also be reduced. The organic fine chemical investigated in this research does not exhibit polymorphism issues.

Batch cooling crystallization processes are commonly used in the production of pharmaceuticals but the analysis of their behaviour is complicated by the transient nature of the crystallization conditions. Due to the time-dependent parameters, the crystallization process has to be controlled. The standard equipment configuration used is an agitated vessel. Generally, in the modelling and analysis of programmed agitated batch cooling suspension crystallizations, it is assumed that the entire volume is well-mixed, with a homogeneous solids concentration present throughout the crystallizer. The effect of scale-up on mixing in suspension crystallizations has not been investigated in detail and will be considered in this research.

One of the most widely used methods to achieve supersaturation, which is essential for crystallization, is by the cooling of a saturation solution. The development of controlled cooling profiles to improve the product quality and crystal size distribution has been subject to numerous investigations (Jones and Mullin, 1974; Jones, 1974; Jones, 1972). In addition to varying with time, the level of supersaturation varies from one location to another in a batch crystallizer and it becomes more significant upon scale-up. Supersaturation is generated locally at heat transfer surfaces, but is consumed as a result of nucleation followed by crystal growth. The rate of supersaturation depletion depends on the total crystal surface area. The crystal growth and rate directly affect the crystal size distribution and product quality; however the effect of mixing and scale-up of batch cooling suspension crystallizations has not been taken much into consideration. The crystallization kinetics include crystal growth and nucleation, which depends strongly on the supersaturation levels. The supersaturation levels are also a direct consequence of the degree of mixing within a crystallizer including the temperature. The crystallization kinetics as well as the mass and heat transfer in the crystallization process is strongly affected by the fluid dynamics within a crystallizer.

With the scale-up of crystallization process, secondary nucleation plays an important role (Garside and Jancic, 1979). Groen et al. (1999) describe the

difficulties encountered during crystallization scale-up and also report the limitations involved with CFD simulations in solving problems. Recent advances in CFD technology has enabled the modelling of multi-phase systems. Montante et al. (2001) observed that using a multi-phase turbulence model in CFD, the effects of the suspension on the hydrodynamics could be predicted. CFD simulation predictions have shown that a gradient in the solids concentration exists in the axial direction including the presence of clear mother liquor in the upper region of a crystallization vessel at low mean specific power inputs. The prediction of the effects of scale-up using mass, momentum and population transfer through the use of CFD simulations is restricted due to computational limitations and solver algorithms. Scale-up is a difficult task as many factors influence the quality and purity of the final product of a process. Successful scale-up requires the utilization of a wide range of techniques and understanding of the problem (Bisio and Kabel, 1985). For crystallization processes, there is a lack of understanding of the physical processes occurring upon scale-up and therefore scale-up of crystallization processes occurs empirically or by trial and error for optimisation, which is costly.

Momonaga et al. (1997), introduced a mixing dependent scale-up factor based on equal power input per unit mass on different scales for a batch precipitation process, but did not determine critical precipitation kinetics studies necessary for scale-up. Ploβ et al. (1976) studied the scale-up of MSMPR crystallizers and observed that the secondary nucleation rate and the growth rates on different scales are the same if the suspension density, specific power input and residence time are held constant with scale-up. Misra et al. (1976) and Ilievski (2001) also found that the growth rate of gibbsite formation during isothermal batch precipitation is independent of the vessel hydrodynamics with scale-up. Qian et al. (1987) observed that scale-up with constant tip speed of the impeller leads to the same nucleation rate on different scales of operation. Zauner (2002) observed that scale-up using constant mean specific power input produced different local energy dissipation profiles thus directly influencing the nucleation rate.

O'Meadra (1995) and Kramer et al. (1996) also observed the importance of attrition kinetics on a evaporative steady state crystallization process, as the attrition fragments produced initiate nuclei formation, which contributed to secondary nucleation. Similarly, secondary nucleation is bound to play an important role in controlled seeded batch cooling crystallization processes.

For the proper design of industrial pharmaceutical suspension crystallizers, a more detailed insight into the local crystallization processes that take place is necessary. Recently much knowledge has been gained from crystallization kinetics (Randolph and Larson, 1988; Van der Heijden et al., 1992; O'Meadra, 1995 and Gahn et al., 1999a,b) and from the dynamic behaviour of industrial crystallizers (Eek et al., 1993). However, most models proposed to simulate crystallization processes are simple input-output models, whereby a well-mixed vessel is assumed. Patience (2002) used a stochastic modelling approach for the modelling of the batch cooling crystallization system under investigation but used a well-mixed assumption. These models are applicable for single configurations, however extrapolation to other scales of operation and crystallizer geometries is not possible. Hence, the design of industrial crystallizers is based on experience only. The deviation of the well-mixed behaviour in a crystallizer is primarily derived from the hydrodynamic conditions, which lead to the development of temperature, supersaturation, energy dissipation and particle concentration profiles within a crystallizer.

An approach that can be adopted to overcome the lack of well-mixed models is the development of a generic compartmental modelling framework. Simplified models or concepts have been proposed (Janger et al., 1991; Daudey et al., 1993; Gerla et al., 1993). In a compartmental model, several compartments represent the total system and modelled as homogeneous well-mixed units. Additionally, they are physically connected to the overall inhomogeneous system. More detailed and complex crystallization compartmental modes will be considered further in this research (Kramer et al., 1999; Zauner and Jones, 2002; Rigopoulos and Jones, 2003).

1.1 PROBLEMS IN CRYSTALLIZATION

Crystallization is one of the oldest unit operations in the pharmaceutical industry but crystallization processes frequently exhibit design and operational problems. These problems are related to product quality requirements such as filterability, caking behaviour, purity and tablet behaviour of pharmaceuticals on the one hand, and process requirements, such as capacity. Pharmaceutical crystallizations frequently produce crystals, which do not satisfy the defined

quality and crystal size distribution characteristics. For example, fine particles are necessary for bioavailability but an excess of fine particles will typically result in poor filterability characteristics. Another problem is the inclusion of mother liquor during subsequent re-crystallization may cause particulate agglomerate formation; a process referred to caking of particles. Operational problems also constitute a large portion of the problems encountered in crystallization processes. Firstly, scale growth or crystal deposition on heat exchanger surfaces as observed in batch cooling suspension crystallizations often reduces production capacity and may even limit plant availability significantly in pharmaceutical processes. Secondly, the type of cooling regime implemented influences the product quality and crystal size distribution characteristics.

1.2 CRYSTALLIZATION DESIGN PROCEDURES AND PREDICTIVE TOOLS

A major challenge involved in the design of industrial pharmaceutical batch crystallizers, is to predict the influence of crystallizer geometry, scale and operating conditions on the process behaviour and crystal size distribution (CSD). The design of industrial crystallizers is hindered by the lack of scale-up rules due to the absence of reliable predictive process models. Currently no predictive or 'dial up a particle size' tool exists for scale-up predictions.

The reason for this is that crystallization and solids processes in general, exhibit a higher degree of complexity than that of most vapour-liquid processes (i.e. distillation). The product quality specification cannot be defined solely in terms of the chemical and phase composition. A crystalline product is also characterised by its size distribution, morphology, crystal habit, polymorphism and the amount of strain in the crystal lattice. There is also the complex thermodynamics of the solid-liquid phase to consider. There are inherent difficulties in predicting the hydrodynamics of the multi-phase flow as a function of crystallizer type and impeller geometry, operating conditions, crystal properties and crystal concentration. As a result of the hydrodynamics, the process conditions affecting the crystallization mechanisms are rarely uniform inside industrial scale crystallization vessels. Variations in local supersaturation levels and energy dissipation rates will affect both the yield and crystal size distribution from the

batch crystallizer. The rates at which crystals are born, grow, dissolve including attrition, agglomeration are not only a function of the liquid phase process conditions but also of distributed crystal properties such as size, surface structure and internal energy.

1.3 IMPORTANCE OF CRYSTALLIZATION

The starting point of a design process is the definition of the design specification. Design specifications are process related, product related and design process related. Process related design specifications include availability, controllability and maintainability including design process related design specifications. Product related design specifications, which refer to both the solid and liquid phase products that result from a crystallization process. The purpose of the crystallization process i.e. purification of the liquid phase or production of a solid phase, determines which phases are the main or by-products. The specifications of a liquid phase (mother liquor) can be expressed in terms of pressure, temperature and composition. In strong contrast, quality specifications of a solid crystalline product are often ambiguous, hard to quantify and difficult to measure. This chapter focuses on (i) characterisation of crystal quality in terms of product performance and product composition, (ii) the crystallization mechanisms that determine the composition of a crystalline product, (iii) the need for a predictive crystallization process model and (iv) application of such a process model for the design of crystallization processes that satisfy both product and process related design requirements. The chain that needs to be captured by a predictive crystallization process model is depicted in the following schematic. Fig.1.1 shows the relationship between product quality, crystallization mechanisms, process conditions, crystallization equipment and operating conditions.

Simulation of process behaviour and product quality for a given crystallizer geometry and operating conditions is a forward problem, whereas optimal design and optimal control are inverse problems which start from desired product quality and process behaviour.

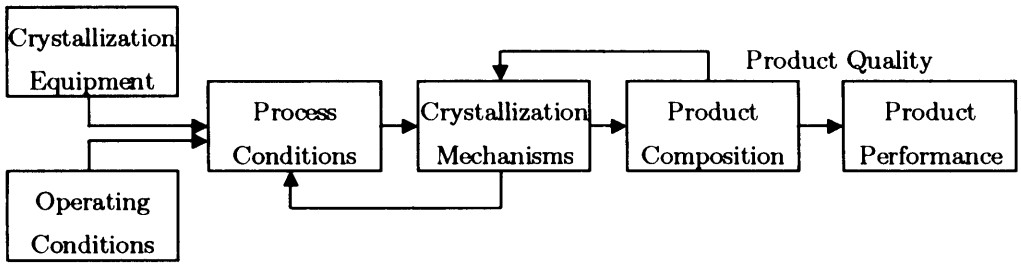

Figure 1.1: *Schematic representation of the chain required to be captured by a predictive crystallization process model (Bermingham, 2003).*

1.4 CRYSTAL QUALITY: PERFORMANCE AND COMPOSITION

Crystal quality can be defined in terms of product performance characteristics and product composition characteristics.

1.4.1 PRODUCT PERFORMANCE

The quality of a crystalline solid is usually expressed in terms of performance characteristics. In the pharmaceutical sector the food and drugs agency (FDA) and downstream solids processing impose most crystal quality requirements. Downstream solids processing issues include filtration, washing and drying behaviour of the crystals. Secondly, caking behaviour and flowability are important characteristics for storage and transport. Caking is usually the result of mother liquor inclusions. During storage, mother liquor may seep from broken particles. Subsequent re-crystallization may cement the crystals together; a process referred to as the caking of crystals.

1.4.2 PRODUCT COMPOSITION

For design purposes, translation of the often ill-defined performance characteristics to well-defined physical parameters is essential. Well-defined physical quantities to describe the quality of a crystalline product include size, purity, lattice structure, morphology and habit. Usually the individual crystals in a

crystalline product do not possess the same history as regards to their formation processes. Consequently, their properties will not be the same. A product that consists of crystals with different sizes and morphologies has distributed properties. The volume of crystalline material is normally considered which is substantially larger than the volume of an individual crystal; the number of crystals is sufficiently large to justify the use of a statistical description to account for the distributed nature of the product properties. The first distributed property in conjunction with industrial crystallization is the crystal size. As crystallization takes place in a vessel with a residence time distribution, the individual crystals will obviously have varying histories. The most noticeable result of this difference in history is usually a distribution of crystal sizes.

1.4.3 PRODUCT-RELATED DESIGN SPECIFICATIONS

Defining product specifications in terms of composition instead of performance is clearly more suitable for modelling and design purposes. Although product composition characteristics are well defined, some are extremely difficult to measure e.g. morphology, particle size and habit. Particle size is considered as a characteristic dimension of particle with growth kinetics describing a rate of change of this characteristic dimension as a function of time. The lack of adequate product performance models i.e. models predicting the performance on the basis of composition; without these models interpretation of product specifications imposed by downstream solids processing and by the FDA remains a serious bottleneck.

All product composition characteristics can be uniquely defined in physical terms, however, in practise a reasonably accurate description of some characteristics would require a very substantial number of parameters.

These three problems are largely related to the distributed nature of crystalline products. In addition to a size distribution, a collection of crystals will usually also possess distributions with respect to morphology, purity and size. A comprehensive description of the product composition therefore involves a multivariable distribution of the crystal population over the various product composition variables.

1.5 CRYSTALLIZATION MECHANISMS

The product composition characteristics constitute the internal states of a crystalline product. The external state of a crystal is its geometric position, and the external velocity of the crystal gives the change in the external state, which is a function of the both the hydrodynamics of the solid-liquid phase system and the internal states of the crystal. This section focuses on the main crystallization fundamentals or mechanisms that can change the internal states of a crystalline product, viz nucleation, growth, dissolution, attrition, agglomeration and breakage. The rates of these crystallization events are largely determined by the same states they affect, i.e. the internal crystal states and slurry states. More specifically, they are a function of rate coefficients and driving forces, which are in their turn determined by slurry states or local process conditions such as supersaturation, energy dissipation, solids concentration, pressure and temperature, as well as internal crystal states, such as size, strain and shape.

1.5.1 NUCLEATION

Nucleation involves the formation of the new crystalline particles and is classified as being primary or secondary according to the mechanism through which it occurs.

1.5.1.1 PRIMARY NUCLEATION

Primary nucleation involves the formation of a new solid phase from a clear solvent. This type of nucleation is further divided into homogeneous and heterogeneous nucleation. In heterogeneous nucleation, nucleation starts on foreign substrates of mostly microscopic particles. If such substrates are absent, new phase formation takes place by statistical fluctuations of solute entities clustering together, a mechanism known as homogeneous nucleation.

The driving force for primary nucleation is the supersaturation of the crystallization system, which is defined as the difference in the chemical potential of the substance in the liquid and in the solid phase. The rate coefficient or

resistance for primary nucleation is a function of the cluster-liquid interfacial tension and diffusion coefficient. The internal states at the time of nuclei formation such as size, lattice structure and purity, are also a function of the supersaturation.

1.5.1.2 SECONDARY NUCLEATION

Secondary nucleation refers to the birth of new crystals at the interface of parent crystals. Contrary to the relatively high supersaturation levels required for primary nucleation, secondary nucleation occurs at low or moderate values of supersaturation. A supersaturated solution nucleates more readily at a lower level of supersaturation, when solute crystals are already present or added. Hydrodynamic conditions and the suspension density also influence secondary nucleation. The most important source of secondary nucleation in batch crystallization is attrition. Attrition is referred to a contact nucleation (Garside and Davey, 1980) and occurs as a result of particle-impeller, particle-vessel wall or particle-particle collisions. The driving force for attrition is determined by the concentration of the various sized particles and their relative motion with respect to the impeller blades, vessels walls or other particles. The relative kinetic energy of a collision is determined by the size and relative velocity of the particle, which in turn is a function of the slurry motion, viscosity and particle inertia. The rate coefficient or resistance for attrition is a function of the shape, surface roughness and mechanical properties of the colliding particle. The rate coefficient is also indirectly influenced by the supersaturation, which determines factors such as surface roughness and healing of corners and surfaces damaged due to previous collisions. The supersaturation also determines the effective secondary nucleation rate as a result of attrition. Secondary nucleation as a result of shear breeding (Daudey et al, 1990) involves the production of nuclei by attrition of macrosteps or other growth formations whereas mechanical breeding involves the attrition of portions of the crystal lattice, which has not been identified previously as a source of nuclei. Daudey suggested that surface relief related nuclei and the mechanical fragments would show different survival kinetics as n mechanical fragments may be more stressed than surface relief fragments (Garside and Larson, 1978). Shear nucleation (Sung et al., 1973) and mechanistic models (Botsaris, 1976) have been

proposed for secondary nucleation as well. Mullin (1993) and Grootsacholten and Jancic (1984) provide detailed descriptions for secondary nucleation mechanisms.

Secondary nucleation rates have been modelled as an 'effective' nucleation rate and related empirically to parameters describing the properties of the crystallizing solution such as supersaturation or average growth rate, the mechanical agitation in the crystallizer (impeller velocity or specific power input) and a property describing the CSD such as the suspension density. These power law correlations give poor descriptions of the dynamics for the systems for which they are modelled on. These correlations have, however, been used for scale-up criteria (Ottens et al., 1972) but not yet developed to predict the nucleation rates based on the vessel geometry, different scales and properties of materials.

1.5.2 CRYSTAL GROWTH

Crystal growth is the addition of solute molecules from a supersaturated solution to the crystal lattice. Growth is a mechanism responsible for increasing crystal size and largely determines crystal morphology. The crystal face growth rates together with the growth mechanism determine the surface structure and purity of the crystal. The growth rate of a particular crystal face is mostly described by its linear growth rate, which refers to the growth rate of that face in the direction normal to the face. Since the growth rates of the various crystal faces are usually not equal, an overall linear growth rate is often used.

Crystal growth is a three-step process consisting of mass transfer, surface integration and heat transfer. Mass transfer and surface integration occur sequentially and in parallel with heat transfer. Mass transfer involves the diffusion of growth units to the crystal surface. Surface integration consists of surface diffusion, orientation and the actual incorporation into the lattice.

Various models have been suggested to describe the growth of crystals during a crystallization process (Wells, 1946; Buckley, 1952; Strickland and Constable, 1968; Lewis, 1980 and Chernov, 1989).

Several theories of crystal growth by surface integration have been developed and successfully applied to model crystal growth. These include the Kossel model (Kossel, 1934), birth and spread model (O'Hara and Reid, 1973), Burton-Cabrera-

Frank (BCF) model (Burton et al., 1951), diffusion-reaction model (Berthoud, 1912) and continuous growth model. The BCF model is based on the assumption that growth occurs along screw locations and is known as spiral growth. The continuous growth model involves the integration of growth units on a rough crystalline surface where their energy demand for orientation is the lowest. Spiral growth is the most encountered growth mechanism under normal operating conditions (Rosmalen, 2000). Heat transfer, is often a rate-limiting step in melt crystallization, but this is practically never the case in solution crystallization. Supersaturation is the driving force for both mass transfer and surface integration. The rate of mass transfer has a first order supersaturation dependency. The supersaturation dependency of the surface integration step is determined by the mechanism: a second, exponential and first order dependency for spiral growth, 'birth and spread' and rough growth respectively.

In Chapter 5, a strong upward curvature in the population density distributions is observed in the small particle size range for MSMPR cooling suspension crystallizations for the organic fine chemical studied. This phenomenon may be attributed to growth rate dispersion (GRD) or size dependent growth (SDG). SDG is explained by three mechanisms, one whereby the particles have the same averaged growth, but that individual particle growth rates fluctuate during growth periods. The second is that crystals are born with a characteristic distribution of the growth rate, but that individual crystals retain a constant growth rate throughout their residence in the crystallizer. The third assumption is that some crystals never grow or that some of the nuclei are dissolved when the nuclei are created by secondary nucleation. The success of the SDG model can be attributed to the fact that for a group of crystals exhibiting a range of growth rates, the fastest growing crystals will reach an appreciable size in a shorter time than the slower growing crystals giving rise to a SDG rate. Wang et al. (1992) found a size-dependence on initial fragment sizes also giving rise to an apparent SDG effect. Wang et al. (1992) also introduced a Gibbs-Thompson effect to explain SDG rate but that was applicable only to particles of sub 1μm region as measurements performed by Van der Heijden et al. (1992) confirmed this effect.

However, the direct observation of individual particles have shown that a particles growth rate is independent of its size and each crystal has its own

intrinsic growth (Jones and Larson, 1999), thus making the SDG concept difficult to accept. The SDG function is equivalent to the conditional mean growth rate at a given size using the intrinsic growth rate dispersion theory (Rojkowski, 1993). Jones (2002) states that the SDG theory is inconsistent with direct observation of crystal growth, thus making SDG model a poor choice as a basis for understanding growth rate phenomena in a continuous MSMPR. The SDG model is also purely empirical and gives no insight into the kinetic processes occurring in the small particle size range. The theory of intrinsic growth rate dispersions, postulates that each particle is born with its own intrinsic growth rate and that particles retain that growth rate as long as they remain in the crystallizer (Ramananarayanan, 1982). The intrinsic growth rate dispersion model has been used to successfully model non-ideal behaviour in both batch and continuous crystallization processes (Wang et al., 1990). The success is due to the consistency with observations of individual growth rate of crystals but this has only been performed on measuring crystal growth when the crystals reach as size greater than 40-50 μm as a result of crystals formed by primary nucleation. Variation in the number of dislocations at the surface of secondary nuclei, induced by the formation process was reported to explain the observed differences in the growth rate (Berglund and Larson, 1984). Ristic et al. (1990) have also experimentally observed growth rate dispersion. Recently internal strain present within a crystal has been proposed to be responsible for GRD. Van der Heijden et al. (1992), proposed that strain energy is added to the internal energy of a crystal, increasing the chemical potential of the solid phase, leading to a decrease in the growth rate. Growth models describing the healing of deformed crystals have also been proposed. Rojkowski (1993) has shown that it is difficult to distinguish between SDG and GRD in an MSMPR crystallizer. Hence from these observations much controversy exists and therefore it is possible for either SDG or GRD mechanisms to occur in solution crystallization.

1.5.3 AGGLOMERATION

Agglomeration is defined as the mass formed by the cementation of individual particles, probably by chemical forces (Randolph and Larson, 1988). A mass formed by a group of particles held together by only interparticle forces is called an aggregate. Agglomerates are undesirable in batch pharmaceutical crystallization

processes because they contain mother liquor between the primary crystals that form the agglomerate. This liquor is difficult to remove during drying, and promotes caking of the product during storage. Furthermore, agglomerates also tend to break more easily than solid crystals, during which they release solvent. Agglomeration requires the collision of two or more particles and the collision mechanism depends on the size of the particles involved: perikinetic, orthokinetic or inertia. Next, these particles must form an aggregate as a result of interparticle forces, such as Van der Waals (attractive), electrostatic (repulsive) and steric forces (Pratola et al., 2002). Finally, cementation of these particles as a result of growth, before the aggregate is disrupted occurs. The driving force for agglomeration is supersaturation. Without supersaturation, aggregates can be formed but agglomerates cannot. The rate coefficient or kernel for agglomeration is a function of the number of particles, the size of particles involved, and in the case of orthokinetic agglomeration the fluid shear or energy dissipation. In Chapter 5, it was observed that during MSMPR cooling suspension crystallizations some agglomeration occurred but it was not the primary mechanism by which the particles formed for the suspension crystallization system under investigation.

1.5.4 ATTRITION

Attrition is a process which involves either particle-particle or particle-solution interactions. This results in the erosion of the particles known as attrition of particles to produce smaller particles. Disruption kinetics can be modelled for attrition based on a disruption rate (Synoweic et al., 1993; Wojcik and Jones, 1998). The disruption process is a function of the degree of supersaturation in the crystallizer and hence high supersaturation levels produce high growth rates and therefore stronger agglomerated particles, which reduces the chance of breakage. With an increase of power input there is an increase in the disruption rate. Attrition of a particle can lead to the formation of two particles, which have the same size or similar size (particle splitting) leading to a uniform breakage function, two particles of different size (attrition) leading to a parabolic breakage function or a number of particles leading to a multiple breakage function (Zauner, 1999).

1.5.5 SEGREGATION

Segregation is not a crystallization mechanism in the sense that it forms a particle, increases or reduces its size. However, it can have a significant effect on the final product quality and is therefore introduced in this section. Particle segregation is a result of slip with respect to the liquid motion. An important effect that can only be described if segregation is taken into account is the non-uniform distribution of solids in a crystallizer. For example, if the circulation intensity in a batch crystallizer is lowered, the relative amount of solids in the lower region of the crystallizer will increase. Particle segregation is a function of particle size, liquid velocity, solids concentration and the difference in material density between the liquid and solid phase.

1.6 MODELLING AND DESIGN OF CRYSTALLIZATION PROCESSES

The product composition or internal state of a crystalline product is determined during its formation by a combination of crystallization mechanisms or events. Furthermore, crystalline products are of a distributed nature, i.e. they possess a range of values for the internal states of the individual crystals constituting the product. The distributed nature is a result of these individual crystals having different formation histories, i.e. during their stay in a crystallizer they do not all experience the various crystallization mechanisms at the same time and at the same rate. The rates of the crystallization mechanisms are a function of both the process conditions (slurry states) experienced by the individual crystal and its crystal properties (internal crystal states).

1.6.1 SPATIAL DISTRIBUTION

Process conditions, such as supersaturation, energy dissipation, pressure, temperature and the concentration of the particles with certain properties, will rarely be uniformly distributed within a crystallizer. Non-uniformity will increase with increased crystallizer scale and increasing rates of crystallization mechanisms that change one or more of these process conditions. The process condition with

the strongest gradients is typically the energy dissipation followed by the supersaturation. Prediction of product composition thus requires knowledge about the crystals location, the process conditions in the various regions of a crystallizer, and the process conditions dependencies of the rates of the various crystallization mechanisms.

Although process conditions are far from uniformly distributed in most crystallizers, geometrically lumped descriptions of the crystallization processes in a vessel still prevail. Such descriptions will rarely provide reliable predictions of product quality for scale-up purposes, as the following issues will illustrate this:

I. The mean specific power input of the impeller, which is often used to predict secondary nucleation due to particle-impeller collisions, contains no hydrodynamic information on the velocity gradients in the vicinity of the impeller. As a result, the differences in collision velocities (magnitude and angle) using two different impellers (pitch and Rushton turbine) operated at the same mean specific power input are not taken into account.

II. A geometrically lumped description only yields one average value for the supersaturation, thus ignoring the presence of peak values. This is to be expected in the upper region of a batch cooling crystallizer, which is a cooler region and therefore high supersaturation levels observed. A lumped description of the batch crystallization process will probably ignore or definitely underestimate the occurrence of certain phenomena, such as nucleation and growth.

III. Whenever there is a difference in material density of the solid and liquid phase, particle segregation will occur to some extent. The particle segregation extent depends on the internal circulation rate induced by the impeller. If particle segregation is such that the smaller particles will have a larger residence time in the cooling zone compared to the larger particles, the growth rate of these particles will be above average. In a geometrically lumped description of such a process, this can be described only by reducing the growth rate constant of the smaller particles. The error in this approach becomes evident when the internal circulation rate is increased, particle segregation decreases and the growth rate of these particles approaches average values.

Other problems encountered in practise when a kinetic model, of which the parameters were estimated from experiments in a non-ideally mixed crystallizer, is applied to another crystallizer scale or type. These kinetic parameters are often significantly contaminated by hydrodynamic information and are therefore crystallizer and operating conditions specific.

1.6.2 DYNAMIC BEHAVIOUR

Process conditions within a pharmaceutical batch crystallizer change with time. Consequently, the product quality resulting from a crystallization process will not always be constant with time. Dynamics in product quality are usually most noticeable in the crystal size distribution. The process behaviour in batch cooling crystallization processes depends on the crystallization mechanisms such as nucleation and growth. Process control of batch crystallization processes is of paramount importance and is reliant on process and operating conditions employed. For instance, if an uncontrolled cooling regime is implemented, primary nucleation occurs due to high supersaturation peaks generated. High supersaturation levels elevate the nucleation and growth rates significantly, resulting in poor product quality and wide crystal size distributions. Controlled cooling combined with seeding in batch processes, allows for the supersaturation to be kept constant and primary nucleation to be significantly reduced. This allows for the product quality to be vastly improved. As decisions taken during design determine to a great extent the controllability of a process, the effect of process dynamics on product quality and process performance should not be postponed to the control system design stage. Dynamic modelling of crystallization processes is therefore essential from the process design stage onwards.

1.7 CRYSTALLIZATION PROCESS MODELLING

Scale-up design of pharmaceutical crystallization processes requires the need for a predictive modelling framework that captures the crystallizer geometry, operating conditions, process conditions, crystallization kinetics, product composition and

finally product performance. This has been discussed in this chapter and the requirements illustrated in the schematic (Fig.1.1.).

A second category of requirements is related to practical considerations such as computational time and robustness. The balance between these two categories of requirements depends on the type of engineering activity. For instance, the requirement for a predictive model decreases as one shifts the emphasis from the design of process equipment and operating conditions to the design of a new operating policy and further to model-based control. At the same time, the need for short computational times and robustness are significantly more important for control than off-line design purposes.

The main focus of this research is on the design of pharmaceutical batch cooling suspension crystallization processes for an organic fine chemical. Therefore, the primary focus here is on the modelling framework with predictive capabilities. Industrial crystallization is a spatially distributed and time dependent process involving a product with distributed properties. A comprehensive crystallization process and product model should consist of a framework providing resolution with respect to (i) the external co-ordinates representing the geometrical shape of the crystallizer (ii) the internal co-ordinates such as crystal size, shape and internal energy (iii) the time co-ordinate. The framework developed contains the following components such as:

I. Development of thermodynamic models to include solubility and physical properties.
II. Development of kinetic models for primary nucleation, secondary nucleation, growth, attrition, breakage and agglomeration.
III. Hydrodynamic models to estimate liquid flow, solid flow, fluid shear and energy dissipation.
IV. Implementation of conservation equations: mass balances, concentration balances, energy balances and population balances. Population balances are used to describe the evolution of distributed properties such as size. The number of distributed properties taken into account determines the number of internal co-ordinates.

Use of such a process model involves first principle modelling of all crystallization phenomena at all scales. At present it is difficult to derive the knowledge and understanding of all these phenomena from first principle models only. Heuristics, laboratory and pilot scale experimental data are therefore still used for the design and optimisation of suspension crystallization processes. Secondly, for certain crystallization process phenomena, present computational capabilities are not sufficient to perform crystallization process simulations and therefore optimisation investigations are out of the question at this moment using a first principle model. For example, morphology predictions and hydrodynamic simulations require computational times on the order of magnitude of days or even weeks. Hence crystallization models developed need to be of a hybrid nature consisting of a combination of first principle and heuristic models as presented in this research.

1.8 CONCLUSIONS

The quality of a crystalline product is in practise defined in terms of product performance characteristics, which are typically of a qualitative nature and equipment dependent, whereas first principal crystallization models predict crystal quality in terms of size, morphology and purity. Bridging the gap between product performance and product composition is a challenging step in the design of crystallization processes and products. A fully predictive model for crystallization processes and products requires a framework that provides resolution in external co-ordinates, internal co-ordinates and time. The modelling framework for a batch cooling suspension crystallization process as investigated in this research must include conservation equations, first principle models for thermodynamics and kinetics, and performance models in order to correctly capture equipment geometry, operating conditions, process condition, crystallization kinetics, product composition and finally product performance. Numerical solution of such a detailed and complex process is currently not acceptable under the timeframe considered and therefore requires the introduction of heuristics.

1.9 RESEARCH OBEJECTIVES

Considering the problems exhibited in pharmaceutical crystallizations including the lack of a generic design and scale-up procedure and predictive tool to overcome these problems, the overall objective of this research is to develop a model for pharmaceutical crystallization systems aimed at obtaining a better design in less time.

This involves crystallization processes producing particles of the desired quality and crystal size distribution. It also includes good performance in terms of the yield, energy efficiency, availability, minimal batch time, stability and controllability. Consequently both product design and process design need to be covered by this design procedure. Less time refers to the fact that at present months or years are spent on the laboratory scale and pilot plant; involving long periods of trouble shooting and optimisation including plant commissioning and satisfactory operation are often required. Reduction of these time losses is highly desirable as there is a high demand in the market for cheap and effective pharmaceutical products. Moreover, the development of a design tool should also result in traceable and transparent design processes. Villadsen (1997) and Wintermantel (1999) observed that no reliable systematic design procedures exist for the design of processes involving structured products, such as crystallization.

Therefore the requirement is for the development of a systematic design procedure to structure and simplify the design of crystallization processes in terms of product design.

Design tools are tools, which represent and generate domain knowledge that is needed to perform one or more design activities. Domain knowledge can be presented as data, models and heuristics. For some crystallization design activities commercial tools are available. A major omission is a design tool for the analysis and optimisation of process design alternatives. The absence of such a tool, which must reliably scale-up molecular scale interactions from the laboratory scale to processes carried out on an industrial scale. Many processes are designed empirically and a large number of process variables must be set and determined by experience. As a result, process yields are often disappointing and particles are frequently too small or oversized or exhibit high coefficient of variations.

Hence there is a need to develop a crystallization process model for predictive scale-up of the product quality and performance as a function of the crystallization method, operating and process conditions including equipment type and size.

To achieve this goal, it is necessary to be able to predict the spatially distributed, crystal size and time dependent crystallization kinetics. The crystallization kinetics determines the quality and crystal size distribution of the pharmaceutical products. To predict crystallization kinetics requires the knowledge of crystal properties, thermodynamic properties, hydrodynamic conditions and particle mechanics including particle interactions. With respect to predictive requirements, use of first principles is desirable. At present though, it is not possible to derive this knowledge and understanding from first principles only. This is due to the lack of physical understanding and computational technology limitations. Consequently, heuristics, data from laboratory and pilot plant scale experiments continues to play a huge role in the domain knowledge necessary for the design and optimisation of crystallization processes as depicted in this research.

1.10 PHARMACEUTICAL CRYSTALLIZATIONS

The research will focus on the crystallization of a relatively moderate soluble organic fine chemical. The crystallization method used by GlaxoSmithKline pharmaceuticals i.e. the method employed to generate supersaturation is by cooling. Supersaturation is the driving force for crystallization, can be created by employing a cooling regime, and otherwise known as cooling crystallization. The operational mode used is batch. A large number of crystallizer types exist in practise (Bamforth, 1965). The most common types are stirred tank, draft tube with and without baffles.

As crystallization is rarely a stand-alone process, it is also important to define the system boundary with respect to the overall process.

The origin of a crystallization system's feed is the upstream part of the overall process. In some cases the mother liquor is recycled after solid/liquid separation of the crystallization systems product. Multiple crystallization stages may occur in the manufacture of a pharmaceutical product.

The product of a crystallization system is a slurry, often referred to as the magma, i.e. consisting of the solid and liquid phase.

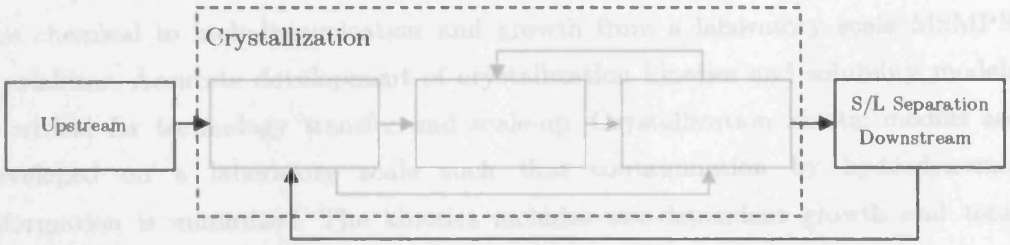

Figure.1.2: *System boundary for a crystallization process in the pharmaceutical industry.*

A solid/liquid separator is often used to separate this slurry into a flow containing predominantly crystals and a flow containing predominantly liquid. The crystalline product typically carries with it adhering mother liquor that is typically in the range of 2-10 weight percent of the crystals. Solid/liquid separation is usually performed with filters or centrifuges. This separation is the first step of the downstream solids processing after the crystallization system. Subsequent steps in the pharmaceutical industry include washing, drying, milling and tabletting.

1.11 THESIS STRUCTURE

The main focus of this research is in the development of a compartmental modelling framework specifically designed for batch cooling crystallization processes.

In chapter 2, a hierarchical design procedure is highlighted that can be applicable to other crystallization processes in addition to batch crystallizations. The design of a crystalline product and crystallization stage is covered.

In chapter 3, the development of an accurate equilibrium solute concentration model based on the use of ATR-UV spectroscopy is described. The experimental results are validated using other solubility techniques. Finally, thermodynamic properties such as the enthalpy of crystallization are estimated.

In chapter 4, the use of Lasentec FBRM, an accurate on-line 'in-situ' measurement technique to monitor crystallization processes including the use of a

process video imaging and development of a novel continuous laboratory scale MSMPR cooling crystallizer is discussed.

Chapter 5 focuses on the development of crystallization kinetics for the organic fine chemical to include nucleation and growth from a laboratory scale MSMPR crystallizer. Accurate development of crystallization kinetics and solubility models is critical for technology transfer and scale-up. Crystallization kinetic models are developed on a laboratory scale such that contamination by hydrodynamic information is minimized. The kinetics includes size-dependent growth and total nucleation.

In chapter 6, the development of an attrition rate model as a function of the supersaturation and specific energy dissipation rate is discussed. The Lasentec FBRM instrument is used in a novel way to monitor particulate disruption on-line and in real time.

In chapter 7, CFD simulations investigating mixing and heat transfer upon scale-up is discussed. In particular there is a focus on using specific power input per unit mass as a scale-up criteria and reasons provided for the failure of common scale-up criteria.

Chapter 8 describes the use of Computational Fluid Dynamics to determine hydrodynamic information including the influence of the presence of the solid phase on the mother liquor during batch cooling suspension crystallizations in agitated vessels. Computational Fluid Dynamics is also used to aid the development of a novel compartmental modelling framework. The development of a hierarchical design procedure and a predictive batch cooling suspension crystallization modelling framework are subjects discussed in Chapter 9. Key elements of the modelling framework are presented using a compartmental modelling approach to separate the effects of the crystallization kinetics (size-dependent growth, secondary nucleation and attrition) and overall hydrodynamics including segregation models.

Chapter 10 describes the use of gPROMS, a dynamic software package used for the predictive scale-up of batch crystallization processes using a lumped description and the compartmental modelling framework proposed in this research. The recommendations for further research development necessary for a robust generic predictive crystallization model are also discussed. This involves developing

physical models to describe crystallization kinetic phenomena and to provide a base for linking molecular and macroscale interactions.

Chapter 2

HIERARCHICAL DESIGN PROCEDURE FOR CRYSTALLIZATION PROCESSES

2.1 INTRODUCTION

Predictive process and product models are necessary but not sufficient for the design of crystallization processes and products that meet the specified performance criteria. In addition to models, there is also a need for a systematic design procedure outlining the various steps in the design process and the design tools necessary. Typical benefits to arise from the use of a systematic design procedure are as follows,

I. The ability to deliver crystallization process designs of a higher quality.
II. A reduction in the duration of the overall design process, e.g. by removing the need for pilot scale experiments for scale-up purposes (design efficiency). This is the most important design requirement aspect as there is a need to reduce the time necessary to introduce innovative pharmaceutical drug candidates into the market.
III. Reproducibility of the design process. This is essential to improve on existing designs and to identify any remaining errors in the applied domain knowledge and/or design procedure.
IV. A mutual awareness in a design team of the tasks that the various members have in the various stages of the design process.

A systematic and sufficiently detailed procedure is not yet available for the design of crystallization processes. One of the reasons for the lack of activity in this research area is undoubtedly the lack of predictive models for analysis and optimization of design alternatives. Villadsen (1997) and Wintermantel (1999) also identified a lack of systematic procedures and design tools for structured products for general separation/crystallization processes.

Starting with the field of systematic design procedures for chemical engineering processes, Rajagopal et al. (1992) developed a hierarchical design procedure for solids processes. This procedure is based on the pioneering work of Douglas (1985) concerned with the conceptual design of vapour/liquid processes. More specific design procedures have been developed for fractional crystallization (Dye and Ng, 1995), reactive crystallization (Berry and Ng, 1997) and the interactions between the crystallization step and the downstream processing (Rossiter and Douglas, 1986). These procedures mainly focus upon the synthesis and (economic) evaluation tasks of the design process.

Design procedures originating from the field of crystallization include work by de Jong (1984), Bennett (1984, 1993) and Mersmann (1988). These procedures contain many useful elements with respect to process and equipment design, but pay little attention to product design. Whereas these procedures obviously incorporate more detailed crystallization knowledge than those developed by Douglas, Ng and co-workers, they lack some significant elements. For instance, following one of the procedures developed by de Jong, Bennett and Mersmann can lead to a considerable number of implicit decisions. Furthermore, if the design resulting from one of these procedures does not satisfy all the design specifications, there is usually no methodology for generating design alternatives. The systematic design procedure presented in the remainder of this chapter contains many elements from both the field of systematic design procedures for chemical engineering processes in general as well as from the field of crystallization. Models used within this procedure are of both a rigorous and empirical nature. Heuristics are considered useful because their application is usually rapid and relatively simple. Furthermore, heuristics are often the only alternative for domains where fundamental knowledge is not available or applicable.

There are also a large number of design variables that can influence the filterability of a pharmaceutical development process for example and therefore design tasks muse be considered as well (Fig.2.1).

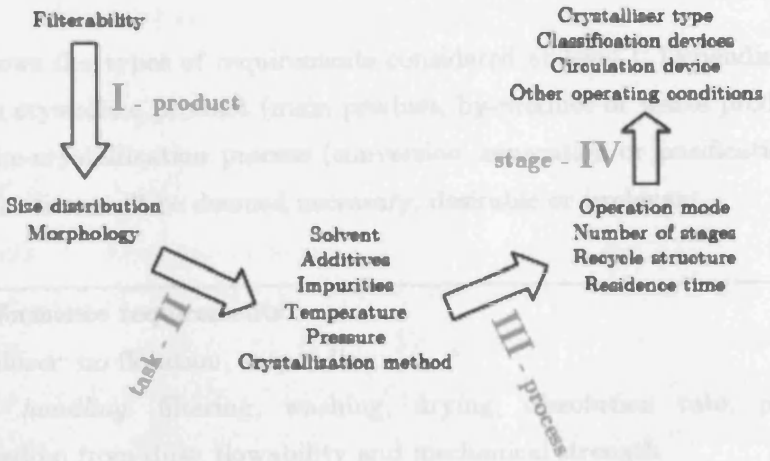

Figure 2.1: Design tasks required in crystallization processes (Bermingham, 2003).

2.2 DESIGN HIERARCHY

The design of crystallization products and processes involves too many design specifications and degrees of freedom to be considered simultaneously. The first step in the development of a systematic design procedure for crystallization processes and products is to decompose the design process into sub problems concerned with fewer design specifications and degrees of freedom. Here a hierarchical decomposition proposed by Bermingham (2003) that largely resembles the chain consisting of equipment geometry and operating conditions, process conditions, crystallization kinetics and product composition is considered. The design hierarchy consists of one level at which the initial design specifications are formulated and four design levels and are summarized as follows,

I. Initial design specifications
II. Design of the crystalline product
III. Physical/Chemical Design of the crystallization process
IV. Flowsheet design of the crystallization process
V. Design of the crystallization process

2.3 INITIAL DESIGN SPECIFICATIONS

Table 2.1 shows the types of requirements considered at level I. Depending on the nature of the crystalline product (main product, by-product or waste product) and the role of the crystallization process (conversion, separation or purification) some design specifications will be deemed necessary, desirable or irrelevant.

Product performance requirements
In the crystallizer: no flotation, suspending
Downstream handling: filtering, washing, drying, dissolution rate, pneumatic handling, freedom from dust, flowability and mechanical strength
Customer application: no caking in storage, dissolution rate, mechanical strength, freedom from dust, bulk density or porosity
Process requirements
Feed composition, production capacity, yield, energy consumption, controllability, reproducibility, resiliency, availability and SHE considerations
Design process requirements
Design budget, time to market, in-house or licensed technology, available skilled design staff, traceability, and explicitness of design decisions

Table 2.1: *Shows the initial design specifications: Design level I*

The product performance requirements listed in Table 2.1 above are examples of criteria used in practice to specify the required quality of a crystalline product. A detailed explanation of some of these requirements is given. First of all, the yield of crystallization processes is described. For cooling crystallization processes, the yield is calculated from the initial or feed solution composition and the solute solubility at the final or product temperature for respectively batch operation. If the crystalline product is a hydrate, account must be taken of the water incorporated in the crystal lattice, since this water is not available for retaining the solute in solution (Bennett, 1993). The yield is also influenced in most processes by the removal of some mother liquor as a result of adherence to the crystal surface

during solid/liquid separation. The adhering mother liquor is typically in the range of two to ten percent of the crystal weight (Bennett, 1984).

Secondly, the reliability of the crystallization process must be considered. The main phenomenon is to determine whether a batch crystallization process is prone to fouling. For batch processes, controlling the fouling is the determining factor in improving their economic performance

Whether fouling or encrustation will occur depends firstly on the solubility characteristics of the fouling component. The location in the crystallizer where fouling occurs, depends on the method of supersaturation generation, e.g. on heat exchange surfaces in cooling crystallizers and on the walls. As with regards to the design process requirements, these are also largely self-explanatory and are mainly taken into account implicitly in the remainder of this chapter.

2.4 DESIGN OF THE CRYSTALLINE PRODUCT

At this design level, the aim is to determine which product composition is required to meet the product performance criteria, i.e. the product related initial design specifications. Some examples of the relationship between product performance and product composition criteria are,

I. Filterability and freedom of dust are strongly related to the content of fine particles. Reduction of the fines content is a common requirement in practice, in order to increase the throughput and availability of downstream solids handling.

II. Although large crystals are preferred for many applications, there are also cases where small crystals are favoured, e.g. dry powders for inhalation products.

III. The liquor inclusion content is in its turn related to crystal size or more specifically to the surface area per unit crystal mass. As small crystals have a relatively large surface area, they will typically contain more adhering mother liquor after filtration than larger crystals.

IV. The bulk density is determined by polymorphism and morphology of the crystals.

V. The caking tendency in storage is related to the liquor inclusion content.

Design specifications Objectives and Constraints		Design Variables	Domain knowledge
Product:	• SHE considerations	*Discrete:*	• Filterability tests and models: permeability and compressibility
• Filterability	• Pneumatic handling	• Polymorphism	
• No caking in storage	• Freedom from dust		
	• Flowability	*Continuous:*	
• No flotation	• Mechanical strength	• Morphology	• Shear tests
• Suspendability		• Crystal size distribution	• Indentation tests
• Washability	• Abrasion resistance		• Caking tests
• Dryability	• Bulk density or porosity	• Purity	• Flowability tests
• Dissolution rate		• Maximum inclusion content	• Safety aspects
	• Aesthetic appearance		

Table 2.2: *Design Level II - Design of the crystalline product (Bermingham, 2003).*

Most of the relevant domain knowledge for this design level belongs to the field of particle technology, and has a strong empirical character. This is mainly due to the fact that product performance criteria are often equipment specific and hence cannot be defined and quantified generically. The development of fundamental knowledge in this field is further complicated by the need to account for distributed properties. Depending on the importance of the product performance criteria, much experimental work may be needed for this design level. The design alternatives, i.e. sets of design variables, are propagated to design level II, where they are treated as design specifications.

2.4.1 PHYSICAL/CHEMICAL DESIGN OF THE CRYSTALLISATION TASK

The design specifications of level III, the physical/chemical design of the crystallization task, are composed of process requirements from level I and propagated product composition characteristics from level II.

2.4.2 SOLVENT, ADDITIVES AND IMPURITIES

The polymorphism and morphology of the crystalline product are influenced by the choice of solvent and additives, crystallization temperature and crystal growth rates. The domain knowledge required for this selection issue was traditionally obtained from experimental work, but the latter is increasingly being replaced by molecular modelling.

Design specifications Objectives and Constraints	Design and Operational Variables	Domain knowledge
Process: • Production capacity • Feed composition • Yield • Energy consumption • Availability • SHE considerations *Product* • Polymorphism • Morphology • Crystal size distribution • Purity • Maximum inclusion content	*Discrete:* • Crystallization method • Feed purification • Recrystallization step • Solvent(s) • Additive(s) • Material of construction *Continuous:* • Pressure range • Temperature range • Concentration solvent(s) • Concentration additive(s)	• Thermodynamic activity of species, components in solid, liquid and vapour phase • Adsorption (energy) of components, species on the various crystal faces • Scaling or encrustation tendency of components, species • Metastable zone with respect to homogeneous and heterogeneous primary nucleation • Physical properties, e.g. material densities and specific heats • Safety aspects

Table 2.3: *Design Level III - Physical/chemical design of the crystallization task (Bermingham, 2003).*

This modelling technique involves first principles calculations for the adsorption energy of a component on a specific crystal face. The same knowledge is also essential to determine the sensitivity of the crystal purity, morphology and polymorphism for impurities in the feed, and hence determine the need for feed purification. Another possible source of impurities is the construction material used for the crystallizer, auxiliary equipment and piping. Solvent selection also has a significant influence on the attainable size range of a crystalline product. Selecting a solvent that results in a high solubility for a given solute typically leads to low relative supersaturation levels, low primary nucleation rates, high crystal growth rates and hence to large crystal sizes. Recently, predictive polymorphism and crystal habit software based on pattern recognition and not on first principles has made the need for high throughput screening to potentially become obsolete.

2.4.3 CRYSTALLISATION METHOD

The crystallization method is mainly selected on the basis of the thermodynamics of the solid/liquid equilibrium. A heuristic scheme for this selection process, based upon melt temperatures, *Tmelt*, and equilibrium concentrations, *Ceq*, is given in Figure 2.2.

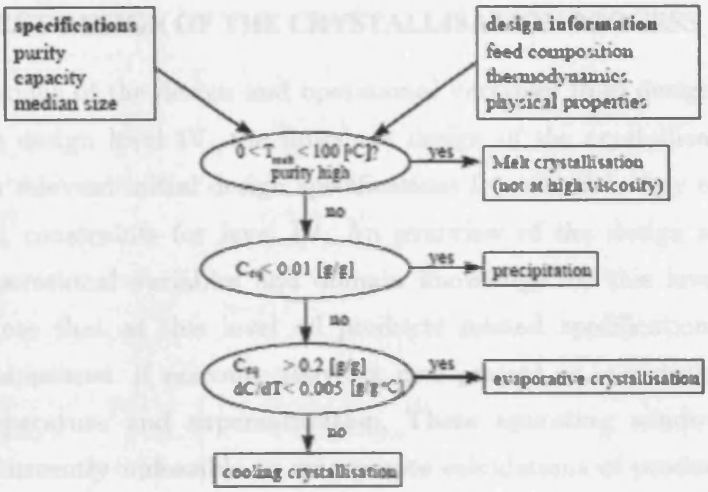

Figure 2.2: *Heuristic scheme available for typical crystallization selection (Bermingham, 2003).*

Other factors influencing this selection are the scaling tendencies of components present in the solution and the production capacity. For instance, the availability of a direct cooling crystallization process can be reduced significantly by scaling on the cooling surface. Depending on the added value of the product, this loss in availability may or may not be considered a problem.

2.4.4 OTHER DESIGN VARIABLES

Operating conditions such as pressure and temperature are chosen such to obtain the highest possible yield, while obeying SHE constraints. Purity considerations determine the necessity for re-crystallization steps and the maximum crystal growth rate. With increasing growth rates the tendency of components to co-crystallize and entrapment of mother liquor increase. This introduces an upper limit for the supersaturation. The maximum allowable supersaturation also depends on the metastable zone. When the concentration significantly exceeds this zone, excessive primary nucleation may occur, which is usually undesirable as it decreases the average crystal size.

2.5 FLOWSHEET DESIGN OF THE CRYSTALLISATION PROCESS

The realizations of the design and operational variables from design level III are propagated to design level IV, the flowsheet design of the crystallization process. Together with relevant initial design specifications from level I, they constitute the objectives and constraints for level IV. An overview of the design specifications, design and operational variables and domain knowledge for this level is given in Table. 2.4. Note that at this level all products related specifications except the CSD have disappeared. If relevant, they are now present as operating windows for pressure, temperature and supersaturation. These operating windows are used, because it is currently unfeasible to incorporate calculations of product properties, such as morphology and polymorphism, into dynamic process models including population balances.

To analyze the consequences of the choices at this design level on the CSD, a predictive process model consisting of thermodynamics, kinetics, mass, energy and population balances are required. As mentioned before, kinetic models cannot yet be derived from first principles only. Experimental design, experimentation and parameter estimation are hence an intrinsic step in crystallization design. The following chapters of this thesis are concerned with the development of a general crystallization process model for analysis and optimization with respect to the CSD as well as domain knowledge acquisition concerning the kinetics, solubility and thermodynamics.

2.5.1 OPERATION MODE

Criteria to select batch or semi-batch operation include a low production capacity, short time-to-market, a short product lifetime, high value products, severe encrustation problems and a narrow CSD. According to Bennett (1993), continuous operation is typically only economically viable for relatively large production rates, viz from approximately 50 tons of product per day and upward. Nevertheless, a bulk product such as sugar is still produced batch wise because it leads to much narrower crystal size distributions than can be obtained from continuous processes.

Design specifications Objectives and Constraints	Design and Operational Variables	Domain knowledge
Process: • Production capacity • Feed composition • Crystallization method • Yield • Pressure range • Temperature range • Supersaturation range • Energy consumption • Availability, controllability and Resiliency • SHE considerations *Product:* • Crystal size distribution	*Discrete:* • Operation mode • Number of stages • Feed configuration • Recycle structure • Location purge streams *Continuous:* • Residence time in each stage or batch time • Recycle flow rates • Purge flow rate • Pressure and/or temperature in each stage • Heating/cooling duty or trajectory • Heat exchange rates	• Thermodynamic activity of species, components in solid, liquid and vapour phase • Physical properties, e.g. material densities, specific heats and viscosities • Crystallisation kinetics, i.e. rate expressions for the nucleation, growth, attrition, agglomeration and breakage of crystals • Fouling kinetics • Shape factors of the crystalline components • Fire and explosion index

Table 2.4: *Design Level IV - Flowsheet design of the crystallization process (Bermingham, 2003).*

Another reason for producing bulk crystalline materials via batch operation is the presence of materials that have a very strong fouling tendency and consequently lead to frequent interruption of an otherwise continuous operation. Batch crystallization is also employed when temperature or product characteristics require unusual precautions, or where very expensive materials are being handled and losses must be minimized, or when the cooling range is very wide (Bennett, 1984). Finally, batch operated processes provide more flexibility with respect to feedstock and product requirements as they can be more easily adapted.

2.6 DESIGN OF A CRYSTALLISER STAGE

Practically all the design specifications from the previous level are present at this design level. The set is extended with equipment related specifications and with design and operational variables propagated from the previous level (Table 2.5).

All product related specifications except the CSD appear implicitly in the form of operating windows for pressure, temperature and supersaturation.

Design specifications Objectives and Constraints	Design and Operational Variables	Domain knowledge
Process: • Production capacity • Feed composition • Crystallization method • Yield • Operation mode • Pressure and temperature range • Supersaturation range • Residence time (distribution) • Heat exchange rates • No boiling in heat exchanger • No entrainment of droplets by vapour • Suspension criterion • Availability, controllability and resiliency • SHE considerations *Product:* • Crystal size distribution	*Discrete:* • Crystalliser type • Fines classification and dissolution/clear liquor advance • Product classification • Heat exchanger type • Circulation device *Continuous:* • Equipment dimensions • Feed location • Product removal location • Solids concentration • Circulation flow rate • Operating conditions of classification devices • Flow rate through heat exchanger	• Equipment characteristics • Hydrodynamics • Thermodynamic activity of species, components in solid, liquid and vapour phase • Physical properties, e.g. material densities, specific heats and viscosities • Crystallization kinetics, i.e. rate expressions for the nucleation, growth, attrition, agglomeration and breakage of crystals • Fouling kinetics • Shape factors of the crystalline components

Table 2.5: *Design level V- Design of a crystallization stage.*

At this level, hydrodynamics is added to the fields of domain knowledge. Applications of this knowledge include the sizing and operation of classification devices, determination of minimum circulation rates for adequate particle suspension and optimization of the product removal location. The use of computational fluid dynamics (CFD) packages to obtain hydrodynamic information is on the increase for crystallization processes. However, it is not yet feasible to combine CFD techniques with population balance modelling.

To analyze the influence of kinetic-hydrodynamic interactions on the product CSD, the general crystallization model mentioned at the previous design level can be used in a compartmental manner to account for spatially distributed process conditions. The final design alternative can be propagated to a next level, design of instrumentation and control. This design level is not considered in this thesis.

2.7 DISCUSSION

Although the scope of this thesis does not include crystallization methods such as precipitation, melt crystallization, evaporative crystallization and super critical crystallizations, the hierarchical design procedure review in this chapter is equally applicable and generic to all crystallization processes.

Similarly, whereas the main focus of this thesis is on (grass roots) design of crystallization processes, the presented hierarchical procedure should also be of use for other engineering activities, such as debottlenecking and optimizing the operation of an existing plant.

However, the real validation of this hierarchical design procedure requires (industrial) case studies. Recently, Westhoff (2002) presented the first real crystallizer design based upon this procedure. He found the design procedure useful to structure the design process of a pilot plant crystallizer and to identify design problems at an early stage. An interesting alternative for further testing of the proposed design procedure is to let rather inexperienced designers use this procedure and see whether they can come up with designs that are considered of a high quality by experienced designers.

2.8 CONCLUSIONS

The hierarchical decomposition used in the design procedure presented in this chapter is believed to provide a rational and useful breakdown of the crystallization process and product design problem. However, so far this has only been confirmed by one application (Westhoff, 2002). The hierarchical design procedure allows one to systematically deal with the large number of initial design specifications, design and operational variables and the wide variety of domain knowledge involved. Structuring of the relevant specifications, variables and knowledge at each design level simplifies the design problem and provides valuable insights for designers. It also ensures that design decisions are taken explicitly, which is of essence for the reproducibility of the design process. Furthermore, the design procedure also serves to highlight major shortcomings in design knowledge, i.e. product performance/composition relations (level II) and predictive models for the concise analysis of flowsheets (level IV) and comprehensive analysis of single crystallizers (level IV) with respect to the CSD and supersaturation.

The hierarchical decomposition does not imply a once through process with respect to the design levels.

The value of heuristics and shortcut models on the one hand and rigorous first principle models on the other are both acknowledged. The heuristics and shortcut models as used in many conventional design procedures for crystallization are valuable synthesis tools as they allow a rapid development of a base case design, in particular with respect to most of the discrete design decisions. Rigorous first principle models play an important role in both synthesis (mathematical optimization) and analysis (simulation).

The ultimate aim of this design procedure, viz better designs in less time, cannot be guaranteed until the procedure as a whole is validated by means of industrial case studies. Main achievements so far are improved understanding of the design process and identification of bottlenecks in domain knowledge. Finally, although the design procedure has been presented in the light of grassroots design, it can also be largely applied to retrofit and optimization of process operation. One should think of synthesis at levels II and III and analysis tools at all levels.

Chapter 3

SOLUTE CONCENTRATION MEASUREMENT USING ATR-UV SPECTROSCOPY INCLUDING OTHER TECHNIQUES

ABSTRACT

Modelling, design and control of organic batch cooling crystallization processes requires accurate solute concentration and supersaturation measurement. De-supersaturation rate controls the crystallization kinetics and determines the crystal size distribution (CSD) and product quality. In this thesis, a quick, robust and convenient technique for the successful measurement of solute concentration of an important organic fine chemical using Attenuated Total Reflectance Ultra-Violet (ATR-UV) spectroscopy is described. The use of multivariate analysis (chemometrics) and Partial Least Squares (PLS) using UMETRICS SIMCA-P software for the calibration and measurement of solute concentration is also briefly described.

3.1 INTRODUCTION

The production of organic fine chemicals requires the final drug substance to comply with the required specifications for chemical purity and physical form. Physical form specifications will often require that important organic compounds conform to a specific crystal size distribution (CSD). Crystallization is a critical unit operation, not only for separation and purification but also as a method of obtaining the correct physical form. Control of physical form in pharmaceutical batch cooling crystallizations requires accurate control of supersaturation and de-supersaturation. Several methods for the measurement of concentration and supersaturation are available but often require sampling and analysis of solution at different temperatures. These techniques are tedious and are prone to sampling errors.

Various on-line techniques have been used to monitor solute concentration, including conductivity (Hlozny et al., 1992), density measurement (Qui and Rasmuson, 1994; Miller and Rawlings, 1994), and measurement of refractive index (Nývlt, 1994), but all of these suffer serious shortcomings.

Recently, Attenuated Total Reflectance Fourier Transform Infrared (ATR-FTIR) spectroscopy has been reported as an accurate on-line technique for the measurement of supersaturation and solute concentration. Dunuwila used the ATR-FTIR probe to successfully measure the solubility and supersaturation of aqueous citric acid solutions (Dunuwila et al., 1994) and investigated the application of using the ATR-FTIR probe to monitor crystallization phenomena in batch crystallizations (Dunuwila, 1996a; Dunuwila and Berglund, 1996b). The metastable zone limit was also measured using ATR-FTIR spectroscopy (Dunuwila and Berglund, 1997). Groen et al. (1999) and Lewiner et al. (2001) also successfully measured solute concentrations using an ATR-FTIR probe. Togkalidou et al. (2001) included the use of chemometrics in ATR-FTIR spectroscopy to predict solute concentrations. Derdour et al. (2003) used an ATR-FTIR probe to measure the supersaturation levels on-line during crystallization and successfully measured the concentration of impurities with high solids content during organic solution crystallization. Groen et al. (2003) used ATR-FTIR spectroscopy in a novel application to control batch-cooling crystallization processes based on

supersaturation measurements. Furthermore, Groen and Roberts (2004) also used ATR-FTIR spectroscopy for the in-situ process monitoring of urea crystallization. However ATR-FTIR spectroscopy units are typically not mobile and maybe difficult to set-up and bulky depending on the type of spectrometer used and laboratory culture.

In this section, the use of ATR-UV for the *'in-situ'* measurement of solution concentration as an attractive alternative to ATR-FTIR spectroscopy is described. Multivariate data analysis incorporating partial least squares (PLS) is a powerful tool that uses all the relevant absorption spectrum of the organic compound. This provides for a more accurate calculation of the solute concentration rather than using peak height analysis for this system under investigation. The analysis of UV spectra requires PLS treatment due to the spectra being rather featureless.

3.2 ATR-UV SPECTROSCOPY TECHNIQUE

3.2.1 THEORY

ATR is based on light passing from a material with a high refractive index (Attenuated Total Reflection crystal) to a material with lower refractive index (solution).

Basic reflection optics under total internal reflection conditions provides a damped evanescent wave travelling normally to the reflection surface and can be partially absorbed by the solute before being reflected back into the probe. The reflected light is therefore attenuated, causing a measurable reduction in the output signal dependent upon the absorbance of the solution. The measuring head of the probe is made from sapphire (Fig. 3.1a) and is equipped with three reflecting surfaces. Each immersion probe has two fibre-optic cables. One is used for transmission of the light from the light source of the spectrophotometer to the measuring head of the immersion probe. The second conducts the signal, which is the light that has passed through the sample and back to the spectrophotometer.

The glass fibres transmit light inside the fibre-optics. The ends of the fibre-optic cables are connected to the spectrophotometer using SMA connectors. ATR-UV probes are suitable for the direct measurement of strongly absorbing solutions in which the UV absorption of the solvent does not mask the solute absorption and where standard transmission probes cannot be used.

The advantages offered by the use of the ATR-UV probe for the measuring of supersaturation levels and monitoring crystallization processes on-line are significant,

I. No sampling is required. Problems with the use of temperature-controlled external sampling loops and phase separation devices (i.e. syringe filters) are eliminated.
II. The technique is relatively insensitive to the presence of solid particles in solution as the ATR probe is based on surface measurements and is not affected by particles and bubbles.
III. There is no disturbance of equilibria in the system during the experiment.
IV. On-line measurements of slurries with high solids content are possible.
V. Flexible fibre optics connection to the probe facilitating easy set up.

The following need to be considered when using the ATR-UV probe,

I. The solute must have a high UV absorption compared to the solvent. The solute needs to have a sufficiently different absorbtion so that it can be measured in the presence of solvent. Care needs to be taken that the solvent spectrum does not saturate the detector.

II. The fibre optics of the particular spectrophotometer used limits the range of measurement from 220 – 600 nm.

In certain crystallization systems it maybe possible that during the onset of crystallization subsequent particle formation may occur on the ATR crystal surface and cleaning maybe necessary. This however was not evident for the solute concentration measurement for this organic fine chemical under investigation.

3.3 EXPERIMENTAL SYSTEM AND PROCEDURE

The ATR-UV spectroscopy system used in this study consisted of 4 four Hellma 661.812 immersion UV probes, fitted with fibre optic cables (Hellma GmbH). The UV system was a Zeiss MCS 551 spectrophotometer coupled to an MCM 400 Multiplexer and MCM monitoring software was used for data acquisition. Absorbance spectra were obtained with ATR-UV probes, which use 3-bounce sapphire ATR probe tips. The ATR-UV probes were directly immersed in the suspension to be measured contained in 50 ml HEL AutoMate mini-reactor vessels (Fig. 3.1b). The solution temperatures and other process variables were controlled by the use of HEL winISO software, for on-line monitoring of process conditions. Temperature control was achieved using jacketed vessels connected to Julabo heater chiller units. Temperature control was achieved using the external vessel jackets only. The internal coil heaters provided with the HEL equipment was not used in order to prevent localised superheating. The solvents used were rigorously purged with nitrogen to remove oxygen and to minimise oxidation of the organic compound. The small vessel size ensures homogeneity of particles in the slurry and heat losses are negligible. *'In-situ'* measurements were performed using four ATR-UV probes located in each of the four HEL AutoMate vessels. In order to measure the concentration of the organic compound in solution, a calibration model was necessary and achieved using chemometrics. Chemometrics is defined as the use of multivariate data analysis and mathematical tools to extract information from chemical data.

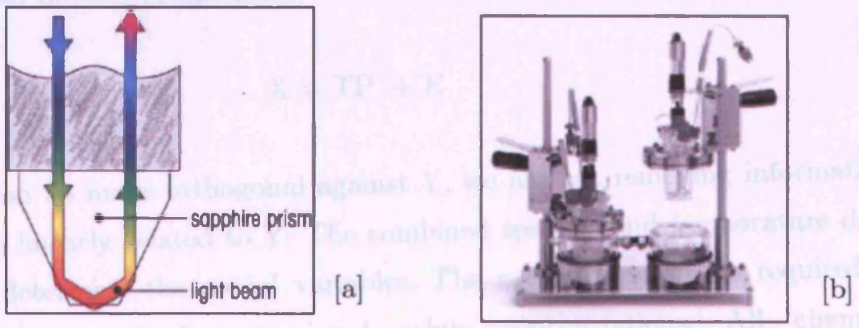

Figure 3.1: *[a] UV probe head with path taken by the UV light off three reflecting surfaces (left) [b] HEL AutoMate reaction vessels (right).*

The UV absorbtion is directly proportional to the concentration of the solution according to the Beer-Lambert law. However, the intensity of the spectra was temperature dependent due to changes in refractive index and hence changes in path length for the ATR crystal. A temperature correction was applied to the absorption spectra prior to construction of the calibration model. This was achieved by using multivariate analysis (Chatfield and Collins, 1980) and a Partial Least Squares (PLS) model (Geladi, 1988; Höskuldsson, 1988).

Multivariable calibration for ATR-UV spectroscopy is used to develop a quantitative relation between the absorbance spectra (the matrix X) and the solute concentrations (in the matrix Y). Multivariable calibration of UV absorbance spectra therefore requires the pre-processing of experimental data. The reason is that the UV spectra contain systematic variations such as baseline drift that is unrelated to the responses (Y). The variation in X that is unrelated to Y may pose problems in multivariate modelling and produce inaccurate solute concentration predictions when applied to new samples.

OSC is a baseline correction solution in our case that removes bilinear components from X, which are orthogonal to Y, i.e. make a signal correction that does not remove information about Y from the absorbance spectra. A PLS related filtering solution is established that removes only so much of X as is unrelated (orthogonal) to Y. X denotes the (N x K) matrix of unfiltered, uncorrected, set of absorbance spectra. The number of samples and variables of the calibration set are N and K respectively, while E is the (N x K) matrix of 'filtered' absorbance spectra, T is a (N x A) matrix of scores, and P' a (K x A) matrix of filters. A is the number of OSC components.

$$X = TP' + E \qquad [3.1]$$

If T can be made orthogonal against Y, we are not removing information from X that is linearly related to Y. The combined spectral and temperature data were used to determine the model variables. The predictor variables required for the PLS model were the associated solute concentrations. All chemometrics calculations were performed using UMETRICS SIMCA-P software, which is a statistical data analysis package developed by UMETRICS (www.umetrics.com).

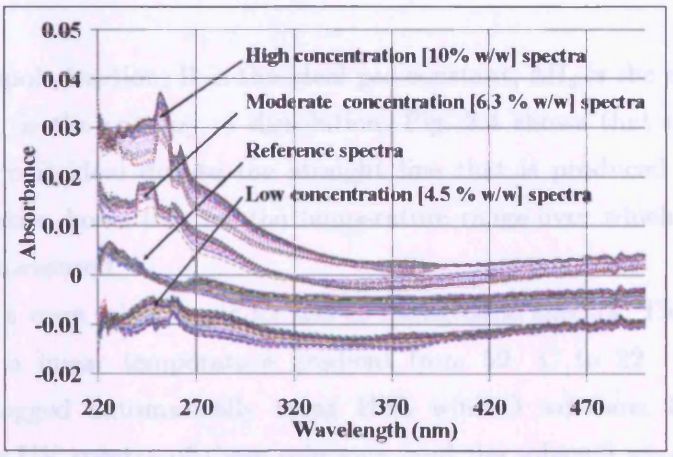

Figure 3.2: UV calibration spectra – uncorrected.

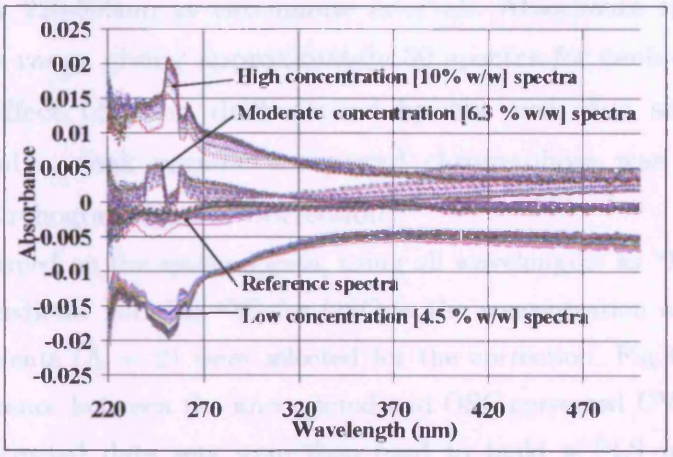

Figure 3.3: UV calibration spectra – OSC corrected data.

Three standard solutions were prepared using a low (4.5% w/w), moderate (6.3% w/w) and high (10% w/w) solute concentration in a binary solvent mixture of isopropyl-alcohol-water (93/7% v/v) including a reference solvent solution. Three standard solute concentrations were sufficient for the calibration of the organic fine chemical system as the system is ideal (Fig.3.4). The revised van't Hoff equation for the mixing of solutions (Beiny and Mullin, 1987) was used to describe the solubility of any solute in a solvent mixture providing that the solution exhibits ideal behaviour and is represented as follows,

$$\ln X = -\frac{\Delta H_d}{RT} + \frac{\Delta S_d}{R} \qquad [3.2]$$

Where X is the mole fraction, R is the ideal gas constant, ΔH_d is the enthalpy of dissolution and ΔS_d is the entropy of dissolution. Fig. 3.4 shows that the organic fine chemical system is ideal due to the straight line that is produced and hence the van't Hoff equation holds true for the temperature range over which the solute concentration was measured.

Reference spectra were taken in air for use as background spectra. The solutions were cooled using a linear temperature gradient from 59 C to 22 C and the temperature was logged automatically using HEL winISO software. During the cooling process, the UV spectra of these solutions (and the solvent) were measured automatically over 220-500nm at two-minute intervals. Absorbance spectra were recorded over this range giving approximately 50 spectra for each calibration standard. The effect of lamp drift caused by the use of a single beam spectrometer, and a weak organic compound chromaphore was minimised by using OSC (Orthogonal Signal Correction).

OSC was performed on the spectral data, using all wavelengths as "X" variables and setting the predictor variable "Y" for OSC as the concentration as discussed. Two OSC components (A = 2) were selected for the correction. Fig.3.2 and Fig. 3.3 show the difference between the uncorrected and OSC corrected UV calibration spectra. These corrected data sets were then used to build a PLS model. After OSC was performed, the temperature was re-included in the "X" data. The "X" data were mean-centered (Temperature also scaled to univariance) and the "Y" data mean-centered and scaled to univariance.

The optimum model contained 2 PLS components, which accounted for 99.9% of the variance in the data. By looking at the scores plot for the model (Fig. 3.6), it can be seen that the data points were grouped in approximately parallel lines. The spacing between the lines shows the effect of concentration and the spacing between the points for each standard the effect of temperature. The four separated points in the bottom right hand side of the plot were caused by significant temperature differences caused by poor reactor temperature control. This is as a result of the slow response time of the HEL AutoMate reactor vessels. However, these points are still valid for use in the PLS model.

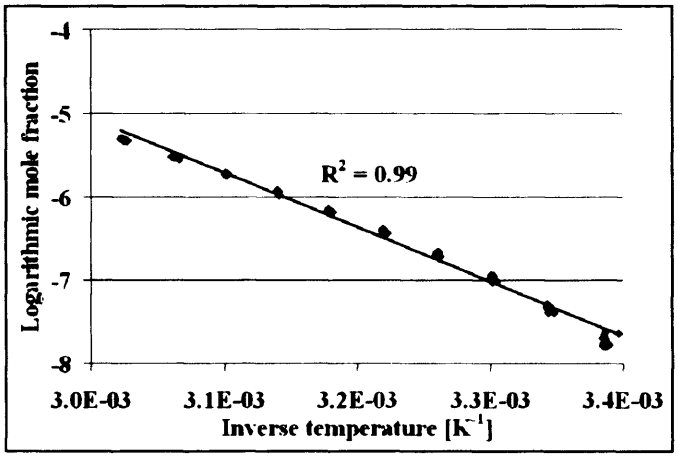

Figure 3.4: *Van't Hoff plot of the organic fine chemical solubility data.*

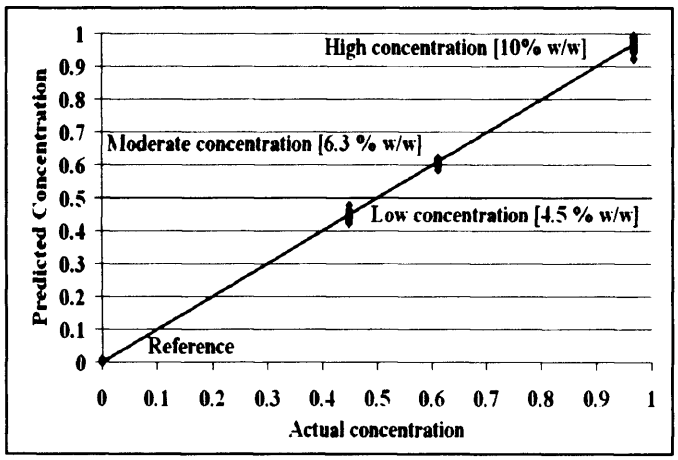

Figure 3.5: *OSC PLS validation model split into 2 showing the predicated and actual concentrations.*

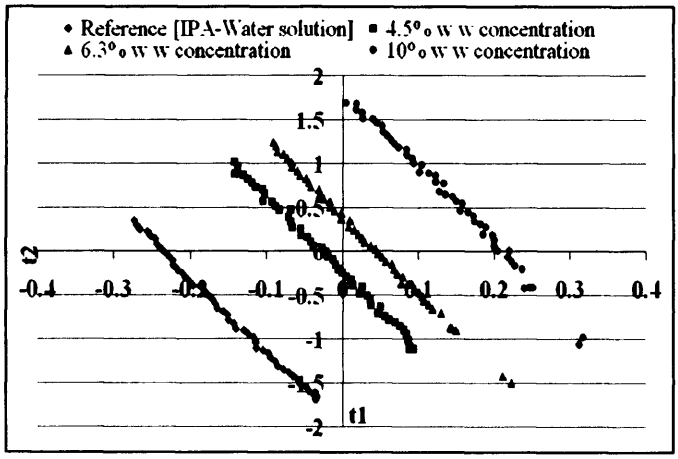

Figure 3.6: *Scores plot for PLS model.*

The model was validated by splitting the data set into two halves (alternate odd and even observations) and rebuilding the model using one half of the dataset, with the unused data now being used as the prediction set. The whole UV spectrum was used in the PLS model, and no variable selection was performed. Fig. 3.5 shows the observed and predicted concentrations for the PLS model. This model using 2 components was used to determine solubility of the organic fine chemical.

3.4 RESULTS AND DISCUSSION

Once the calibration was complete, the UV-ATR measurement was used to determine solubility data using a ramping technique and to determine the time required for the organic compound in aqueous isopropyl alcohol system to reach equilibrium.

Saturated slurry consisting of 13% w/w of the organic compound in an isopropyl-alcohol-water solvent system (93/7% v/v) was used in each of the four HEL AutoMate reaction vessels and the absorbance spectra of each solution was measured over a range of temperatures. In two HEL AutoMate vessels the temperature was set to 22 °C and spectra taken every 20 minutes (isothermal). In the remaining two vessels, the solution temperature was set to 22 °C then automatically increased by increments of 4 °C to 57 °C and allowed to equilibrate for 6 hours at each new temperature. Fig.3.7 shows the absorbance spectra with respect to the wavelength as the temperature was increased. UV absorption spectra were collected at intervals of 20 minutes. Spectral data showed a proportional increase in the absorbance as the solubility increased with temperature. Negligible differences in absorption spectra towards the end of each temperature step clearly showed that the system was at equilibrium. The combined spectral and temperature data were imported into SIMCA-P and pre-treated and scaled in the same way as the calibration set data (Section 3.3). By plotting the predicted concentration against temperature, an equilibrium solubility curve was constructed (Fig.3.8-3.9). The ATR-UV solubility data for the organic fine chemical was cross-validated by comparing the results with those obtained from a polythermal solubility measurement technique. The discrepancy between the two techniques

maybe due to the polythermal solubility data being overestimated due to continual ramping and solid dissolution leading to a dynamic equilibrium achieved or the poor UV absorbance of the organic fine chemical (Fig.3.9).

3.5 CONCLUSION

A calibration curve and a PLS temperature correction model was successfully constructed and validated using multivariate analysis.
OSC was applied to remove the effects of baseline drift. The calibration procedure used was simple and the method described in this paper can be applied to other organic compounds provided that the UV absorbance is sufficiently strong and that the spectrum of the solvent does not interfere with the compound spectrum. The ATR-UV spectroscopy unit is flexible, mobile and provides a convenient alternative for the accurate 'in-situ' real time measurement of solute concentration when compared to other techniques available. Solute concentration measurement using ATR-UV spectroscopy is an accurate technique for the measurement and monitoring of supersaturation levels during organic batch cooling crystallization processes. This is critical as the de-supersaturation rate determines the crystallization kinetics and the crystal size distribution.

3.6 POLYTHERMAL TECHNIQUE

3.6.1 EXPERIMENTATION

A polythermal or ramping technique is used to determine the equilibrium solute concentration including the metastable zone width of the organic fine chemical under investigation. The experimental apparatus used in this study consisted of a 250 ml closed glass jacket vessel as a water bath. Standard solutions of the organic fine chemical in a binary solvent mixture of isopropyl-alcohol-water (93:7% v/v) were prepared in 10 ml vials used as reaction vessels. The suspensions were injected into the vials containing miniature magnetic stirrers to provide efficient mixing. The vials were subsequently placed into the water bath whose temperature is regulated using a Grant heater/chiller unit.

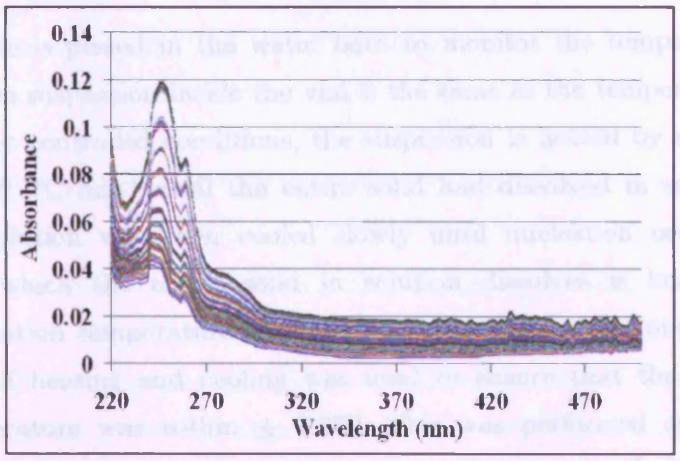

Figure 3.7: *UV absorbance spectra taken as the temperature is ramped.*

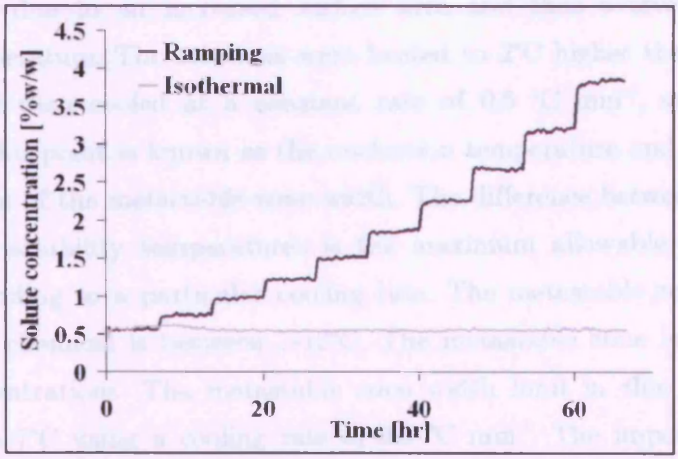

Figure 3.8: *Organic fine chemical solute concentration as the temperature is ramped from 22-55 °C including concentration under isothermal conditions.*

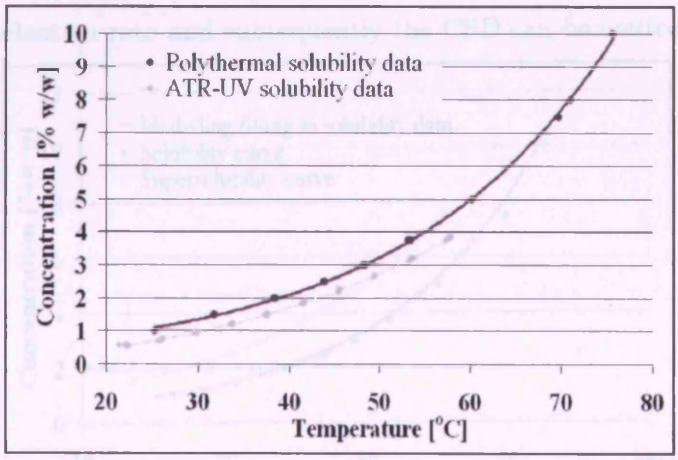

Figure 3.9: *Solubility curve for the organic compound using the ATR-UV spectroscopy technique and compared to a polythermal measurement technique.*

A thermocouple is placed in the water bath to monitor the temperature. The temperature of the suspension inside the vial is the same as the temperature of the water bath. Under controlled conditions, the suspension is heated by using a slow ramping rate of 0.1°C min^{-1} until the entire solid had dissolved in solution. The supersaturated solution was then cooled slowly until nucleation occurred. The temperature at which the entire solid in solution dissolves is known as the equilibrium saturation temperature and was determined by visual observation. A repetitive cycle of heating and cooling was used to ensure that the equilibrium saturation temperature was within ± 0.2°C. This was performed as the initial suspension contained agglomerated particles and would subsequently take a longer time to dissolve due to an increased surface area and thus overestimating the equilibrium temperature. The solutions were heated to 2°C higher than saturation temperature and then cooled at a constant rate of 0.5 °C min^{-1}, until the first nuclei formed. This point is known as the nucleation temperature and hence allows for the evaluation of the metastable zone width. The difference between nucleation and equilibrium solubility temperatures is the maximum allowable undercooling ($\Delta\theta_{max}$) corresponding to a particular cooling rate. The metastable zone width for the organic fine chemical is between 7-12°C. The metastable zone is narrower at the higher concentrations. The metastable zone width limit in this investigation was found to be 7°C using a cooling rate of 0.5 °C min^{-1}. The importance of the solubility and supersolubility curves is for the level of supersaturation to be maintained within the metastable zone in batch cooling suspension crystallizations such that the nucleation rate and subsequently the CSD can be controlled.

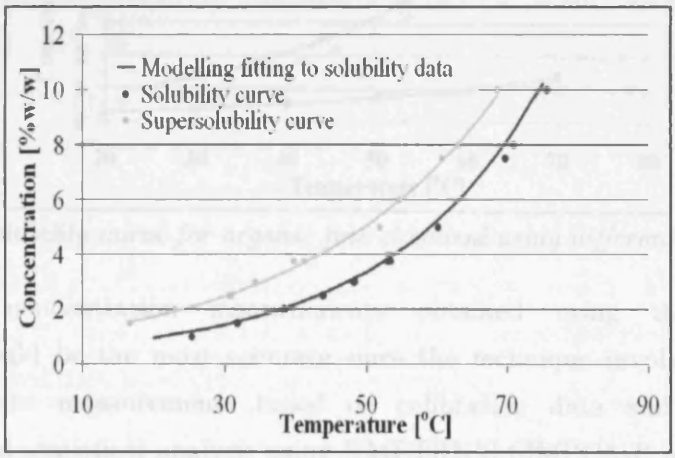

Figure 3.10: *Solubility and supersolubility curves of the organic fine chemical.*

Fig.3.10 shows the solubility and supersolubility curves for the organic fine chemical.

3.7 ISOTHERMAL SOLUBILITY USING HPLC TECHNIQUE

An isothermal solubility method using HPLC analysis to measure the solute concentration of the organic fine chemical was also used. The experimental apparatus used for the experiments were four HEL AutoMate reactor vessels. Oversaturated suspensions were prepared using excess solid phase and equilibrium achieved by increasing the temperature automatically from 20 °C to 70°C in increments of 10°C. The solutions were allowed to reach equilibrium for a period of two hours at each new temperature. Multiple samples were taken from the reactor vessels using pre-heated syringes fitted with filters at each temperature. The syringes were pre-heated using a hot blow drier in order to prevent spontaneous nucleation. HPLC was used to determine the equilibrium solute concentration. The type of HPLC instrument used to analyse samples was an Agilent 1100 with a diode array detector. Fig.3.11 shows the solubility curves produced using ATR-UV spectroscopy, HPLC and a polythermal (ramping) technique.

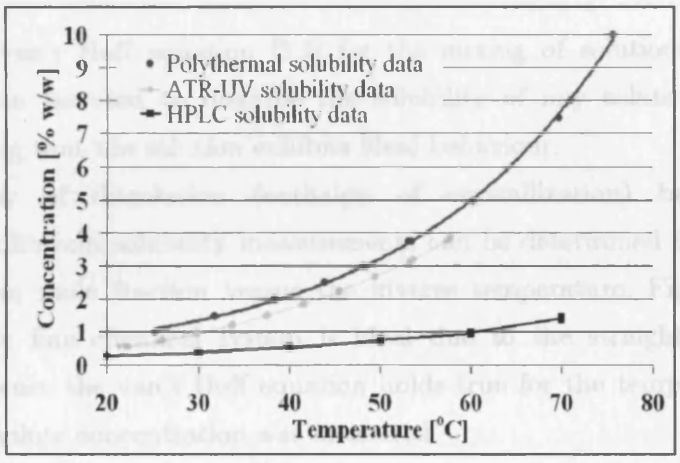

Figure 3.11: *Solubility curve for organic fine chemical using different techniques.*

The solute concentration measurements obtained using the ATR-UV spectroscopy should be the most accurate since the technique involves obtaining on-line and in-situ measurements based on calibration data and the use of chemometrics and statistical analysis using UMETRICS SIMPCA-P software. The

great advantage of using ATR-UV spectroscopy is that the time required for equilibrium to be obtained can be precisely determined. The discrepancy between ATR-UV spectroscopy and polythermal solute concentration measurements may be due to the organic fine chemical exhibiting poor UV absorbance. Another possible explanation is that during long periods of agitation the organic fine chemical is susceptible to aerial oxidation. HPLC analysis showed the presence of impurities in the solute whose concentration increases with an increase in temperature. The impurities may have influence the equilibrium solute concentration.

The disadvantage of using off-line methods such as HPLC is that accurate standardized solutions and dilutions are necessary, as this will affect the solute concentration measurements. The effectiveness of the sampling technique used also influences the solute concentration measurements significantly and off-line analysis is time consuming. The polythermal equilibrium solubility measurements show an excellent agreement with literature (Patience, 2002). But, the polythermal solubility measurements may be overestimated as a fast ramp rate is used and is also based on a dynamic and not a static equilibrium being achieved.

3.8 ENTHALPY OF CRYSTALLIZATION

The revised van't Hoff equation [3.2] for the mixing of solutions (Beiny and Mullin, 1987) can be used to describe the solubility of any solute in a solvent mixture providing that the solution exhibits ideal behaviour.

The enthalpy of dissolution (enthalpy of crystallization) based on the polythermal equilibrium solubility measurements can be determined from a plot of natural logarithm mole fraction versus the inverse temperature. Fig. 3.12 shows that the organic fine chemical system is ideal due to the straight line that is produced and hence the van't Hoff equation holds true for the temperature range over which the solute concentration was measured.

The enthalpy of dissolution (mixing) was determined to be -37.42 $kJmol^{-1}$ whereas the enthalpy of crystallization has a positive value. The entropy of dissolution was determined to be 0.07 $kJmol^{-1}$. For organic fine chemicals, typical enthalpies of crystallizations range from 5-20 $kJmol^{-1}$.

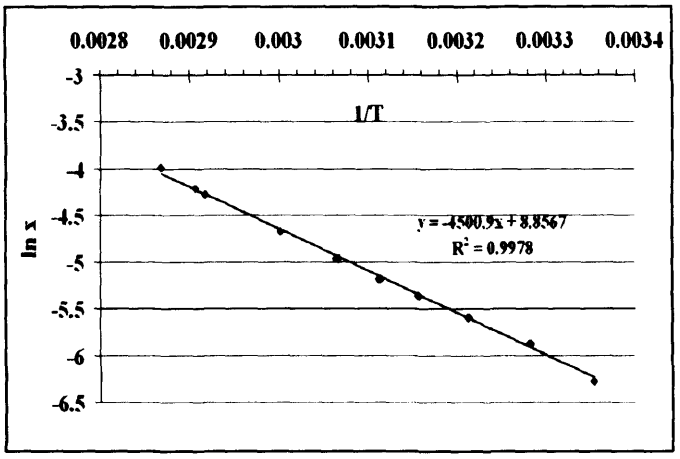

***Figure 3.12**: van't Hoff plot for organic fine chemical.*

The melting (fusion) temperature of the organic compound can be determined from the following relationship as follows,

$$\Delta H_d = T_m \Delta S_d \qquad [3.3]$$

The melting temperature was determined to be 236 ° C, whereas the actual melting point temperature of the pharmaceutical is 245 ° C.

3.9 EQUILIBRIUM SOLUTE CONCENTRATION MODEL DEVELOPMENT

The polythermal equilibrium solubility data can be directly fitted to the following equilibrium saturation solubility model,

$$C^*[T(t)] = a_o + a_1 T(t) + a_2 T^2(t), \qquad 20^o C \le T \le 70^o C \qquad [3.4]$$

where a_0, a_1 and a_2 are constants. Supersaturation (concentration driving force) can be defined as,

$$\Delta C(t) = C[T(t)] - C^*[T(t)] \qquad [3.5]$$

The relative supersaturation (σ) can be determined from the following expression as follows,

$$\sigma = \frac{C[T(t) - C^*[T(t)]}{C^*[T(t)]} = \frac{\Delta C(t)}{C^*[T(t)]} = S - 1 \qquad [3.6]$$

The final modelling equation for the polythermal equilibrium solubility is,

$$\log_{10} C^*[T] = 142 - 128 \log_{10} T + 28\left((\log_{10} T)^2\right) \qquad [3.7]$$

3.10 FURTHER WORK

The Lasentec FBRM probe is a powerful monitoring tool that can be applied to determine the point at, which material is completely dissolved in solution using a polythermal (ramping) method. User interfaces can be implemented to automatically monitor and record the temperature. The nucleation temperature can also be determined more precisely using the Lasentec FBRM method rather than visual observation. A more detailed investigation into the effects of the cooling rate and specific power input on the metastable zone all merit a closer examination. The of near infrared (NIR) spectroscopy as another process analytical technique combined with more advance chemometrics to measure and monitor solute concentration within batch pharmaceutical suspension cooling crystallizations should be considered.

Chapter 4

FOCUSED BEAM REFLECTANCE MEASUREMENT (FBRM) AND PROCESS VIDEO IMAGING (PVI) IN A MODIFIED MIXED SUSPENSION MIXED PRODUCT REMOVAL (MSMPR) COOLING CRYSTALLIZER

ABSTRACT

The FBRM instrument is a 'powerful' tool developed by Lasentec as an 'in-situ' particle monitoring technique for in-line real time measurement of particle size. This technique was successfully used to monitor steady state operation in a modified MSMPR crystallizer. The FBRM technique was also used to estimate crystallization kinetics. The FBRM particle size measurements were complimented by an in-line process video imaging (PVI) system developed 'in-house' by GlaxoSmithKline pharmaceuticals (Jennings et al., 2000), to visualize habit and crystal behaviour within an MSMPR crystallizer. SEM and light microscopy were used to study the crystal habit of the organic fine chemical in detail. The habit changes from acicular needle-like crystals during batch crystallizations to irregular parallelepiped crystals during MSMPR crystallizations. A comparison of the steady state crystal size distributions measured by low angle light scattering (LALLS) and FBRM was made, showing poor sensitivity of the FBRM technique to particles of less than 1μm hence the technique was not suitable for the measurement of crystallization kinetics for this pharmaceutical system.

4.1 INTRODUCTION

Crystal size distribution (CSD) measurements can be taken *off-line*, *on-line* or *in-line*. The FBRM method is a relatively new method developed by Lasentec and marketed by Mettler-Toledo to perform particle size measurements in the range of 0.25-1000 μm. The great advantage of this technique is that data is acquired on-line and in real time to give particle size data and population trends of particles in suspension. The technique does not require sampling or isolation that may contribute to changes in particle size and distribution due to breakage or agglomeration. The FBRM method allows an in-situ on-line measurement of particle size distribution technique of high concentration. It is non-invasive process analytical technique allowing for process control of crystallisation processes. It can be used to monitor polymorphic transitions including solvate formation during cooling crystallisations. The onset of nucleation can be detected and dissolution. These are all advantages over the Malvern MasterSizer. The FBRM, however, does not give a true particle size as it measures chord length distribution and hence produces a probability distribution that has to be converted using weight functions.The FBRM technique has been used widely in monitoring of crystallization processes. Wood-Kaczmar (2002) successfully used the FBRM technique for steady state CSD measurements in an MSMPR crystallizer, for the on-line measurement of crystallization kinetics for citric acid, which exhibits size-independent growth. Barett et al. (2002) applied the use of the FBRM technique to measure solubility and determine the metastable zone width for potash alum using a ramping method. Carreta et al. (2000) used FBRM to control the CSD using batch crystallizations.

This chapter reports an investigation into the *'in-situ'* use of the FBRM technique to monitor particle trends in-line and steady state operation in a modified continuous cooling MSMPR crystallizer. Also described is the use of process video imaging (PVI) developed by GlaxoSmithKline pharmaceuticals (Particle Science Group, Chemical Development Division) to monitor the progression of the MSMPR crystallizations in-line and used to provide additional information on particle habit for comparison with the FBRM measurements. The

limitation of using the Lasentec FBRM technique to estimate crystallization kinetics from CSD data for an organic fine chemical studied is discussed.

4.2 EXPERIMENTAL SYSTEM

The *Lasentec*© D600L FBRM instrument involves the use of a beam of laser light focused on the outside of a sapphire window. The beam is rotated at a constant speed of 2 $m.s^{-1}$ and the laser energy is reflected back into the probe by backscatter from particles on or close to the sapphire window. The duration of the backscatter is measured and represented as a particle chord length. Fig. 4.1 shows the operating principle of the Lasentec FBRM probe. The FBRM technique offers some attractive advantages over forward light scattering devices allowing the measurement of higher particle concentrations. A problem associated with backward light scatter is in the difficulty in detecting smooth spherical particles or particles suspended in liquids with refractive indices close to that of the particle. Smooth faceted particles will also strongly influence the backscatter pulse duration that is a measure of chord length. The Lasentec was programmed to measure the number of particles in the size range from 1-1000 μm being categorized into 38 channels.

The number based mean chord length $\left(\bar{Cn}\right)$ and the cube weighted chord length $\left(\bar{Cv}\right)$ (analogous to volume), are defined as follows,

$$\bar{Cn} = \frac{\sum_{i=1}^{k}\left[n_i \Big/ \sum_{i=1}^{k} M_i\right]}{\sum_{i=1}^{k} n_i \Big/ \sum_{i=1}^{k} n_i} = \frac{\sum_{i=1}^{k} n_i M_i}{\sum_{i=1}^{k} n_i M_i^0} \qquad [4.1]$$

$$\bar{Cv} = \frac{\sum_{i=1}^{k}\left[\left(n_i M_i^3 \Big/ \sum_{i=1}^{k} niM_i^3\right) M_i\right]}{\sum_{i=1}^{k} n_i M_i^3 \Big/ \sum_{i=1}^{k} n_i M_i^3} = \frac{\sum_{i=1}^{k} n_i M_i^4}{\sum_{i=1}^{k} n_i M_i^3} \qquad [4.2]$$

Where n_i = counts in individual measurement channel, M_i = midpoint of an individual channel and k is the upper channel number. For best results, the *Lasentec*© D600L probe tip, is located in a region of high turbulence above the

impeller in order to monitor the crystallization process (Fig.4.2). The measured chord lengths are counted, categorised and displayed as a distribution curve or as a trend of selected size ranges. The chord lengths may be represented as non - weighted, linear, square or cube-weighted distributions.

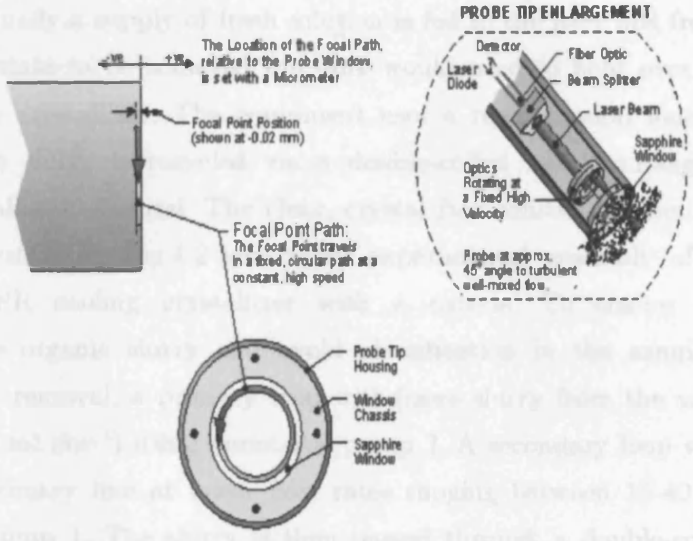

Figure 4.1: *Principles of Lasentec probe operation mechanism showing the focal point travelling in a fixed circular path at constant high speed.*

The PVI system, developed in-house by GlaxoSmithKline (GSK), consists of a video microscope, stroboscopic light source and video acquisition PC (Fig.4.2). The video microscope (Sony XC-55 CCD camera, Navitar Precise Eye Primary optics [x1 or x2 magnification] and Mitutoyo x2 long distance objective lens) was positioned perpendicular to the reactor, with the focus set just inside the inner glass wall of the MSMPR crystallizer. To minimize distortion through the curved crystallizer wall, an optical window was constructed from a flat glass plate attached to the outer wall of the crystallizer with optically matched adhesive. Blur free imaging of the moving particles was achieved using stroboscopic illumination via a liquid light guide (Polytec BVS-60, Lamda Photometrics. Uncompressed video (640x480 pixels at 30 frames per second) was captured direct to hard disk using Video Savant ™ software (IO Industries, London, Ontario, Canada). Size calibration was performed using a certified graticule positioned and imaged inside the crystallizer before commencing the experimental runs.

A modified continuous MSMPR crystallizer is briefly described in this chapter, in which a feed tank to continuously supply feed solution into the crystallizer is eliminated. The advantage of this modification is that it requires considerably less material than conventional MSMPR crystallizers. Organic fine chemicals are expensive and often only available in very limited quantities in early stages of development. Normally a supply of fresh solution is fed to the MSPMR from a feed tank. For steady state to be achieved the tank would need to hold over 10 times the volume of the crystallizer. The equipment uses a re-circulation loop through which the organic slurry is recycled via a double-coiled heat exchanger to re-dissolve the crystallized material. The clear, crystal free solution is then returned back into the crystallizer. Fig.4.2 shows the experimental assembly of the 0.5l continuous MSMPR cooling crystallizer with a recycle. To ensure isokinetic withdrawal of the organic slurry and avoid classification in the sampling tube during slow slurry removal, a primary loop withdraws slurry from the vessel at a high flowrate (350 ml min^{-1}) using peristaltic pump 2. A secondary loop withdraws slurry from the primary line at lower flow rates ranging between 15-40 ml min^{-1} using peristaltic pump 1. The slurry is then passed through a double-coiled heat exchanger to re-dissolve the suspended solid. The clear solution is then re-directed back into the MSMPR crystallizer. The mean residence time is calculated from the flow rate through the secondary circulation.

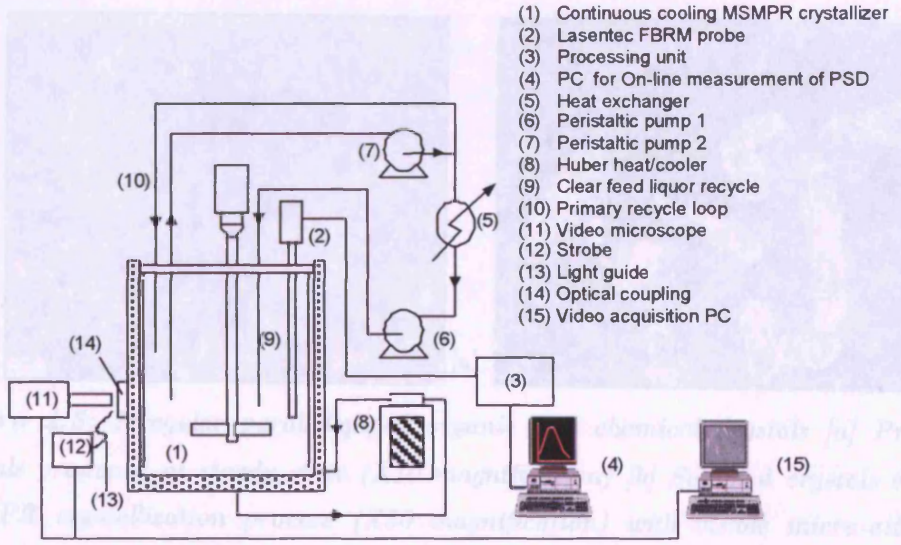

Figure 4.2: *Modified MSMPR crystallizer with FBRM and PVI systems.*

4.3 RESULTS AND DISCUSSION

4.3.1 CRYSTAL HABIT DETERMINATION

The crystal habit of the organic fine chemical was investigated using both light and scanning electron microscopes during programmed batch cooling crystallizations and continuous cooling MSMPR crystallizations. An Olympus BX 60M light microscope was used with magnifications ranging from x10 to x50. Particles were sampled during and at the end of the experiments and analysed visually. Scanning electron microscope (SEM) images were also taken using a JOEL JSM-820 instrument, capable of magnifications of up to x20000. The product crystals from the steady state continuous MSMPR cooling crystallizations (Fig.4.3a) including crystals sampled during the MSMPR crystallization process (Fig.4.3b) were found to be irregular and parallelepiped in shape. However, during rapid batch cooling crystallizations acicular needle-like product crystals are produced (Fig.4.4a). The crystal habit is therefore dependent on the operational mode. There is also some evidence to suggest that some agglomeration (cementation) or aggregates (loosely bonding) including significant micro-attrition of the organic fine chemical particles occurs during MSMPR crystallizations (Fig.4.4b and Fig.4.5b).

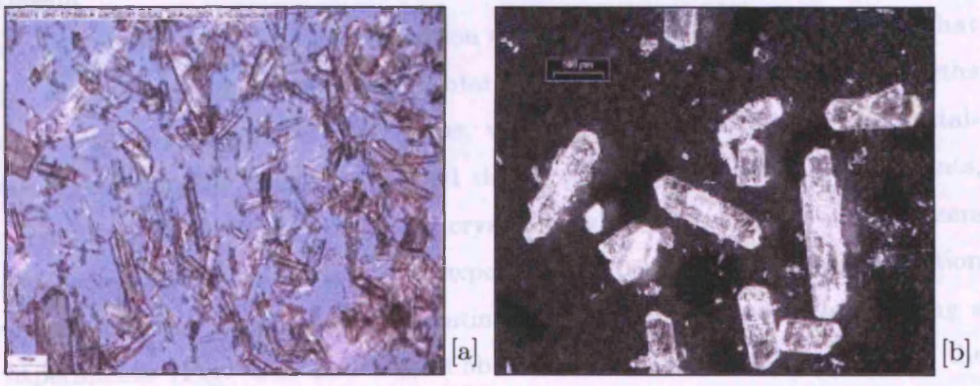

Figure 4.3: *Irregular parallelepiped organic fine chemical crystals [a] Product crystals produced at steady state (X10 magnification) [b] Sampled crystals during MSMPR crystallization process (X50 magnification) with visible micro-attrition fragments evident in both images.*

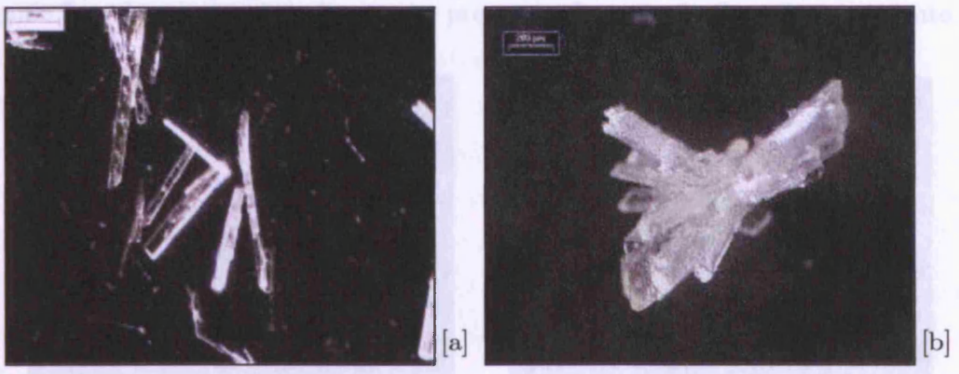

Figure 4.4: *[a] Acicular needle-like organic fine chemical crystals produced during rapid batch cooling crystallization [X10 magnification] [b] Agglomerated or aggregated organic fine chemical crystal [X50 magnification].*

From light microscope images there is not enough depth in the field and magnification to determine whether the particle formed is due to loose bonds, cementation or intergrowth. It is also difficult to distinguish from the light microscope images, whether the fine attrition particles, which are typically less than 10 μm, have sharp or rounded (due to healing and further growth) edges. A scanning electron microscope can be used to distinguish between these two phenomena.

Fig. 4.4b shows a 500-fold magnification of an organic fine chemical crystal that clearly exhibits agglomeration and intergrowth. There are also outgrowths (dendrites) from the main crystal stems, which may have formed after crystal-crystal, crystal-impeller collisions or fluid shear producing fine attrition fragments, while leaving micro-cavities within the crystalline structure. These cavities seem to have healed with time as they are exposed to supersaturation. Agglomeration effects were minimal under typical operating conditions but were evident during a few experiments (Fig. 4.5a and Fig. 4.5b). Therefore agglomeration is not the primary mechanism by which particles are formed and hence a size-dependent or independent agglomeration model to account for agglomeration events between particles of different size classes is not necessary. The agglomeration effects are typically observed, when long residence times are used for the MSMPR crystallizations.

A possible explanation for this phenomenon is that aerial oxidation of the organic fine chemical occurs due to the presence of oxygen in the solvent mixture.

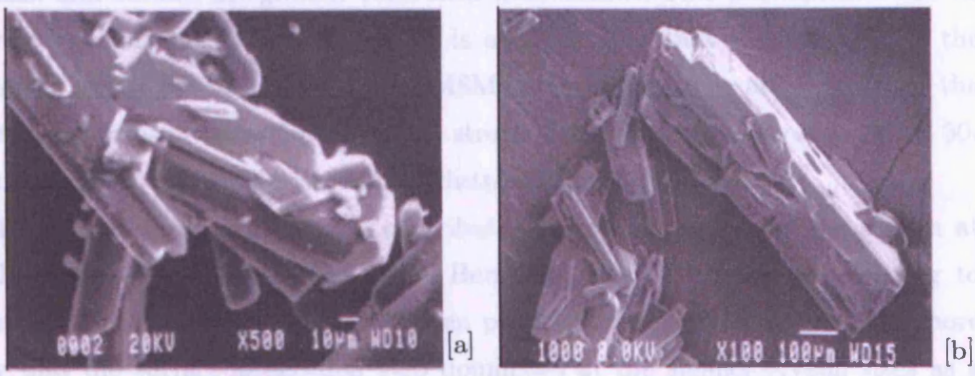

[a] [b]

Figure 4.5: *SEM images [a] Particulate agglomerate [b] Particulate attrition.*

This may have the effect of producing impurities within the crystallization system resulting in the induction of agglomeration effects. Moreover, it was also observed that in some steady state continuous cooling MSMPR crystallizations, lower growth and higher nucleation rates were estimated. Impurities may have been physically incorporated into the crystal lattice preventing the organic fine chemical molecule integration process. This was also confirmed as a result of higher levels of supersaturation being measured. Chen and Larson (1985) studied the effects of impurities on the calcium nitrate tetrahydrate system and also found the same evidence as described.

When attrition fragments are produced it is difficult to determine whether they are growing slowly, dissolving or a proportion are non-growers within the suspension. During rapid batch cooling crystallizations only crystal growth occurs with no secondary nucleation, attrition and agglomeration being observed (Fig.4.4a). Patience (2002) also observed the same behaviour under programmed batch cooling crystallizations for the organic fine chemical. Typically crystals larger than 150 µm are subject to micro-attrition effects during the MSMPR crystallization process as seen on the crystalline surface in Fig. 4.5b including intergrowth being evident. SEM microphotographs show that large crystals have rough surfaces as a result of the attrition process, whereas crystals less than 100

μm have smooth surfaces. The consequence of this observation is that the growth mechanism of the organic fine chemical may involve a combination of both diffusion and surface integration controlled mechanisms. This phenomenon can be described by an effectiveness factor. It is also assumed that the majority of the secondary nuclei produced during the MSMPR crystallizations are a result of the attrition mechanism contributing to the strong deviation at a size range below 50-80 μm ranges in the population density distributions.

These attrition fragments may contribute to growth rate dispersion affects at small sizes (Garside and Davey, 1980; Berglund, 1980; Ulrich, 1989), leading to different growth rates of crystals at given particle sizes. Therefore it will be more likely that the surface-integration step dominates at the smaller crystal sizes as a result of growth rate dispersion. Zacher and Mersmann (1995) showed that size-dependent growth is a direct manifestation of GRD in the potassium alum-water system and maybe a possible phenomenon occurring in this crystallization system. Fig. 4.3b also shows that as a result of the attrition process the crystal corners and edges become more rounded.

Tanrikulu (2000) and O'Meadra (1995) studied ammonium perchlorate and potassium sulphate crystals respectively and observed the same phenomena. However, from the population density distributions very little deviation from the ideal MSMPR theory occurs at the larger crystal sizes, which suggests that the attrition volume is low but the attrition rate seems significant leading to the assumption a micro-attrition mechanism. Attrition of particles may be due to the weak crystal structure or due to internal lattice strains (Van der Heijden, 1992).

Attrition rates have been modelled by carrying out experiments under non-growing conditions using different mean specific power inputs (Wojcik and Jones; 1998 and Mazarotta; 1992). These workers assume that distribution of fragments, rate and source of fragments will be representative in suspension crystallizers under growing conditions. This is unlikely however, due to the crystals losing their sharp edges and corners (O'Meadhra, 1995) and is confirmed in this work. The numerical technique used by Wojcik and Jones will be used to model attrition in this work due to its ease for evaluating disruption kernels and development of an attrition model. The effect of supersaturation on the attrition process can be assumed using the growth rate and supersaturation dependency.

4.3.2 REPRODUCIBILITY

The reproducibility of the steady state crystal size distributions from the MSMPR crystallizations for different runs using the Lasentec FBRM instrument was excellent (Fig.4.6). The runs were performed on different days with different solvent solutions made up under identical operating conditions. The reproducibility of the CSD should be high due to it being of paramount importance when using numerical regression techniques to determine crystallization kinetic parameters.

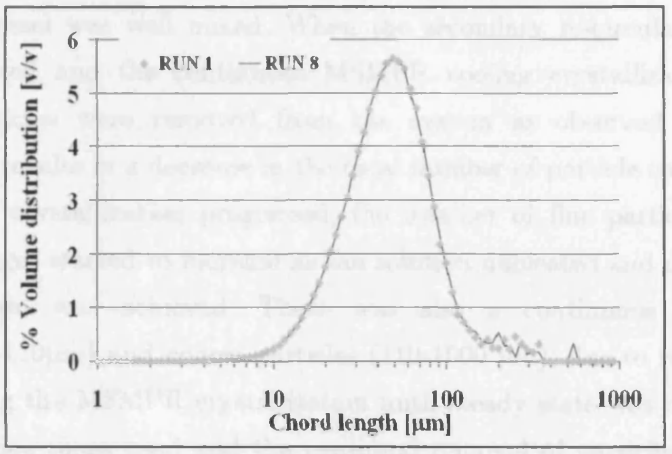

Figure 4.6: *Crystal size distribution reproducibility using Lasentec FBRM probe.*

4.3.3 LASENTEC FBRM MONITORING IN BATCH AND CONTINUOUS OPERATIONS

Fig. 4.7 shows the trend history of different particle size groups (fine, intermediate and coarse) using the Lasentec FBRM D600L instrument showing rapid crystallization onset and how the particle size range count changes with time during the course of a batch cooling crystallization. The Lasentec instrument was used to follow and monitor dissolution, re-crystallization, during MSMPR crystallizer operation and eventual steady state. A decrease in particle counts was observed when the organic fine chemical slurry was heated at 1°C min^{-1} representing dissolution as shown in Fig. 4.7 (Region 1). The supersaturated solution that is produced is then cooled at 1°C min^{-1} to 10°C. The FBRM detects the onset of crystallization as the solution is cooled. A thermocouple can be connected via a user interface allowing for the nucleation temperature to be

recorded. The number of particle counts approaches a maximum as the crystallization reaches equilibrium and supersaturation depleted. The effect of re-circulation of the slurry via the peristaltic pump was monitored using the FBRM. The particle trends over several size ranges remained constant after 30 minutes operation Fig. 4.7 (Region 3). This also confirmed that the peristaltic pump action was not damaging the particles in suspension. The high flowrate also ensured that external classification effects were kept to a minimum. Internal classification effects (segregation) were also assumed to be at a minimum as the working volume is small and the vessel was well mixed. When the secondary re-circulation loop or recycle was started and the continuous MSMPR cooling crystallization process commences, particles were removed from the system as observed in Fig. 4.7 (Region 4). This results in a decrease in the total number of particle counts. As the MSMPR cooling crystallization progressed, the number of fine particles (1-11μm and 11-32μm range) started to increase as the solution nucleated and crystals grew until steady state was achieved. There was also a continuous decrease in intermediate (32-110μm) and coarse particles (110-1000 μm), due to removal from the system during the MSMPR crystallization until steady state was reached. The low mean residence times used and the continual removal of particles resulted in few particles growing into or remaining in the large particle (110-1000 μm) range. Steady state shown in Fig.4.7 (Region 5) was reached after operating the MSMPR cooling crystallizer continuously for between 6-9 mean residence times depending on the initial solids loading and secondary re-circulation flowrate. These two factors affected the crystallizer performance and time required to reach steady state.

4.4 PROCESS VIDEO IMAGING

Video data of the whole continuous MSMPR cooling crystallization history using the PVI system was reviewed and selected video stills taken to illustrate changes in crystal morphology during the MSMPR crystallization phase (Fig.4.9). Initially, a large number of coarse and intermediate acicular crystals were evident as a result of the initial crystallization.

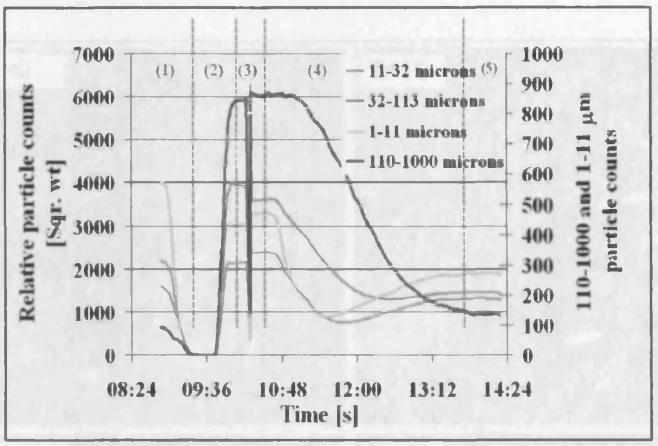

Figure 4.7: *In-line FBRM particle trends monitoring to include (1) Dissolution, (2) Re-crystallization, (3) Isokinetic withdrawal, (4) MSMPR operation and (5) Steady state.*

Fig. 4.8 shows the steady state crystal size distributions measured using the Lasentec FBRM instrument remaining unchanged for a period of over one mean residence time for a typical run.

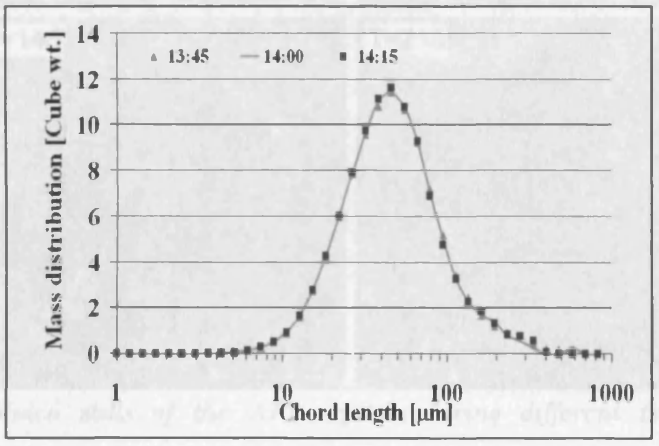

Figure 4.8: *Steady state MSMPR crystal size distributions.*

As the MSMPR crystallization progressed larger particles were gradually removed, while the nucleation and growth of finer particles became more evident. Excessive growth of individual crystals was prevented as a result of continuous removal from the crystallizer.

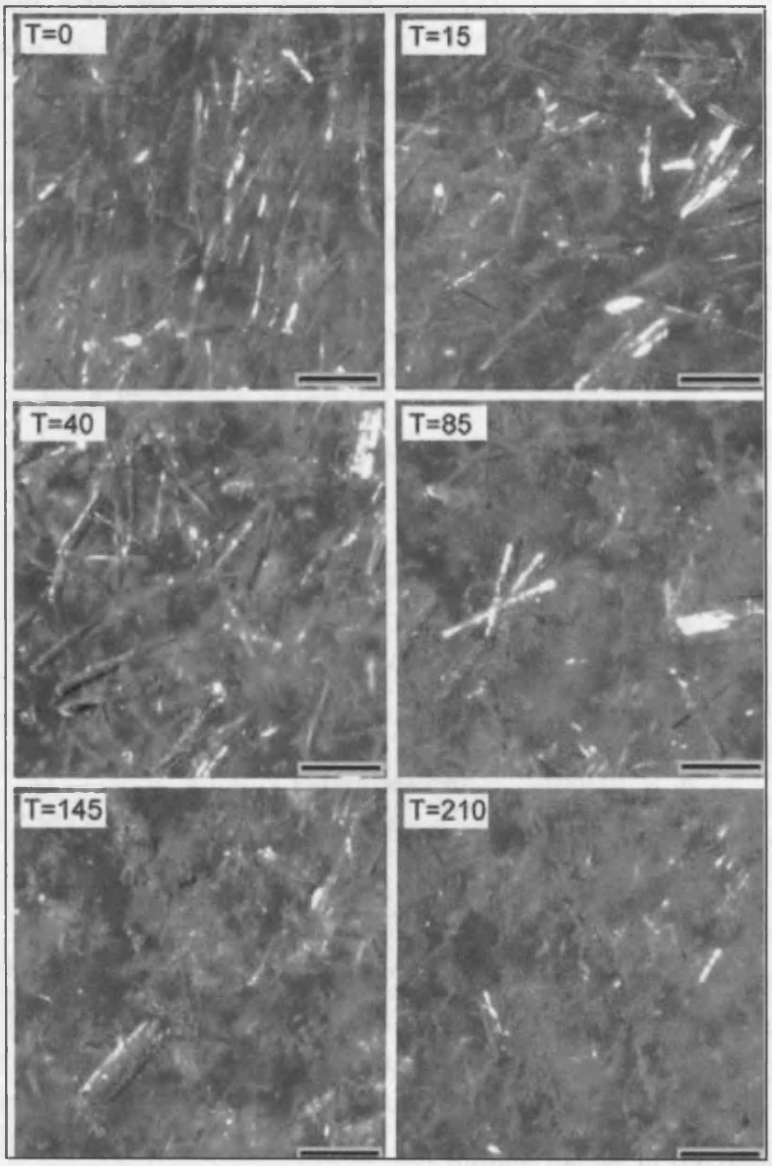

Figure 4.9: *Video stills of the API crystals during different times into the MSMPR crystallization process, showing a reduction in particle size as the coarse particles are removed from the crystallizer. Once steady state is reached, a few coarse particles remain. Nucleation and growth of new crystals is also evident. T = time in minutes. Scale bar = 300 μm.*

When steady state conditions were achieved, only a small proportion of large crystals greater than 100 μm in length remained after 200 minutes. These observations concurred with the Lasentec FBRM trend measurements.

Finally, Fig.4.10 shows a typical CSD produced during the initial batch cooling crystallization stage (07:00am) using a Lasentec FBRM and the change in the CSD during the continuous MSMPR crystallization stage at different times. At 07:25 am, an unsteady state CSD is evident, whereas after 11:00 am steady state operation within the MSMPR crystallizer is approached.

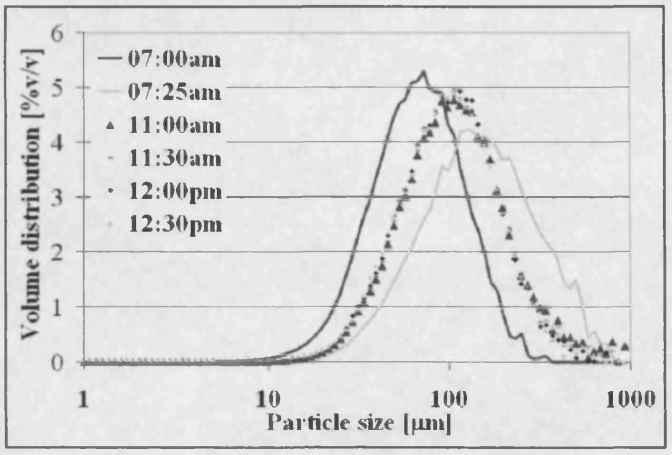

Figure 4.10: *CSD during batch and MSMPR crystallizer modes of operation for a typical run.*

We have shown that the Lasentec FBRM probe was ideally suited for monitoring the MSMPR crystallization process and steady state operation. The steady state CSD results measured using the Lasentec FBRM during the crystallizations were used to produce population density distributions from which growth and nucleation rates for the organic compound can be estimated using empirical correlations. However, the FBRM is not suitable for use in the estimation of growth and nucleation rates for the organic fine chemical. The FBRM probe significantly underestimated the number of small particles below 1μm.

4.5 COMPARISON BETWEEN LASENTEC FBRM AND MALVERN SYSTEMS

Crystallization kinetic studies carried out have shown that the organic fine chemical exhibits either growth rate dispersion (GRD) or size-dependent growth (SDG). It is difficult to distinguish between these two growth mechanisms in an

MSMPR crystallizer as described in Chapter 1. These growth phenomena give rise to a strong upward curvature of the population density distribution at particle sizes below 50-80 μm (Fig.4.10b). The upward curvature is not correctly captured when the Lasentec FBRM particle size measurements were used particularly at particle sizes less than 1μm. Hence it was not possible to model SDG or GRD growth mechanisms using empirical models effectively. A Malvern instrument was used to measure CSDs and successfully develop crystallization kinetic models for the suspension crystallization system. Due to its higher resolution, the Malvern was more capable of detecting these finer particles down to 0.1 μm giving rise to a bimodal distribution and hence more suitable for crystallization kinetic estimations (Fig.4.11a). The Malvern Mastersizer instrument measures the diameter of a sphere of the same-cross-sectional area as an average projected area of crystals randomly orientated in the laser beam. From investigations carried out on the habit, it was determined that the crystals are parallelepiped. The Malvern assumes that particles are spherical and thus the deviation from sphericity is taken into account via a shape factor. The measured size is a correlation and not an absolute value. For such a non-spherical particle shape, the Malvern size (L_M) must be re-calculated to give the characteristic size or dimension, L, by using the volumetric shape factor and is given by,

$$L_M = L.\left(\frac{6.k_v}{\pi}\right)^{\frac{1}{3}} \qquad [4.3]$$

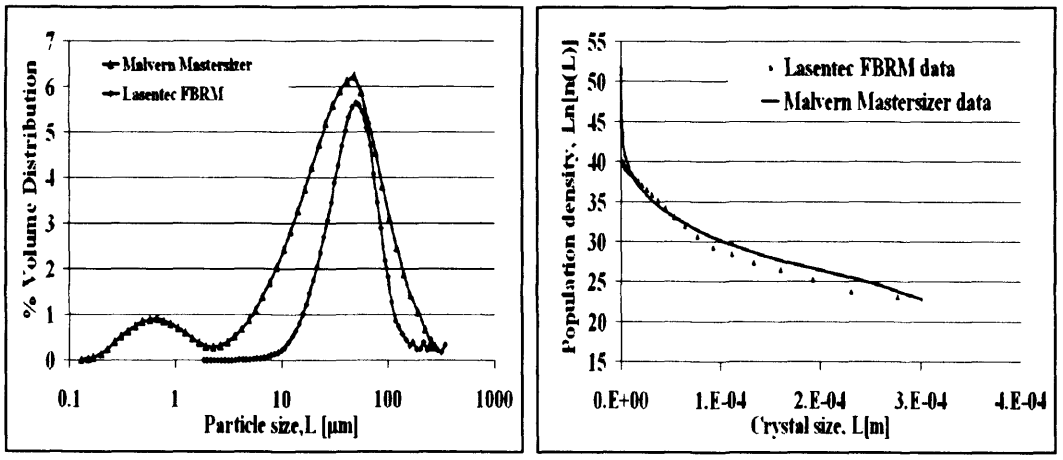

Figure 4.11: Comparison between Lasentec and Malvern instruments [a] Crystal size distribution (left) [b] Population density distribution (right).

4.6 CONCLUSIONS

The Lasentec FBRM probe is a useful *'in-situ'* measurement technique that was successfully used to monitor MSMPR crystallizations and steady state in-line. The PVI system was an excellent complementary instrument with the Lasentec FBRM providing additional crystal habit information. Due to the nature of the organic crystals and opacity at the smaller particle sizes, the Lasentec FBRM was not suitable for the measurement of crystallization kinetics for the organic compound. The technique should be used with caution when applied to other organic compounds exhibiting similar crystal habit, size-dependent growth or growth rate dispersion mechanisms as a result of these observations discussed in this chapter.

Chapter 5

ESTIMATION OF CRYSTALLIZATION KINETICS USING A MODIFIED CONTINUOUS COOLING MIXED SUSPENSION MIXED PRODUCT REMOVAL (MSMPR) CRYSTALLIZER

ABSTRACT

The crystallization kinetics of an important organic compound is determined using a modified laboratory scale continuous cooling Mixed Suspension Mixed Product Removal (MSMPR) crystallizer with a product recycle loop designed for use with limited quantities of pharmaceutical at 29°C. The effect of supersaturation, suspension density of the crystallizer content, impeller velocity (turnover time) and configuration on the growth and nucleation rates is studied. A convenient method of monitoring steady state in the MSMPR using Lasentec Focussed Beam Reflectance Measurement (FBRM) is also described.

An observed deviation in non-ideal systems from the McCabe ΔL law for small crystal sizes is attributed to either size-dependent growth (SDG) or growth rate dispersion (GRD) mechanisms and hence complicates the estimation of both growth and nucleation rates. The shape factors of the organic fine chemical including the relationship between crystal growth and particle size were investigated. SDG was successfully modelled using a three-parameter exponential size-dependent growth model by direct fitting to the experimental population density distribution. Growth rates estimated from the SDG model where compared to a GRD model using discrete growth probability distributions. The relationship between growth rate and particle size shows that the apparent growth rate is linear with respect to particle size to about 1 μm and is extremely low, strongly size dependent when the particle size is between 1-200 μm, and size independent at greater than 200 μm. The total nucleation rate is proportional to the suspension density, average crystal growth rate, supersaturation and specific power input.

5.1 INTRODUCTION

Reliable kinetic data are of paramount importance for the modelling and predictive scale-up of organic crystallization processes. In order to scale-up organic crystallization processes, the simulation, design and control of batch crystallizers is dependent on the accurate prediction of the crystal size distribution (CSD). The CSD is determined by the crystallization kinetics, which include growth, nucleation, agglomeration and disruption. The CSD is also affected by the residence time distribution of the crystals within a crystallizer.

Mixed-Suspension Mixed-Product removal (MSMPR) cooling crystallizers are well-mixed, continuously operated vessels often used, at steady state to determine crystallization kinetics (Zauner and Jones, 2002; Tanrikulu et al., 2000; Sha et al., 1996; Chen and Larson, 1986) using population balance techniques (Randolph and Larson, 1988) at a given mean residence time. A typical MSMPR crystallizer is operated between 7-10 residence times until steady state and constant supersaturation is achieved.

In many systems a sharp upward curvature in the population density distribution is observed at least for the small crystal sizes, leading to a deviation from the McCabe ΔL law (McCabe, 1929). The production of non-linearity in the population density distributions is possibly due to growth rate dispersion, nucleation dispersion, size dependent growth, classification and agglomeration or any combination of these phenomena may occur in an MSMPR crystallizer. Size-dependent growth and growth rate dispersion are the most likely mechanisms (Garside et. al, 1976; Janse and de Jong, 1976). In mechanically agitated vessels, the hydrodynamic conditions related to the slip velocity differ between small and large crystals, hence if bulk diffusion occurs it may lead to size dependent growth rates. From mechanism studies carried out, each crystal can grow at a different or constant growth rate and some crystals may not grow or even dissolve. This produces a discrepancy between the total nucleation and effective nucleation rates.

Size dependent growth (SDG) has been modelled by direct fitting methods to the population balance using empirical correlations (Bransom, 1960; Canning and Randolph, 1967; Abegg et al., 1968; Mydlarz and Jones, 1989, 1990). Mydlarz and

Jones (1993) have developed an exponential model, which has been successful in modelling size-dependent growth rates as a function of the effective size-independent growth rate and crystal size and also applies to systems, which obey the McCabe law. Sha et al. (1996) estimated growth kinetics from an MSMPR crystallizer using the exponential model successfully. Tanrikulu et al. (2000) used the ASL power model (Abegg et al., 1968) to model growth but was not suitable for the system under investigation as the growth rate was overestimated at the larger particle sizes. The advantage of the ASL power model is that it can estimate the growth at zero particle size, which is not possible using the exponential model. A size-dependent growth model (Wang et al., 1992) has also been successfully used to model growth by O'Meadhra (1995). Sikdar (1977) and White et al (1976) proposed methods to estimate size-dependent growth rates directly from the population balance. White-Bendig-Larson method can be used to predict growth whether there is size dependency or independency and gives good estimations but the method proposed by Sikdar over predicts the growth at large particle sizes.

Size dependent growth models have been used to model growth because it is more difficult to describe growth rate dispersion models mathematically. Growth rate dispersion models have been recently modelled with intrinsic growth rate dispersion mechanisms in MSMPR crystallizers (Jones, 2002) using discrete distributions. The growth kinetics obtained from this model using MSMPR crystallizations can be transferred to batch cooling crystallizations. Zumstein and Rousseau (1987) use the random growth diffusivity model to describe growth and this mechanism may give the appearance of deviation from the ΔL law and hence SDG. Rojkowski (1993) showed that it is difficult to distinguish between SDG and GRD mechanisms in MSMPR crystallizers.

In this chapter, the successful exponential model proposed by Mydlarz and Jones (1994) will be used to model size dependent growth whereas the ASL power model will be used to model the growth at zero particle size. The SDG model is compared to growth results obtained using the GRD model (Jones, 2002).

The aim of this chapter is to describe and develop crystallization kinetic models using a modified MSMPR crystallizer with a recycle for the important pharmaceutical product. The effect of supersaturation, suspension density, impeller type and velocity on the crystallization kinetics is investigated using this system.

5.2 THEORY

In crystallizer design, MSMPR assumptions are commonly used (Randolph and Larson, 1988). The basic assumptions are that all species in the fluid phase are well mixed spatially, and furthermore, each fluid element contains the same composition and size distribution of crystals. With respect to the size distribution the crystals are of the same shape and are characterized by a linear dimension, L. This means that there are no special gradients of species concentration, solids volume fraction or particle size. In an MSMPR crystallizer, the product streams draw off a mixture containing the mean composition of the well-mixed liquid and particulate phases. A typical laboratory scale crystallizer is suitable for measuring kinetic data and is operated for between 7-10 residence times in order to achieve steady-state conditions within the vessel before taking a sample of the magma to assess the crystal size distribution. For a cooling crystallization only one feed system is necessary. MSMPR vessels with small volumes of even 250ml have been successfully operated. The larger the working volume, the more meaningful will be the nucleation data, particularly for scale up purposes, but it is more difficult to achieve good mixing and MSMPR conditions in larger vessels.

The problem that is created in small MSMPR units is that the low feedstock flowrates cause crystallization blockage in the supply line. For crystallization processes the supersaturation should be kept below a value of one coupled with secondary nucleation. In practise, although it is relatively straightforward to achieve a well-mixed solid-liquid phase, it is difficult to suspend the solid phase homogenously at economic power inputs (Nienow, 1995). Zweitering (1958) showed that a stirred tank vessel should be operated at an impeller velocity in excess of the velocity required to just suspend the solids. Other MSMPR assumptions are as follows:

1. The crystallization vessel operates continuously
2. There are no crystals present in the feed stream to the crystallizer.
3. Operation is at steady state and thus mass does not accumulate in the balance volume.
4. No agglomeration or attrition of crystals occurs.

5. No internal/external classification effects.
6. The linear growth rate $G(L,t)$ of crystals, $G = dL/dt$ and all crystals grow at the same rate irrespective of their size. This assumption of size-independent growth is known as McCabe's ΔL law (McCabe, 1929).

The population balance can be reduced as a result of the above assumptions (Randolph and Larson, 1988) to the following,

$$\frac{\partial n(L,t)}{\partial t} = 0 \qquad \text{steady state}$$

$$n(L,t).\frac{dV}{dt} = 0 \qquad \text{constant volume}$$

$$B = 0 \quad D = 0 \qquad \text{no agglomeration, no breakage}$$

$$\frac{\partial\left(G(L).n(L,t)\right)}{\partial L} = G(L).\frac{dn(L,t)}{dL} \qquad \text{size-independent growth}$$

$$\frac{\left|q_e n_e(L,t) - q_f n_f(L,t)\right|}{V} = \frac{n(L,t)}{\tau} \qquad \text{mixed suspension discharge}$$

$$\tau = \frac{V}{Q} \qquad \text{mean residence time}$$

Hence the macro-distributed population balance reduces to the following,

$$G(L).\frac{\partial n(L,t)}{dt} = -\frac{n(L,t)}{\tau} \qquad [5.1]$$

which upon integration produces,

$$n(L,t) = n_0 \exp(-L/G(L).\tau) \qquad [5.2]$$

An isothermal, unseeded, steady state MSMPR crystallizer of constant volume with a clear liquor feed stream is considered in this research. We assumed that all new crystals are secondary nuclei and the breakage and agglomeration are neglible as a first approximation. Furthermore the crystal growth rate was found to be size-dependent. Under these conditions the population balance becomes,

$$\frac{\partial[G(L).n(L,t)]}{\partial L} = -\frac{n(L,t)}{\tau} \qquad [5.3]$$

Hence the population density is given as follows,

$$n(L) = n_O \exp\left(-\frac{L}{G_e \tau}\right) \qquad [5.4]$$

The crystal growth may be determined from the slope of semi-logarithmic population density plot, while the intercept gives the value of nuclei population density, n_o, with the latter being related to the total nucleation rate (B_{TOT}).

Mydlarz and Jones (1993) express the size dependent growth (SDG) exponential model as follows,

$$G(L) = G_e\{1 - \exp[-a(L+c)]\} \qquad [5.5]$$

When this expression is substituted into the general population balance equation, the following population density equation is obtained,

$$n(L) = n_O \exp(aL)\left(\frac{\exp[a(L+c)}{\exp(ac)-1}\right)^{\frac{-1-(a\tau G_e)}{(a\tau G_e)}} \qquad [5.6]$$

Abegg et al., (1968) express the power model for SDG as follows,

$$G(L) = G_O(1+aL)^b \qquad [5.7]$$

The rate of change of the growth rate with the crystal size can be calculated by taking the differential of the growth rate equation for the exponential model and is defined as,

$$\frac{dG(L)}{dL} = aG_e \exp[-a(L+c)] \qquad [5.8]$$

The total nucleation rate can be expressed in the form of an empirical power law equation,

$$B_N = k_n M_T^i G_{av}^j \varepsilon^k \qquad [5.9]$$

The total nucleation rate is the number of new particles formed per unit volume of solution per unit time and is the sum of primary and secondary nucleation. The formation of nuclei is dependent on the relative supersaturation levels (σ),

suspension density (M_T) and the fluid dynamics. After the formation of stable nuclei, the nuclei begin to grow into crystals. Two steps in mass deposition are suggested, bulk or volume diffusion to the crystal surface and integration on the crystal surface. A power model describes the effective size-independent growth rate as follows,

$$G_e = k_g' \sigma_g' \qquad [5.10]$$

The growth rate at zero particle size is given as follows,

$$G_o = k_g \sigma^g \qquad [5.11]$$

The total nucleation rate can be determined by the following equation,

$$B_{TOT} = \tau^{-1} \int_0^\infty n(L) dL \qquad [5.12]$$

The average growth rates(G_{av}), were calculated by the equation,

$$G_{av} = \frac{M_t}{3\rho_S \not{d} k_v \int_0^\infty n(L) L^3 dL} \qquad [5.13]$$

The population density may be calculated by using the mass distributions of the steady state CSD,

$$n(L) = \frac{\Delta M M_t}{\Delta l k_v \rho_S L^3} \qquad [5.14]$$

In crystallization processes, the weighted mean size of particles is used to characterise the crystal size distribution. The general expression for the mean size is defined as follows,

$$L_{ij} = \left(\frac{\int L^i n(L) dL}{\int L^j n(L) dL} \right)^{\frac{1}{i-j}} = \left(\frac{m_i}{m_j} \right)^{\frac{1}{i-j}} \qquad [5.15]$$

The shape of a particle can be defined by using shape factors whose calculation is based on one characteristic size dimension of the particle, usually the equivalent

diameter and is typically the second largest dimension. The volume and area shape factors are used and defined by (Allen, 1981),

$$k_v = \frac{v}{d^3} \qquad [5.16]$$

$$k_a = \frac{a}{d^2} \qquad [5.17]$$

Another quantity that has been used to characterize crystal shape is the sphericity and is defined as the ratio of the surface area of a sphere having the same volume as the particle to the apparent estimated surface area of the particle (Waddell, 1932) as,

$$\psi = \left(\frac{d_v}{d_s}\right)^2 \qquad [5.18]$$

It was also redefined (Nývlt, 1989) in terms of the shape factors as,

$$\psi = \frac{(6k_v/\pi)^{2/3}}{k_a/\pi} \qquad [5.19]$$

Patience (2002) describes the shape factors in terms of length to width (l_w) and depth to width (d_w) ratios as follows,

$$k_v = l_w d_w \qquad [5.20]$$

$$k_a = 2(l_w d_w + l_w + d_w) \qquad [5.21]$$

5.3 EXPERIMENTATION

Investigations of the kinetic parameters that influence the crystallization process of the organic fine chemical in an isopropyl alcohol-water system is performed. Experiments were carried out using different mean residence times, impeller velocities (300, 400, 500 and 600 rpm), impeller types and initial solids concentration (4, 5, 6 and 7% w/w) at 29 °C. A modified cooling MSMPR crystallizer (1) is used in this investigation. The experimental set-up is shown in Fig.4.2. A glass jacketed round-bottomed crystallization vessel (1) (500 ml, d = 100 mm) fitted with either a flat (paddle) blade impeller (d =65mm) or a four bladed 45° angle pitch blade impeller (d = 46 mm). The 0.5 litre MSMPR

crystallizer is equipped with 3 baffles when using the pitch blade impeller to provide for axial and radial flow whereas no baffles are used with the flat blade impeller due to the large impeller diameter resulting in the formation of a vortex. An IKA motor drives the impellers. The product slurry withdrawal pipe was located approximately half way up the inside of the crystallizer. Slurry was continuously drawn-off from the MSMPR using a primary circulation loop, which is set at a slurry withdrawal rate of 350 ml min^{-1} using the peristaltic pump (7). Lasentec FBRM monitoring experiments have shown that crystal breakage and attrition are neglible after 30 minutes of slurry re-circulation through the peristaltic pump. This arrangement ensured that classification effects were minimised and isokinetic removal of the magma from the crystallizer occurred. A secondary re-circulation loop was used to withdraw slurry from the primary loop at flow rates of between 15-40 ml min^{-1} using a second peristaltic pump (6). The slurry passed through a double-coiled heat exchanger (5) such that the solid dissolved to produce clear solution to be re-cycled back into the crystallizer as feed solution. Fig.5.1 shows a photograph of the continuous cooling MSMPR set-up and Fig.5.2 shows a mechanical drawing of the MSMPR crystallizer with dimensions. The residence time within the heat exchanger was at least 2 minutes based on the highest flowrate (lowest mean residence time) and the set temperature of the double-coiled heat exchanger was sufficient to ensure that the slurry was completely dissolved. Visual and microscopic examination of the re-cycled solution exiting the heat exchanger and entering the MSMPR crystallizer showed no crystals present.

The feed pipe was located one third of the way up from the surface of the contents of the crystallizer and the heat exchanger temperature was maintained at a constant temperature by a Julabo heater/chiller unit. The Huber Tango (2) automated heater/chiller unit maintained the crystallizer vessel at a constant operating temperature. The recycle pipeline (9) that was lagged with cotton wool and aluminium foil and with a heat tracer to prevent heat losses maintained a constant feed solution temperature and prevented nucleation occurring in the line. The heat exchanger temperature in the product recycle loop was increased as required to ensure complete dissolution of the solid in suspension and to ensure a crystal free recycle feed solution. The desired withdrawal and feed flow rates were maintained using two digital Watson-Marlow peristaltic pumps that provided a

constant mean residence time within the MSMPR crystallizer. The crystallizer was also fitted with a condenser to prevent solvent loss and maintain a constant volume. Hot solutions of the organic compound were susceptible to aerial oxidation and had to be kept under nitrogen for the entire duration of the experiments. Kinetic data is usually measured using the MSMPR crystallizers running at steady state that is achieved by running the system for up to 10 residence times from a feed reservoir. The total volume of feed solution must hold over 10 times the crystallizer volume to achieve steady state. However, during the early stages of development, pharmaceutical compounds are often available in very limited quantities and by using a recirculation loop the quantity of pharmaceutical required was minimised.

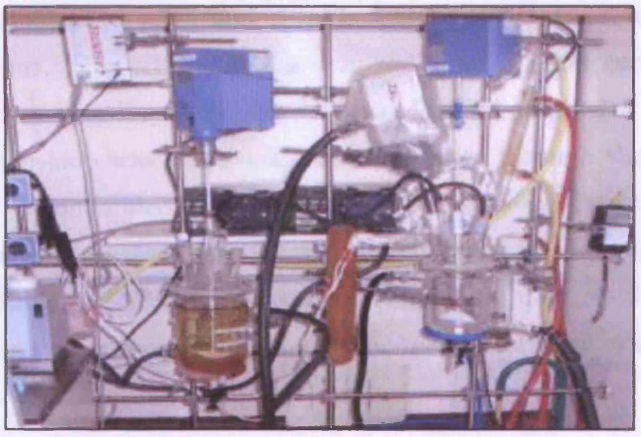

Figure 5.1: *Photograph of the continuous cooling MSMPR crystallization set-up.*

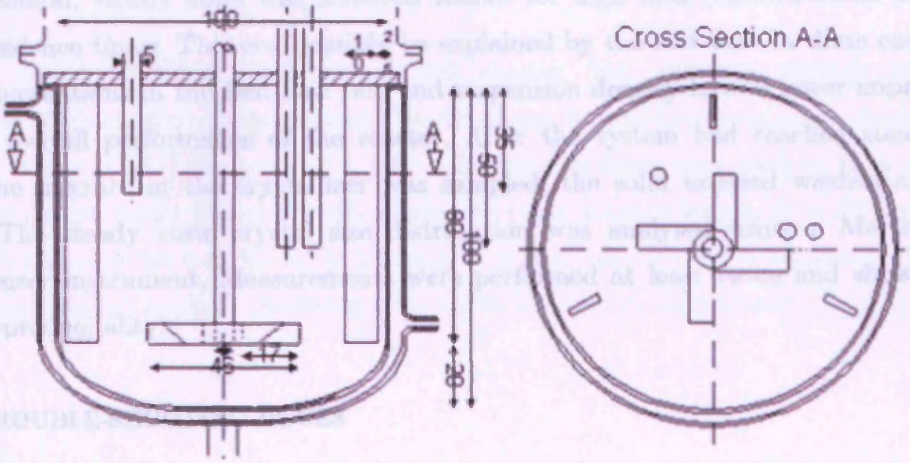

Figure 5.2: *Mechanical drawing of MSMPR crystallizer including cross-sectional view (all dimensions given in mm).*

A Lasentec FBRM D600 Probe (2) was used to monitor the MSMPR crystallization in-line and to determine when steady state conditions have been achieved. The FBRM instrument was positioned in an area of high turbulence above the impeller blade and measured the chord lengths of particles in the slurry by using a rotating laser beam, which was focussed, onto the outside of a sapphire window. A particle on or close to the window will reflect the laser energy back into the probe by backscatter and the duration of the reflectance is a measure of the chord length of the particle. A process video imaging system was used to monitor the crystal habit and behaviour during the MSMPR experiments.

The continuous MSMPR crystallizer was initially operated in batch mode by heating the slurry to dissolve solid and then cooled at 0.5°C min^{-1} to allow re-crystallization to occur. The crystallization was not seeded upon cooling. Once particle trends monitored on-line using the Lasentec FBRM reached a maximum, the primary circulation loop was started. Particle breakage through the peristaltic pump was minimal as indicated by the number of particles detected by the Lasentec probe remaining constant after 30 minutes of operation. Steady state was achieved after operating the MSMPR crystallizer for six to nine residence times. Achieving steady state operation depends on the mean residence time and the initial solids loading.

In general, steady state was achieved sooner for high feed concentrations and long residence times. This can possibly be explained by the fact that in these cases slight fluctuations in the feed flow rate and suspension density have a lower impact on the overall performance of the reactor. After the system had reached steady state the mixture in the crystallizer was sampled, the solid isolated washed and dried. The steady state crystal size distribution was analysed using a Malvern Mastersizer instrument. Measurements were performed at least twice and showed good reproducibility.

5.3.1 TROUBLE-SHOOTING ISSUES

Previous experimental set-ups involved using only the secondary loop by drawing off of a high slurry density but this resulted in crystal formation within

the outlet pipeline from the coiled heat exchanger, which then enters the reactor. Drawing-off at low flowrates introduced classification of particles (detected by FBRM probe). Remedial methods to prevent crystal formation producing blockage included lagging pipes, introducing heat tracers, reducing length of transport pipes, increasing the heat exchanger temperature, reducing slurry concentration and increasing the flow to reduce classification effects. Increasing the heat exchanger temperature significantly leads to the slurry boiling in the coils. To prevent classification of particles drawing off from the bottom of the reactor was attempted, however this resulted in aggregate particulate formation resulting in blockage and hence the loss of steady state operation.

5.4 RESULTS

5.4.1 SHAPE FACTORS

The organic fine chemical particles under investigation are needle-like in nature and are approximated to be parallelepiped shaped in structure. Shape factors have been calculated for continuous mixed suspension mixed product removal (MSMPR) cooling crystallizations and for rapid batch cooling crystallization experiments. It has been shown that the crystal habit changes from batch cooling crystallization to continuous crystallization processes.

For the MSMPR crystallizations, 100 organic fine chemical crystals were analysed off-line using image analysis. An Olympus BX 60M microscope, a charged couple device (CCD) camera and a PC with frame grabber were used to take and analyse images using Image Pro plus software. The average length to width ratio was calculated to be 6.4. Similarly a length to width ratio of 9.58 is obtained when analysing product crystals produced from batch cooling crystallizations (Fig.5.4).

The depth to width ratio, d_w, is not measured using the images due to the crystals alignment in the same direction making the depth direction impossible to observe. A depth to width ratio of 0.25 will be used, as a result of SEM analysis of the samples. For the crystallization studies, a size independent shape factor will be used, as there is no correlation between crystal size and shape factor (Fig.5.3). Hence the calculated shape factors from the MSMPR crystallizations are: $k_v = 1.6$ and $k_a = 16.5$, with a sphericity, ψ, value = 0.4. The sphericity value confirms needle-like nature of particles.

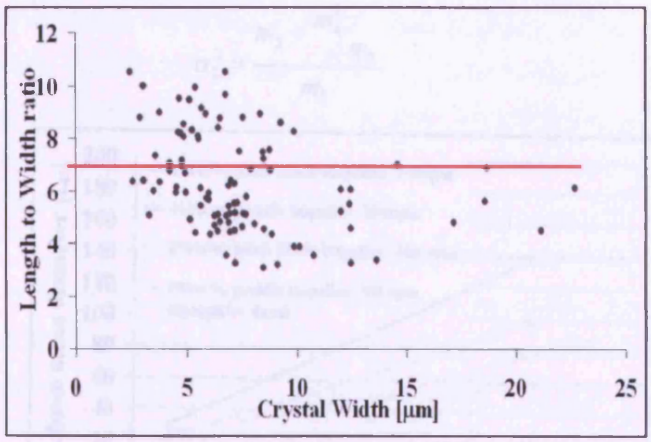

Figure 5.3: *Length to width ratios used to calculate shape factors for continuous MSMPR crystallizations.*

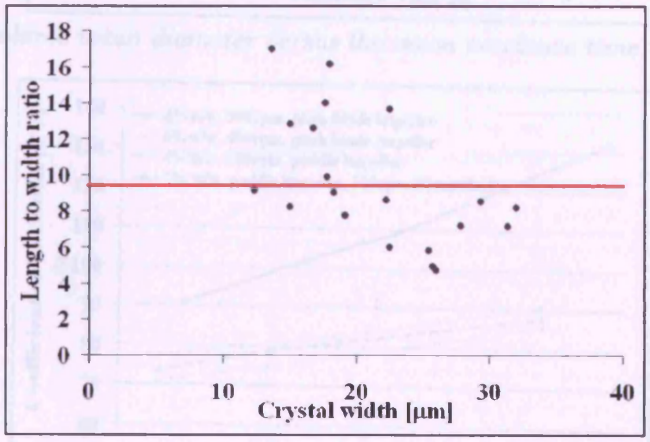

Figure 5.4: *Length to width ratios used to calculate shape factors for batch cooling crystallizations.*

5.4.2 VOLUME MEAN SIZE (L_{43})

The populations weighed mean crystal sizes can be expressed in terms of the first four moments of the crystal size distribution, which are the total number, length, area and volume of crystals. The volume mean size is defined as follows,

$$L_{43} = \frac{m_4}{m_3} \qquad [5.22]$$

and the variance of the CSD about that mean,

$$\sigma_L^2 = \frac{m_5 - m_4^2 / m_3}{m_3} \qquad [5.23]$$

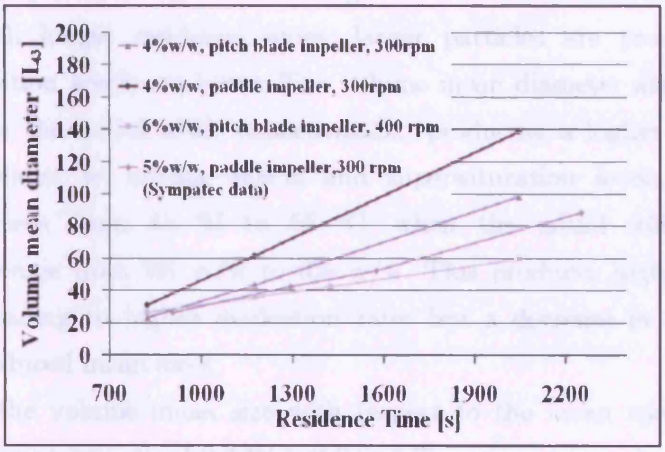

Figure 5.5: *Volume mean diameter versus the mean residence time.*

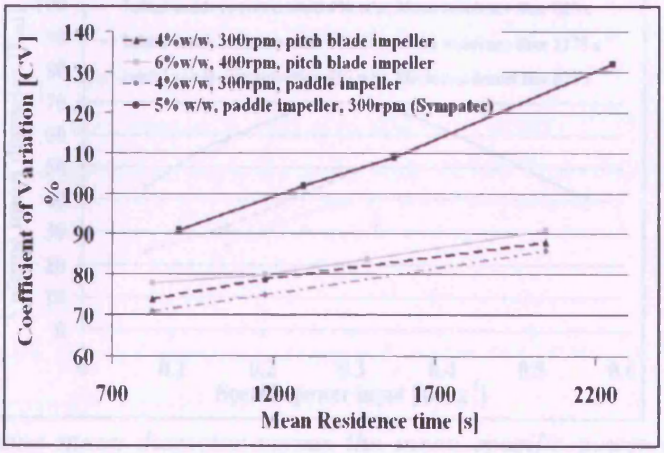

Figure 5.6: *Coefficient of variation versus mean residence time for different impeller types and initial solids concentration.*

Hence the coefficient of variation based on the number mean size, which describes the relative spread of the distribution is given by,

$$C_{VL} = \frac{\sigma_l}{L_{43}} \qquad [5.24]$$

The coefficient of variation increases with respect to an increase in the mean residence time (Fig.5.6). This is expected, as the crystals remain within the MSMPR crystallization vessel for longer periods of time. This leads to larger-sized crystals being produced and an increased spread in the CSD. The volume mean diameter L_{43} shows a linear dependence of the mean diameter on the residence time at a constant mean specific power input (Fig.5.5). The behaviour is the same as that predicted by population balance modelling with MSMPR assumptions. This is reasonable, as with longer residence times, larger particles are produced even though supersaturation levels are lower. The volume mean diameter also decreases with an increase in the initial solids concentration, producing a higher suspension density and is related to mixing effects and supersaturation levels. The feed temperature increases from 45 °C to 55 °C, when the initial solids loading concentration increases from 4% w/w to 6% w/w. This produces higher levels of supersaturation, leading to higher nucleation rates but a decrease in the growth rate resulting in reduced mean sizes.

The curves of the volume mean size with respect to the mean specific power input show a maximum at around 0.3 W kg^{-1} (Fig.5.7).

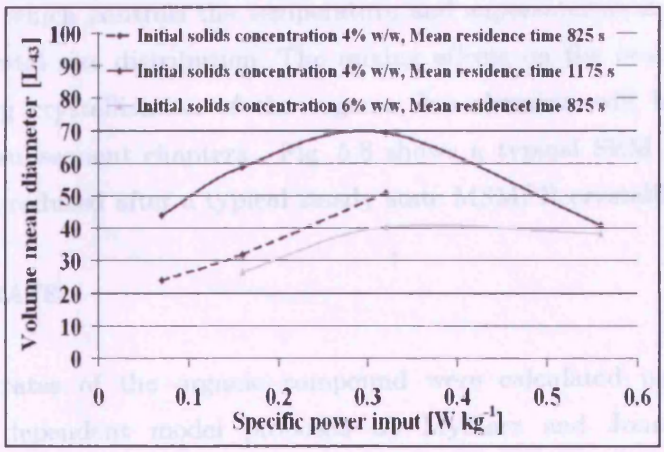

Figure 5.7: *Volume mean diameter versus the mean specific power input (pitch blade impeller).*

This phenomenon can be explained in terms of a change from a macromixing to a micromixing-controlled system whereby attrition may dominate the crystallization process. For low specific power inputs, macromixing seems to be limiting, however it is increased significantly with a small increase in power input, leading to an increase in particle size because the bulk convective mixing of the crystallizer is improved in terms of temperature distribution (heat transfer), supersaturation levels and suspension density. The secondary nucleation rate is also controlled and is not excessive. However, a further increase of power input results in a reduction in particle size and is probably due to attrition. This could be attributed to high fluid shear rates due to increased fluid velocities produced at higher power inputs including particle-particle and particle-impeller collisions. This produces particulate attrition and occurs on a micromixing scale. In this system, it is possible that at low power inputs macromixing dominates, whereas at higher power inputs micromixing dominates leading to particulate attrition, and reduced growth rates.

The turbulent dispersion on a micromixing scale based on the power input per unit mass and macromixing in an agitated crystallization vessel producing backmixing due to the high non-symmetry of the turbulent velocity field promoting bulk convective mixing in solid-liquid systems due to density differences in physical properties (Hinze, 1975), affects the degree of mixing within a crystallization process. Mixing is critical in batch cooling suspension crystallization processes due to heat transfer, which controls the temperature and supersaturation distribution, and thus the crystal size distribution. The mixing effects on the heat transfer for the batch cooling crystallization of the organic fine chemical will be subject to investigation in subsequent chapters. Fig. 5.8 shows a typical SEM image of the organic crystals produced after a typical steady state MSMPR crystallization.

5.4.3 GROWTH RATE

The growth rates of the organic compound were calculated using a three-parameter size dependent model proposed by Mydlarz and Jones. A typical MSMPR population density distribution is shown in Fig. 5.9. The population density distribution is calculated using the steady state mass distribution of the crystals (Malvern Mastersizer) and the volume shape factor determined.

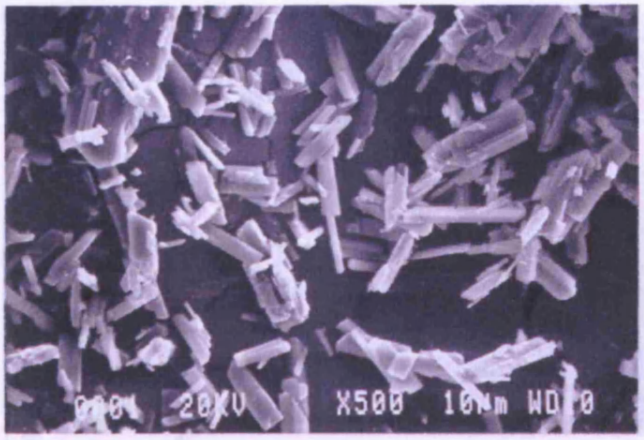

Figure 5.8: *Photomicrograph of organic crystals showing typical parallelepiped and irregular crystals produced during the MSMPR crystallization.*

The population density distribution exhibits a strong upward curvature for crystals sizes between 40-80µm and is attributed to either SDG or GRD as agglomeration and classification effects in the crystallization process are neglible. The size-dependent exponential model was fitted to the experimental data through the use of DataFit version 8, which is a curve-fitting software program using equation [5.6] and the growth rates determined as function of crystal size using equation [5.5]. No direct comparison of the kinetic data is possible as kinetic studies on the organic fine chemical are limited. Patience (2002), performed batch-cooling crystallizations, to determine growth data using a population balance coupled with energy balance and mass balances for the same organic fine chemical.

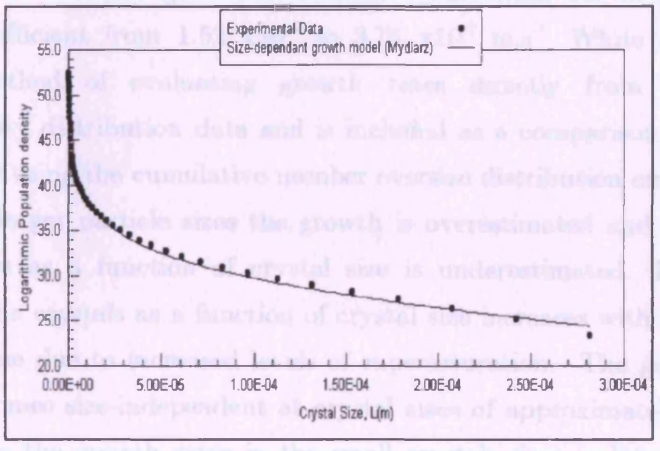

Figure 5.9: *Typical MSMPR population density distribution with experimental data fitted to size-dependent growth rate model (Mydlarz and Jones, 1993).*

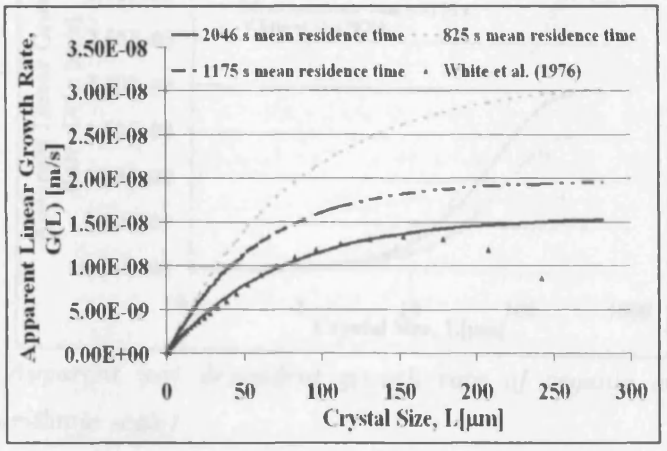

Figure 5.10: *Apparent size dependent growth rate of organic crystals versus crystal size (pitch blade impeller).*

The population balance for each run was solved using the method of moments. An apparent growth rate dispersion model was considered with results showing large variations and the growth being overestimated.

Fig.5.10 shows the apparent linear growth rate versus crystal size using an initial solids concentration of 4% w/w, a pitch blade impeller operating at 300rpm with different mean residence times.

Patience found that the growth rate order varied from 0.8 to 1.54 and the growth rate coefficient from 1.52 $x10^{-6}$ to 3.73 $x10^{-7}$ $m.s^{-1}$. White et al. (1976) proposed a method of evaluating growth rates directly from experimental population density distribution data and is included as a comparison. The growth rate is estimated using the cumulative number oversize distribution curve.

However, at larger particle sizes the growth is overestimated and consequently the growth rates as a function of crystal size is underestimated. The apparent growth rate of the crystals as a function of crystal size increases with a decrease in the residence time due to increased levels of supersaturation. The growth rate of the crystals becomes size-independent at crystal sizes of approximately 200μm. In order to examine the growth rates in the small crystals sizes, a logarithmic scale was used on the particle size axis (Fig.5.11).

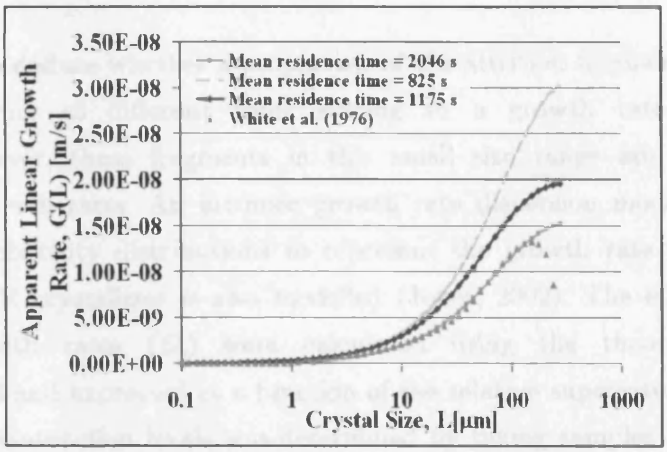

Figure 5.11: *Apparent size dependent growth rate of organic crystals versus crystal size (logarithmic scale).*

Using equation [5.8], the rate of change of crystal growth with crystal size can also be evaluated. Figs.5.11-5.12 shows that the rate of change of crystal growth with crystal size below 1μm is extremely low and strongly size-dependent between 1-200μm. Attrition fragments act as secondary nuclei and it is possible that these fragments grow at different rates leading to a growth rate dispersion mechanism producing the upward curvature in the population density distribution. In this research, it is assumed that most attrition fragments formed are typically less than 10μm and the CSD from the Malvern Mastersizer provides evidence for this including microscopic analysis.

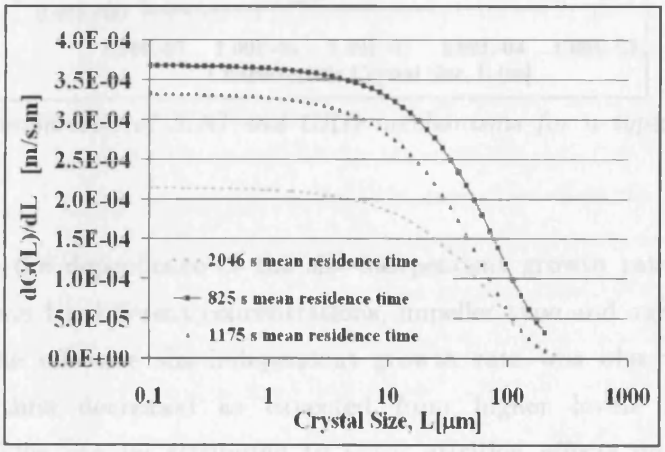

Figure 5.12: *Rate of change of crystal growth with crystal size at different residence times (pitch blade impeller) versus crystal size.*

It is difficult to deduce whether a proportion of the attrition fragments are non-growers or growing at different rates leading to a growth rate dispersion mechanism. However, these fragments in this small size range are growing at extremely low growth rates. An intrinsic growth rate dispersion model based on using discrete probability distributions to represent the growth rate distribution within an MSMPR crystallizer is also modelled (Jones, 2002). The effective size-independent growth rates (G_e) were calculated using the three parameter exponential model and expressed as a function of the relative supersaturation level. The relative supersaturation levels was determined by taking samples after steady state conditions had been reached in the MSMPR crystallizer and analysis of solute concentration carried out with HPLC.

Fig.5.13 shows that it is difficult to distinguish between SDG and GRD mechanisms within an MSMPR crystallizer as Rojkowski (1993) also observed.

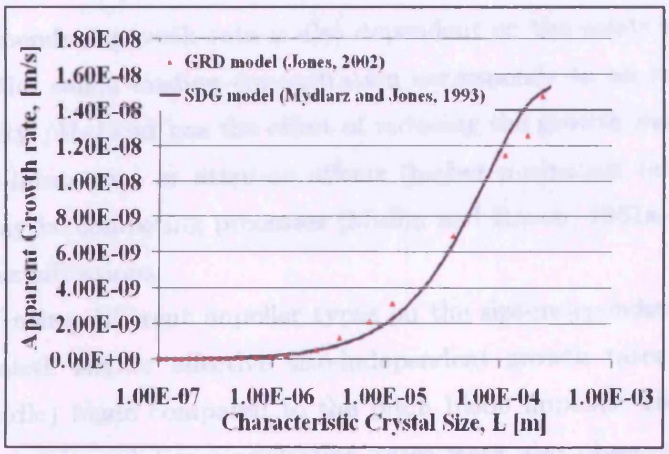

Figure 5.13: *Comparison of SDG and GRD mechanisms for a typical MSMPR crystallization.*

Fig.5.14 shows the dependence of the size-independent growth rate versus the mean residence time for different concentrations, impeller type and agitator speed. An increase in the effective size-independent growth rate was observed, as the mean residence time decreased as expected from higher levels of constant supersaturation. This can be attributed to lower attrition effects on the steady state CSD due to mechanical agitation periods being shorter. However, using a pitch blade impeller, a solid loading of 6% w/w, and 400 rpm at a mean residence time of 825s, a lower size-independent growth rate was observed than expected.

A possible explanation maybe due to oxidation effects producing impurities that limit the growth of the organic fine chemical.

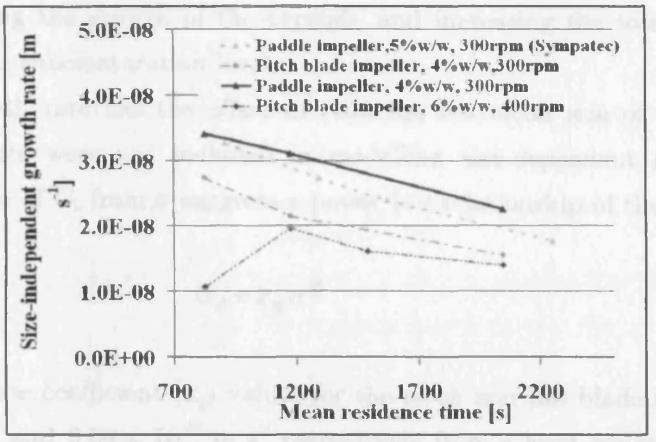

Figure 5.14: *Effective size-independent growth rate versus mean residence time.*

The size independent growth rate is also dependent on the solids concentration. An increase in the solids loading concentration corresponds to an increase in the suspension density (M_T) and has the effect of reducing the growth rate and may be due to diffusion-limitations or attrition effects (higher nucleation rates). Attrition and diffusion may be competing processes (Mullin and Raven, 1961a and b) within the MSMPR crystallizations.

The effect of using different impeller types on the size-independent growth rate is also investigated. Higher effective size-independent growth rates were evident with a flat (paddle) blade compared to the pitch blade impeller. Higher constant supersaturation levels and lower nucleation rates were also observed for the flat blade impeller compared to the pitch blade impeller for the same initial solids concentration and mean residence times. Performing Computational Fluid Dynamic (CFD) simulations to determine hydrodynamics conditions prevailing within the MSMPR crystallizer, it was found that higher shear rates are produced using the pitch blade impeller than when compared to the flat blade impeller at a constant agitation speed. This has the effect of increasing the particulate attrition rate and reducing the growth rate of crystals. Fig. 5.15 shows the relationship between the effective size-independent growth rates versus the relative supersaturation for both the pitch blade and flat blade impellers. Data points indicated as circles represent lower growth rates being estimated at higher levels of

supersaturation and are probably due to impurities limiting crystal growth. Impurities are produced as a result of known aerial oxidation of the organic fine chemical, reducing the growth of the crystals, and increasing the total nucleation rate and constant supersaturation levels.

A lower growth rate has the effect of reducing the mean size of the crystals. These data points were not included in modelling size-dependent growth. The linear dependence of G_e from σ suggests a power law relationship of the form,

$$G_e = k_g \sigma^g \qquad [5.25]$$

The growth rate coefficient (k_g) values for the pitch and flat blade impellers are 3.25 x 10^{-08} m s^{-1} and 3.06 x 10^{-08} m s^{-1} respectively from a least squares fit with g =1.

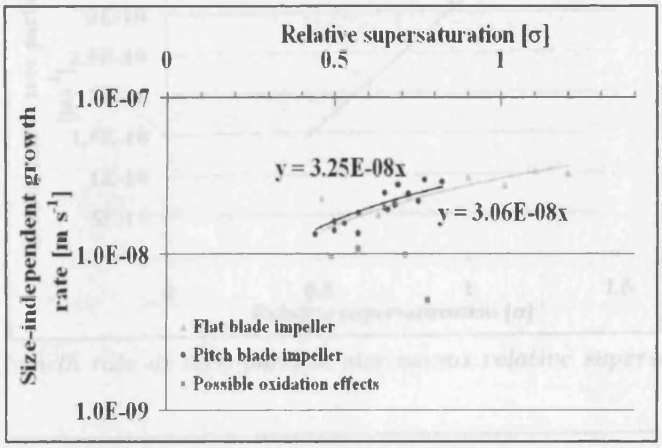

Figure 5.15: *Effective size-independent growth rate versus the relative supersaturation.*

This suggests that the type of impeller used does affect the mass transfer (diffusion step) rate of crystal growth but not significantly. The size-independent growth rates measured range from 5.01 x 10^{-9} to 3.41 x 10^{-8} m s^{-1}.

Budz and Jones (1986), found that the contribution of the bulk diffusion and surface-reaction resistances to the crystal growth process vary with crystal size by using a surface integration effectiveness factor (Garside et al., 1974). However, in this investigation dissolution kinetics were not carried out and therefore it was difficult to quantify this phenomenon. The average value for 'a' was determined to

be 17 400 from fitting the growth model for each MSMPR experiment and 'c' was taken as 1 x 10^{-7} m in equation [5.3], producing the final modelling equation for size-dependent growth as a function of crystal length and supersaturation levels as follows,

$$G(L) = k_g \sigma(1 - \exp[-17400(L + 1e^{-07})]) \quad for\ L \le 200\mu m \quad and\ 0.45 \le \sigma \le 1.2$$

Hence, [5.26]

$$L > 200\mu m, G \to G_e$$

The ASL power model (Abegg et al., 1968) is used to predict the growth at zero particle size (G_o). Fig. 5.16 shows the relationship between the growth at zero particle size and the relative supersaturation.

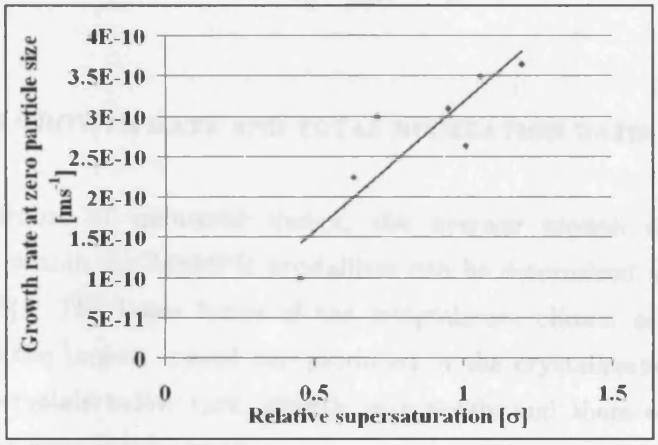

Figure 5.16: *Growth rate at zero particle size versus relative supersaturation (flat blade impeller).*

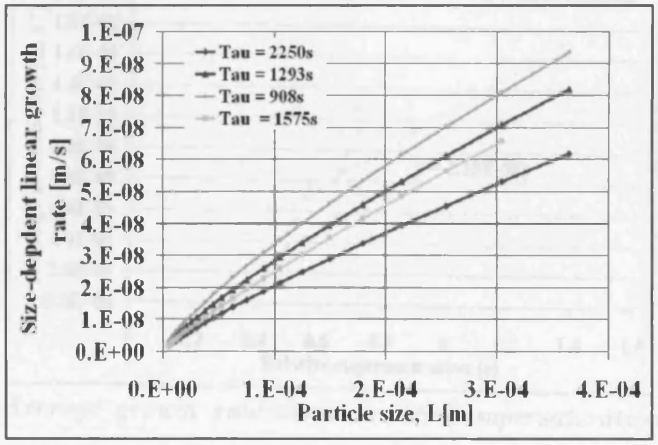

Figure 5.17: *Size-dependent linear growth rate for a solids loading of 5% w/w at different mean residence times using a flat blade impeller using the power model.*

However, if the ASL power model was used to predict size dependent growth rates as a function of the mean residence time, the growth will tend to be well predicted in the small particle sizes but deviations and large inaccuracies occur at larger particle size due the power model used. Fig.5.17 shows the linear growth rate for different residence times using a flat blade impeller estimated using the power model and is significantly different to the size-dependent growth predictions observed in Fig.5.10.

Hence the following relationship is produced for the growth at zero particle size,

$$G_o = 3x10^{-10}\sigma \qquad [5.27]$$

5.4.4 AVERAGE GROWTH RATE AND TOTAL NUCLEATION RATE

For the purpose of industrial design, the average growth rate and total nucleation rate within the MSMPR crystallizer can be determined using equations [5.12] and [5.13]. The lower limits of the integrals are chosen as 1μm and the upper limits as the largest crystal size produced in the crystallization vessel. The reason is that crystals below 1μm, growth very slowly and there contribution to the final product mass is very small.

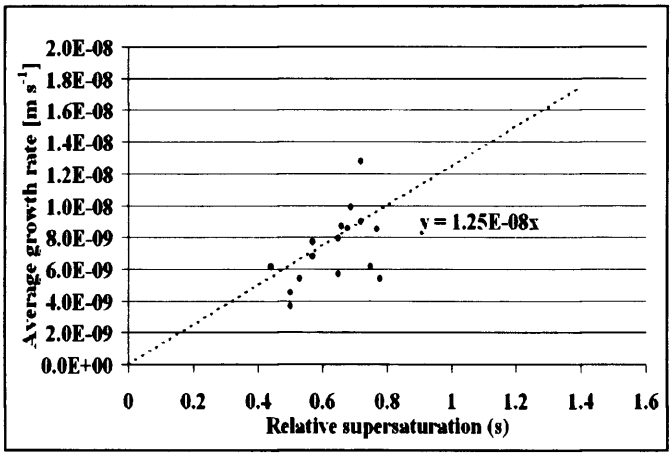

Figure 5.18: *Average growth rate versus relative supersaturation (pitch blade impeller).*

If the average kinetic growth rate is expressed in a power law form as a function of supersaturation (Fig.5.18) using a least squares fit the growth kinetic constant is 1.25×10^{-8} m/s and the growth kinetic order is 1.26.

The kinetic growth order suggests that there is also a significant contribution of surface reaction resistance to the growth process and is likely to be more significant as the crystal size decreases. The growth kinetic order is used to describe the rate of particle growth and is correlated to the type of growth mechanism of the organic fine chemical. Is does not describe a physical aspect.

Therefore, it will be necessary to determine a dissolution model for the organic fine chemical, to provide more comprehensive details on the contributions of both surface-reaction and bulk diffusion on the growth process with respect to crystal size. The total nucleation rate was the sum of the contribution of primary and secondary nucleation and calculated such that it represented most of the product crystals. The reason for using equation 5.13 was that on average all the crystals within the MSMPR crystallizer were removed within one residence time and the total nucleation rate is the total number of crystals in the crystallizer divided by the residence time. The total nucleation rates cover a range from 1.06 x 10^{10} to 2.29 x 10^{11} m^{-3} s^{-1}. The total nucleation rate increases with an increase in suspension density (Fig.5.20), as a result of an increase in supersaturation levels. This corresponds to a decrease in growth rates as observed by Tanrikulu (2000). Total nucleation rates were higher at lower residence times as would be expected with higher levels of supersaturation (Fig.5.19).

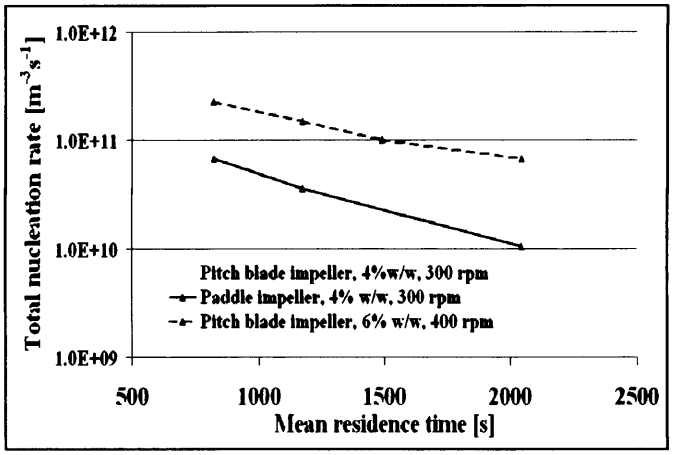

Figure 5.19: *Total nucleation rate versus mean residence time.*

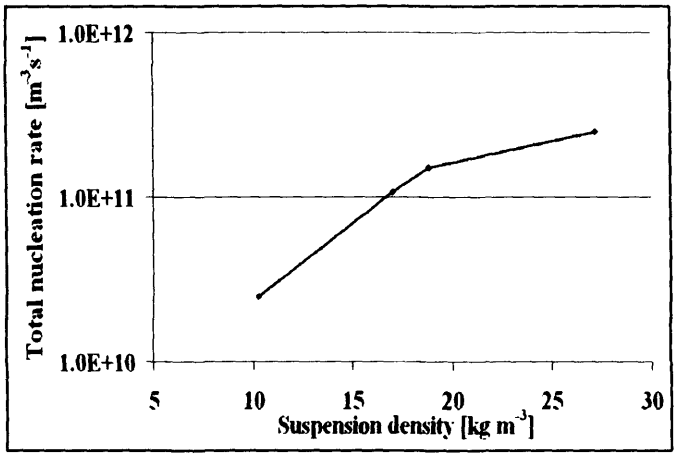

Figure 5.20: *Total nucleation rate versus suspension density (pitch blade).*

Values for the kinetic orders, 'i', 'j' and 'k' were determined by best fit to equation 5.9 and the following empirical power law total nucleation rate expression for the 0.5 litre MSMPR crystallization vessel equipped with a pitch blade impeller was developed as follows (Fig.5.21),

$$B_{TOT} = 1.0e^{19} M_T^{1.55} G_{av}^{1.2} \varepsilon^{0.15} \qquad [5.28]$$

The nucleation rate was proportional to the suspension density, average growth rate, supersaturation and the impeller velocity. The nucleation rate is strongly dependent on the suspension density if 'i', is greater than zero. The growth rate is a function of the supersaturation levels and since 'j' is greater than unity, the supersaturation levels affect the steady state crystal size distribution.

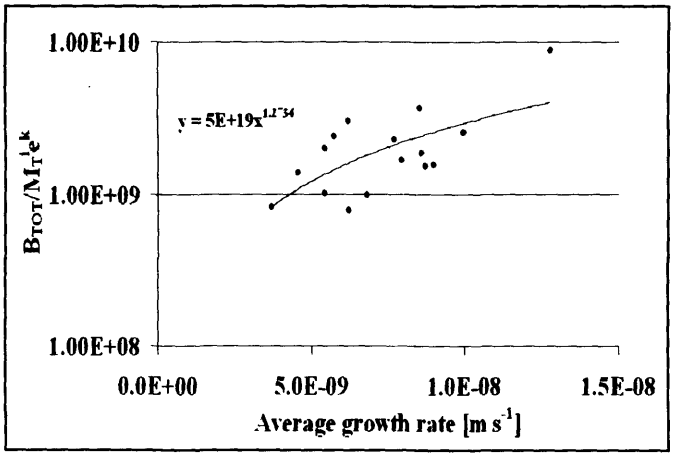

Figure 5.21: *Total nucleation rate versus average growth rate (pitch blade impeller).*

The dependency of the impeller velocity on the nucleation rate is not significant and may be due to the small range of impeller velocities used for the 0.5 litre MSMPR vessel. The total nucleation rate can also be expressed in terms of relative supersaturation and suspension density by treating the data in the same way (Fig.5.22) as described previously to produce the following modelling equations for both the pitch and flat blade impellers,

$$\text{Pitch blade impeller}: B_{TOT} = 4.0e^{09} M_T^{1.57} \sigma^{2.64}$$
$$\text{Flat blade impeller}: B_{TOT} = 1.98e^{09} M_T^{1.64} \sigma^{2.93} \qquad [5.28/5.29]$$

It was found that the kinetic order dependence of relative supersaturation was 2.64 and 2.93 for the pitch blade and flat blade impeller respectively, suggesting some evidence primary nucleation occurring.

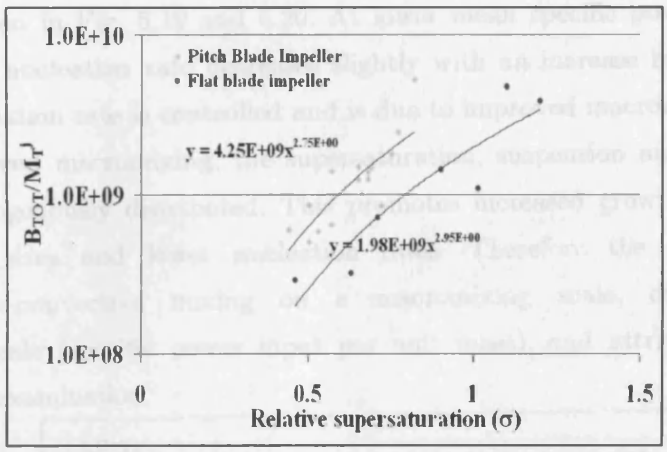

Figure 5.22: *Total nucleation rate versus the relative supersaturation.*

This is to be expected as the area surrounding the exit of the clear feed solution re-cycle feed pipe is where significant spontaneous primary nucleation will occur. This is due to the hot feed stream cooling rapidly as it enters the crystallizer.

The MSMPR experiments using a 4% w/w initial solids loading concentration produce lower nucleation rates over the whole range of residence times investigated than when using a 6% w/w initial solids loading concentration (Fig.5.19). Zauner and Jones (2000), investigating the calcium oxalate system observed the same

behaviour. This observation is expected, as higher suspension densities are produced at steady state and hence the frequency of particle-impeller, particle-particle and particle-wall interactions increase. When using a 4% w/w initial solids loading concentration, the total nucleation rate is also dependent on the type of impeller used. Higher total nucleation rates are produced when using a pitch blade impeller compared to a flat blade impeller.

The difference is due to geometries of the impellers and thus different hydrodynamics conditions produced by the impellers in terms of energy dissipation, degree of mixing and flow pattern affecting the attrition rate, with more secondary nuclei being produced with the pitch blade impeller. These results are confirmed from the use of computational fluid dynamics (CFD).

From Fig.5.23, we can see that there is some dependence of the specific power input on the total nucleation rate. Higher total nucleation rates are produced at higher suspension densities and shorter residence times, which confirms the observations seen in Fig. 5.19 and 5.20. At lower mean specific power inputs per unit mass, the nucleation rate decreases slightly with an increase in power input. The total nucleation rate is controlled and is due to improved macromixing.

With improved macromixing, the supersaturation, suspension and temperature are more homogenously distributed. This promotes increased growth rates, larger mean crystal sizes and lower nucleation rates. Therefore the mixing effects involving bulk-convective mixing on a macromixing scale, diffusion on a micromixing scale (specific power input per unit mass), and attrition affects all merit a closer examination.

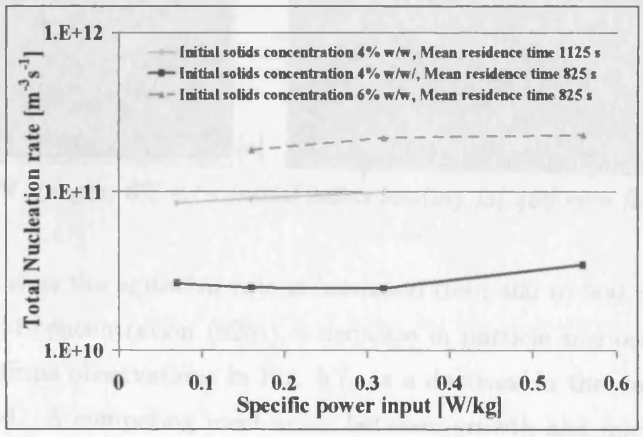

Figure 5.23: *Total nucleation rate versus specific power input per unit mass.*

The measured average linear growth rate (G_{av}) can be converted into an overall mass rate (R_G) by using the following equation,

$$R_G = \frac{3.k_a.\rho_c}{k_v}.G_{av} \qquad [5.30]$$

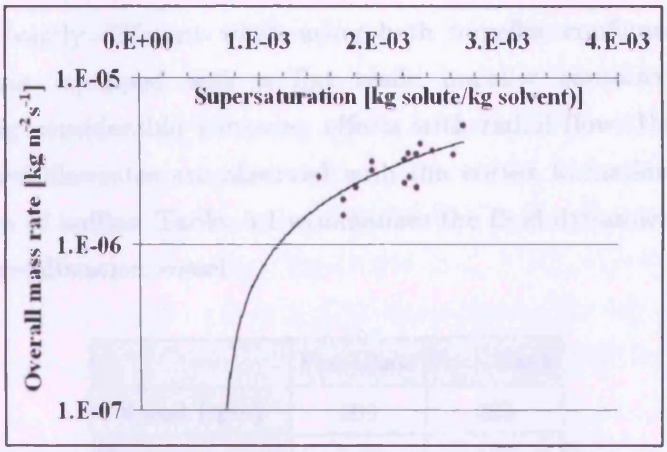

Figure 5.24: *Overall mass growth rate versus supersaturation.*

Fig.5.24 shows the overall mass growth rate as a function of the relative supersaturation level.

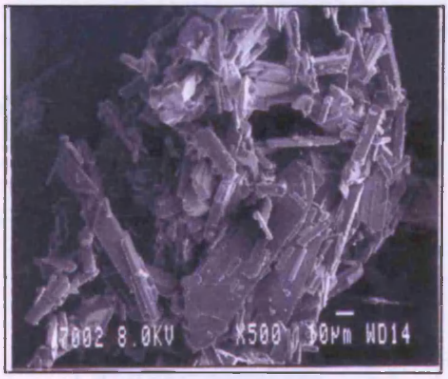

[a]

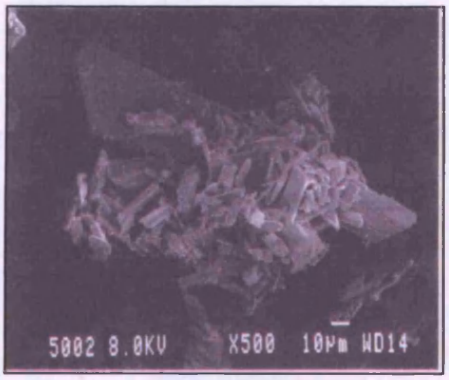

[b]

Figure 5.25: *SEM images: 6% w/w initial solids loading [a] 400 rpm [b] 500 rpm.*

Fig. 5.25 ahows that as the agitation rate is increased from 400 to 500 rpm using a 6% w/w initial solid concentration (825s), a decrease in particle size occurs due to attrition. This confirms observations in Fig. 5.7, as a decrease in the volume mean size is also observed. A competing mechanism between growth and micro-attrition occurs because an increase in growth rate is observed at 500 rpm (Fig.5.29).

5.4.5 COMPUTATIONAL FLUID DYNAMICS

Computational Fluid Dynamics is a powerful tool that can be used to provide an explanation for the higher nucleation rates that are observed using a pitch blade impeller compared to a flat blade impeller. The overall flow pattern produced in the crystallizer is vastly different when using both impeller configurations. The MSMPR crystallizer equipped with a flat blade impeller contains no baffles therefore producing considerable vortexing effects with radial flow. Using a pitch blade impeller, lower flowrates are observed with the vortex formation eliminated due to the presence of baffles. Table. 5.1 summarises the fluid dynamic information of the MSMPR crystallization vessel.

	Flat Blade	Pitch Blade
Speed (rpm)	300	300
Tip speed (m/s)	1.02	0.72
Re imp	7190	3600
Q_p (m^3/s)	3.07E-04	1.67E-04
t_{circ} (s)	1.79	3.29
Po	0.76	1.24
Power (W)	0.09	0.03

Table 5.1: *Hydrodynamic information for 0.5l MSMPR cooling crystallizer.*

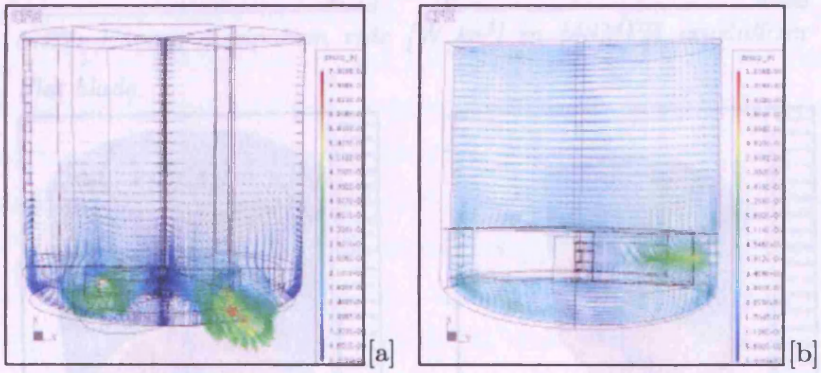

Figure 5.26: *Velocity profiles [m s^{-1}] [a] Pitch blade [b] Flat blade impeller.*

As expected higher tip speeds, impeller Reynolds numbers and pumping volumetric rates are produced using a flat blade impeller at the same agitator speed.

The mixing intensity and local energy dissipation rates within the MSMPR crystallizer using a flat blade impeller is significantly much higher than when using a pitch blade impeller configuration. This phenomenon does not affect the mass transfer and growth rate significantly but affects the nucleation rates. We should observe higher nucleation rates using the flat blade impeller. However, the results from the shear rate distribution profiles suggest that higher shear forces are produced in the impeller zone when using a pitch blade. Furthermore, the pitch blade impeller consists of four blades providing for a higher shear region. The shear is a possible reason for explaining the difference observed in nucleation. Fig. 5.26a and 5.26b shows the velocity profiles within the MSMPR crystallizer using a pitch and flat blade impeller respectively. Fig. 5.27a and 5.27b shows the energy dissipation rate profiles within the MSMPR crystallizers. Fig.5.28a and 5.28b shows the normalized shear distribution profiles within the MSMPR crystallizers.

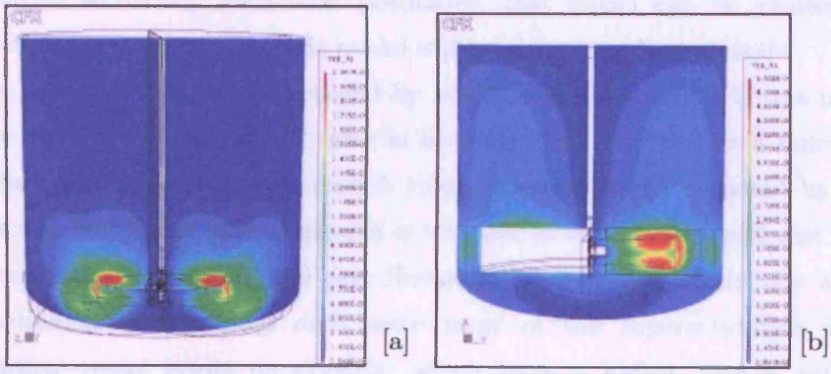

Figure 5.27: *Energy dissipation rate [W kg^{-1}] in MSMPR crystallizer [a] Pitch blade [b] Flat blade.*

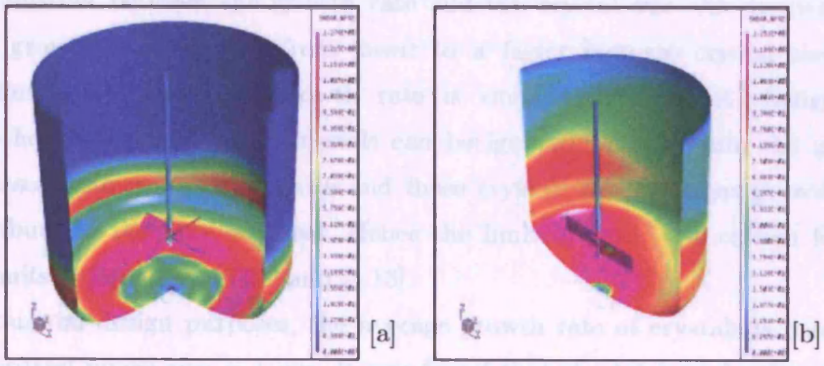

Figure 5.28: *Normalized shear distribution in MSMPR crystallizer [a] Pitch blade [b] Flat blade.*

5.5 DISCUSSION

Estimating crystallization kinetics in systems, which exhibit size-dependent growth pose problems in the estimation of growth and nucleation rates. Previous workers (Randolph et al, 1972; Budz and Jones, 1986; Sha et al., 1996) studying the potassium sulphate system found very little agreement for the estimation of growth and nucleation kinetics.

Published data varied greatly for the estimation of nucleation rates and was due to the technique used for estimation. The effective nucleation rate is mostly used. Some workers suggest that the effective nucleation rate can be calculated by using a single size crystal nucleation rate and that all crystals grow from this size. The effective nucleation rate was chosen as the smallest crystal size before the strong curvature on the population density distribution but this is arbitrary. The mechanism of secondary nucleation postulates, that nuclei can be created in a range of crystal sizes but only some nuclei will grow into product crystals.

In this research, the model proposed by Mydlarz and Jones (1994) was used to determine apparent linear growth rates in a steady state MSMPR as a function of crystal size and compared to the growth rate dispersion model proposed by Jones (2002). It was found that crystal growth is very low in the small crystal size ranges and increases linearly with crystal size. However, these crystals contribute a small mass fraction to the product and hence most of the supersaturation in the crystallization vessel grows on crystals, which have a higher growth rate and consequently are of a larger size. Thus the total nucleation rate was determined from the relation between the growth rate and the crystal size. As discussed, at 1μm, the growth rate changes from linear to a faster increase crystal size. For crystal sizes below 1μm, the growth rate is small and does not change and therefore the state of the small crystals can be ignored. Above 1μm, the growth rate increases faster with crystal size and these crystals with a larger growth rate will contribute to the product mass. Hence the limit of 1μm, was chosen for the integral limits in equations [5.12] and [5.13].

For industrial design purposes, the average growth rate of crystals is used and that the critical nuclei size is 1 μm. It was found that the total nucleation rate is proportional to the suspension density and supersaturation with an order

dependency greater than 1. Thus it possible that particle-impeller, particle-crystallizer, particle-particle contacts and fluid shear, all contribute in the production of attrition fragments. Synoweic et al (1993) carried out detailed investigations, to determine attrition rates in stirred tank reactors using low solids concentrations.

From SEM analysis, crystal breakage into two identical daughter particles is not observed but instead small attrition fragments less than 10 μm are produced from crystals larger than 150μm, which leads to the assumption that fluid shear and crystal-crystal contacts may play part in attrition. However, the majority of attrition is due to particle-impeller contacts. The high dependency order on the suspension density may be due to the moderate suspension densities used for the MSMPR crystallizations. Synoweic et al (1993), also postulates that attrition fragments produced by crystal-impeller and crystal-fluid shear show a first order dependency, whereas crystal-crystal contacts imply a second order dependency. Therefore a combination of crystal-impeller, crystal-crystal and crystal-fluid shear contribute to the production of attritions.

It is deduced that these small attrition fragments grow at a very low growth rates. It maybe also possible that the upward curvature in the population density distributions may be produced as a result of growth rate dispersion, and that these fragments may grow at different rates at a specific crystal size, or may exhibit a constant growth rate which is independent of crystal size. It is also difficult to determine, if any attrition fragments acting as secondary nuclei dissolve or are non-growing. Using the exponential size-dependent growth model the growth rate dependency of crystal size was determined as well as being able to deduce at which, crystal size the growth of crystals becomes size-independent.

The impeller type used did not affect the growth rate of the organic compound significantly and the mechanism of crystal growth (bulk diffusion and surface integration contribution) can be described by an effectiveness factor as function of crystal size. However, the impeller type did affect the nucleation rate significantly due to the different shear forces produced and affected the CSD due to attrition effects, reduction in growth and crystal size.

Accurate estimation of crystallization kinetics is of paramount importance in crystallization processes as they determine the crystal size distribution. The modified MSMPR crystallizer used in this investigation allows for a convenient and

successful method of estimating crystallization kinetics that is not heavily contaminated with hydrodynamic information. Computational Fluid Dynamics (CFD) can be used to evaluate hydrodynamic phenomena on different scales of operation and combined with the crystallization kinetics through the use of compartmental modelling to predict the crystal size distribution and will be covered in subsequent chapters. The modified MSMPR crystallizer developed in-house is suitable for pharmaceutical compounds that are available in limited quantities during the early stages of development.

5.6 CONCLUSIONS

From our investigations we can conclude the following,

I. The habit of the crystals is parallelepiped and irregular from MSMPR crystallizations.
II. The crystal size distribution is affected by supersaturation, suspension density, impeller velocity and type.
III. The exponential size dependent growth model proposed by Mydlarz and Jones was successfully used to model crystal growth.
IV. It is difficult to distinguish between GRD and SDG in an MSMPR crystallizer.
V. Impurities affect the growth kinetics of the organic fine chemical.
VI. The total nucleation rate is proportional to the suspension density, average growth rate and energy dissipation.
VII. The total nucleation rate is estimated based on the relationship between the growth rate and the crystal size.
VIII. Growth shows a first order dependency on the supersaturation for crystals greater than 200μm, and is size independent.
IX. Mixing effects involving macromixing and micromixing are important factors influencing the crystallization process. In order to provide more insight into mixing effects in crystallization, Computational Fluid Dynamics (CFD) is a powerful tool that can be used to investigate mixing effects on different scales.

5.7 FURTHER WORK

Industrial batch cooling crystallization systems are often dominated by secondary nucleation, particularly contact nucleation and crystal growth. The formation of secondary nuclei is a complex process and depends on the hydrodynamics within the crystallizer as explained in this chapter. The secondary nucleation, however, also depends on the attrition behaviour of the organic fine chemical including the growth of attrition fragments produced. Crystallization kinetic models developed describing secondary nucleation are of an empirical nature and are true of the secondary nucleation models used in this research. They do not contain the particle mechanics of importance for attrition and miss the link between the attrition process and prevailing hydrodynamics within a batch cooling crystallizer. As a result the secondary nucleation model has to be re-derived for different crystallizer configurations and impeller types as undertaken in this work. These models are therefore not very reliable for scale-up purposes. More recently, Gahn and Mersmann (1999a; 1999b) have developed a modeling framework for attrition, secondary nucleation and growth. This framework contains a more physical basis than any previous work: the secondary nucleation rate caused by crystal-impeller collisions is calculated largely from first principles. The framework consists of three further models as follows:

I. Method to determine the total number of crystals colliding per second with the faces and edges of the impeller blades including the impact energy per collision (Mersmann et al., 1988; Ploß et al., 1989).
II. A relation between the impact energy and the attrition volume produced due to a single collision of a crystal corner with a hard, flat surface and the resulting number and size distribution of resulting attrition fragments (Gahn et al., 1997).
III. A relation to derive the growth rate of the fragments formed by the attrition process.

This model is expected to have the predictive characteristics necessary for scale-up and process design and is recommended for future modeling development. The attrition model developed in this research (Chapter 6) is based on the average

energy dissipation rate and does not consider the physical and mechanical properties of the organic fine chemical. The crystallization kinetic models determined for growth and nucleation have been evaluated at a constant temperature. The effects of temperature on the mass transfer and crystal growth have to be investigated including the evaluation of the activation energy necessary for growth. The effect of temperature on the growth and nucleation rate constant can be expressed by an Arrhenius-type relationship (Mullin, 1972) as follows,

$$k = k_{\infty} \exp\left(\frac{-E}{RT}\right)$$

The crystallization kinetic models have also been determined at steady state at a constant supersaturation level and therefore the transfer of these crystallization kinetic models to batch operations leads to the under prediction of the particle size distribution as shown in Chapter 9. Therefore it is necessary to develop crystallization kinetic models for the organic fine chemical using batch cooling kinetic experiments. Furthermore, the stress and strains, the crystalline structure experiences under over a range of crystal sizes should be investigated including mosaic spreads using diffraction techniques to determine the crystal growth mechanism and the effects of dislocations in the crystalline structure.

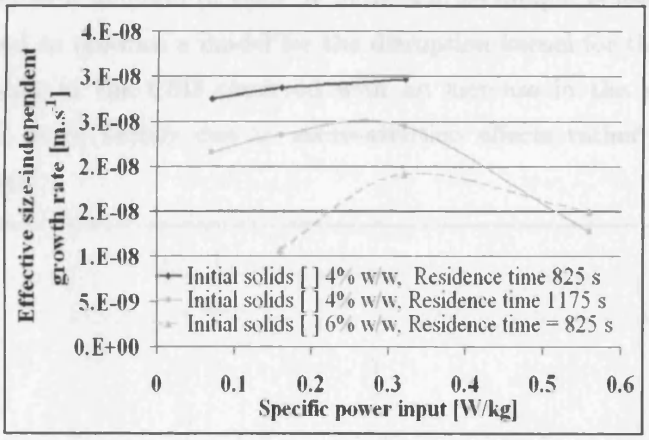

Figure 5.26: *Effective size-dependent growth rate versus specific power input using different initial solids concentration and mean residence times (pitch blade impeller).*

Chapter 6

MODELLING PARTICLE DISRUPTION USING LASENTEC FOCUSSED BEAM REFLECTANCE MONITORING (FBRM) IN AGITATED SUSPENSIONS

ABSTRACT

The FBRM instrument developed by Lasentec is a 'powerful' tool used an *'in-situ'* particle monitoring technique for in-line real time measurement of particle size. This technique was successfully used to monitor particulate attrition of an important organic compound in a turbulently agitated suspension. The great advantage of using the FBRM technique is that the change in the crystal size distribution (CSD) for different particle size classes (fine, intermediate and coarse) can be monitored as a function of time. A numerical technique is used to evaluate attrition rates and to produce a model for the disruption kernel for the organic fine chemical. The shift in the CSD observed with an increase in the specific power input was found to be largely due to micro-attrition effects rather than particle breakage (splitting).

6.1 INTRODUCTION

FBRM method is a relatively new method developed by Lasentec to perform particle size measurements in the range of 0.25-1000 μm. The great advantage of this technique is that data is acquired on-line and in real time to give particle size data and population trends of particles in suspension. The technique does not require sampling or isolation that may contribute to changes in particle size and distribution due to breakage or agglomeration. The FBRM technique has been used widely in monitoring of crystallization processes Wood-Kaczmar, 2002; Barett et al., 2002; Carreta and Liebel, 2000). Barrett et al., (1999) successfully used the Lasentec FBRM technique to monitor particle size in dilute agitated suspensions. This chapter reports an investigation into the *'in-situ'* use of the FBRM technique to monitor particle trends in-line and monitor the changes in the crystal size distribution as a result of attrition effects in a dilute turbulently agitated suspension. Crystal attrition is a secondary process that has been found to occur during the continuous MSMPR crystallization process of the organic compound and has the effect of increasing the effective nucleation rate. Randolph (1969) studied the effect of crystal breakage on the CSD in a continuous MSMPR crystallizer and described the influence of attrition. Halfon and Kaliaguine (1979) observed breakage in the batch crystallization of alumina trihydroxide but did not account for its effect in their model. Synoweic et al. (1993) investigated theoretical and experimental particle attrition of potash alum and potassium sulphate crystals in dilute turbulently stirred suspensions. Wójcik and Jones (1998) investigated particle disruption of precipitated calcium carbonate agglomerates in turbulently agitated suspensions by fitting the population balance for agglomeration and disruption to the experimental CSD data using a non-linear least squares fit.

6.2 THEORY

The function most often used in modelling attrition and disruption processes has the form,

$$\beta_d(L_i,L_j)=k_d[L_i+L_j]^3 \qquad [6.1]$$

Disruption rate is described as the rate at which particulate attrition occurs i.e. a

parent particle disrupting to produce multiple daughter fragments of different sizes, two daughter particles of different particle sizes or the same particles. The disruption rate is proportional to the particle volume and the disruption rate is dependent on the particle volume. A third-order dependence on the particle size (proportionality to particle volume) was determined (Synoweic et al., 1993) and explained by both turbulence particle shear and particle-impeller collisions. The disruption rate of particles is also a function of the degree of supersaturation levels within a batch cooling crystallizer. The seeded batch attrition experiments in this work are carried out at $\sigma = 0$ (S=1) and hence the effects of supersaturation on the disruption process is not taken into account. Increasing supersaturation levels increases the growth rate and thus results in a reduction in particle disruption. In addition, the disruption rate increases with increased power input.

$$\beta_d \propto \varepsilon \qquad [6.2]$$

Hence, the disruption rate function is described as follows,

$$\beta_d(L_i, L_j, \varepsilon, S) = k_d \varepsilon^r S^s f(L_i, L_j) \qquad [6.3]$$

For simultaneous attrition and agglomeration the population balance equation (PBE) using particle volume as the internal coordinate is given as follows (Randolph and Larson, 1988),

$$\begin{aligned} \frac{dn(v)}{dt} &= B - D \\ &= \beta_d(n(v+dv) - n(v)) + \beta_a(0.5 \int_{vo}^{v-vo} n(u)n(v-u)du - \int_{vo}^{\infty} n(u)n(v)du \end{aligned} \qquad [6.4]$$

The population can be written in discretised form with constant volume intervals for the first class (there being no birth by agglomeration and no death via disruption) as follows,

$$B_{d1} - D_{a1} = \frac{\Delta n_1}{\Delta t} \qquad [6.5]$$

For the last class (there being no death through agglomeration or death due to disruption),

$$B_{an} - D_{dn} = \frac{\Delta n_n}{\Delta t} \quad [6.6]$$

For the other classes it is postulated that,

$$B_{ak} - D_{ak} + B_{dk} - D_{dk} = \frac{\Delta n_k}{\Delta t} \quad [6.7]$$

For size-dependent agglomeration,

$$B_{ak} = 0.5 k_a \Sigma N_i N_j (v_j + v_j) \quad [6.8]$$

While for size-independent agglomeration,

$$B_{ak} = 0.5 \beta_a \Sigma N_i N_j \quad [6.9]$$

For size-dependent agglomeration,

$$D_{ak} = k_a N_k \Sigma N_i (v_k + v_j) \quad [6.10]$$

For size-independent agglomeration,

$$D_{ak} = \beta_a N_k \Sigma N_i \quad [6.11]$$

For size-dependent particle disruption,

$$B_{dk} = k_d N_{k+1} v_{k+1}^{5/3} \quad [6.12]$$

And for size-independent particle disruption,

$$B_{dk} = \beta_d N_{k+1} \quad [6.13]$$

A birth event of a disrupted particle within class k is assumed to occur only if in the k+1 class death via a disruption event occurs as follows,

$$D_{dk} = k_d N_k v_k^{5/3} \quad [6.14]$$

$$D_{dk} = \beta_d N_k \quad [6.15]$$

Equations [6.1] to [6.15] assume that the volume of particles disrupted is equal to Δv.

6.3 EXPERIMENTATION

The *Lasentec*© D600L FBRM instrument is used in this investigation to monitor the shift in the crystal size distribution at various specific power inputs and to model particulate attrition. A detailed operating mechanism of the Lasentec FBRM technique is described in Chapter 4. Stirred seeded batch experiments were carried out using the organic fine chemical in a 0.5l batch crystallization vessel (1) equipped with three baffles and a four-blade 45° pitch impeller under fully turbulent conditions. The critical Reynolds number for turbulent flow is greater than 3×10^3 and the Reynolds numbers produced in this investigation cover a range from 4×10^3- 7×10^3 producing fully turbulent conditions in each case. A series of three experiments was performed in which the organic compound was suspended in a saturated solution of pure filtered isopropyl alcohol-water at equilibrium in order to minimize crystallization (nucleation, growth and agglomeration), dissolution and Ostwald ripening. The dilute slurry consisted of 10 g organic compound in 500 ml solvent (93:7 %v/v isopropyl alcohol-water). For best results, the *Lasentec*© D600L probe tip, is located in a region of high turbulence above the impeller zone. Fig.6.1 shows a schematic diagram of the apparatus used for the batch attrition experiments including the Lasentec instrument. The batch crystallizer was also fitted with a condenser to prevent solvent loss and to maintain a constant volume. The compound is susceptible to aerial oxidation and had to be kept under a blanket of nitrogen for entire duration of the experiment. The Huber Tango (5) automated heater/chiller unit maintained the crystallizer vessel at a constant operating temperature of 20 °C. The dilute suspension was agitated for 150 minutes at 300 rpm. The impeller frequency was then increased to 400 rpm and 500 rpm respectively and agitated for a further 150

minutes at each new impeller frequency. The change in the initial CSD was measured automatically at one-minute intervals using the Lasentec FBRM D600L probe at each new impeller frequency. The Lasentec FBRM CSD data for the population balance was discretised into 200 uniform classes. Values for disruption rates (β_{dist}) and disruption coefficients (k_d) were evaluated from the measured CSD and equations [6.1] to [6.15] by means of a non-linear least-squares fit to the experimental CSD data using Wójcik and Jones (1998) numerical technique. Fortran 90 code is enclosed in Appendix A and uses an external routine from the NAG library. Additionally, the net attrition fragmentation rate per crystal dn_e'/dt was calculated (Synoweic, 1993).

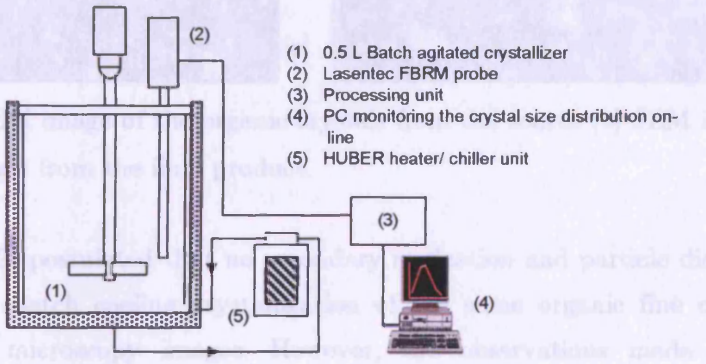

Figure 6.1: *Schematic representation of the experimental apparatus used for attrition.*

6.4 RESULTS AND DISCUSSION

The disrupted material was isolated, washed and dried after agitation at 500 rpm (Fig. 6.2a and 6.2b) and examined by scanning electron microscopy (SEM). The images were compared with SEM images of original input material. This provided evidence that any change observed in the crystal size distribution is purely as a result of crystal attrition. Careful comparison of the images shows that there was little evidence to suggest particle breakage (splitting) and a more detailed analysis using the FBRM particle numbers distribution revealed the presence of micro-attrition consistent with observations of both Wòjcik and Jones (1993) and Randolph (1969). The final product contains significantly more fine

particles (chippings) than the source. Micro-attrition was also observed from continuous steady state MSMPR crystallizations as detailed in Chapter 5 and it is likely that this gives rise to bimodality in both batch and continuous crystallization particle size distributions for the compound due to the attrition of particles (Fig.4.10a).

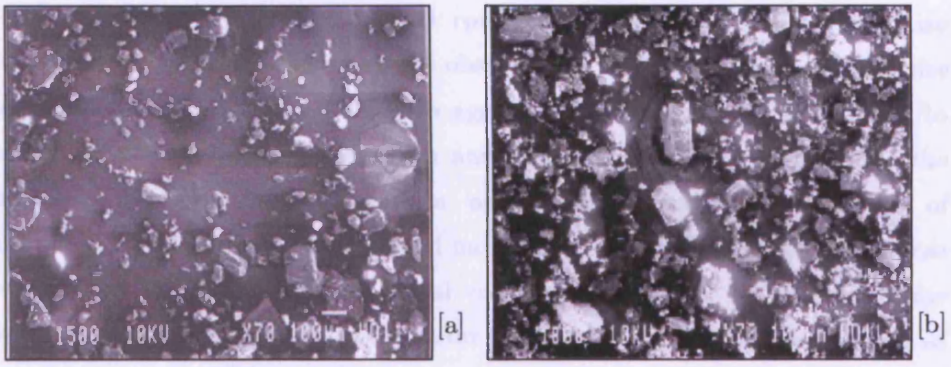

Figure 6.2: [a] SEM image of the organic crystals from the source [b] SEM image of the organic crystals from the final product.

Patience (2002) postulated that no secondary nucleation and particle disruption occurred for the batch cooling crystallization of the same organic fine chemical based on light microscopy images. However, the observations made in this investigation are consistent with research carried out by Jones (1974) using the potassium sulphate in batch cooling crystallizations.

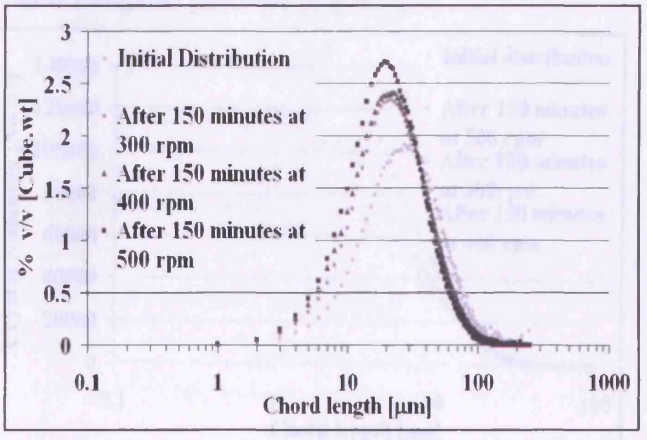

Figure 6.3: *Effects of attrition on the crystal frequency at different agitator speeds using Lasentec FBRM.*

Jones showed that significant secondary nucleation effects were evident as a result of particulate attrition and breakage, even at low levels of supersaturation. The attrition rates and disruption kernel need to be taken into account for the purpose of predictive scale-up modelling of batch suspension crystallization processes in order for the system to be accurately described.

Using an impeller frequency of 500 rpm, a small shift in the particle size distribution to a coarser particle range is observed for the intermediate particle size range (20-40 μm), which may be due to agglomeration of particles in addition to disruption effects. Agitation at 300 rpm and 400 rpm yielded zero values for the agglomeration kernel. At 500 rpm an agglomeration kernel of an order of magnitude of 10-13 # min^{-1} was obtained indicating some agglomeration but it was not considered to be significant. Aerial oxidation is known to promote some particulate agglomeration especially after prolonged periods of agitation as discussed previously (Chapter 5). However, particulate agglomeration is not the primary mechanism of particle formation for the crystallization system and hence will not be modelled as the crystallizations on a large scale are performed in an inert atmosphere even though agglomeration events are postulated to increase upon scale-up. Furthermore, the total number of particles measured by the Lasentec FBRM system increased as a result of each attrition event producing a number of daughter particles as shown in Fig.6.4. The population density distribution also changes with an increase in specific power input per unit mass due to the birth of new daughter particles (Fig.6.5).

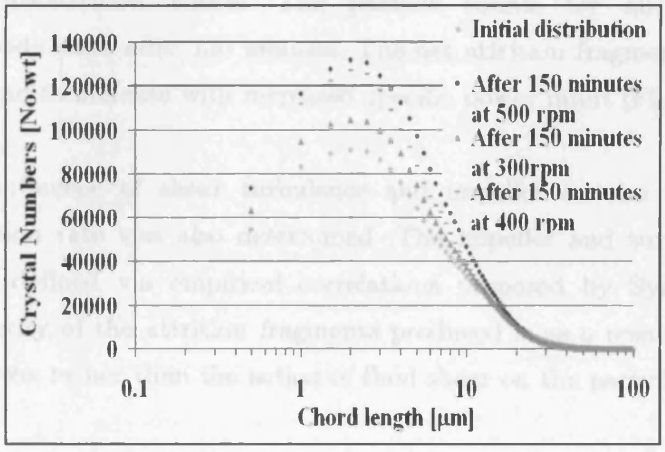

Figure 6.4: *Effects of agitator speed on the crystal numbers due to attrition using Lasentec.*

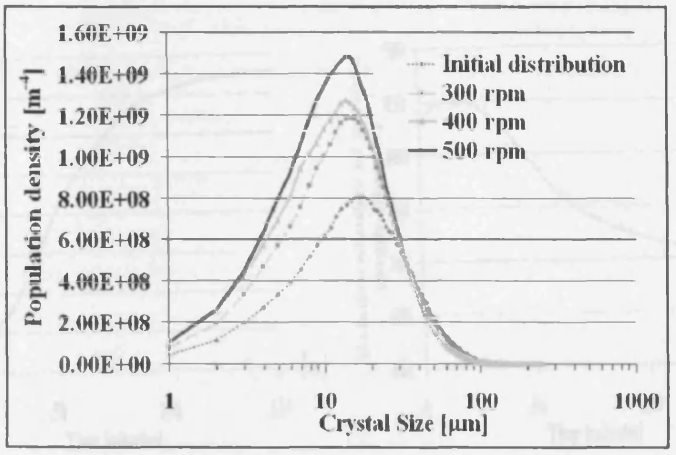

Figure 6.5: *Population density distribution shift as the agitator speed is increased.*

The advantage of using the Lasentec FBRM technique in this investigation is that the number of particle counts for a size range or bound can be measured independenlty of other size ranges. Fig. 6.6 shows that the number of fine particles (0-10 µm) increased and the number of coarse particles (100-300 µm) decreased continuously. Initially, the intermediate particle counts (50-100 µm) increased due to breakage, reaching a maximum after six minutes followed by a decrease.

The intermediate particle counts (10-50 µm) increase, reaching a maximum after twenty minutes as a result of disruption of particles in the 50-100 µm particle size range. The Lasentec FBRM system is successful in monitoring the death and birth of particle by disruption for different particle size classes and provides evidence of micro-attrition effects. The particle counts for all size groups approached a steady state after 150 minutes. The net attrition fragment generation rate was also found to increase with increased specific power input (Fig.6.7).

The individual influence of shear turbulence and impeller on the net attrition fragment generation rate was also determined. The impeller and turbulent shear contribution are defined via empirical correlations proposed by Synoweic et al (1993). The majority of the attrition fragments produced is as a result of particle-impeller interactions rather than the action of fluid shear on the particles (Fig.6.8).

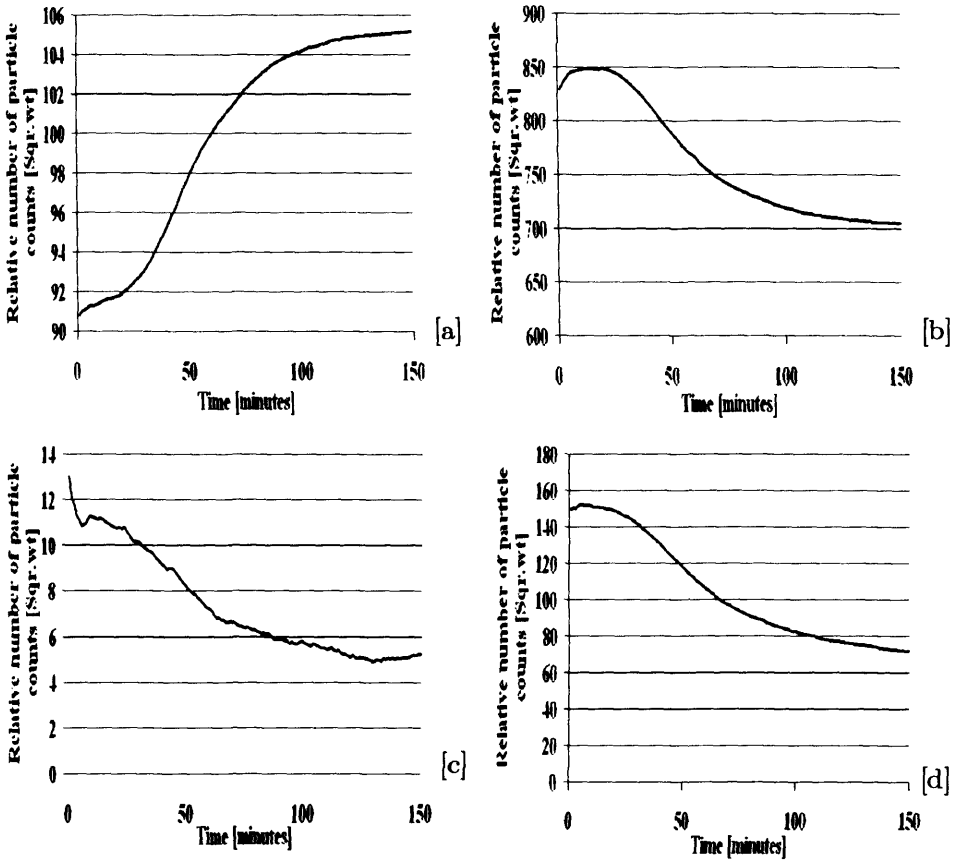

Figure 6.6: In-line FBRM monitoring attrition showing particle trends (square weight) over time for different particle size groups: [a] 0-10μm, [b] 10-50μm, [c] 50-100μm and [d] 100-300μm at an impeller speed of 300 rpm.

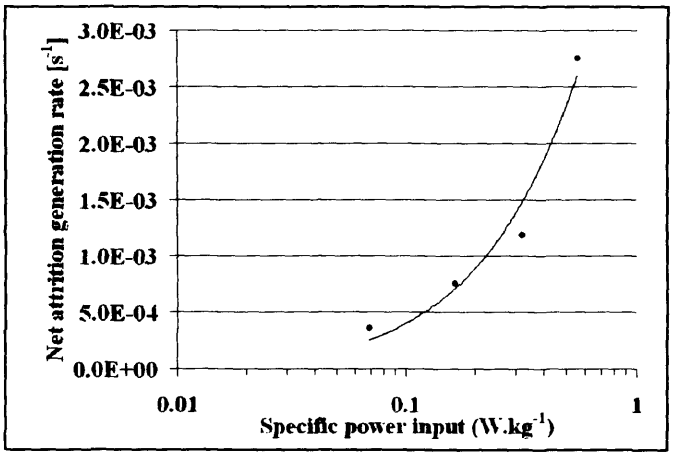

Figure 6.7: *Power input influence on net attrition fragmentation generation rate.*

Fig.6.9 shows the influence of the specific power input on the disruption kernel. Hence a linear increase of the disruption kernel with the growth rate is used producing the following relationship,

$$\beta_d \propto G^{-1} \quad or \quad \beta_d \propto \sigma^{-1} \qquad [6.16]$$

The final relationship proposed for the disruption kernel is as follows,

$$\beta_d = 2.05x10^{-6} \varepsilon\sigma^{-1} \qquad [6.17]$$

$$\beta_d = k_d \varepsilon\sigma^{-1} \qquad [6.18]$$

6.5 CONCLUSIONS

The Lasentec FBRM instrument is a powerful and convenient tool that was successfully used to monitor the shift in the crystal size distribution using increased specific power inputs as a function of time. This technique therefore has a distinct advantage over other measurement techniques as monitoring is performed in-line and in real time. The Lasentec instrument provides evidence of micro-attrition effects rather than particle breakage. The importance of modelling particle attrition and disruption is such as that it can be taken into account for the accurate prediction of crystallization behaviour upon scale-up. This is due to attrition and secondary nucleation being ignored in the models resulting in poor predictions.

6.6 FURTHER WORK

As determined from experiments carried out using a modified MSMPR crystallizer to estimate growth and nucleation kinetics, the total nucleation rate model is also dependent on the suspension density, in addition to the energy dissipation. Further experiments need to be carried out to determine the effects of the suspension density on the disruption kernel. Detailed investigations with regards to the effects of supersaturation including the development of a physical model based on impeller contacts and material properties also merit examination.

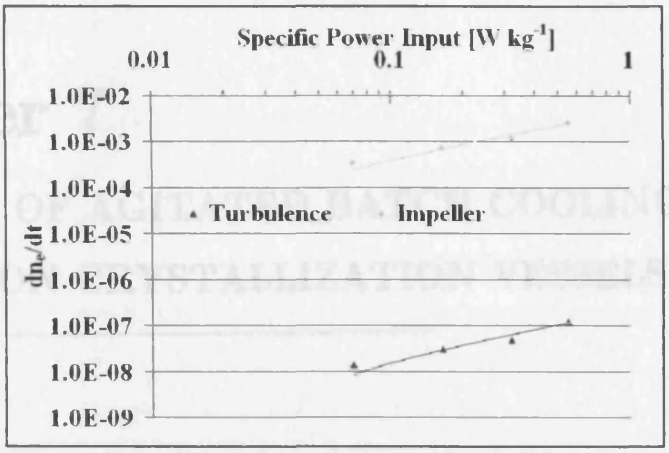

Figure 6.8: *Attrition fragment generation rate due to fluid shear and particle-impeller collisions.*

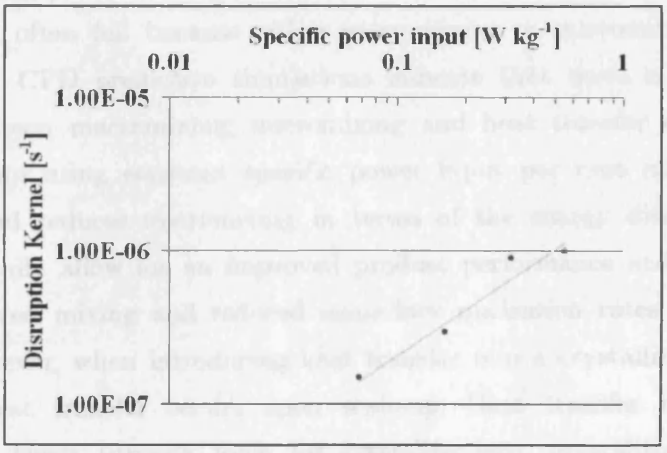

Figure 6.9: *Influence of specific power input on disruption kernel.*

The steady state CSDs produced from the modified MSMPR crystallizations exhibit bimodality (Malvern instrument). Such bimodality combined with analysis of SEM and photomicrograph images of the organic fine chemical suggests some evidence of size-dependent particulate attrition. Continuous MSMPR crystallizations carried out using the organic fine chemical at higher suspension densities produced as increase in the constant supersaturation levels. This corresponds to a higher nucleation rate and reduced growth rates. Based on these findings an increase in the disruption rate of the organic fine chemical with a reduced apparent growth rate will be assumed.

Chapter 7

SCALE-UP OF AGITATED BATCH COOLING SUSPENSION CRYSTALLIZATION VESSELS

ABSTRACT

The scale-up of batch cooling suspension crystallization vessels can be characterised using predictive computational fluid dynamics simulations. Common scale-up criteria often fail because either macromixing or micromixing processes can be limiting. CFD predictive simulations indicate that there is a competing mechanism between macromixing; micromixing and heat transfer existing upon scale-up. Scale-up using constant specific power input per unit mass, improves macromixing and reduces micromixing in terms of the energy dissipation. This should theoretically allow for an improved product performance and quality as a result of improved mixing and reduced secondary nucleation rates (micromixing decreases). However, when introducing heat transfer into a crystallization system, less efficient heat transfer occurs upon scale-up. Heat transfer influences the supersaturation levels (driving force for crystallization), crystallization kinetics including the final product performance significantly. The heat transfer effect with scale-up, will impact the crystallization process behaviour more significantly than the macromixing and micromixing effects. Therefore common scale-up criteria fail to take this into account. This severe problem posed can be overcome by introducing a compartmentalization approach for common crystallization scale-up problems.

7.1 INTRODUCTION

For many unit operations in chemical engineering, theoretical or empirical scale-up rules are developed. In processes, such as seeded batch cooling crystallizations, where the crystallization kinetics is controlled by the degree of mixing and relative supersaturation levels, these simple scale-up criteria fail. Therefore, resource is spent on trial and error experimentation during the scale-up of pharmaceutical crystallization processes. A cooling compartmental modelling framework is developed in this thesis and takes into account these mixing effects upon scale-up and is applied for a seeded batch cooling suspension crystallization process. Implementation of the population balance within the CFD environment is not feasible due to the excessive computational requirements because the Navier-Stokes equation for fluid flow must be solved simultaneously with the conservation equations. Compartmentalisation with regards to fluid flow simplifies the complexity of the problem and allows the population balance to be introduced to reduce the computational time required to simulate particulate processes The conventional approach to scale-up is based on the principal of similarity, which is aimed at maintaining similarity of equipment, flow characteristics, specific power input and temperature profiles. The maintenance of geometrical similarity requires identical ratios of corresponding dimensions in two scales. In this contribution geometrically similar batch agitated crystallization vessels are used. Geometric similarity is assessed by the tank height to diameter ratio including impeller to tank diameter ratio. However, the exact scale-up of crystallizers is not possible because it would be necessary to preserve similar flow characteristics of both the solid and liquid phases together with identical temperature and supersaturation profiles in all regions. The common scale-up criteria used include constant agitator tip speed, constant power input per unit mass (volume), constant Reynolds number and constant agitator speed.

7.2 THEORY

Using geometrically similar agitated crystallization vessels allows dimensional analysis to be used to describe the power requirements of the system. The

dimensionless terms typically associated with momentum transfer are described below. The Reynolds number describes the ratio of inertial to viscous forces prevailing in crystallizers and is given by,

$$\mathrm{Re} = \frac{\rho_F N d_i^2}{\mu} \qquad [7.1]$$

In agitated crystallizers fully turbulent flow is produced at Re > 20 000 with Po = constant. The Power number is given by,

$$P_O = \frac{P}{\rho_F N^3 d_i^5} = \frac{2\pi NM}{\rho_f N^3 d_i^5} \qquad [7.2]$$

Where P is the power drawn by the agitator, N is the agitator speed (rps) ρ_f is the slurry (suspension) density. In the turbulent regime, the power number remains constant. The power number value depends on the impeller type and is independent of scale, providing that geometric similarity is maintained as is presented in this thesis. The Froude number is defined as follows,

$$Fr = \frac{N^2 d_i}{g} \qquad [7.3]$$

The above relationship can be developed to produce a power curve, which is a plot of the Power number versus the Reynolds number for different geometrical set-ups (Harnby et al, 1992).

If an agitated vessel is equipped with baffles and there is a high Reynolds number producing turbulent conditions, the Froude number is neglible and ignored, hence producing the following relationship,

$$P_O = f(\mathrm{Re}) \qquad [7.4]$$

The Flow number is defined as follows,

$$Fl = \frac{Q_p}{N d_i^3} \qquad [7.5]$$

Where Q_p is the volumetric pumping flowrate just off the blade. In our crystallization process development study we are considering a pitch blade and Rushton turbine impeller only.

The volumetric pumping flowrate that moves perpendicularly through the swept circle directly below the edge of the impeller gives a value of 0.79 for a pitch blade impeller with 4 blades and a 45° inclination. For a high-entrained flow, a P_o of 1.27 is obtained. For the same type of impeller, the ratio of the Power to Flow number is constant. For constant power for different scale of operation with geometric similarity, the following pumping flowrate relationship is used,

$$Q_p \propto N d_i^3 \qquad [7.6]$$

Hence large impeller diameters produce high pumping volumetric flowrates. To maintain a constant turnover time upon scale-up, a constant N must be used.

Using dimensional analysis the following heat transfer correlation can be used to model the heat transfer coefficient in batch cooling crystallization vessels as follows,

$$Nu = f(\mathrm{Re}, \mathrm{Pr}, \mu/\mu_W, \textit{Impeller geometry}) \qquad [7.7]$$

The correlation used is as follows,

$$Nu = C\,\mathrm{Re}^a\,\mathrm{Pr}^b(\mu/\mu_W)^c \qquad [7.8]$$

$$C = f(\textit{geometry and flow regime}) \qquad [7.9]$$

For turbulent flow: a = 2/3 b = 1/3 c = 0.14.

At a constant energy dissipation and geometrical similarity the heat transfer coefficient relationship is as follows,

$$h \propto d_i^{-1/9} \qquad [7.10]$$

Hence the heat transfer coefficient is reduced when scaling up with constant specific power input per unit mass. Appendix H provides details of the heat transfer properties and liquid side heat transfer coefficients. Table 7.1 shows the operating and process conditions in a 1l, 5l and 25l crystallizer equipped with a pitch blade and Rushton turbine impeller respectively.

7.3 SOLID SUSPENSION

The condition of suspension of solid particles in an agitated vessel is defined in several ways. The degrees of suspension in order of increasing uniformity are described as follows,

I. **Nearly complete suspension with filleting:** Most of the solid is suspended in the solvent, with a few percent in stationary fillets of solid at the outside periphery of the bottom.

II. **Complete particle motion:** Particles are either suspended or moving along the tank bottom. Particles moving on the bottom have a much lower mass transfer coefficient than suspended particles and may affect crystallization process.

III. **Complete suspension:** All particles are suspended off the bottom of the tank or do not stay on the bottom for more than one to two seconds. In the suspension there will be concentration gradients and a clear solvent region maybe evident in the upper region of the tank, when this condition is reached.

IV. **Uniform suspension:** The suspension is uniform and there is no clear solvent region, however, vertical concentration gradients exist, especially if the solid has a wide size distribution.

For most manufacturing and process purposes a complete suspension is satisfactory. This, however, is not satisfactory for crystallization processes where the degree of suspension achieved affects the crystallization kinetics, crystal size distribution and final product performance. It is crucial to achieve a uniform suspension in seeded batch cooling crystallizers but it is difficult to be achieved in reality as seed growth leads to a wide CSD and concentration gradients.

7.4 MIXING

Mixing can be divided into three processes on different scales: (1) Macromixing (2) Mesomixing (3) Micromixing. The hydrodynamics of a batch crystallization vessel vary from one location to another, in terms of macromixing and micromixing. Macromixing occurs on a large scale and is mainly backmixing due to convection motion and is defined by a circulation time as follows,

$$t_{circ} = \frac{V}{Q_p} = \frac{V}{FlNd_i^3} \qquad [7.11]$$

Micromixing however comprises of the viscous-convective deformation of fluid elements, followed by molecular diffusion on the Kolmogorov scale. The rate of micromixing depends on the local rate of dissipation of the turbulent energy especially in the impeller region. The local rate of energy dissipation affects the crystallization kinetics of separations processes. The local energy dissipation is pertinent with respect to the attrition and secondary nucleation rates. For example, in the impeller zone and vessel walls most attrition and secondary nucleation rate and is dependent on the local value of energy dissipation or shear.According to Baldyga and Bourne (1992), the characteristic time for micromixing can be related to the engulfment rate, E, and thus to the turbulent energy dissipation rate,

$$t_{micro} = E^{-1} = 17.2\left(\frac{\varepsilon}{\nu}\right)^{-0.5} \qquad [7.12]$$

7.5 SCALE-UP RECOMMENDATIONS

7.5.1 SCALE-UP WITH CONSTANT AGITATION SPEED

This scale-up criterion is based on achieving a constant pumping volumetric rate per unit volume with scale-up. Based on a constant pumping rate we should expect to see similar macromixing performances or circulation times on different scales. However, solid-liquid phase CFD simulations predict that when scaling up with constant agitation speed for a 5l and 25l, the solids concentration profile is more homogenously distributed throughout the vessel with a reduction or

disappearance in the clear solvent region being observed even though the pumping volumetric flowrate per unit volume with scale-up is the same. From CFD simulations the volumetric pumping rate per unit volume can be determined. Using equation [7.11] circulation times were calculated to be 4.18s and 3.93s for the 5l and 25l vessels respectively and are similar as expected. Fig.7.1a and 7.1b show that when a dilute suspension of 5% v/v with a mean particle size of 200 μm, which is typically produced towards the end of the batch cooling crystallization process for the organic fine chemical on a 5l and 25l scale operating at 300 rpm the predicted solids concentration profile is vastly different. The reasons for this are that there is an increase in the specific power input per unit mass, tip speed and Reynolds number. A uniform suspension is produced on a 25l scale compared to a complete suspension on a 5l scale where a clear solvent region in the upper part of the agitated vessel is observed. The scale-up criteria for constant agitator speed is described as follows,

$$N_1 = N_2 \qquad [7.13]$$

Additionally, scale-up with constant N is almost impossible due to the large power requirements that will be necessary as follows,

$$P \propto d_i^5;\ \bar{\varepsilon} \propto d_i^2 \qquad [7.14]$$

Scale-up using constant agitator speed is not recommended due to the above observation in addition to excessive fine production. Another complication associated with the homogeneity of the solids within a seeded batch cooling crystallization process is that there is a wide crystal size distribution present. Therefore there will be continual changes in the vertical gradient with respect to the solids concentration throughout the crystallization process. Due to the high spatial resolution required with CFD simulations, it is not yet feasible to model the evolution of a crystal size distribution and solids concentration for a transient process as is the case with batch crystallizations.

7.5.2 SCALE-UP WITH CONSTANT TIP SPEED

If the tip speed of the impeller blades is kept constant upon scale-up then,

$$N_1 \pi d_1 = N_2 \pi d_2 \qquad [7.15]$$

Upon scale-up with constant tip speed we should expect to observe constant shear in the impeller zone. However, Oldshue (1993) observed that with larger scales, the maximum shear rate in the impeller zone increases while the average shear rate in this zone decreases. Hence the shear rate distribution changes with scale-up. The scale-up criterion is as follows,

$$N_2 = N_1\left(\frac{V_2}{V_1}\right)^{-1/3} \qquad [7.16]$$

7.5.3 SCALE-UP WITH CONSTANT POWER INPUT PER UNIT MASS

This scale-up criterion is the most commonly used in mixing limited unit operations and is based on constant mean energy dissipation rate per unit mass according to Harnby et al. (1985).

$$\varepsilon_{av} = \frac{P}{\rho_F V} = \frac{P_o \rho_F d^5 N^3}{\rho_F V} = constant \qquad [7.17]$$

This produces the following criteria,

$$N_2 = N_1\left(\frac{V_2}{V_1}\right)^{-2/9} \qquad [7.18]$$

The importance of the local energy dissipation rate and hence the specific power input for a batch cooling crystallization process is directly associated with the attrition and secondary nucleation rates. CFD simulations predict that when scaling up with the application of constant power input per unit mass, there is a competing mechanism between macromixing and micromixing phenomena that can influence the crystallization kinetic rates and product performance. CFD simulations on 1l, 5l and 25l batch crystallizer scales at a constant power input per unit mass using a pitch blade impeller and Rushton turbine impeller show, that the effects of micromixing on a local scale are reduced upon scale-up as the local energy dissipation profiles are not identical (Fig. 7.3 and Fig.7.4). The reason for this observation is that energy is dissipated over larger distances due to the increase in vessel size. In addition to this observation, the results of solid-liquid phase simulations predict that even though the macromixing (circulation) times increase with scale, the solids concentration profile is more homogenous. This is

attributed to the increase in the tip speed and Reynolds number with an increase in scale, producing higher volumetric flowrates within the crystallizers.

The type of impeller used also influence the micromixing and macromixing effects using the same constant power input per unit mass. The pitch blade impeller operates at higher impeller frequencies producing higher tip speeds and pumping rates. This produces reduced macromixing times at the same vessel scale. However, the solids concentration profiles do not differ significantly. The significance of these observations in terms of a batch cooling crystallization process is that upon scale-up with a constant power input per unit mass, the product performance and quality should be improved. However, contrary to these predictions we also need to investigate the effect of heat transfer upon scale-up before this can be confirmed as discussed in Section 7.5.4. The other important factor affecting the process performance in a crystallization process is the type of impeller used in terms of efficiency and power requirements. Constant Reynolds number is another scale-up criterion used but this scale-up criterion also produces different macromixing and micromixing effects during scale-up. However scale-up using constant Reynolds number should not be used for the following reasons,

$$P \propto N^3 d_i^5 \ and \ \mathrm{Re} \propto N d_i^2 \qquad [7.19]$$

$$N \propto d_i^{-2} \quad \therefore P \propto (d_i^{-2})^3 d_i^5 \propto d_i^{-1} \qquad [7.20]$$

The failure of conventional scale-up criteria may be due to the fact that it is only one mixing process that can be limiting, however, it is shown from the above predicted CFD simulations that a competing mechanism between macromixing and micromixing performances exist upon scale-up.

7.6 HEAT TRANSFER

Scale-up with constant specific power input per unit mass results in reduced heat transfer coefficients for both Rushton turbine and pitch blade impeller types. CFD simulations show that the temperature profiles produced after 360s simulation using a linear cooling profile are not identical. Upon scale-up from 1l to 25l using a constant specific power input per unit mass, heat transfer becomes less efficient when cooling occurs resulting in higher temperatures being observed at

different time intervals (Fig.7.2). The reason for this is that the local energy dissipation is reduced upon scale-up as discussed previously and less efficient heat removal occurs. A uniform bulk temperature with no temperature gradients is observed upon scale-up, however, the size and volume of the cooling zones increases. CFD predicts that the temperature difference between the cooling zone (wall) and the bulk remains the same for a specific impeller configuration. The temperature distribution within crystallizers directly influences the supersaturation levels. Therefore in the cooling zones, increased supersaturation levels will be evident leading to an increase in the undercooling, nucleation and growth rates. Upon scale-up, encrustation may also occur due increased level of undercooling including a reduction in heat transfer and process performance. On a 25l batch crystallizer scale, less efficient heat transfer occurs using a constant specific power input with a Rushton turbine impeller compared to using a pitch blade impeller. The reason for this is that at constant specific power input a pitch blade impeller operates at a higher tip speed, Reynolds number and produces higher energy dissipation rates (Fig.7.3 and Fig.7.4). Upon scale-up, the mixing is expected to improve and the secondary nucleation and attrition rate is expected to reduce using constant power input per unit mass. However, CFD simulations predict that the heat transfer is less efficient upon scale-up. The supersaturation level is the main driving force for a crystallization process and may influence the kinetics more significantly than when compared to energy dissipation rates. This observation may provide an explanation for the failure of robust batch cooling crystallization processes giving a consistent crystal size distribution upon scale-up. Furthermore, even though heat transfer is more efficient using a pitch blade impeller when compared to a Rushton turbine impeller a larger gradient in temperature between the bulk zone and cooling zone exists when using a pitch blade impeller due to the flow being less turbulent in this region when using a pitch blade. The liquid side heat transfer coefficient is considered and not radiation.

7.7 SCALE-UP USING A COMPARTMENTALIZATION APPROACH

To account for both macromixing and micromixing effects and the failure of common scale-up criteria described above, a compartmentalization approach

known as the batch cooling compartmental model for batch cooling suspension crystallization processes is proposed. The model must be capable of predicting the influence of mixing on the crystal size distribution and crystallization kinetics using different impeller configurations and operating conditions. Key process engineering information has been determined on a laboratory scale to include solubility, thermodynamics and crystallization kinetic models for size-dependent growth, total nucleation and attrition rates. CFD is used to determine the hydrodynamic phenomena prevailing upon scale-up (Chapter 8) and is used as an aid to develop the compartmental modelling framework (Chapter 9) for scale-up predictions of the crystallization behaviour.

	Rushton turbine impeller					Pitch blade impeller				
Size (L)	Speed (rpm)	Re imp.	Tip Speed (m/s)	C/H	t_{circ} (s)	Speed (rpm)	Re imp.	Tip Speed (m/s)	C/H	t_{circ} (s)
1	300	3370	0.82	0.182	3.18	460	5121	1.24	0.182	2.24
5	289	6920	0.98	0.184	4.50	450	10800	1.53	0.184	2.96
25	201	13799	1.16	0.188	6.56	313	21500	1.81	0.188	4.30

Table 7.1: *Impeller speed, impeller Reynolds number, impeller clearance/tank height ratios and circulation times for geometrically similar agitated crystallizer vessels at constant power input per unit mass [0.12 W kg^{-1}].*

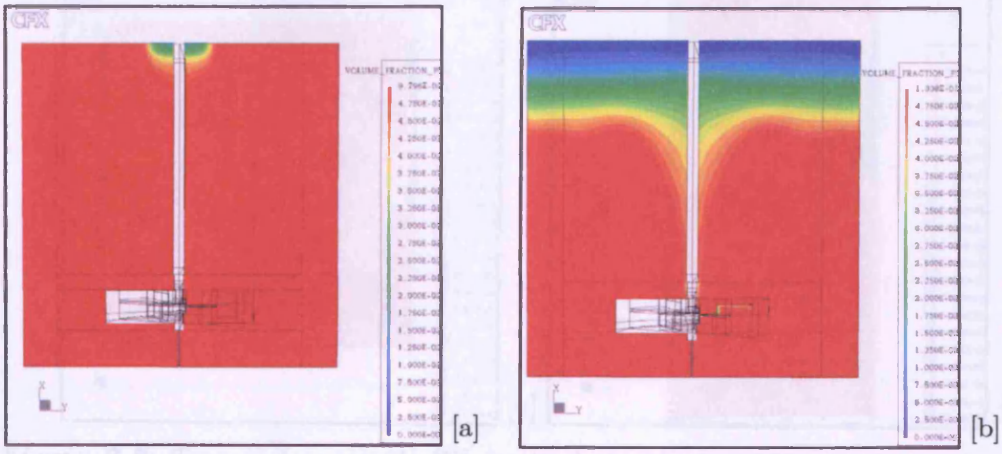

Figure 7.1: *Maximum solids concentration hold up (5% v/v) with mean particle size 200 μm for batch crystallizers operating at 300 rpm equipped with a Rushton turbine impeller: [a] 25l [b] 5l.*

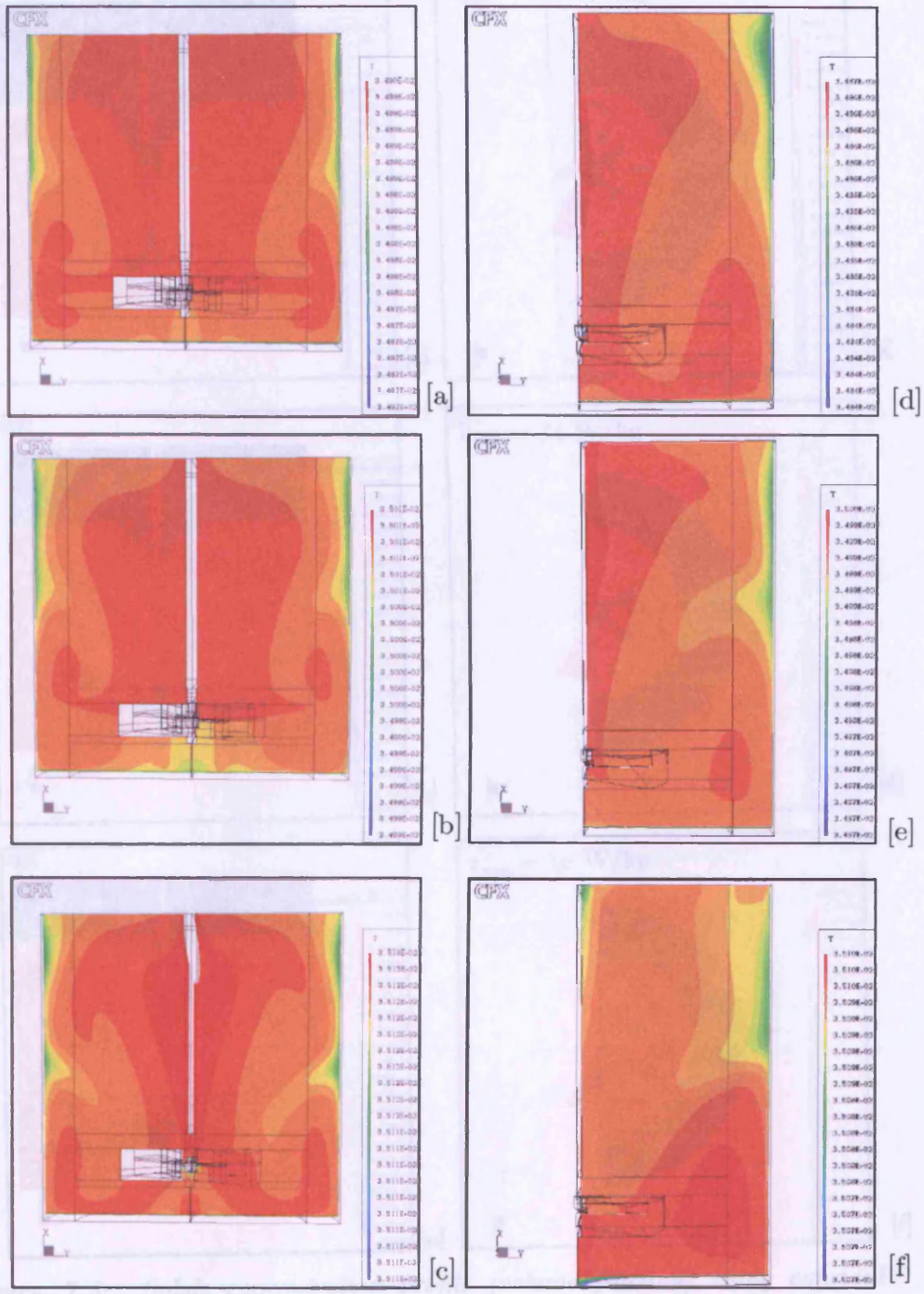

Figure 7.2: *Temperature profile [K] (vertical plane) after 360s simulation for batch cooling crystallizers on different scales at constant specific power input (0.12 W kg^{-1}) equipped with Rushton impellers [a] 1l [b] 5l [c] 25l and pitch blade [d] 1l [e] 5l [f] 25l.*

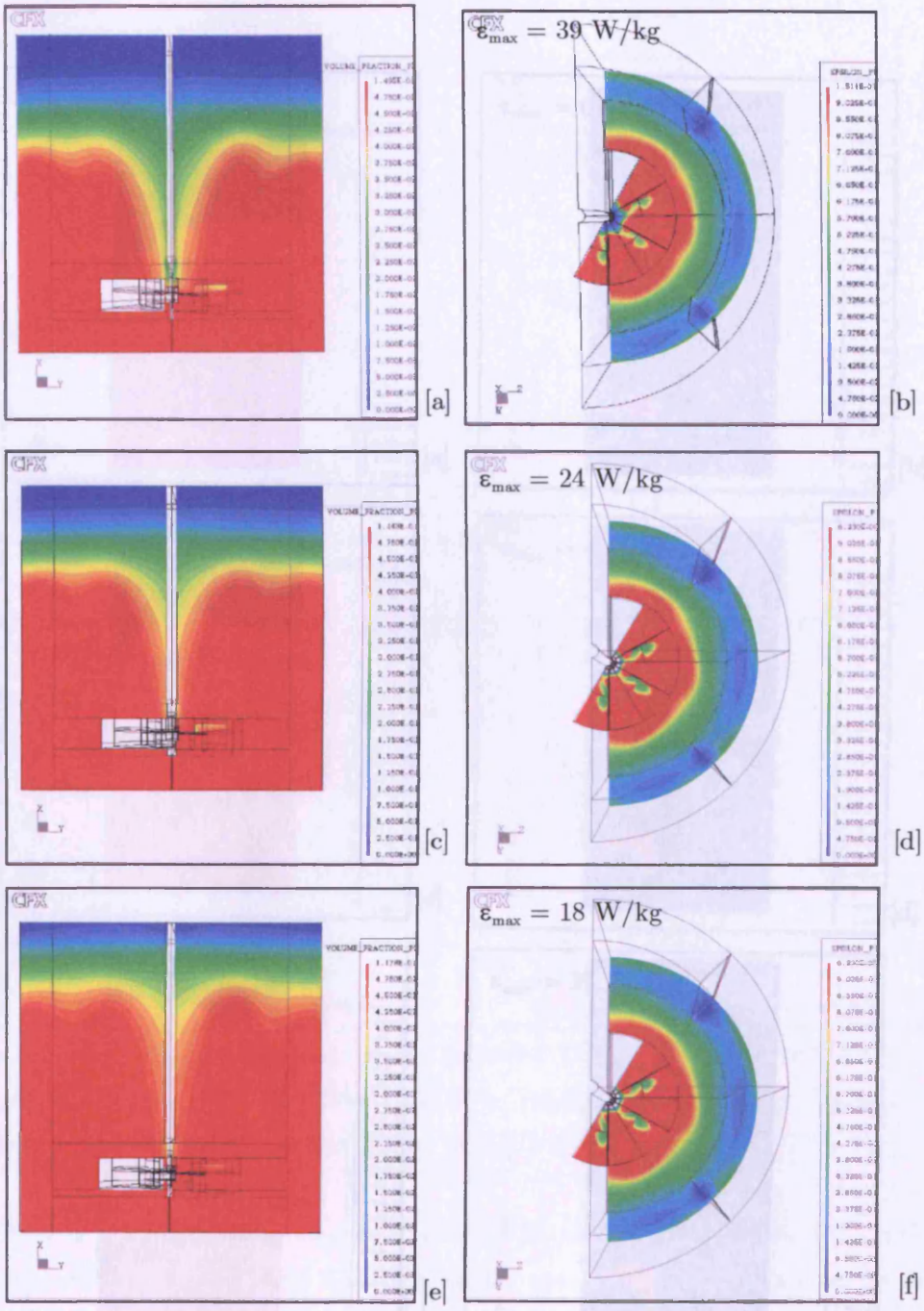

Figure 7.3: *Solids concentration profile (volume fraction) using constant specific power input per unit mass on different batch crystallizer scales [a] 1l [c] 5l [e] 25l including the local energy dissipation rate profiles (W kg^{-1}) [b] 1l [d] 5l [f] 25l using a Rushton turbine impeller.*

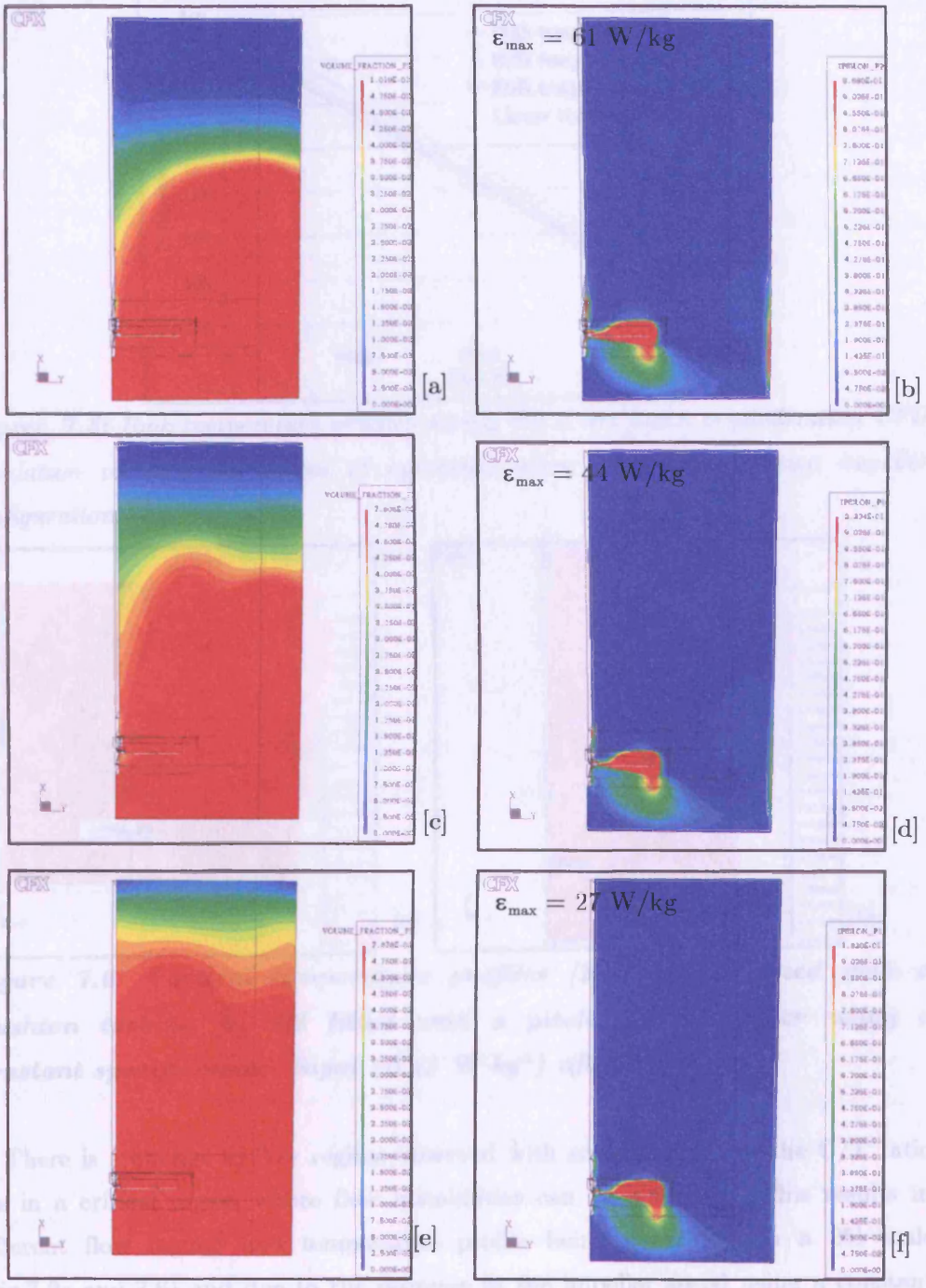

Figure 7.4: *Solids concentration profile (volume fraction) using constant specific power input per unit mass on different batch crystallizer scales [a] 1l [c] 5l [e] 25l including the local energy dissipation rate profiles (W kg^{-1}) [b] 1l [d] 5l [f] 25l using a pitch blade impeller configuration.*

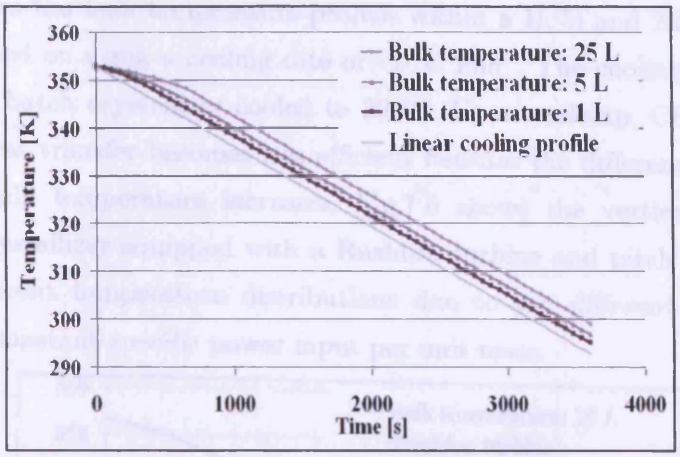

Figure 7.5: *Bulk temperature profiles during the entire batch crystallization CFD simulation on different scales of operation using a Rushton turbine impeller configuration.*

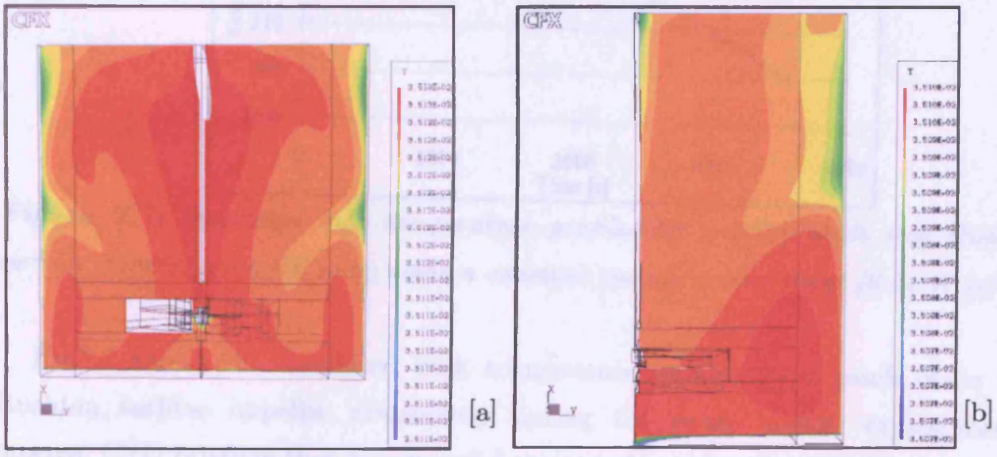

Figure 7.6: Vertical temperature profiles [K]: [a] 25l fitted with a Rushton turbine [b] 25l fitted with a pitch blade impeller using a constant specific power input (0.12 W kg^{-1}) after 360 s.

There is a change in flow regime observed with scale-up because the C/T ratio lies in a critical region where flow instabilities can be generated. This results in different flow regime and temperature profile being generated on a 25l scale (Fig.7.2c and 7.6) and due to the decrease in the impeller speed using a constant specific power input per unit mass. The double loop circulation pattern is not present due to the different discharge angle (Montante et al. 2001).

Fig.7.5 shows the bulk temperature profiles within a 1l, 5l and 25l batch cooling crystallizer based on using a cooling rate of –1 °C min^{-1}. The cooling is initiated at 80 °C and the batch crystallizer cooled to 20 °C. Upon scale-up, CFD simulations predict that heat transfer becomes less efficient because the difference between the coolant and bulk temperature increases. Fig.7.6 shows the vertical temperature profiles in a crystallizer equipped with a Rushton turbine and pitch blade impeller exhibiting different temperature distributions due to the different flow patterns produced at a constant specific power input per unit mass.

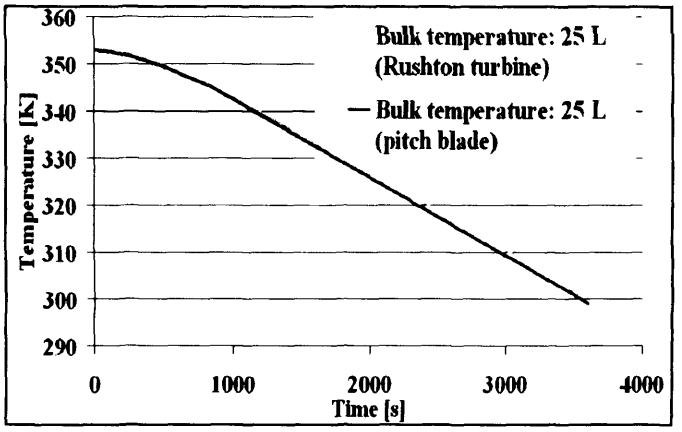

Figure 7.7: *Simulated bulk temperature profiles for a pitch blade and Rushton turbine impeller on a 25l scale using a constant specific power input [0.12 W kg^{-1}].*

Fig.7.7 shows the simulated bulk temperature profiles for a pitch blade and Rushton turbine impeller respectively during the entire cooling crystallization process. CFD predicts that the overall heat transfer with the pitch blade impeller is more efficient than when compared to a Rushton turbine at a constant specific power input due to the increased agitator speed, Reynolds number and reduced mixing times. However, due to the different impeller configurations different flow patterns are produced. With a pitch blade impeller, mixing is less efficient in the upper region leading to the formation of a larger cooling zone and increased temperature gradient within this cooling zone when compared to a Rushton turbine impeller.Fig.7.8 shows the temperature profile as a function of the distance from the centre of the crystallizer equipped with a pitch blade impeller and Rushton turbine impeller operating at 0.12 W kg^{-1} after 360 s predictive CFD

simulations chosen at a selective vertical plane. There is a 0.2 °C difference in the cooling zone between using a pitch blade impeller and Rushton turbine impeller.

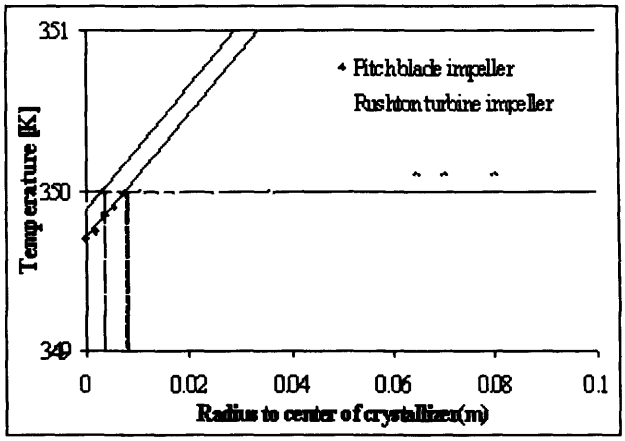

Figure 7.8: *Predicted temperature profile across a 5l crystallizer equipped with a pitch blade and Rushton turbine impeller respectively at a constant power input per unit mass.*

7.8 CONCLUSIONS

To account for the failure of common scale-up criteria due to either macromixing, micromixing and heat transfer limiting processes a compartmental modelling approach is necessary in order to capture these phenomena for a batch cooling crystallization process. CFD predictions indicate that when scaling up a batch cooling suspension crystallization process macromixing efficiency improves with a reduction in the micromixing effects. However, heat transfer is predicted to become less efficient upon scale-up and this competing mechanism between macromixing, micromixing and heat transfer will influence the product performance and quality significantly. The lack of understanding of these phenomena upon scale-up is a major contributing factor for the absence of robust batch cooling crystallization processes giving consistent particle size and performance in the pharmaceutical industry. CFD will be used in this research to aid the development of a novel compartmental modelling framework to take into account both mixing and heat transfer phenomena for predictive crystallization scale-up aspects and is described in the following chapter.

Chapter 8

CFD MODELLING OF MIXING AND HEAT TRANSFER IN BATCH CRYSTALLIZERS: AIDING THE DEVELOPMENT OF A NOVEL PREDICTIVE COMPARTMENTAL MODEL

ABSTRACT

A novel predictive compartmental modelling framework for the dynamic simulation and scale-up of batch cooling suspension crystallization vessels based on CFD simulations is presented. The design of the compartmental structure is based on high-resolution simulations of the internal flow, particle-solvent phase mixing and heat transfer.

CFD simulations of the turbulent flow field were carried out using the standard k-ε turbulence model and particle-solvent phase simulations based on the advanced Multi-Fluid phase model (MFM). A detailed compartmental model is constructed for batch crystallizers equipped with two different impeller configurations based on the overall flow pattern, local energy dissipation, and solids concentration and temperature distribution from predictive CFD simulations.

8.1 INTRODUCTION

Computational Fluid Dynamics (CFD) is becoming an increasingly useful and powerful tool for the numerical analysis of systems involving transport processes. This includes the simulation of multi-phase flow, heat transfer, chemical reactions and particulate processes (Versteeg and Malalasekera, 1995). Recently CFD simulations have been used for the development of compartmental modelling frameworks for the predictive scale-up of crystallization processes. CFD simulations have been used successfully to combine hydrodynamic information to include local energy dissipation rates and flowrates with crystallization kinetic models using a compartmental modelling approach to predict the crystallization behaviour upon scale-up. Compartmentalisation using CFD has been successfully applied to continuous steady state evaporative crystallizers (Bermingham et al., 1998; Kramer et al., 1999; Kramer et al., 2000 and ten Cate et al., 2000), reactive semi-continuous and continuous precipitation processes (Zauner and Jones, 2002) and gas-liquid precipitation processes (Rigopoulos and Jones, 2003). The modelling, design and optimisation of crystallization processes using CFD requires the implementation of the population balance and crystallization kinetic models within the CFD environment. Crystal population balances have been successfully integrated into CFD codes for the simulation of reactive precipitation processes (Wei and Garside, 1997; Al-Rashed and Jones, 1999; Rousseaux et al., 2001; Jaworski and Nienow, 2003). Liiri et al., 2002 successfully modelled secondary nucleation effects in vessels using CFD simulations. A serious problem involved in directly integrating the crystal population balance within the CFD environment is that simulations are computationally expensive. The technique is also limited by the accuracy of the approximation of the population balance due to the method of moments being used and cannot be used to account for attrition. For predictive modelling of crystallization processes an order of magnitude of days is necessary. Compartmentalisation can be introduced to overcome this severe limitation.

Ten Cate (2000) used CFD to model a *'pseudo-single'* phase whereby the fluid phase is treated as a single phase with a uniform effective slurry viscosity.
The Large Eddy Simulation (LES) turbulence model; a more advanced turbulence model was successfully used to estimate the local energy dissipation rates and

therefore predict mass transfer coefficients. The LES turbulence model based on the lattice-Boltzman model increases the predictive accuracy but the price paid in computational time is far too expensive and not feasible for predictive scale-up crystallization processes. Therefore the standard k-ε turbulence model offers a compromise between accuracy and computational efficiency and was successfully used implement by Ranade (1997). Manninen and Syräjnen (1998) also modelled turbulent flow in stirred tanks and tested various turbulence models. The standard k-ε model predicted the experimentally determined flow pattern the best. However, caution should be exercised, when interpreting CFD simulations when using the standard k-ε turbulence model. Zauner and Jones (1998) determined that the local energy dissipation rates are underestimated resulting in reduced micromixing and mesomixing times. Therefore the segregated feed model (MFM) based on compartmentalization underestimated the volume mean sizes and predictions became less reliable upon scale-up. Furthermore, it is expected that mass transfer coefficients, secondary nucleation and attritions rates will also be underestimated as a result of using the k-ε turbulence model.

The effects of particle concentration and size on the degree of mixing are often neglected. Imperfect mixing in crystallizers is common and this lack of homogeneity affects the process performance, product quality and crystal size distribution. Maggioris et al. (1998) successfully used CFD to model particle size in suspension polymer reactors. Micale et al. (2000a and 2000b) and Montante et al. (2001) have recently developed the Multi-Fluid model (MFM) to model dilute particle suspensions with monodisperse particle sizes in agitated vessels. Size-dependent classification effects within crystallizers are also not considered. Sha et al. (2001) have used CFD simulations to model size-dependent classification in suspension crystallizations but are also computationally expensive. Knowledge of internal classification effects and solid phase distribution within crystallizers is necessary for process design and scale-up. Most predictive batch cooling crystallization processes have not considered the effects of mixing, hydrodynamics and heat transfer on the process performance upon scale-up. The majority of CFD simulations used for the development of existing compartmental models described

consider a *'single'* phase only. They also assume a well-mixed crystallizer and that no particle segregation occurs, which can potentially lead to poor predictions.

In this research, a novel compartmental modelling framework is presented for the predictive scale-up of seeded batch cooling suspension crystallization processes for an organic fine chemical using a hybrid CFD technique. The hybrid CFD approach uses a heuristic approach involving combining CFD hydrodynamic information with physical, thermodynamic and kinetic data obtained on a laboratory scale within a dynamic modelling package known as gPROMS is presented. Details of the compartmental modelling framework and implementation within gPROMS are presented in Chapter 9-11. CFD simulations were carried out to simulate particle-solvent phase mixing; local energy dissipation rates and heat transfer to aid the development of the compartmental modelling framework. The presence of particles is also considered in the development of the predictive compartmental modelling framework.

8.2 RESEARCH OBJECTIVES

Scale-up CFD simulations of agitated vessels using different impeller configurations and solid-solvent phase were performed to determine overall flow patterns, velocity profiles and local energy dissipation rates as described in Chapter 7. Furthermore, CFD simulations were carried out in order to investigate the effects of the solids concentration and particle size on the overall hydrodynamics upon scale-up. Heat transfer CFD simulations were also carried out to determine the temperature distribution within a crystallizer and to investigate whether there is evidence to suggest the presence of 'cooling zones'. The CFD heat transfer simulations were based on estimated heat transfer coefficients with a linear cooling profile implemented to predict the temperature during a batch mode of operation. The compartmentalization procedure is achieved based on CFD hydrodynamic information and heuristics.

8.3 CFD SIMULATION THEORY

Numerical simulations of particle concentration distribution inside baffled agitated crystallizers were carried out using an advanced model available in CFX 4.4 code (AEA technology, Harwell): the Multi-Fluid Model (MFM), which belongs to the class of Euler-Euler methods. The standard MFM is coupled with the standard k-ε turbulence model (Launder and Spalding, 1974) and is solved using the Inter-Phase Slip algorithm (IPSA).

The model solves the continuity and momentum equations for a generic multi-phase system and determines separate flow fields for each phase simultaneously. In the case of two-phase flow, the particle phase is treated as a separate fluid and occupies disconnected regions of space in the continuous liquid phase. The different inertia of the liquid and solid phase is taken into account when using the MFM and will be closer to reality when compared to the Settling Velocity model (Micale et al., 2000a and 2000b). In addition, the effect of the solid phase concentration on the liquid flow field can be considered. The standard MFM model used in this contribution suffers from limitations in that the second order effects relating to the influence of particles on the turbulence structure (particle-liquid) and particle-particle interactions (two-way or four-way coupling) are not taken into account (Micale et al., 2000a and 2000b). Kuipers and Swaaj (1997), however, consider two-way and four-way coupling effects and could be used for further work. Furthermore, the MFM needs to be coupled with the crystal population balance so that the growth of initial seed crystals in a batch cooling crystallizer can be modelled using CFD. The prediction of the MFM based on monodisperse particle sizes also becomes less realistic as the particle concentration increases. The multiple frames of reference (MFR) technique was coupled with the MFM to model impeller rotation.

The equation sets for the general case of Newtonian two-phase systems (only the continuous phase equations are shown as they are exactly the same as the disperse phase).

Continuity:
$$\frac{\partial}{\partial t}(r_c \rho_c) + \overline{\nabla} \bullet (r_c \rho_c \overline{U}_c) = 0 \qquad [8.1]$$

Volume balance:
$$r_d + r_c = 1 \qquad [8.2]$$

Momentum:

$$\frac{\partial}{\partial t}(r_c\rho_c\overline{U_c})+\overline{\nabla}\bullet(r_c(\rho_c\overline{U}_c\otimes\overline{U}_c-\mu_c(\overline{\nabla U}_c+(\overline{\nabla U}_c)^T)))$$
$$=r_c(\overline{B}-\overline{\nabla}p_c)+c_{cd}^{(id)}(\overline{U}_d-\overline{U}_c), \qquad [8.3]$$

where r is the volumetric fraction of the relevant phase and the subscripts d and c refer to the dispersed and continuous phase respectively. The momentum transfer between the two phases is accounted for via inter-phase drag terms, $c_{dc}^{id}=c_{cd}^{id}$, which are then computed from non-dimensional drag coefficients from the following equation,

$$c_{cd}^{(id)}=\frac{3}{4}.\frac{C_D}{d_p}.r_d.\rho_c\left|\overline{u}_d-\overline{u}_c\right| \qquad [8.4]$$

Estimations of the drag coefficient are important in order to correctly model the momentum transfer. The total number of equations is equal to the total number of unknowns. There are 9 equations with 9 unknowns: the two volumetric fractions r_d and r_c, the six velocity components and the pressure ($p_c = p_d$) since all the phases share the same pressure field. The standard k-ε turbulence model was chosen to estimate local energy dissipation and turbulent kinetic energy rates. A homogeneous approach was employed whereby both phases share the same values for k (turbulence kinetic energy) and ε (turbulent energy dissipation) and the inter-phase turbulence transfer is not considered. The standard k-ε assumes that turbulence is isotropic i.e. has no favoured direction.

The transport equations for k are:

$$\frac{\partial}{\partial t}(r_c\rho_c k_c)+\nabla\bullet(r_c(\rho_c u_c k_c-\left(\mu_c+\frac{\mu_{tc}}{\sigma_K}\right)\nabla k_c))=r_c S_{kc}+c_{cd}^{(k)}(k_d-k_c) \qquad [8.5]$$

The transport equations for ε are:

$$\frac{\partial}{\partial t}(r_c\rho_c\varepsilon_c)+\nabla\bullet(r_c(\rho_c u_c\varepsilon_c-\left(\mu_c+\frac{\mu_{tc}}{\sigma_\varepsilon}\right)\nabla\varepsilon_c))=r_c S_{\varepsilon c}+c_{cd}^{(\varepsilon)}(\varepsilon_d-\varepsilon_c) \qquad [8.6]$$

where for the continuous phase,

$$\mu_{tc}=\rho_c C_\mu.\frac{k_c^2}{\varepsilon_c} \qquad \text{(Rodi, 1984)} \qquad [8.7]$$

$$S_{kc} = \mu_{tc}\overline{\nabla U}\left(\overline{\nabla U_c} + (\overline{\nabla U_c})^T\right) - \rho_C \varepsilon_C \qquad [8.8]$$

$$S_{\varepsilon c} = C_1 \frac{\varepsilon_c}{k_c}\mu_{tc}\overline{\nabla U}\left(\overline{\nabla U_c} + (\overline{\nabla U_c})^T\right) - C_2 \rho_c \frac{\varepsilon_c^2}{k_c} \qquad [8.9]$$

The above modelling equations describe an isothermal system, however, for batch cooling crystallizations the energy equation must be implemented and is as follows:

$$\frac{\partial}{\partial t}(r_c\rho_c\overline{H_c}) + \overline{\nabla}\bullet(r_c(\rho_c\overline{H}_c \otimes \overline{U_C} - \lambda_C\overline{\nabla T_c}) = c_{cd}(\overline{T}_d - \overline{T}_c) \qquad [8.10]$$

In the modelling of the k and ε transport equations, new unknown 'inter-phase' turbulence transfer terms arise, ($c_{dc}^{(k)} = c_{cd}^{(k)}$ *and* $c_{dc}^{(\varepsilon)} = c_{cd}^{(\varepsilon)}$). These account for turbulence promotion or damping due to the presence of the solid phase. Since there is no reliable knowledge of the quantification of these terms a simplified version of the model is used. In this case the previous equations for k and ε are,

$$\frac{\partial}{\partial t}(\rho k) + \nabla\bullet(\rho u k - (\mu + \frac{\mu_T}{\sigma_k})\nabla k)) = S_k \qquad [8.11]$$

$$\frac{\partial}{\partial t}(\rho \varepsilon) + \nabla\bullet(\rho u \varepsilon - (\mu + \frac{\mu_T}{\sigma\varepsilon})\nabla \varepsilon)) = S_\varepsilon \qquad [8.12]$$

Where,

$$\rho = r_c\rho_c + r_d\rho_d$$

$$u = \frac{1}{\rho}(r_c\rho_c u_c + r_d\rho_d u_d)$$

$$\mu_T = r_c\mu_{tc} + r_d\mu_{td}$$

$$S_k = r_c S_{kc} + r_d S_{kd}$$

$$S_\varepsilon = r_c S_{\varepsilon c} + r_d S_{\varepsilon d}$$

For all the two phase CFD simulations the turbulent Schmidt number was taken as equal to 0.8 according to suggestions by Micale et al. (2000) for the liquid phase.

The numerical solution of the resulting system equations was achieved using the finite volume method, together with the Rhie and Chow algorithm to prevent

'chequer-board' oscillations. The SIMPLEC algorithm was used to couple pressure and velocity. The hybrid-upwind discretization scheme was used for convective terms and a linear-logarithmic 'wall function' used on the crystallizer walls.

Estimations of the particulate drag coefficient are important in order to correctly model the momentum transfer. The particle drag coefficient depends only on the particle Reynolds number and can be determined experimentally for fluids at rest as follows,

$$\mathrm{Re}_p = \frac{\rho u_t d_p}{\mu} \qquad [8.14]$$

For different particle Reynolds numbers the particle drag coefficient is given as follows,

$$C_D = \frac{18.5}{\mathrm{Re}_p^{0.6}} \quad for\ 0.3 < \mathrm{Re}_p < 10^3 \qquad [8.15]$$

$$C_D = \frac{24}{\mathrm{Re}_p} \quad for\ \mathrm{Re}_p < 0.3 \qquad [8.16]$$

However, in batch cooling suspension crystallizers the organic fine chemical particles are free falling in a turbulent fluid the particle drag coefficient is not the same as that when observed in a fluid where there is no free-turbulence stream. The effect on the particle drag coefficients is complex and depends on the hydrodynamic regime (Clift et al, 1978) and literature data of the effect of free turbulence on drag coefficients is rare. The drag coefficient is also dependent on the sphericity ($\psi = 0.4$) of the crystals and increases with increased sphericity. In the case of the organic fine chemical particles falling in the isopropyl-alcohol-water fluid system, the effect of the free turbulence stream increases the particle drag and therefore decreases the particle settling velocity (Magelli et al., 1990).

Brucato et al (1998) proposed a new correlation for predicting the drag coefficient in turbulent velocity whereby a correlation between particle size and Kolmogorov length scale of dissipative eddies was used. This correlation is sufficient for the batch cooling crystallization of the organic fine chemical as dilute suspensions of up to 5% v/v are only considered.

$$\frac{C_D - C_O}{C_D} = 8.76 \times 10^{-4} \left(\frac{d_p}{\lambda} \right)^3 \qquad [8.17]$$

The Kolmogorov length scale is given as follows,

$$\lambda = \left(\frac{\nu^3}{\varepsilon} \right)^{1/4} \qquad [8.18]$$

The drag coefficient of particles whose size is comparable with that of the turbulent eddies is practically unaffected by the free-turbulence stream. For larger particles, the fluid-mechanical interaction with turbulent eddies becomes more significant and leads to an increase in the particle drag. This increase becomes larger as the ratio of the particle size to λ increases. Batch settling experiments were performed using different particle size ranges in order to determine terminal settling velocities allowing for the particle Reynolds number and subsequently the modified drag coefficients to be estimated. Modified drag coefficient values as a function of agitation speed and particle size can be found in Appendix G. The particle drag coefficients are comparable to those determined by Micale et al. (2001).

CFD simulations were also used to model heat transfer (Yang et al., 2002) based on estimated liquid side heat transfer coefficients on various geometrically similar crystallizer scales and operating conditions, combined with the implementation of a linear cooling profile within the CFD environment. CFD is used to model heat transfer in order to determine if 'cooling zones' or surfaces exist within batch cooling crystallizers. Heat transfer is directly associated with the mixing intensity, cooling profile and impeller configuration used. The existence of cooling zones results in the production of temperature and supersaturation gradients within agitated crystallization vessels. These cooling zones can also affect the process performance as in reality fouling occurs on the cooling surfaces. The importance of supersaturation is that it is the driving force for a crystallization process and affects the crystallization kinetics, particle size distribution and product performance.

8.4 MODELLING IMPELLER ROTATION

A significant problem arises in modelling of baffled stirred tanks due to the relative motion between impeller and baffles since there is no single frame of reference for computation. The sliding grid technique is commonly used. In this method, the section of the grid surrounding the impeller is allowed to rotate stepwise, and the flow field is recalculated for each time step. However, this method is computationally demanding. Two-phase simulations require even more computational time since the number of equations used increases and obtaining a steady-state particle distribution is a slow procedure. If the sliding grid technique is used, a time dependent calculation must be carried out using a large number of small time steps, which leads to large computational requirements. Mixing is better than indicated by static CFD and therefore a transient method is required but a static method is used to due excessive computational time.

An alternative method, the Multiple Frames of Reference (MFM) technique is used in this contribution. Lane et al. (1999) successfully used the MFM technique to model gas-liquid phase CFD simulations. In this method, two coupled frames are adopted: a rotating frame of reference surrounding the impeller, where the impeller blades appear stationary and a normal inertial frame of reference in the rest of the crystallizer. Hence, the finite volume grid remains fixed in position and the equations can be solved in steady-state mode, leading to a much more efficient computation. This method has been adopted here for two-phase flow.

8.5 EXPERIMENTAL

Batch settling experiments were carried out to estimate particle drag coefficients using different particle size ranges: 1-20μm, 50-150 μm and 150-350 μm. The terminal velocities of the particles were measured in a vertical tube, with a diameter of 50 mm over a length of 400mm. Saturated isopropyl alcohol-water solvent mixture was used as the test medium at 20 °C. Measurements were made for many particles due to their variation in size and shape, giving a mean terminal velocity value of 2 $mm.s^{-1}$, 10 $mm.s^{-1}$ and 13.43 $mm.s^{-1}$ for the three particle classes investigated. The experimental and modified drag coefficients can be calculated

using the particle Reynolds number, particle size and the average energy dissipation rate.

8.6 CFD SIMULATION CONDITIONS AND PROCESS

A 3-D finite volume grid (Fig.8.1) and geometry for the crystallizers was generated using a mesh generating software package called CFX-Promixus. The crystallizer scale, type of impeller used, crystallizer dimensions and number of hexahedral grid cells adopted for each CFD simulation is shown in Table 8.1. The crystallizers used exhibit geometrical similarity, are cylindrical with a flat bottom and are fitted with 4 baffles. In the case of using a 45° pitch blade with 4 blades and a rushton turbine impeller with 6 blades, the computational domain was limited to π and $\pi/2$ respectively as periodic boundary conditions in the azimuthal direction was imposed. No slip conditions were specified on the crystallizer walls, except for the surface, which is located at the top of the surface and a horizontal flow was allowed due to turbulent flow. Refinement of the grid cells was not carried out in order for the converged solution to be grid-independent due to time constraints. It is assumed that the grid cells adopted in the CFD simulations is fine enough to ensure a fully converged solution. Each simulation used 8000 iterations achieving absolute mass residuals between $1e^{-06}$-$1e^{-07}$. Under-relaxation factors were also applied to the velocity components equal to 0.3. CFD simulations to determine the hydrodynamics and mixing were carried out using the MFR technique until a steady state solution was obtained. Computations were done on twin Intel Xeon 3 GHz processors with 1 GB RAM. Scale-up CFD simulations were carried out using constant specific power input per unit mass and impeller frequencies between 300 and 500 rpm. The Reynolds numbers studied cover a range of $1.87 \times 10^4 - 2.5 \times 10^5$, producing fully turbulent conditions in each CFD simulation case, allowing the use of the k-ε turbulence model. Transient heat transfer simulations were carried out using the steady state solutions for the flow fields and local energy dissipation obtained from previous simulations that used the MFR technique. The heat transfer simulations therefore only consider the enthalpy balance.

Scale	Batch Cooling Crystallizer Dimensions				Grid cells using different impellers	
	d [m]	Z [m]	h [m]	H [m]	Rushton turbine	45° Pitch blade
1 L	0.040	0.105	0.035	0.110	135 648	62 217
5 L	0.065	0.180	0.060	0.190	114 588	53 294
25 L	0.110	0.300	0.100	0.320	114 588	53 294

Table 8.1: *Batch cooling crystallizer scales, dimensions and number of grid cells adopted using different impeller types.*

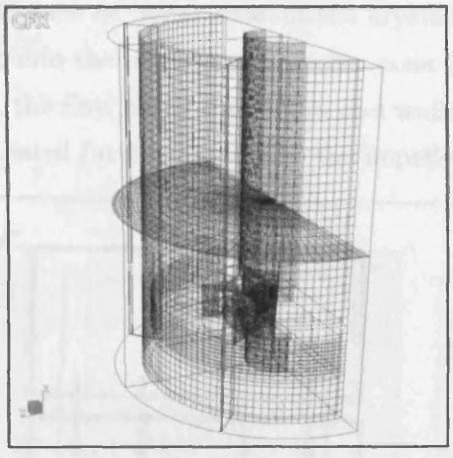

Figure 8.1: *The computation domain and grid generated using CFX-Promixus (J-plane). A horizontal grid plane, grid plane near the crystallizer wall and impeller/shaft plane are shown.*

8.7 CFD SIMULATION RESULTS AND DISCUSSION

A 5l batch cooling crystallizer equipped with a Rushton turbine and pitch blade impeller operating at 300 rpm will be used as a case study throughout this chapter, for the development of the compartmental model framework based on solid-liquid phase CFD simulations. CFD simulations show that batch suspension cooling crystallizers consist of four distinct zones: [1] bulk zone [2] impeller zone [3] high solids concentration zone and [4] cooling zone.

8.7.1 OVERALL FLOW PATTERN

Based on the overall flow pattern produced from CFD simulations, a classic double vortex pattern above and below the impeller zone is obtained when using a Rushton turbine. The highest velocities and gradients occur in the impeller zone both in the radial and tangential direction (Fig.8.2). The baffles have the effect of guiding particles and mother liquor along the walls into the upper region of the crystallizer. The flow in the bulk zone of the crystallizer has less steep gradients and a more reduced and uniform velocity when compared to the flow in the impeller zone. In the bulk zone or 'inner core' of the crystallizer, axial flow in the downward direction back into the crystallizer impeller zone dominates. As the z/H ratio increases (Fig. 8.3), the flow along the baffles and walls becomes significantly reduced as energy is dissipated further away from the impeller along the walls.

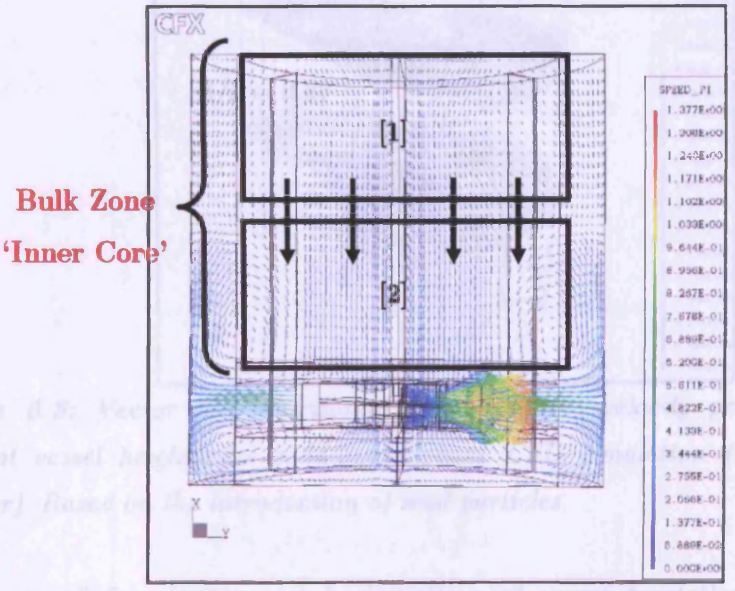

Figure 8.2: *Vector plot (vertical plane) of velocity profile [m s^{-1}] at a 45° angle between two baffles for solid-liquid phase CFD simulation (Rushton impeller). Based on the introduction of seed particles.*

The overall flow pattern produced using a pitch blade impeller configuration, is vastly different from that when using the Rushton turbine. The impeller zone is situated in a different position due to the downward pumping of the solid-liquid phase as a result of the inclined blades (Fig. 8.4). Between the impeller and baffles,

recirculation zones lead to an increase in the axial flow within the crystallizer. Below the impeller, however, a dead zone exists with the flow velocities being significantly reduced where the particle and mother liquor phase is stagnant. The baffles aid the flow into the upper region but due to the lower specific power input per unit mass, the velocity profiles are less than that when using a Rushton turbine impeller at the same impeller frequency (Fig.8.5).

Hence the upper region has a mixing intensity that is significantly reduced. The flow again is directed back into the bulk zone or 'inner core'.

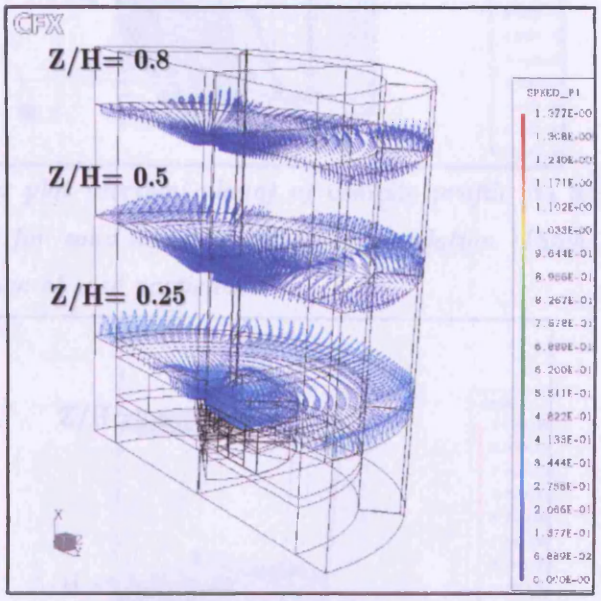

Figure 8.3: *Vector plot (horizontal planes) of the velocity profiles [m s^{-1}] at different vessel heights for solid-liquid phase CFD simulation (Rushton turbine impeller). Based on the introduction of seed particles.*

The overall flow pattern can be initially used to construct the compartmental modelling framework for the batch cooling crystallizer. However, this is rather arbitrary and is subject to further refinement using energy dissipation rates, solids concentration and temperature distribution profiles. The bulk zone is split into two compartments for both impeller types to take into account the main flow circulation flow pattern and the lower velocities being evident in the upper region of crystallizer.

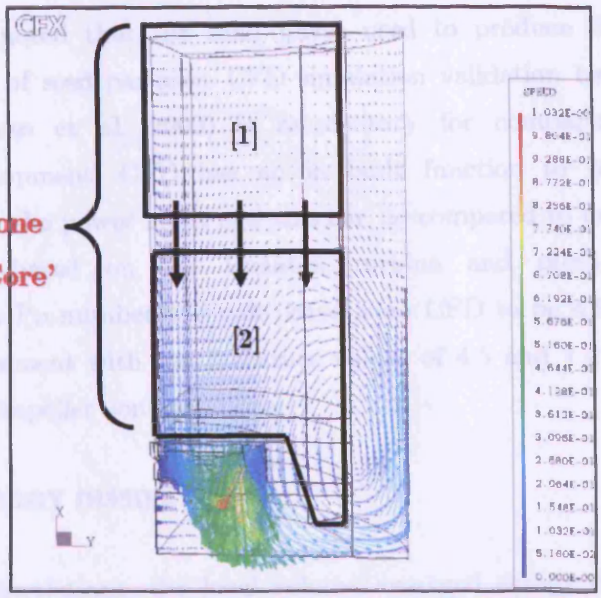

Figure 8.4: *Vector plot (vertical plane) of velocity profile [m s^{-1}] at a 45° angle between two baffles for solid-liquid phase CFD simulation (Pitch blade impeller). Based on the presence of seed particles.*

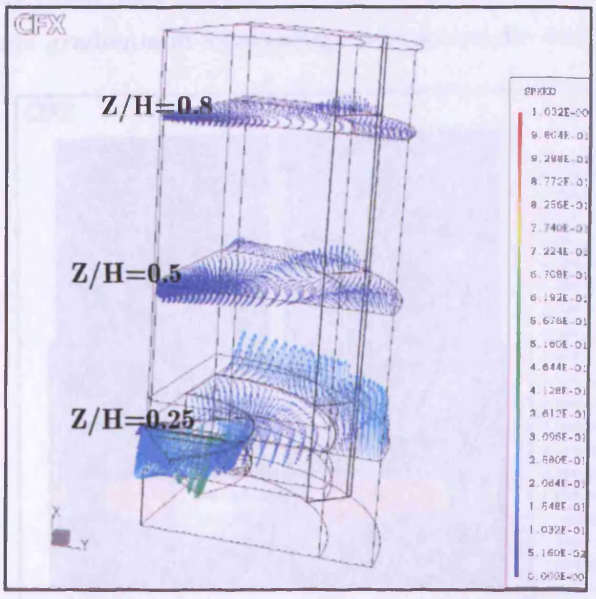

Figure 8.5: *Vector plot (horizontal planes) of the velocity profiles (m.s^{-1}) at different vessel heights for solid-liquid phase CFD simulation (Pitch blade impeller). Based on presence of seed particles.*

It should be noted that the solid phase used to produce the following flow patterns consists of seed particles. CFD simulation validation based on the power number (ten Cate et al. 2000) is satisfactory for compartmental modelling framework development. CFD has an in built function to predict the power number based on the power input and this can be compared to experimental power number values based on the Rushton turbine and pitch blade impellers respectively. The Po number was calculated from CFD to be 4.56 and 1.25 and is in excellent agreement with the literature values of 4.5 and 1.27 for the Rushton and pitch blade impeller configurations.

8.7.2 LOCAL ENERGY DISSIPATION

From CFD simulations, the local volume averaged energy dissipation rates in different regions of a crystallizer can be predicted. As expected, the highest local energy dissipation rates are observed in the impeller zone, whereas in the bulk zone, significantly lower and uniform energy dissipation rates are observed. In the impeller zone large gradients in local energy dissipation are evident (Fig. 8.6-8.8).

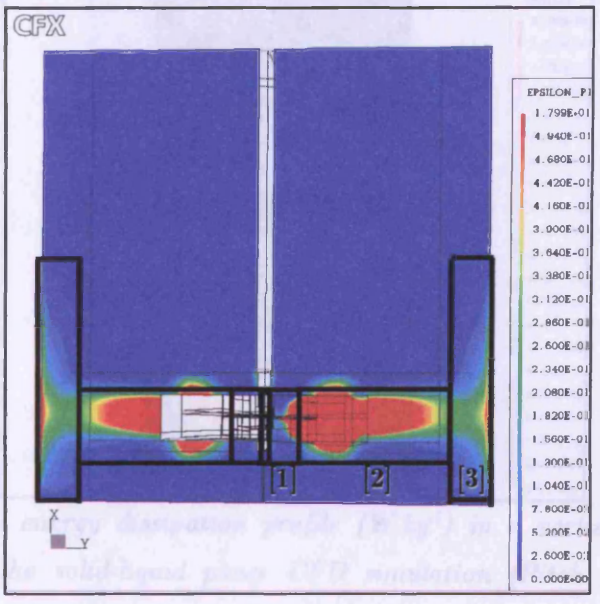

Figure 8.6: *Local energy dissipation profile [W kg^{-1}] in a vertical plane for the solid-liquid phase CFD simulation (Rushton turbine impeller).*

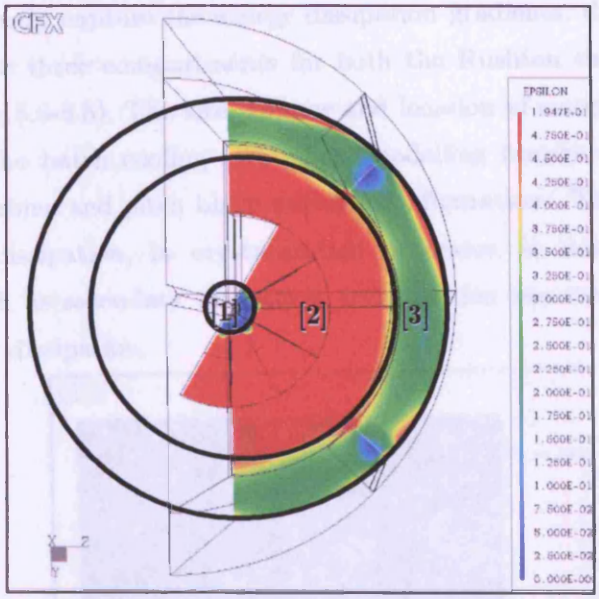

Figure 8.7: *Local energy dissipation profile [W kg^{-1}] in a horizontal plane in the impeller zone for the solid-liquid phase CFD simulation (Rushton turbine impeller).*

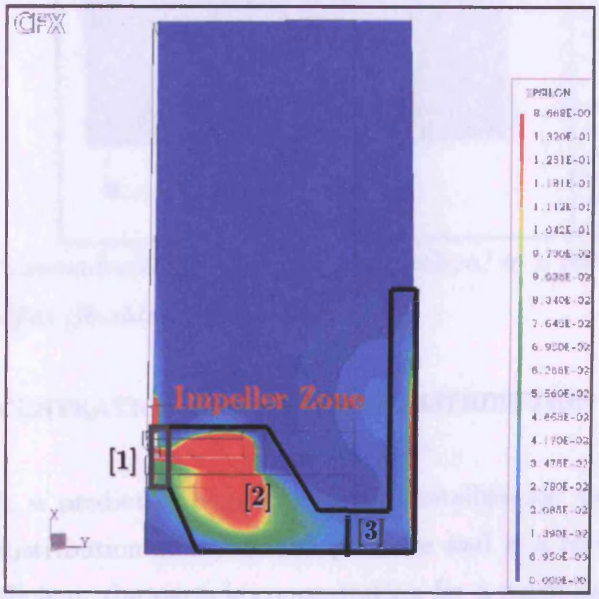

Figure 8.8: *Local energy dissipation profile (W.kg^{-1}) in a vertical plane in the impeller zone for the solid-liquid phase CFD simulation (Pitch blade impeller). Based on presence of seed particles.*

particles is evident under the impellers at the bottom of the tank for both impeller configurations studied. The high solids concentration zone is therefore split into a single and two compartments to take into account the large gradients in solids concentration for a pitch blade and Rushton turbine impeller respectively. This is as result of a dead zone present, due to reduced velocities and mixing intensity in this region producing internal classification effects. This causes unwanted particle deposition and the formation of a high solids concentration zone. Upon addition of seed particles, the overall flow pattern throughout the vessel bulk remains unchanged when compared to flow fields using only the mother liquor phase.

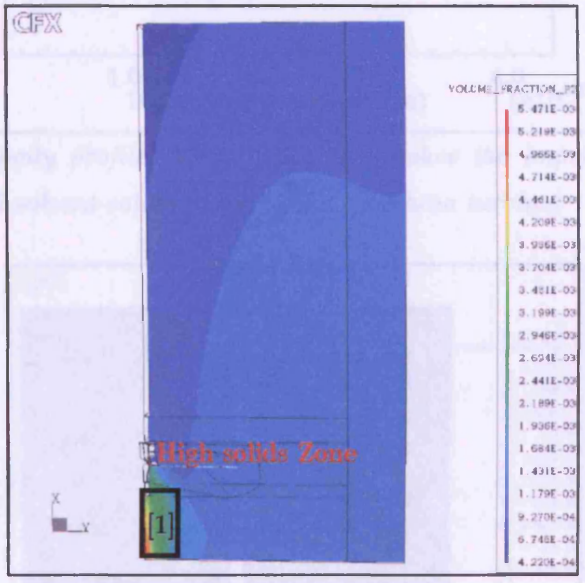

Figure 8.10: *Seed concentration profile (volume fraction) in a vertical plane at a 45° angle to the baffles (Pitch blade impeller).*

Fig. 8.11 shows the predicted velocity profiles for both the liquid phase (IPA) and solid phase (API) above the impeller zone having the same velocity at different distances in the radial direction from the impeller shaft when seed particles are used. Therefore the seed particles are carried in the mother liquor phase streamlines and negligible particle settling occurs. Due to CFD limitations, it is not yet possible to model the growth of seed particles, size-dependent classification, evolution of the crystal size distribution and increase in the solids concentration as the batch crystallization process proceeds.

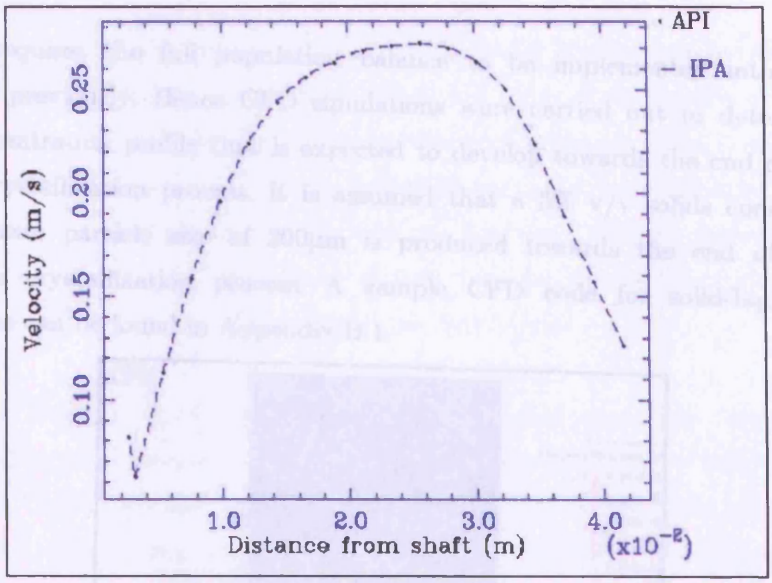

Figure 8.11: *Velocity profile (horizontal plane) below the impeller for the seed particles (API) and solvent-solute phase (IPA). [Rushton turbine]*

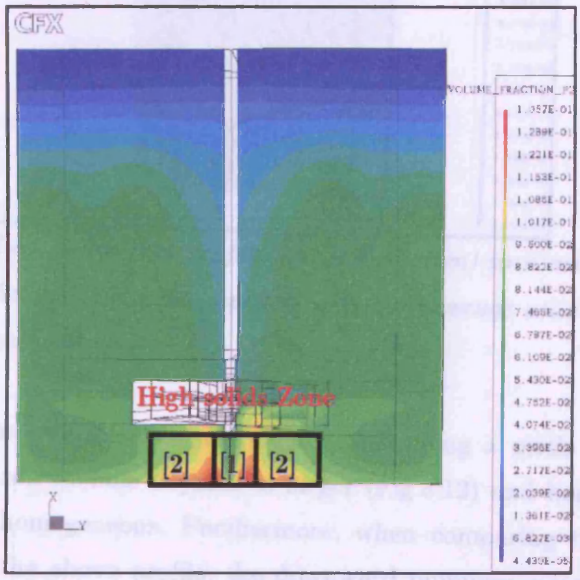

Figure 8.12: *Solid concentration profile (volume fraction) in a vertical plane at a 45° angle to the baffles (Rushton turbine impeller) using an average solids concentration of 5% v/v and 200μm particle size.*

This requires the full population balance to be implemented into CFD as discussed previously. Hence CFD simulations were carried out to determine the solid concentration profile that is expected to develop towards the end of a batch cooling crystallization process. It is assumed that a 5% v/v solids concentration with a mean particle size of 200μm is produced towards the end of a batch suspension crystallization process. A sample CFD code for solid-liquid phase simulations can be found in Appendix B.1.

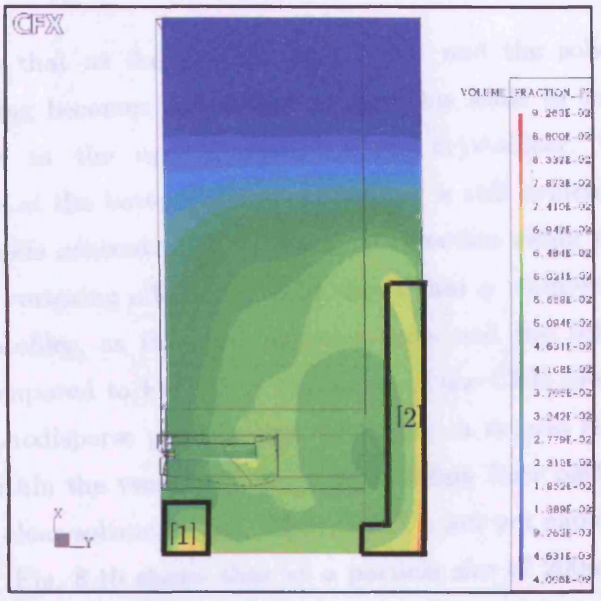

Figure 8.13: *Solid concentration profile (volume fraction) in a vertical plane at a 45° angle to the baffles (Pitch blade impeller) using an average solids concentration of 5% v/v and 200μm particle size.*

Fig.8.13 shows that the clear liquor region when using a pitch blade impeller compared to a Rushton turbine impeller is larger (Fig.8.12) and hence the mixing at 300 rpm is less homogeneous. Furthermore, when comparing the seed solids profile (Fig.8.10) to the above profile, the downward pumping action of the pitch blade impeller results in solids deposition on the walls of the crystallizer as shown in Fig.8.13. Therefore a second compartment must is introduced to take into account which has the same volume as that introduced to capture the energy dissipation gradient in the impeller zone.

Fig.8.16 predicts that as the agitator rate increases the mixing becomes more homogeneous for a fixed particle size of 200μm and solids concentration of 5% v/v. Additionally, as the particle size increases; the mixing becomes less homogeneous (Fig. 8.15). Therefore a concentration gradient in particle size should exist within a batch cooling crystallizer equipped with a Rushton turbine impeller. This phenomena combined with the effects of heat transfer should affect the process performance and the final product crystal size distribution.

Fig. 8.17 infers that as the seed particles grow and the solids concentration increases, the mixing becomes less homogeneous. This leads to the formation of a clear liquor layer in the upper region of the crystallizer. The high solids concentration zone at the bottom of the crystallizer is still evident. There is also a gradient in the solids concentration is the axial direction along the impeller shaft including a solids vortexing effect. Fig. 8.14 shows that a *'dampening'* effect occurs on the velocity profiles, as the seed particles grow and the solids concentration increases when compared to Fig.8.2. A limitation of the CFD predictions is that it is based on a monodisperse particle size. In reality, a crystal size distribution of particles exists within the vessel and hence will contain finer particles that may be suspended in the clear solvent region. Thus, CFD is not yet capable of providing a complete picture. Fig. 8.15 shows that at a particle size of 200μm with a 5% v/v solids concentration, the mother liquor phase is moving at a lower velocity than the solid phase due to gravitational effects. The reverse is true when the flow direction is from above, into the impeller zone. The difference between the two velocities is known as the particle slip velocity and results in some particle segregation. A negligible change in the solvent and solids velocity occurs from seeding to the production of a 5% v/v suspension. However, when a 10% v/v suspension is considered there is a significant reduction in the solid and solvent velocity indicative of less efficient mixing as a result of increase particle segregation (Fig.8.20). Using different monodisperse particle sizes, it was observed that negligible particle settling occurs up to particle sizes of 50μm. The reason for this is that the extent of particle settling velocity not only depends on the size but also on the density difference between the solid and liquid phase. For the organic fine chemical crystallization system, the density difference is not significant. Therefore, limited particle settling is expected to occur with an increase in particle size.

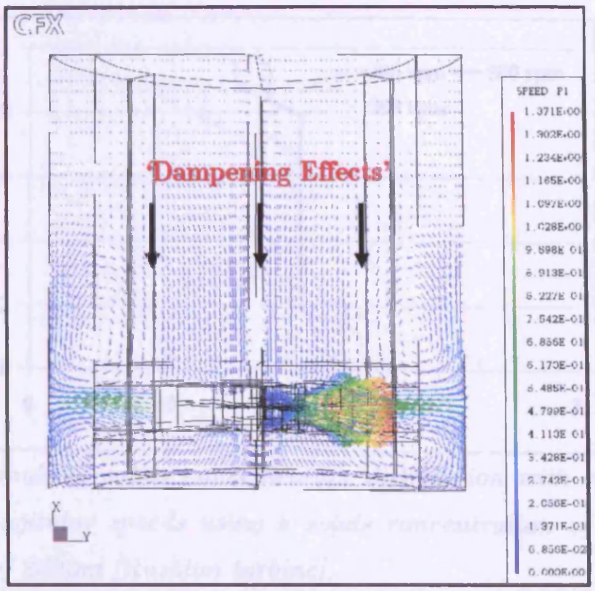

Figure 8.14: *Vector plot (vertical plane) of velocity profile [m s^{-1}] at a 45° angle between two baffles for solid-liquid phase CFD simulation (Rushton impeller). Based on a 5% v/v solids concentration with 200μm particles.*

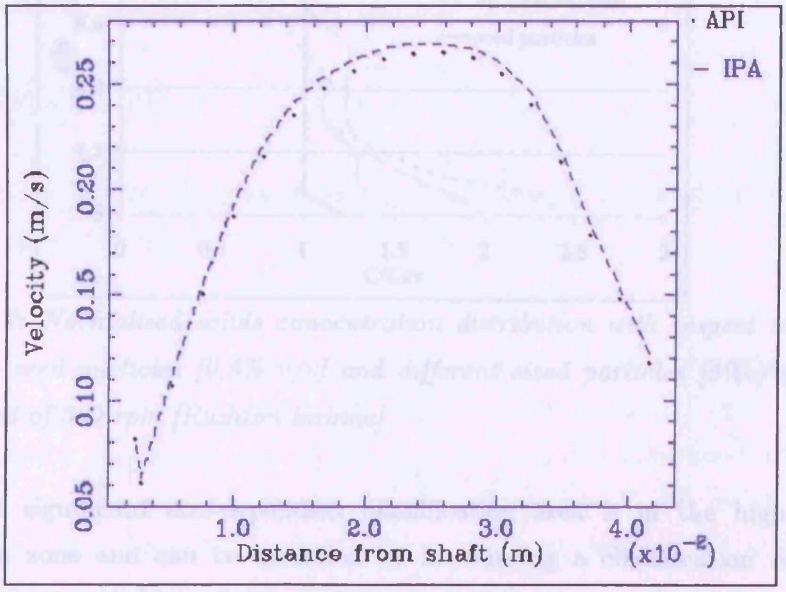

Figure 8.15: *Velocity profile (horizontal plane) below the impeller based on a 5% v/v solids concentration with 200 μm particles (API) and solvent-solute phase (IPA).*

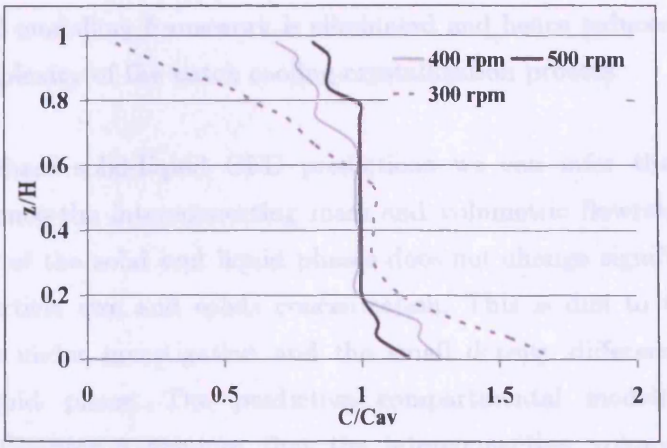

Figure 8.16: *Normalized solids concentration distribution with respect to vessel height at different agitator speeds using a solids concentration of 5% v/v with a mean particle size of 200μm [Rushton turbine].*

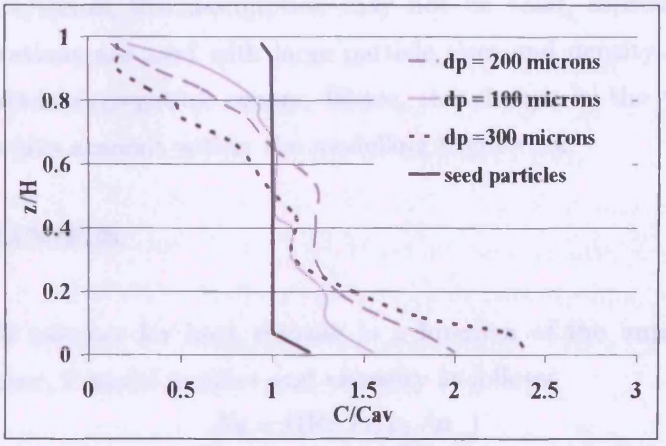

Figure 8.17: *Normalised solids concentration distribution with respect to vessel height using seed particles [0.5% v/v] and different sized particles [5%v/v] at an agitator speed of 300 rpm [Rushton turbine].*

The most significant size-dependent classification area is in the high solids concentration zone and can be modelled by introducing a classification function into the compartmental population balance-modelling framework as discussed in Chapter 9. By increasing the agitator speed to 500 rpm, the suspension can be homogeneously mixed with respect to solids concentration and particle size throughout the batch cooling suspension crystallization process .At this impeller frequency, the need for a classification function (Chapter 9) within the

compartmental modelling framework is eliminated and hence reduces the predictive modelling complexity of the batch cooling crystallization process.

Based on these solid-liquid CFD predictions we can infer that the velocity profiles and hence the interconnecting mass and volumetric flowrates between the compartments of the solid and liquid phases does not change significantly with an increase in particle size and solids concentration. This is due to the dilute solid concentrations under investigation and the small density difference between the solid and liquid phase. The predictive compartmental modelling framework presented in Chapter 9 assumes that the interconnecting volumetric and mass flowrates between the compartments for the population, mass and heat balance will remain unchanged during the batch crystallization process. In other crystallization systems, this assumption may not be valid, especially where high solids concentrations are used with large particle sizes and density differences, and significant particle segregation occurs. Hence, the change in the velocity profiles must be taken into account within the modelling framework.

8.8 HEAT TRANSFER

The Nusselt number for heat transfer is a function of the impeller type used, Reynolds number, Prandtl number and viscosity as follows,

$$Nu = f(\mathrm{Re}, \mathrm{Pr}, \mu_b/\mu_w)$$

During the simulation, the initial solution, saturated at 353K, was cooled down to 293K over a period of one hour. The heat transfer coefficient was estimated using an impeller frequency used of 300 rpm for both the Rushton turbine and pitch blade impeller respectively. During the simulation of the batch cooling crystallization, the temperature distribution was recorded at 60 s intervals corresponding to a cooling rate of $-1\mathrm{K\ min^{-1}}$.

A sample CFD heat transfer code is provided in Appendix B.2. The transient CFD simulations were performed using the steady state hydrodynamic information and hence only the cooling profile, enthalpy balance and film heat transfer coefficient were implemented into the CFD model. CFD was used to identify any

'cooling zones' or surfaces where steep gradients in the temperature distribution are likely to occur. Gradients in the temperature distribution affect the supersaturation profiles within a batch cooling crystallization vessel. Supersaturation is the driving force for a crystallization process, and affects both the crystallization kinetics and the final product performance. In comparison with the temperature distribution, higher levels of supersaturation correspond to lower temperatures. Fig. 8.18 shows the temperature distribution in a vertical plane within the batch cooling crystallizer after 360 s simulation equipped with a Rushton turbine impeller. The temperature distribution is uniform in the bulk zone, which can be explained by the efficient turbulent heat transfer. Similarly, no temperature gradients exist in the impeller zone as well. However, cooling zones exist in the upper region of the crystallizer where temperatures are the lowest and gradients exist. This can be explained by the effect of the less turbulent flow in this part of the crystallizer and also by the cooling wall temperature on the wall boundary. The temperature difference between the bulk and near the wall of the cooling zones is approximately 0.2 °C. On an industrial scale of say 1500l, however, the temperature gradient between the bulk and the cooling zone may be expected to be much more significant. This could affect process performance significantly as a result of encrustation occurring and large supersaturation gradients being realized. Fig. 8.19 shows the temperature profile after 360s numerical simulation using a pitch blade impeller configuration. The bulk zone has a uniform temperature profile and no temperature gradients exist. However, the size and temperature gradient within the cooling zone when compared to the Rushton turbine impeller is larger. A temperature difference of approximately 0.4 °C is observed between the bulk and temperature near the wall in the cooling zone. This is a result of less efficient turbulent heat transfer using the pitch blade impeller.

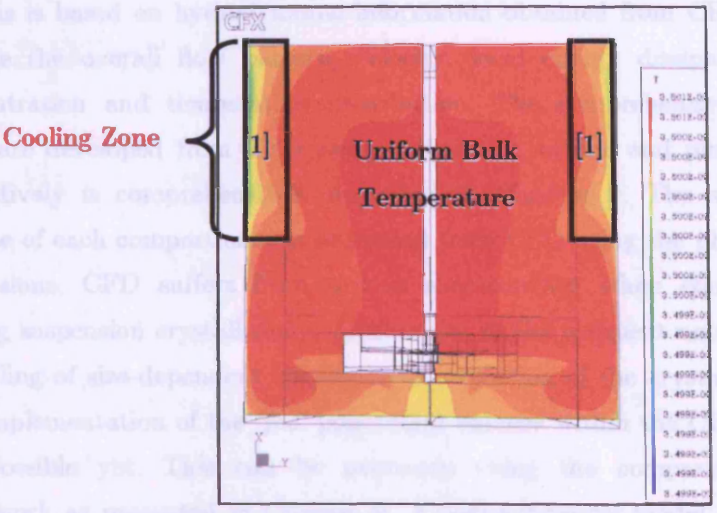

Figure ***8.18:*** *Temperature distribution profile in a vertical plane after 360s heat transfer simulation (Rushton turbine impeller).*

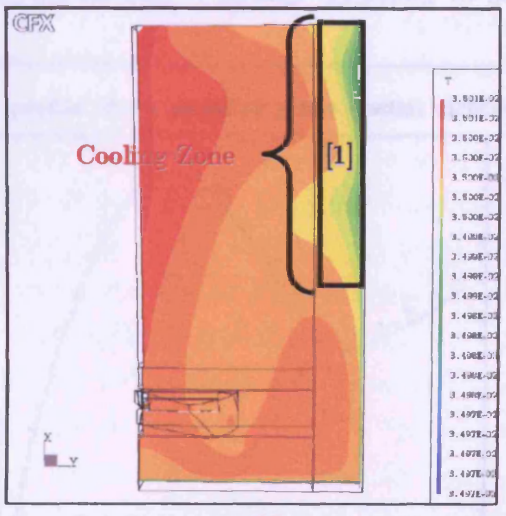

Figure 8.19: *Temperature distribution profile in a vertical plane after 360s heat transfer simulation (Pitch blade impeller).*

8.9 CONCLUSION

CFD simulations are used to determine the effects of mixing with the presence of particles and heat transfer in a seeded batch cooling suspension crystallization process. A compartmentalization approach is proposed and developed for the predictive scale-up of batch suspension crystallizations.

This is based on hydrodynamic information obtained from CFD simulations to include the overall flow pattern, velocity, local energy dissipation rates, solids concentration and temperature distribution. The comprehensive compartmental structure developed from CFD using a Rushton turbine and pitch blade impeller respectively is comprehensively described in Chapter 9. The size, location and volume of each compartment is estimated from CFD using the physical crystallizer dimensions. CFD suffers from serious shortcomings when considering a batch cooling suspension crystallization process due to the transient nature of the system. Modelling of size-dependent classification, evolution of the crystal size distribution and implementation of the *'full'* population balance within the CFD environment is not possible yet. This can be overcome using the compartmental modelling framework as presented in Chapter 9. A compartmental model allows the spatial resolution to be drastically reduced when compared to that used in the CFD environment. This allows estimations of process behaviour to be obtained over a period of a few days.

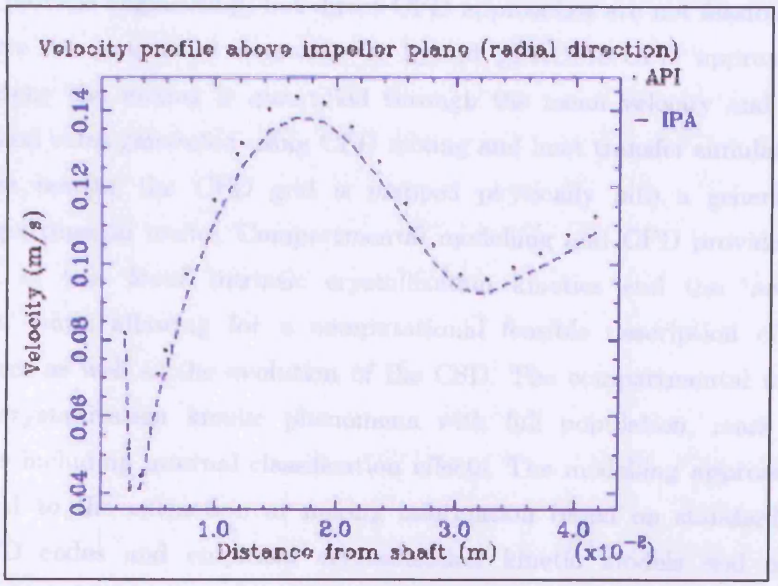

Figure 8.20: *Velocity profile above impeller (horizontal plane) using a 10% v/v solids concentration with a 200 μm mean particle size.*

Chapter 9

A HYBRID gPROMS/CFD-PARTICLE ENGINEERING COMPARTMENTAL FRAMEWORK FOR CRYSTALLIZATION MODELLING: BASIC CONCEPT AND THEORETICAL FRAMEWORK

ABSTRACT

The coupling of turbulent mixing, heat transfer and crystallization phenomena are crucial for particle engineering, but direct CFD approaches are not feasible due to the excessive computational demands. A hybrid gPROMS-CFD approach is presented whereby the mixing is quantified through the mean velocity and local energy dissipation rates generated using CFD mixing and heat transfer simulations. Based on these results, the CFD grid is mapped physically into a generalised gPROMS compartmental model. Compartmental modelling and CFD provides for the separation of the *'local'* intrinsic crystallization kinetics and the *'overall'* hydrodynamics, while allowing for a computational feasible description of the process dynamics as well as the evolution of the CSD. The compartmental model describes the crystallization kinetic phenomena with full population, mass and energy balances including internal classification effects. The modelling approach is not only limited to the extraction of mixing information based on standard k-ε turbulence CFD codes and empirical crystallization kinetic models and could therefore benefit from further development.

9.1 INTRODUCTION

In order to design industrial crystallizers, there is a need to provide insight into the local crystallization processes that occur within crystallizers. Models have been developed to simulate crystallization processes whereby input-output models are used with crystallization kinetics. Batch crystallizers are often treated as a well-mixed MSMPR crystallizer (Melikhov et al., 1981; Rohani and Bourne, 1990; Mohameed et al., 2002). These models have been constructed on a single configuration and therefore cannot be used for scale-up as different crystallizer geometries, scales and operating conditions are used in industry. This affects the quality characteristics of an organic fine chemical in terms of the crystal size distribution. The reason for this is that there is a deviation from well-mixed conditions within a crystallizer due to the hydrodynamic conditions. Hydrodynamics affect the temperature, supersaturation, slurry density, crystal size distribution and energy dissipation profiles within the crystallizer. When a process is scaled-up, different temperature profiles, supersaturation profiles and energy dissipation rates may be evident producing different CSDs. Geometrically lumped regions of a crystallizer are often used to describe a crystallization process, however crystallization phenomena should be described on a local scale where process conditions are uniform. Another reason for scale-up approaches failing is that crystallization kinetic models have been developed from crystallization vessels that have been heavily 'contaminated' with hydrodynamics (Qiu and Rasmuson, 1994).
A compartmental modelling or 'hybrid' approach can be introduced to overcome these difficulties, whereby crystallization phenomena occurring in localized areas of a crystallization vessel can be taken into account. Compartmental modelling is a technique that has long been used in chemical reactor engineering (Kramers and Westerterp, 1963; Levenspiel, 1972), but relatively short in crystallisation (Garside, 1985; Klein, 1991, Jager et al., 1991). This technique comprises the division of the crystallizer into a number of units with well-defined flow patterns (plug flow, perfectly mixed) and was introduced to treat non-ideal flow and mixing problems. Such a problem is defined as one in which fluid dispersion causes the residence time distribution to deviate from that of either ideal extremes, plug flow or perfectly mixed. The non-ideal flow problem is dealt with by introducing a network

of coupled units that have ideal flow characteristic. The objective is to find the combination of interconnected units that best reproduces the measured residence time distribution. These units are also called 'cells' or 'compartments'. As the spatial resolution of a network of compartments is typically a few orders of magnitude less than used in CFD techniques, enough computational power is retained to include crystallisation kinetics, population balances and process dynamics.

However, the use of compartmental models introduces new model parameters that need to be determined, e.g. the number of compartments, the size of the compartments, and the exchange rates between the compartments. The values for these parameters determine whether the influence of crystallizer geometry and operating conditions on the hydrodynamics will be captured correctly. Obtaining correct values for these parameters is thus a key issue in compartmental modelling.

CFD is employed only for hydrodynamic simulations, while the crystallization phenomena are resolved in a compartmental model. Recently, compartmental models have been successfully applied to steady state continuous evaporative crystallizations (Kramer et al, 1999; Kramer et al, 2000; Bermingham et al, 1998 and ten Cate, 2000), reactive semi-batch and continuous precipitation processes (Zauner and Jones, 2002) and gas-liquid precipitation processes (Rigopoulos and Jones, 2003). Alexopoulos et al. (2002) also used a compartmental modelling approach to determine the crystal size distribution in suspension polymerisation reactors by taking into account the large spatial variations of the local energy dissipation rate in vessels. Urban and Liberis (1999), Bezzo et al. (2000), Bezzo et al. (2004) developed a hybrid interface communication between gPROMS modelling and a commercial CFD code. A compartmental approach represents a compromise, as the full CFD solution would require a radical breakthrough in computer technology. Currently, a compartmental model for the predictive scale-up of seeded batch cooling crystallization processes has not been established. The compartmental model is a network of compartments with many degrees of freedom made for flow fields and turbulent mixing.

A novel hybrid gPROMS-CFD compartmental modelling approach is presented here to predict the influence of geometry, scale and operating conditions for the

predictive scale-up of seeded batch cooling crystallization processes of an organic fine chemical. The main concept of a single compartment and the generalised compartmental modelling framework is introduced whereby the CFD hydrodynamic and k-ε turbulence information is linked to the crystallization kinetics via population, mass and energy balances including taking into account internal classification effects.

Both the CFD and compartmental modelling approach can provide resolution in the time, external and internal co-ordinates. However, considering the present computational power and the intended application of these approaches for design purposes, neither can provide the degree of resolution in all co-ordinates required for a general rigorous description of crystallisation processes. One must therefore deliberate upon the dominant crystallisation mechanisms for each crystallisation system, and subsequently determine the resolutions with which the various coordinates will be described.

In batch cooling suspension crystallization with moderately to highly soluble compounds, the supersaturation normally remains low and does not vary considerably over the vessel, while relatively large crystals are formed when compared to reactive precipitation processes. Nuclei (new crystals) are mostly formed by the attrition of larger crystals, the rate of which is determined by the local energy dissipation rate and the surface roughness of the parent crystals. The survival chance of the nuclei depends on the local supersaturation experienced during and shortly after formation. The healing of crystals undergoing micro-attrition as described in Chapter 6 and the formation of liquid inclusions are also related to local supersaturation and energy dissipation rate values. The growth rate is dependent upon supersaturation and for the smaller crystals also upon the remaining stress from the attrition process. In suspension crystallisation, the rates of the dominant mechanisms typically have low order energy dissipation rate and supersaturation dependencies as determined in Chapter 5 and 6. Small changes in supersaturation and/or energy dissipation rates will therefore have a minor effect on the kinetics, thus reducing the need for a high spatial resolution. Furthermore, as relatively large crystals are formed in most batch suspension crystallisation process, particle segregation is often an important phenomenon that needs to be accounted for. Concluding, a compartmental approach is deemed suitable for the

A compartmental model is not specific to a certain crystallization vessel and has to be re-derived for different crystallizer set-ups (i.e. impeller type or crystallizer configuration) and operating conditions.

9.3 SET-UP OF THE COMPARTMENTAL STRUCTURE

The compartmental model is characterised by the structure of the compartments in terms of the location, number, volume and shape including the connectivity between the compartments (input and outputs, interconnecting flow rates and cross-sectional area). To summarise the development of the compartmental model using CFD as described in Chapter 8, the following techniques are used to construct the compartmental model,

I. Compartmental units are introduced to account for the main functional zones and different residence times within a batch crystallizer. For example compartmental units for circulation devices such as impellers can be introduced, as this is a region in which the highest energy dissipation is realized. This is necessary such that crystal impacts on the impeller can be described through the introduction of an attrition (breakage) kinetic model as these collisions are considered as a major contribution to the source of secondary nuclei. Secondary nucleation is the dominant mechanism of nuclei formation in the seeded batch cooling crystallization process providing that operation occurs within the metastable zone. Furthermore, a primary nucleation model must be used if linear or natural cooling profiles are used. The effects of seeding on the nucleation kinetics also merit examination.
II. The compartments should be constructed such that they represent the overall flow pattern within a crystallizer. This is rather arbitrary from CFD simulations but this step functions as a precursor for further refinement.
III. The compartments should be checked for internal supersaturation gradients and the degree of solid-solvent phase mixing analysed. Compartmentalizing with respect to supersaturation levels in reactive precipitation processes is important as large gradients in local supersaturation occur. In batch cooling crystallization processes relatively small supersaturation gradients may exist

and are found at cooling surfaces or 'zones'. In this research, CFD simulations are used to simulate heat transfer to determine the location and volumes of such 'cooling zones'.

The steepness of the supersaturation profile is determined by the cooling regime implemented, rate of energy dissipation and the mother liquor physical properties. The steepness of supersaturation gradients affects the growth kinetics within a crystallizer and hence the product performance, product quality, bulk density, filterability and CSD. However, compartmentalization with respect to supersaturation has little added significance if secondary nucleation is the dominant nucleation mechanism. In batch cooling crystallization processes, supersaturation levels are relatively low thus crystallization kinetics are not affected significantly as long process times are used to obtain large crystals even though the organic fine chemical exhibits size dependent growth.

IV. In the impeller zone, further local gradients in energy dissipation rates will exist. The presence of baffles improves the mixing profile by dissipating energy from the impeller zone upward and downward along the walls. If local gradients in the impeller zones exist the compartments are broken into one or more compartments to account for this.

V. The overall cooling duty should be distributed among the relevant compartments once they have been determined and is approximately distributed according to the fraction of the heat exchanger surface that is present in each compartment.

VI. Finally size-dependent classification functions have to be calculated to describe the non-uniform solids distribution in a crystallizer.

Classification functions act on the interconnecting flows between compartments. The classification function is related to the solids flowrate, flow direction, viscosity and density difference between the solids and liquid phase. Although a compartment may have a classified exit stream, the compartment however is perfectly mixed. At high impeller frequencies higher solid flow rates are realized (homogeneous mixing) hence eliminating the need for a classification function to be applied.

The physical connectivity of the compartments is determined by the magnitude and direction of the liquid flow in the various uniformly mixed regions of a crystallizer.

9.4 SINGLE COMPARTMENTAL MODEL

The model of a gPROMS compartment is the 'building block' for the development of the compartmental modelling framework. Each compartment is a perfectly mixed volume with respect to process conditions such as energy dissipation, temperature distribution and solids distribution. The attributes of a compartment are as follows,

I. Fixed size, volume, cross-sectional area and location (time and space).
II. Number of surfaces is equal to number of outgoing exchange flows.
III. Uniformly distributed intensive properties with respect to spatial domains within the compartment.
IV. Intensive properties include solids volume fraction, energy dissipation rate and temperature.
V. Conservation equations (mass, concentration, energy and population) to calculate changes in intensive properties due to crystal growth, supersaturation depletion and nucleation.
VI. An average energy dissipation rate is estimated from CFD simulations using the standard k-ε turbulence model to represent the hydrodynamic state within the individual gPROMS compartment.
VII. Expressions for physical properties (thermal conductivity, heat transfer coefficient, specific heat capacity of mother liquor, viscosity and mother liquor density).
VIII. Crystallization kinetic expressions describing growth, total nucleation, agglomeration and attrition.
IX. Expression for thermodynamics (solubility and enthalpy of crystallization).
X. Interconnecting or exchange flows between compartments are assumed to be uniform across the cross-sectional area.

description and prediction of process behaviour and product quality of most cooling crystallisation processes involving easily soluble organic fine chemical compounds. When a process is scaled-up, completely different local supersaturation and energy dissipation rate values may arise as predicted in Chapter 7, resulting in different CSDs and often even the development of other polymorphic forms.

9.2 HYBRID CFD AND COMPARTMENTAL MODELLING STRATEGY

The technique used in this research to develop the compartmental model in order to predict the crystal size distribution upon scale-up involves four development stages as follows,

I. Determination of crystallization kinetics, thermodynamics, physical properties and solubility information on a laboratory scale.
II. Scale-up CFD simulations to predict mean time averaged flow fields for solid-liquid phase (based on seeding), energy dissipation and heat transfer in batch crystallizers.
III. Setting up the compartmental model to separate kinetic and hydrodynamic phenomena by analyses of the CFD predictions.
IV. Determination of the process behaviour in terms of the CSD, suspension density and product quality by applying the same crystallization kinetic models and parameters for each individual compartment.

The compartments are to be chosen such that they have neglible internal gradients with respect to energy dissipation, solids concentration, temperature and supersaturation. Gradients between the compartments exist and are influenced by,

I. Crystallization kinetics
II. Material properties of the crystallized material
III. Geometry of the crystallization vessel
IV. Operating conditions

A gPROMS compartmental model is set-up such that there are negligible gradients in process conditions within the compartments but significant gradients can exist between the compartments. The perfectly mixed compartments are modelled as MSMPR compartments. A plug flow compartment model was not developed for the following reasons,

I. A cascade of CSTRs can approximate plug flow perfectly mixed compartments.
II. Dispersion or back mixing in a mainly plug flow region can be accounted for more flexibly using a number of CSTRs in series.
III. Modelling a plug flow compartment that takes into account an axial and optionally radial distribution, involves solution of PDEs as opposed to ODEs for the dynamic conservation equations and introducing additional partial derivatives in the population balance equation. Numerical solution methods for PDEs are not guaranteed to be robust under all circumstances; using a cascade of CSTRs avoids this problem.

A plug flow model should be considered for future predictive modelling as suggested by Bermingham (2003), as it offers the potential in reducing the number of modelling equations by using higher order numerical methods for approximation of partial derivatives. Each compartment must be described with the same compartmental model with respect to equations of conservation, physical properties, thermodynamics (solubility) and crystallization kinetic rate expressions. Differences in crystal growth, nucleation rate and attrition within the compartments are only due to varying process conditions.

The building units or 'blocks' required for developing the compartmental modelling framework should be flexible such that this procedure can be applied to other unit operations such as evaporative, reactive, anti-solvent and flash cooling crystallization processes or for different crystallization configurations and types.
The structure of the generic compartmental unit is such that it has a number of arbitrary input and output streams that enter and leave the compartment (Fig. 9.1). The physical connectivity of the compartments is determined by the magnitude and direction of the liquid and particle flow in the various uniformly mixed regions of a crystallizer. Each input stream is characterised by an overall

flowrate (Q), crystal population density, energy dissipation (ε), enthalpy flow (temperature) and mass (concentration) flow rates. The heat input of a compartment for a batch cooling crystallization process is negative. The states that are evident in each compartment are the temperature, crystal size distribution (CSD) and concentration. Hence in order to predict the rates of crystallization processes and the resulting temperature profile, supersaturation depletion and evolution of the CSD in each compartment requires the following,

I. Determination of thermodynamics such as equilibrium solubility information and enthalpy of crystallization.
II. Physical properties i.e. particle shape factors.
III. Determination of crystallization kinetics.
IV. Convective transport volumetric flows entering and leaving compartments.
V. The overall flow rates (Q), individual volumetric flows (ϕ_V) and mass flows (ϕ_m) are determined from mean velocity information yielded by CFD codes and the cross-sectional areas of each compartment using different operating conditions.
VI. Classification functions that account for slip of the crystals with respect to the liquid flow.

The equations of conservation are directly influenced by the crystallization kinetic models, convective transport and operating conditions. This combination affects the product performance and the crystal size distribution. There are NI inlets and NO outlets, with a heat transfer stream describing the energy transfer across the system.

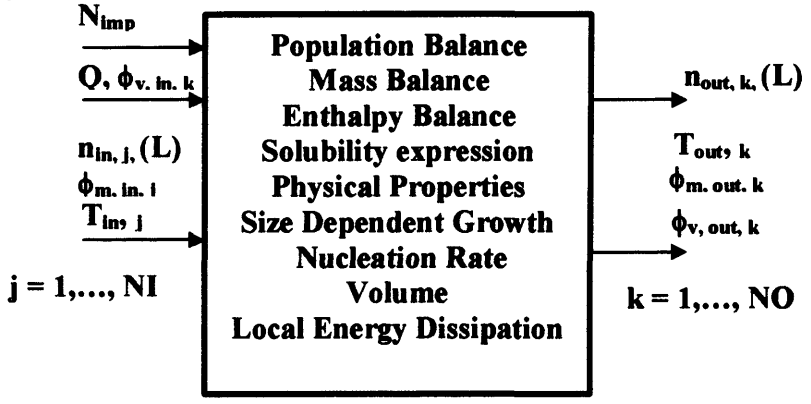

Figure 9.1: Generic Compartmental Structure

9.5 COMPARTMENTAL MODEL ASSUMPTIONS

9.5.1 COMPARTMENT SHAPE

I. A bounded volume in 3-D space, which may have symmetric features, lowering the effective dimensionality to 2-D.
II. A fixed position, size and area in time and space.
III. A finite number of surfaces.

9.5.2 COMPARTMENTAL CONTENTS

I. The solvent phase is the continuous medium.
II. The organic fine chemical phase is the dispersed medium.
III. In the compartment bulk each phase is spatially homogenous.
IV. The particle size distribution changes in time as a direct result of the crystallization kinetic rate expressions.
V. The solid and liquid phase in the bulk compartments have the same temperature
VI. The hydrodynamic state of each compartment is represented by a local energy dissipation rate.
VII. The conservation laws that are applied to each compartment include,
    - Mass and Concentration balance for the solvent phase
    - Population balance for the solid phase particles
    - Enthalpy balance
VIII. Randolph and Larson (1988) well-mixed MSMPR model applies.

9.5.3 COMPARTMENTAL SURFACES

I. Compartment is a control volume that is open to the system capable of exchange of mass and population of crystals by means of volumetric flows from one or more of its surfaces.
II. The volumetric flows are uniform across the entire surface of the compartment.
III. The solvent phase has the properties of the bulk compartment

IV. The solvent phase (flux) is a function of convective volumetric flow and concentration.
V. The particle phase (flux) is a function of size dependent velocity and the particle numbers.

9.5.4 PHYSICAL PROPERTY ASSUMPTIONS FOR THE COMPARTMENTAL MODEL

I. Constant mother liquor density
II. Constant crystalline density
III. Cooling water is used as cooling medium
IV. Constant mother liquor viscosity
V. Constant mother liquor heat capacity
VI. Constant heat transfer coefficients

The shape factors of the organic fine chemical were found to be constant and independent of size as shown from the MSMPR crystallization study carried out to determine crystallization kinetics. It was also difficult to distinguish between size-dependent growth (SDG) and growth rate dispersion (GRD) growth mechanisms in an MSMPR. However, due to the mathematical difficulties involved in modelling GRD, the SDG growth model proposed by Mydlarz and Jones (1994) will be used for modelling growth on transfer to a batch crystallization process. Growth rate dispersion is assumed not to occur and hence fluctuations in the growth velocity are neglible. From the MSMPR crystallization work, the dominating mechanism in the formation of nuclei is secondary nucleation. Primary nucleation will be assumed to be neglible during the batch operation (provided controlled cooling profiles are implemented and operation is within the metastable zone). Significant particulate agglomeration can occur if the crystallization environment has significant levels of oxygen. Providing that crystallization is carried out in an inert environment with rigorous purging of solvents, agglomeration is not the primary mechanism of organic fine chemical particle formation in the crystallizer. Hence there is no requirement for an agglomeration model. The organic fine chemical seed particles consist of trace elements but will be modelled as a single pure component. No energy input via mechanical action of the impeller will be taken into account.

The enthalpy of crystallization estimated from the solubility work will be modelled in the enthalpy balance, as it is significant and may influence the crystallization kinetics. Finally no heat loss to the environment or solvent evaporation providing a constant crystallization volume in the crystallizer will also be assumed.

9.6 GENERALISED COMPARTMENTAL MODELLING FRAMEWORK

The generalised compartmental model is a projective mapping of the CFD grid into a coarser network of fully mixed compartments. The compartmental model framework is characterised by the structure of the compartments in terms of the location, number, volume and shape including the connectivity between the compartments (input and outputs, interconnecting flow rates and cross-sectional area). The equations of conservation consist of mass balances for the liquid solute-solvent phase component, population balances for the particle phase and enthalpy balances. Further details with regards to the derivations of the conservation equations can be obtained from Appendix C. The population balance is a distributed mass balance for the particle phase and is linked to the solute-solvent phase via a concentration (mass) balance combined with the crystallization kinetics (Fig.9.2).

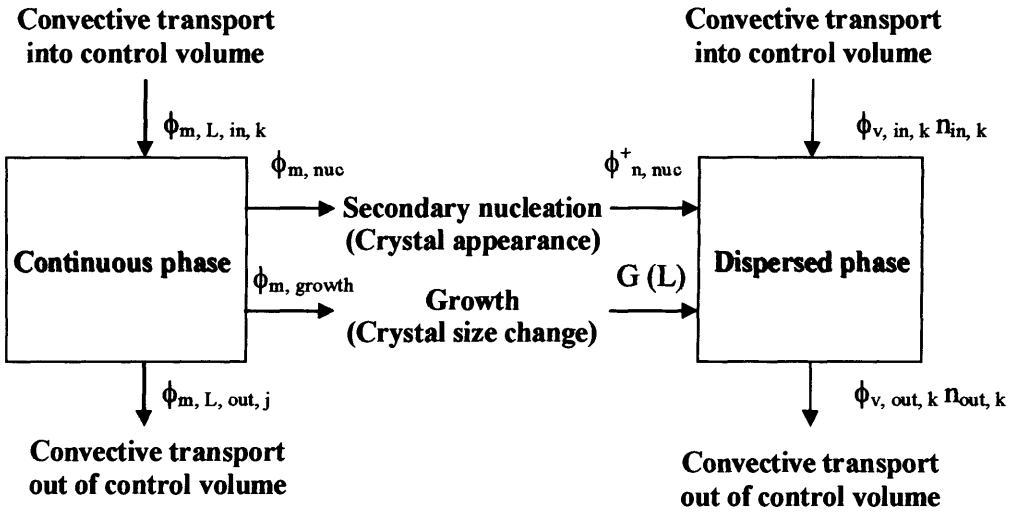

Figure 9.2: *Connection between the mass balance for the continuous phase and the population balance of the dispersed phase.*

9.6.1 COMPARTMENTAL POPULATION BALANCE

The evolution of the CSD is described by the population balance equation and was introduced by Randolph and Larson (1988). The advantage of using a compartmental modelling framework is that the full population balance can be implemented to include size-dependent growth, total nucleation and attrition. The compartmental population balance for the l^{th} compartment of a uniformly mixed compartmental volume, with the amount and size of particles expressed in terms of number density and particle length respectively can be written as follows,

Note: Growth rate dispersion and a size-dependent classification function at the exit streams of the l^{th} compartment have been included to give a complete description of the industrial pharmaceutical crystallization system. The industrial suspension crystallization does not exhibit breakage, agglomeration or primary nucleation (Table 9.1).

$$\overbrace{\frac{\partial(n(L,t)V(t))}{\partial t}}^{\text{number rate of accumulation}} + \overbrace{\frac{\partial(n(L,t).G(L,t))}{\partial L}V(t)}^{\text{rate of number gain due to crystal growth}} - \overbrace{\frac{\partial^2(D_G n(L,t))}{\partial^2 L}V(t)}^{\text{rate of number gain due to growth rate dispersion}} = \sum_{j=1}^{NI}\phi_{V,in,j}(t)n_{in,j}(L,t) - \sum_{k=1}^{NO}\phi_{V,out,k}(t)n_{out,k}(L,t)h_{out}(L) + \overbrace{\phi^{+}_{n,nuc}(L,t)V(t)}^{\substack{\text{number prodcutionrate due to sec ondary nucleation at the critical nuclei size}}} + \overbrace{\phi^{\pm}_{n,attr}(L,t)V(t)}^{\text{number production rate due to attrition}} \quad [9.1]$$

Initial boundary condition:

$$n(L,t=0) = n_O(L) = n_S(L) \quad [9.2]$$

The initial condition will be used to express a size distribution and quantity of seed crystals as we have in our case study for a batch crystallization process as follows,

$$n_S(L) = \begin{cases} n_e \exp(-r_S L), \text{exponential} \\ n_l\left(1-\frac{L}{L_m}\right), \text{linear} \\ n_u \qquad \text{uniform} \end{cases} \quad [9.3]$$

The boundary condition commonly used with respect to the crystal size for the population balance equation is as follows,

$$n(L=0,t)=\frac{B_N(t)}{G(L=0,t)} \qquad G(L)\geq 0 \quad \textit{for all crystal sizes, } G(L=0)>0 \qquad [9.4]$$

The boundary condition is applicable when the growth rate is positive for all crystal sizes.

9.6.2 COMPARTMENTAL MASS BALANCE

The generic transport equation can be described as follows,

$$\frac{\partial \rho_L c}{\partial t}+\nabla(\rho_L \bar{u}c)=S_c \qquad [9.5]$$

In order to discretize the above equation, the crystallizer volume must be broken down into the 'building blocks' or compartments as described previously, which are connected via convective mass fluxes. The source term describes crystal growth of seed and the formation of secondary nuclei. This allows the solution of the time-dependent mass balance for the liquid solute phase in the i^{th} compartment and is described as follows,

$$\frac{\partial m_L(t)}{\partial t}=\overbrace{\sum_{j=1}^{NI}\phi_{m,L,in,j}(t)-\sum_{k=1}^{NI}\phi_{m,L,in,k}(t)}^{\textit{mass flux in and out via convective transport}}+\overbrace{\left(\phi_{m,nuc}(t)+\phi_{m,growth}(t)\right)}^{\textit{int erphase mass flux due to crystal growth and sec ondary nuclei production}} \qquad [9.6]$$

Initial condition: $m_L(t=0)=m_{L,0}$

Kinetic rate terms that are present in both the population balance and mass balance,

$$\phi_{m,growth}(t)=-k_v\rho_S V(t)\int_0^\infty \frac{\partial(n(L,t)G(L,t))}{\partial L}L^3 dL \qquad [9.7]$$

$$\phi_{m,nuc}(t)=-k_v\rho_S V(t)\int_o^\infty \phi_{n,nuc}^{+}(L,t)L^3 dL \qquad [9.8]$$

A concentration balance for the liquid solute phase in the i^{th} compartment can be expressed similarly as follows,

$$\frac{\partial(c_L(t)V(t))}{\partial t} = \sum_{j=1}^{NI} \phi_{v,L,in,j}(t)c_{L,in,j}(t) - \sum_{k=1}^{NO} \phi_{v,L,out,k}(t)c_{L,in,k}(t) + \left(\phi_{m,nuc}(t) + \phi_{m,growth}(t)\right) \quad [9.9]$$

Initial condition: $c_L(t=0) = c_{L,0}$

9.6.3 COMPARTMENTAL ENERGY BALANCE

The potential, kinetic energy and shaft work are neglected to give the following enthalpy in the l^{th} compartment, temperature distribution can be expressed using an enthalpy balance.

$$\overbrace{\frac{\partial H(t)}{\partial t}}^{\text{rate of enthalpy accumulation}} = \overbrace{\sum_{j=1}^{NI} \phi_{h,in,j}(t) - \sum_{k=1}^{NI} \phi_{h,out,k}(t)}^{\text{rate of enthalpy in and out by convection}} + \overbrace{Q(t)}^{\text{net rate of heat removal}} + \overbrace{\phi_{H,c}}^{\text{enthalpy of crystallization due to growth and nucleation}} \quad [9.10]$$

The enthalpy balance can be expressed in terms of the temperature distribution within each compartment as follows,

$$\rho_L(t)V(t)C_p(t)\frac{\partial T(t)}{\partial t} = C_p(t)\left[\sum_{j=1}^{NI} \phi_{m,in,j}(t)T_{in,j}(t) - \sum_{k=1}^{NO} \phi_{m,out,k}(t)T_{out,k}(t)\right] - F(t)A(T - T_C(t)) - 3\rho_S k_v \Delta H_C \int_o^\infty G(L,t)n(L,t)L^2 dL - \rho_S k_v \Delta H_C \int_o^\infty \phi^+_{n,nuc}(L,t)L^3 dL$$

[9.11]

9.6.4 KINETIC SOURCE AND SINK TERMS IN THE COMPARTMENTAL POPULATION BALANCE

The dominant mechanisms in the crystallization of the organic fine chemical from an *iso*-propyl alcohol-water system are size-dependent growth (SDG), secondary nucleation and attrition. The source term for secondary nucleation is calculated as follows,

$$\phi^+_{n,nuc}(L,t) = \delta(L - L_O)B_N \quad [9.12]$$

B_N is the rate at which crystals of the critical nuclei size appear from the population balance as a result of attrition effects. This is also known as the effective nucleation rate. The effective critical nuclei size was determined from MSMPR crystallization kinetic studies to be 1μm. This rate has the units [$m^{-3}.s^{-1}$] with the Dirac function being a distribution having units [m^{-1}]. The function is zero when its argument is non-zero, and has the following property,

$$\int_{o}^{\infty} \delta(L - L_O) dL = 1 \qquad [9.13]$$

The net source term as a result of attrition $\phi^{\pm}_{n,attr}$ is composed of a source and a sink term for the various steps of the attrition process: a sink term for the parent crystals that are subject to attrition, $\phi^{-}_{n,attr}$ and a source term for the birth of crystals, $\phi^{+}_{n,attr}$.

$$\phi^{\pm}_{n,attr} = -\phi^{-}_{n,attr} + \phi^{+}_{n,attr} \qquad [9.14]$$

$$-\phi^{-}_{n,attr} = \beta_d n(L) \qquad [9.15]$$

$$\phi^{+}_{n,attr} = \int_{L_j}^{\infty} \beta_d S'(L_i, L_j) n(L_i) n(L_j) dL \qquad [9.16]$$

The source term comprises of a disruption function S' and β_d is the disruption kernel.

9.6.5 COMPARTMENTAL CRYSTALLIZATION KINETIC MODELS

The industrial crystallization of soluble substances is often dominated by secondary nucleation, in particular contact nucleation, and crystal growth. Jones et al. (1973) showed that secondary nucleation could occur at even low levels of supersaturation, as is the case with our industrial pharmaceutical crystallization system. The formation of secondary nuclei is a complex process depending on the hydrodynamics within a batch cooling crystallizer, the attrition behaviour of the crystals and the growth of the attrition fragments.

In batch cooling crystallizers, the main source of attrition fragment generation is a result of crystal-impeller collisions. The type of impeller used also affects the effective secondary nucleation rate as observed with MSMPR crystallizations to

estimate crystallization kinetics. It is assumed that the 'pure' crystallization kinetic models developed from a well-mixed continuous MSMPR crystallize is transferable to the batch cooling crystallization process of the organic fine chemical on different scales.

From MSMPR crystallization studies it was difficult to determine whether size-dependent growth (SDG) or growth rate dispersion (GRD) was the dominating growth mechanism of the organic fine chemical. Due to difficulties involved in modelling GRD, a three-parameter exponential SDG model proposed by Mydlarz and Jones (1993) is used to model crystal growth as a first approach. Furthermore, although particulate attrition may give rise to GRD, it may be possible that imperfect mixing in industrial crystallizers is mistaken for GRD. The growth and secondary nucleation kinetic rates will also be assumed to be independent of temperature. The crystal growth is a function of the relative supersaturation levels and particle size in the l^{th} compartment and given as follows,

$$G(L,t)=k_g\sigma^g(1-\exp[-a(L+c)]) \quad for\ L\leq 200\mu m \qquad [9.17]$$

$$G(L,t)=k_g\sigma^g \quad for\ L>200\mu m \qquad [9.18]$$

The growth rate coefficient (k_g) is dependent on the impeller type used as both bulk diffusion and surface integration resistances contribute to crystal growth and are also dependent on the crystal size.

The average kinetic growth expression was also determined from MSMPR crystallizations as follows,

$$G_{av}=k_g\sigma^f \qquad [9.19]$$

The total nucleation rate (secondary nucleation dominant) in the l^{th} compartment can be expressed in the form of empirical correlation as follows,

$$B_N=k_b M_T^i G_{av}^j \varepsilon_{loc}^k \qquad [9.20]$$

The total nucleation rate is a function of the suspension density, average growth rate and energy dissipation rate. The nucleation rate is also dependent on the impeller type and geometry used. The suspension density can be determined from the third moment of the crystal size distribution as follows,

$$M_T = k_v \rho_S \int_o^\infty n(L,t) L^3 dL \qquad [9.21]$$

The relative supersaturation in the i^{th} compartment is defined as follows,

$$\sigma = \frac{c_L(t) - c^*(T,t)}{c^*(T,t)} = \frac{\Delta c(t)}{c^*(T,t)} = S - 1 \qquad [9.22]$$

The equilibrium solubility is expressed as a function of the solution temperature in the i^{th} compartment as follows,

$$c^*(T,t) = a + bT + cT^2 \qquad [9.23]$$

The nucleation rate kinetic model will be implemented into the impeller zone and it is assumed that neglible nucleation (secondary) will occur in the bulk zone and high solids concentration zone. The overall total nucleation rate within a batch cooling crystallizer is defined as follows,

$$B_{TOT} = \frac{\sum_{j=1}^{NC} B_N V(t)}{\sum_{j=1}^{NC} V(t)} \qquad [9.24]$$

The attrition rate can also be determined using a disruption kernel. The disruption kernel is a function of the energy dissipation rate and supersaturation levels as follows,

$$\beta_d = k_d \varepsilon_{loc} \sigma^n \qquad [9.25]$$

The mean size of crystals in the i^{th} compartment can be calculated using the following relation as follows,

$$L_{i,j} = \frac{m_i}{m_j} \quad where\ i = 1,...,4\ and\ j = i - 1 \qquad [9.26]$$

Finally the moments of the crystal size distribution can be represented as follows,

$$m_j = \int_o^\infty n(L) L^i dL \quad for\ i = 1,...,4 \qquad [9.27]$$

9.6.6 COMPARTMENTAL VOLUMES

CFD is used to determine the number, location, cross-sectional area and volume of each compartment. In batch cooling crystallization processes, the feed and product flow rates are zero. However due to the transient nature of the system, the volume of each compartment may change due to a change in density and viscosity. An additional complication that may arise with batch cooling crystallizations is that as the volume changes during the batch process, compartments may become partially full or completely empty. In the modelling framework, it will be assumed that the i^{th} compartmental volume and location will remain unchanged during the batch process hence allowing for simplification producing the following expression,

$$\frac{dV(t)}{dt} = 0 \qquad [9.28]$$

9.6.7 ENERGY BALANCE COOLING REGIME IMPLEMENTATION

The compartmental modelling framework is flexible in terms of the type of cooling regime that can be used for the batch cooling crystallization process. The different cooling profiles that can be implemented into the compartmental modelling framework are as follows,

1. Natural cooling

$$T_C(t) = T_C + \exp\left(\frac{1}{\tau}\ln\left\{\frac{T_O - T_C}{T_f - T_C}\right\}t(T_O - T_C)\right) \qquad [9.29]$$

2. Linear cooling

$$T_c(t) = T_o - \frac{(T_o - T_f)}{\tau}t \qquad [9.30]$$

3. Constant nucleation rate controlled cooling (Jones, 1973)

4. Metastable zone cooling: optimal cooling with constant supersaturation (Jones, 1973).

9.6.8 HEAT TRANSFER COEFFICIENT

Batch cooling crystallizers have a heat transfer surface in the form of a cooling jacket for heat removal. The intensity of heat transfer depends on the type of impeller used, crystallizer geometry and process conditions. Heat transfer from the cooling fluid to the heat transfer area at the crystallizer wall can be characterized by a film heat transfer coefficient $[h(t)]$. Heat transfer in crystallizers is complex to model and hence an empirical approach based on dimensionless analysis has been used to predict the average heat transfer coefficient at the crystallizer wall. The following dimensionless equation is used for estimating heat transfer coefficients as follows,

$$Nu = \frac{F(t,T)d_t}{\lambda(t,T)} = C\left(\frac{\rho_L(t,T)Nd_i^2}{\mu(t,T)}\right)^a \left(\frac{C_p(t,T)\mu(t)}{k(t,T)}\right)^b \left(\frac{\mu_w(t,T)}{\mu_b(t,T)}\right)^c \qquad [9.31]$$

The coefficients C, a, b and c are dependent on the type of impeller used. We will also assume a constant heat transfer coefficient as physical property data (density, specific heat capacity, thermal conductivity and viscosity) for the solvent as a function of temperature is not available.

9.69 INTERNAL CLASSIFICATION MODELLING

When there is a density difference between the solid and solvent phase, particles will not always follow the streamlines of the solid phase. Hence, the flow pattern and distribution of solids in the crystallizer may differ from the solvent phase.

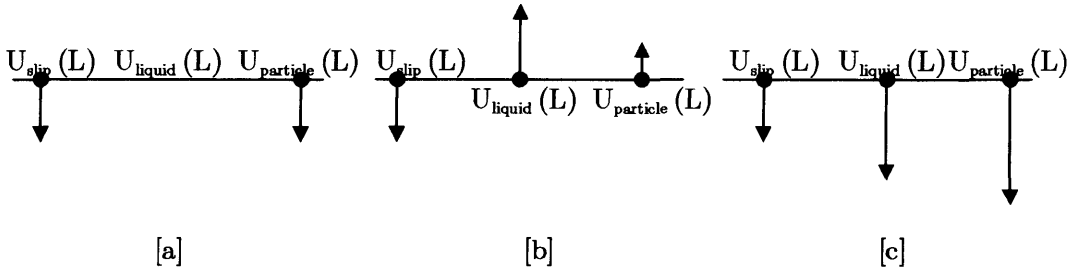

Figure 9.3: *Particle slip velocity, absolute liquid velocity and particle velocity in three different cases: (a) Stagnant liquid (b) Upward flowing liquid (c) Downward flowing liquid.*

This phenomenon will increase as the particle size, suspension density and density difference increases (Fig.9.3). Computational Fluid Dynamics (CFD) can be used to correctly account for this effect using the multi-phase model.

A simplified approach can be implemented into the compartmental modelling framework. The approach comprises calculation of classification functions, to account for the difference in flow pattern of the liquid and solid phase due to particle slip. The particle slip is defined as its relative motion with regard to the liquid. As slip is a result of inertia, the slip velocity of a particle depends on its size. The slip velocity also depends on the density difference between the solid and liquid phase, particle shape and the dynamic viscosity of the solvent phase.

Furthermore, if many particles are present, the volume fraction of solids and the particle size distribution also influence the particle slip. In a moving liquid, the absolute particle velocity is defined as the sum of the absolute liquid velocity and the particle slip velocity as follows,

$$U_{particle}(L) = U_{liquid} + U_{slip}(L)$$

The classification function accounts for the difference in the flow pattern of the solute-solvent and solid particle phase by rendering the residence time of the crystals in a compartment size dependent (Fig.9.3). The ratio of the crystal number density in an outlet stream and in the compartment is defined as the classification function of that stream as follows,

$$h_{out}(L) = \frac{n_{out}(L)}{n(L)} \qquad [9.32]$$

The introduction of a size-dependent classification function allows one to have compartments that are perfectly mixed internally but not with respect to the outlet stream. Bermingham (2003) derived the following expression for the determination of size-dependent classification functions as follows,

$$h_{out}(L) = \frac{U_{slip}(L)}{U_{\sup,out}} + \frac{\varphi_{out}}{\varphi} \qquad [9.33]$$

For low to moderate solids concentrations, as we have in the industrial crystallization system, the superficial velocity can be assumed to be the liquid velocity. The slip velocity is defined as follows,

$$U_{slip}(L) = \left(\frac{-B(L) + \sqrt{B(L)^2 + AC(L)}}{C(L)} \right)^2 \qquad [9.34]$$

Where parameters A, B and C are defined as follows,

$$A = \sqrt{\alpha_1}$$

$$B(L) = 0.5\sqrt{\alpha_2 \alpha_4}$$

$$C(L) = \sqrt{\alpha_2 \alpha_3}$$

And $\alpha_1, \alpha_2, \alpha_3$ *and* α_4 given as follows,

$$\alpha_1 = g\frac{\rho_S - \rho_L}{\rho_S + \rho_L}$$

$$\alpha_2(L) = 0.75\frac{1 + (1-\varphi)^{0.33}}{(\rho_S + \rho_l)L^2\varphi}$$

$$\alpha_3(L) = 0.63\sqrt{L\rho_L}$$

$$\alpha_4 = 4.80\sqrt{\eta_L}\exp\left[\frac{5}{6}\frac{1-\varphi}{\varphi}\right]$$

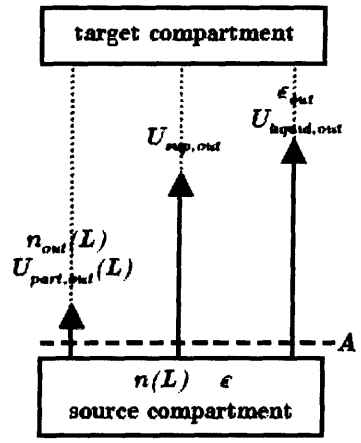

Figure 9.4: *Particle velocity, superficial velocity, liquid velocity, crystal size distribution and cross-sectional area of a flow connecting two compartments.*

The compartmental structure and interconnecting flows developed from CFD simulations between the compartments are shown in Fig. 9.4 and Fig. 9.5 for batch cooling crystallizers equipped with a Rushton turbine and pitch blade impeller respectively.

9.7 GENERALISED COMPARTMENTAL MODEL IMPLEMENTATION

The physical and crystallization mechanisms that govern the time dependent behaviour of a uniformly mixed region are complex. The equations describing the industrial batch cooling crystallization system are derived from first principals in terms of the conservation laws and physical constraints that describe the crystallization phenomena. The generalised gPROMS compartmental model contains a combination of differential, partial differential, integral and algebraic equations. The model is implemented into the gPROMS process modelling software. This software is specifically designed to allow the direct specification of all of the above classes of equations in a high level language and has powerful numerical methods for their solution. gPROMS is used to simulate a continuous MSMPR and batch cooling suspension crystallizers based on a single 'lumped' compartment and a compartmentalization approach in Chapter 10.

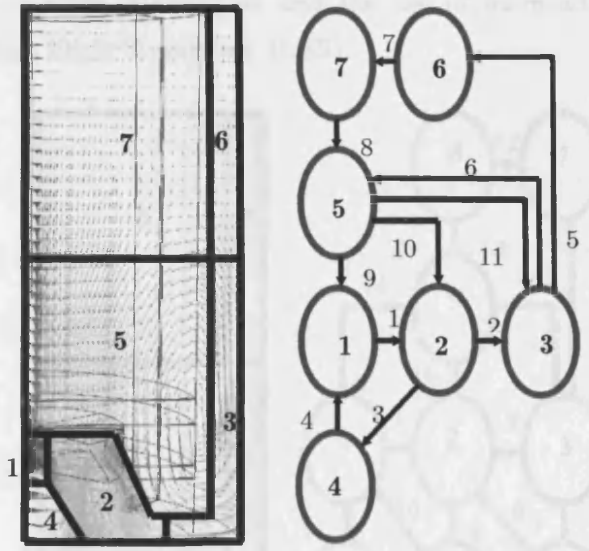

Figure 9.4: *Comprehensive compartmental modelling framework for a batch cooling crystallizer fitted with a pitch blade turbine impeller (due to symmetry only one quarter of the crystallizer is shown): location of compartments [a] and connectivity diagram [b].*

9.8 CONCLUSION

A compartmental modelling framework for the predictive scale-up of batch cooling crystallization processes is presented. gPROMS compartmental modelling and CFD provides for the separation of the '*local*' intrinsic crystallization kinetics and the '*overall*' hydrodynamics, while allowing for a computational feasible description of the full process dynamics as well as the evolution of the crystal size distribution. The compartmental procedure presented involves heuristics and depending on the availability of CFD information the quantity of heuristics can be diminished.

The CFD hydrodynamic information to include the mean velocity and local energy dissipation rates are linked to the compartmental model. The gPROMS compartmental model describes the crystallization phenomena including the population, mass and energy balances associated with the batch cooling crystallization process. The compartmental model could benefit from further development in terms of introducing more physical models such as the Gahn model

to model particle-impeller interactions and the use of more advanced turbulence models such as Large Eddy Simulation (LES).

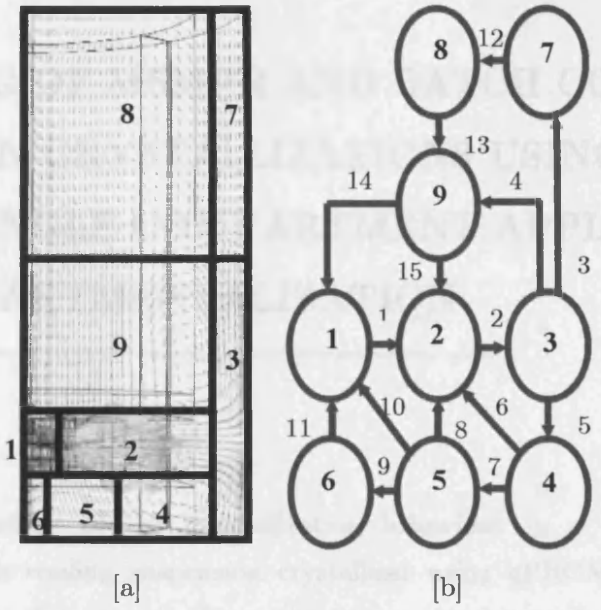

Figure 9.5: *Comprehensive compartmental modelling framework for a batch cooling crystallizer fitted with a Rushton turbine impeller: location of compartments (a) and connectivity diagram (b).*

Table 9.1: *Source and sink terms that are set to zero in the compartmental population balance*

$\phi^{\pm}_{n,break}(L,t) = 0$
This term is set to zero in the PBE, as breakage is not a dominant mechanism for the batch cooling crystallization of the organic fine chemical.
$\phi^{\pm}_{n,aggl}(L,t) = 0$
This term is set to zero in the PBE, as agglomeration is not a dominant mechanism for the batch cooling crystallization of the organic fine chemical.
$\phi^{\pm}_{n,primary}(L,t) = 0$
This term is set to zero in the PBE, as primary nucleation is not the dominant mechanism for the batch cooling crystallization of the organic fine chemical.

Chapter 10

MODELLING OF MSMPR AND BATCH COOLING SUSPENSION CRYSTALLIZATIONS USING gPROMS: SINGLE COMPARTMENT APPLICATION AND COMPARTMENTALIZATION

ABSTRACT

Predictive modelling of the crystallization behaviour in a laboratory scale MSMPR and batch cooling suspension crystallizer using gPROMS as a process-modelling tool for the organic fine chemical is investigated. The predictive crystallization behaviour using different mean residence times and impeller configurations for an MSMPR crystallizer shows a good agreement between experimental and predictive results. The predictions based on using a laboratory scale batch cooling crystallizer give a good indication of the crystallization behaviour with different operating and process conditions. However, the reliability of predictions for the batch crystallizer is poor because the crystallization kinetics developed from the MSMPR crystallizer is transferred to the batch process. This results in the CSD being significantly underestimated. Furthermore, a single compartmental approach was used to model batch cooling crystallizers and hence the effects of scale-up in terms of the mixing, hydrodynamics, local energy dissipation and temperature distribution in localised regions is not taken into account. Moreover, the effects of scale-up on the crystal size distribution and product performance cannot be captured using a lumped description. The heuristic compartmental modelling framework developed in previous chapters is also introduced into a hybrid gPROMS/CFD environment.

10.1 INTRODUCTION

The modelling of particulate processes poses problems not encountered in more conventional process operations. The state of such systems is characterized by the particle size distribution in addition to properties such as the concentration and temperature. Population balances describe the steady state and dynamic behaviour of crystallization system including mass, concentration and energy balances. The physical properties of solids encountered in particulate systems are generally less well characterized than those of fluids.

In the previous chapter the compartmental modelling framework for seeded batch cooling suspension crystallization was emphasised. This is achieved by means of the compartmental modelling framework using a general single compartmental model as its building block. In this section, the focus is on selecting a single modelling tool that can be used for [1] implementing the compartmental model to model the crystallization processes as discussed [2] optimal design of the crystallization processes based on modelling activities. The requirements of a modelling tool are to enable for steady state and dynamic modelling within the time domain. A modelling tool must also be capable of solving the mathematical problem of the crystallization system. Simulation involves the solution of a so-called forward problem: given a model, model parameters and inputs allowing the calculation of a model output, i.e. the behaviour of the crystallization process and the quality of the resulting product. The model inputs include process and operating conditions.

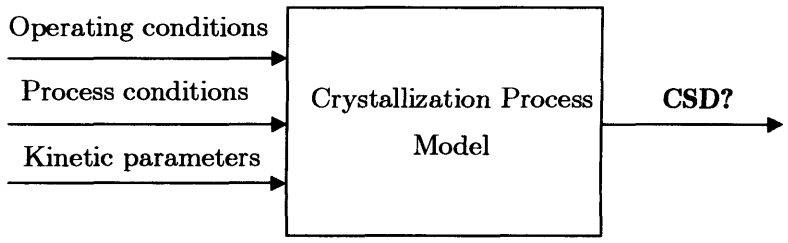

Figure 10.1: *Schematic of the simulation.*

gPROMS is chosen for process modelling because it has a powerful modelling language and provides support for hierarchical modelling. gPROMS is a modelling tool that can simultaneously solve mixed systems of algebraic equations and ordinary differential equations with respect to time. These systems are known as systems of differential-algebraic equations. The batch cooling crystallization compartmental modelling framework presented also consists of partial differential equations, i.e. population balance and integral equations for the calculation of the crystal size distribution and moments of the distribution. In order to solve these equations in gPROMS they must be reduced to a set of differential algebraic equations.

The reductions concern all derivatives with respect to independent variables other than time, as well as all integrals over other independent variables than time. The independent variable is the crystal size. gPROMS has been successfully used to model crystallization processes (Oh and Pantelides, 1996; Bermingham, 2002).

The next section will discuss the discretization of the crystal size domain, the reduction to differential algebraic equations of the population balance, which contains a partial derivative with respect to the crystal length, and the reduction to DAEs of integrals over crystal size.

10.2 DISCRETIZATION OF THE CRYSTAL SIZE DOMAIN

Discretization of the crystal size domain involves at least three aspects:

1. The lower bound of the domain, L_{min}.
2. The upper bound of the domain, L_{max}.
3. The discretization resolution.

For given upper and lower bounds, the resolution is not only determined by the number of elements but by the spacing between the elements as well. The simplest spacing is equidistant, but sometimes it may be more convenient to have a smaller

spacing (higher resolution) in certain parts of the domain and larger spacing in other parts of the domain. However, most numerical methods for the reduction of PDEs only apply to equally spaced elements.

Depending on the employed crystallization kinetic models, e.g. size-dependent or independent growth, the use of crystal size domain, L, with non-equidistant elements (logarithmic scale) is more favourable.

Values for lower and upper bounds of the domain should also be defined. The lower bound is equal to the critical nuclei size. The upper bound should be chosen such that the concentration of crystals at this point could be assumed to be zero:

$$n(L_{\max}, t) \approx 0 \qquad [10.1]$$

The location of L_{max} depends on the crystallization kinetic rates including the residence times for continuous crystallizations and the batch times for batch processes. Consequently when one changes to a new chemical system, another crystallizer or a different set of operating conditions, the location of the lower and upper bound need to be reconsidered.

10.3 DERIVATIVES WITH RESPECT TO CRYSTAL SIZE

The dynamic form of the PBE is partial differential equation and thus needs to be reduced to a set of differential algebraic equations. For this purpose, numerical methods belonging to the family of the Method of Lines are considered.

10.3.1 METHOD OF LINES

The family comprises of a number of finite difference, finite volume and weighted residual methods. The method of lines involves the discretization of the non-temporal variable domains and the use of piecewise local or global functions to approximate the derivatives with respect to the non-temporal variables. The resulting ordinary differential equations, one for each point, are integrated over time along lines parallel to the time axis in the time-space domain. The techniques in the Method of Lines differ in the grid discretization and in the approximation

for the spatial derivatives. Whether a numerical method is suitable for the reduction of the PBE to a set of DAEs is determined by the crystallization mechanisms. If there is no crystal growth and only agglomeration and breakage, the PBE is an ODE with a time derivative of a distributed variable.

Accurate methods for the approximation of birth and death terms within the PBE require the need for the conservation of the mass and number of population of crystals. If crystal growth occurs, the PBE has a convective character and is classified as a hyperbolic PDE. Hyperbolic PDEs are best solved with an upwind finite difference method or finite volume method. Although the first order upwind finite difference method and finite volume method do not suffer from numerical instabilities when used correctly, they do invariably exhibit numerical diffusion (Lapidus and Pinder, 1982). Therefore only fine grids produce acceptable solutions. More efficient methods that are numerically more stable and exhibit less numerical diffusion include orthogonal collocation on finite elements using an adaptive size grid for error control and a finite difference method combined with the methods of characteristics (Kumar and Ramkrishna, 1996a and 1996b). The two methods, however, cannot be directly implemented in a DAE solver such as gPROMS because they involve a changing number of equations during the simulation. Based on the positive experience by Oh (1995) and Barton and Pantelides (1994) the upwind finite difference method for the solution of the PBE in combination with size-dependent growth will be applied in this investigation.

10.3.2 LOGARITHMIC TRANSFORMATION OF THE NUMBER POPULATION DENSITIES

Another degree of freedom with respect to the numerical solution of the PBE is the form in which the number density appears in the PBE: normal number densities or logarithms of the number densities. The advantage of taking the logarithms of the number densities is numerical scaling. To illustrate the transformation to obtain a PBE in terms of logarithms of number densities the following example is used based on a compartmental population balance,

$$\frac{\partial[n(L,t)V(t)]}{\partial t} = -V(t)\frac{\partial[n(L,t)G(L,t)]}{\partial L} + \phi_{V,in}(T)n_{in}(L,t) - \phi_{v,out}(t)n_{out}(L,t) + \phi_n^{\pm}(L,t)V(t) \quad [10.2]$$

Note that the terms relating to the convective transport into and out of the compartments have been simplified to account for one flow only, and that the various number production rate terms have been lumped into one.
The next step involves splitting the partial derivative,

$$\frac{\partial[n(L,t)V(t)]}{\partial t} = -V(t)\left|n(L,t)\frac{dG(L,t)}{dL} + G(L,t)\frac{\partial n(L,t)}{\partial L}\right| + \phi_{v,in}(t)n_{in}(L,t) - \phi_{v,out}(t)n_{out}(L,t) \phi_{v,out}(t)n_{out}(L,t) + \phi_n^{\pm}(L,t)V(t) \quad [10.3]$$

Each term is then multiplied by $d\ln n(L,t)/dn(L,t)$,

$$\frac{d\ln n(L,t)}{dn(L,t)}\frac{\partial[n(L,t)V(t)]}{\partial t} = -V(t)\left[n(L,t)\frac{d\ln(L,t)}{dn(L,t)}\frac{dG(L,t)}{dL} + G(L,t)\frac{d\ln n(L,t)}{dn(L,t)}\frac{\partial n(L,t)}{\partial L}\right] + \phi_{V,in}(t)n_{in}(L,t)\frac{d\ln n(L,t)}{dn(L,t)} - \phi_{V,out}(t)n_{out}(L,t)\frac{d\ln n(L,t)}{dn(L,t)} + \phi_n^{\pm}(L,t)V(t)\frac{d\ln n(L,t)}{dn(L,t)} \quad [10.4]$$

With the following relationships,

$$\frac{d\ln n(L,t)}{dn(L,t)} = \frac{1}{n(L,t)} \quad [10.5]$$

$$\frac{d\ln n(L,t)}{dn(L,t)}\frac{\partial n(L,t)}{\partial L} = \frac{\partial \ln n(L,t)}{\partial L} \quad [10.6]$$

$$\frac{\partial[n(L,t)V(t)]}{\partial t} = -n(L,t)V(t)\left|\frac{dG(L,t)}{dL} + G(L,t)\frac{\partial \ln n(L,t)}{\partial L}\right| + \phi_{v,in}(t)n_{in}(L,t) - \phi_{v,out}(t)n_{out}(L,t) + \phi_n^{\pm}(L,t)V(t) \quad [10.7]$$

This completes the transformation of the partial derivative term in the PBE. Finally, the number densities are written in terms of logarithms for the compartmental population balance,

$$\frac{\partial[\exp(\ln(n(L,t)V(T))]}{\partial t} = -\exp(\ln(n(L,t)V(t))\left[\frac{dG(L,t)}{dL} + G(L,t)\frac{\partial \ln n(L,t)}{\partial L}\right] \quad [10.8]$$
$$+ \phi_{v,in}(t)\exp(\ln n_{in}(L,t)) - \phi_{v,out}(t)\exp(\ln n_{out}(L,t)) + \exp(\ln(\phi_n^{\pm}(L,t)V(t))$$

10.4 LABORATORY SCALE MSMPR CRYSTALLIZER WITH SIZE-DEPENDENT GROWTH AND TOTAL NUCLEATION

A continuous mixed suspension mixed product removal crystallizer operating in cooling mode to produce organic fine chemical crystals from an aqueous organic solution is described in this section. A compartmental modelling approach is not applied to this system because the MSMPR on a 0.5l scale is considered and is well mixed (hydrodynamics do not influence kinetics significantly).

10.4.1 MODELLING EQUATIONS

The temperature in the MSMPR crystallizer is constant. From MSMPR crystallizations, the organic fine chemical system exhibits neglible agglomeration and crystal attrition is ignored. A mass balance on the solute in both the liquid and solid phase yield the following equation,

$$V\rho\frac{\partial \bar{c}}{\partial t} = W(c_{in} - \bar{c}) \quad [10.9]$$

where $\bar{c}$ denotes the combined solid and liquid phase concentration of the solute, defined as follows,

$$\bar{c} = c + \frac{M_t}{\rho} \quad [10.10]$$

The suspension density is given as follows,

$$M_t = \rho_S k_v \int_0^{\infty} L^3 n(L,t)dL \quad [10.11]$$

A continuous population balance on the particles yields the following differential equation,

$$\frac{\partial n(L,t)}{\partial t}+\frac{\partial(G(L,t)n(L,t))}{\partial L}+\frac{n(L,t)}{\tau}=0 \qquad [10.12]$$

However, this equation may pose numerical problems because of the potentially large magnitude of the particle number concentrations $n(L,t)$, and it is therefore preferable to express it in terms of the natural logarithm of these quantities,

$$\frac{\partial \ln(L,t)}{\partial t}+G(L)\frac{\partial \ln n(L)}{\partial L}+\frac{\partial G(L)}{\partial L}+\frac{1}{\tau}=0 \qquad [10.13]$$

The boundary condition for this equation is of the form,

$$n(0,t)=\frac{B_0}{G_0} \qquad [10.14]$$

which can also be expressed in logarithmic terms,

$$\ln n(0,t)=\ln\left(\frac{B_o}{G_o}\right) \qquad [10.15]$$

The residence time in the MSMPR system is related to the mass flowrate as follows,

$$\tau=\frac{V\rho}{W} \qquad [10.16]$$

The crystal growth rate $G(L)$, the nucleation rate and the nuclei growth rate are all functions of the relative supersaturation of the solution as follows,

$$\sigma=\frac{\Delta c}{c_{eq}} \qquad [10.17]$$

The following correlations obtained from experimental data on the crystallization of the organic fine chemical from an aqueous organic solution are used,

$$G(L,\sigma)=0.0313\sigma(1-\exp(-0.0174(L+0.1)) \qquad [10.18]$$

Total nucleation rate models were developed for both pitch blade and flat blade impellers as follows,

$$\textit{Pitch blade}\quad B_o=4.9e^9M_t^{1.57}\sigma^{2.64} \qquad [10.19]$$

$$\textit{Flat blade} \quad B_O = 1.9e^9 M_t^{1.64} \sigma^{2.93} \qquad [10.20]$$

$$\textit{Pitch blade} \quad B_O = 1e^{19} G_{av}^{1.2} M_t^{1.5} \varepsilon^{0.15} \qquad [10.21]$$

A constant shape factor is used with the saturation concentration of the organic fine chemical in aqueous organic solution,

$$c_{eq} = 0.0035\exp(0.0443T) \qquad [10.22]$$

Overall, the model of the crystallizer comprises of the partial differential population balance equation, the ordinary differential concentration balance equation, integral and algebraic equations. The model of the MSMR crystallization unit is expressed in gPROMS language (Appendix F). Crystal sizes up to 300 μm were considered corresponding to the parameter MaxSize in the gPROMS model. A first-order backward finite difference method with 252 nodes was used for the discretization of the crystal size domain. Simulations with different numbers of nodes were carried out to verify that this scheme leads to sufficiently accurate results without incurring excessive computation. The properties and stream specifications for the simulations are defined in Table 10.1. The initial conditions for the simulations are that no crystals and pure solvent present is present during the start-up of the MSMPR crystallization process.

Parameter	Value
c_{in} (kg solid/kg solvent)	0.0371
W (kg/s)	$5.3e^{-04}$
T (°C)	29
V (m^3)	$5.5e^{-04}$
ρ (kg/m^3)	800
ρ_s (kg/m^3)	1400

Table 10.1: *Input stream specifications and parameter values for simulation investigation.*

The results of the continuous MSMPR simulations are shown in Fig.10.2-10.8. Fig.10.2 shows the mass distribution comparison between simulated and experimental results using a pitch blade and flat blade impeller respectively using the conditions in Table 10.1.

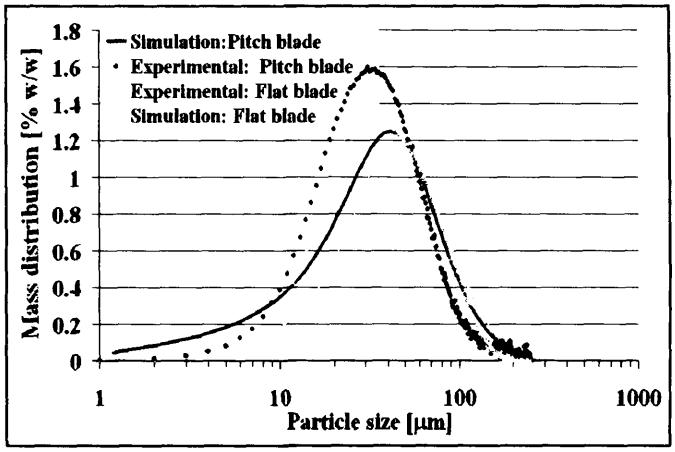

Figure 10.2: *Predicted and experimental continuous MSMPR crystal size distributions based on an initial concentration of 3.71 %w/w and a mean residence time of 825s for a pitch and flat blade impeller respectively using an agitation rate of 300 rpm.*

The trend observed in the simulated and experimental distributions (Fig.10.2) is as expected because the total nucleation rate using a flat blade impeller is less than that when compared to a pitch blade impeller thus allowing for the growth of larger particles. The simulations underestimate the crystal size distribution for both impeller configurations. The difference in the crystal size distributions may be due to particulate attrition not being taken into account within the population balance and the use of the Lasentec FBRM technique to measure the experimental particle trends (bimodality in terms of micro-attrition is not detected by the Lasentec). The experimental volume mean size is 57.07 μm and 60.45 μm for a pitch blade impeller and flat blade impeller respectively. Albeit that attrition is not taken into account the experimental results compare well to the simulated volume mean size values of 60 μm and 65 μm respectively.

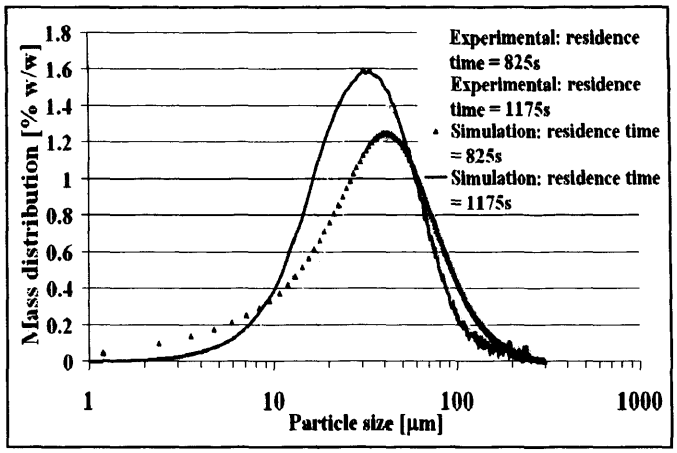

Figure 10.3: *Simulated and predicted mass crystal size distributions based on different residence times using a pitch blade impeller with a initial concentration of 3.71 % w/w and agitation rate of 300 rpm.*

Fig.10.3 shows the simulated and experimental mass distributions for the MSMPR crystallizer using a pitch blade impeller and different residence times. The trends in the simulated and experimental results are as expected as longer residence times corresponds to longer periods over, which crystal growth takes place resulting in the formation of large crystals corresponding to a shift in the right in the CSD.

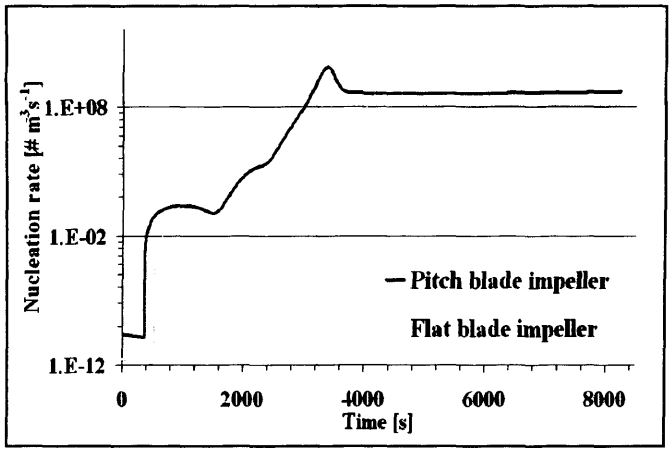

Figure 10.4: *Predicted nucleation rates during MSMPR operation until steady state operation achieved using a pitch and flat blade impeller respectively with an initial solids concentration of 3.71% w/w; 300 rpm and 825 s mean residence time.*

The experimental and simulated results compare well as the volume mean size for a residence time of 1175s is 71 μm and 60 μm respectively for simulated and experimental results. Fig. 10.3 shows the nucleation rate based on using a pitch blade and flat blade impeller. The predicted steady state operation in an MSMPR crystallizer is achieved earlier when using a pitch blade impeller (5 mean residence times) when compared to a flat blade impeller (6 mean residence times).

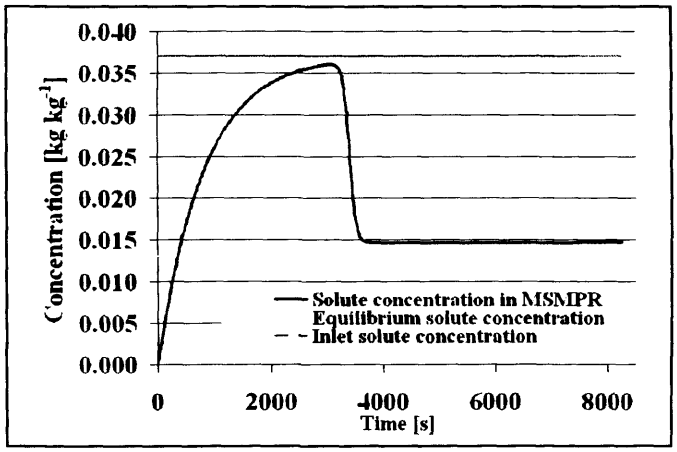

Figure. 10.5: *Concentration evolution prediction during the MSMPR operation until steady state operation is achieved using a pitch blade impeller operating at 300 rpm.*

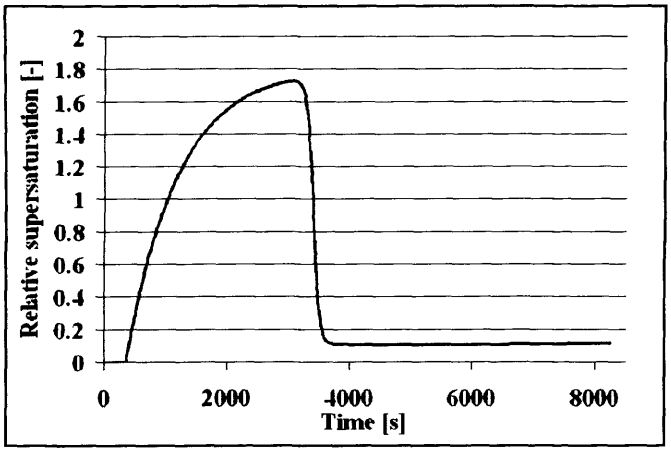

Figure. 10.6: *Supersaturation generation and depletion until steady state operation achieved using a pitch blade impeller operating at 300 rpm.*

Fig.10.4 and Fig.10.5 show the evolution of the solute concentration within the MSMPR crystallizer during operation based on a pitch blade impeller and a mean residence time of 825s. As the driving force for crystallization increases, a point occurs in which nucleation and crystal growth results in the solute concentration being consumed until a constant supersaturation and steady state operation is achieved.

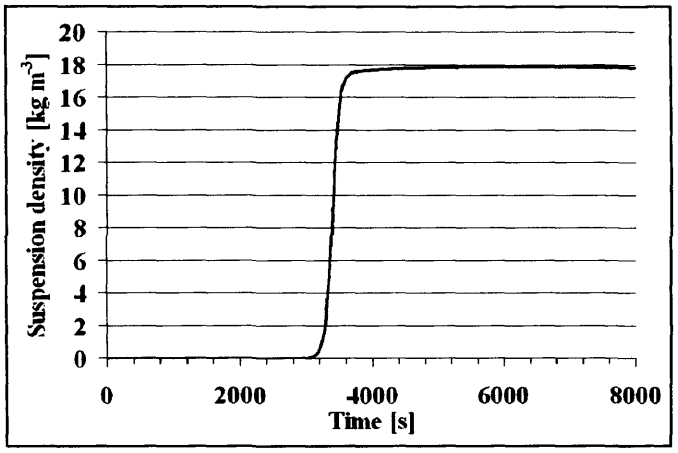

Figure. 10.7: *Prediction of the suspension density using a pitch blade impeller, mean residence time of 825s, initial concentration of 3.71% w/w and an agitation rate of 300 rpm.*

Fig.10.6 shows the evolution of the suspension density based on a pitch blade impeller and mean residence time of 825s.

To check the accuracy of the numerical solution based on the discretization scheme employed a check on the mass balance on the solute concentration and suspension density was performed with all gPROMS simulations. Using a pitch blade impeller with 825s mean residence time as an example a mass loss of 0.15% was evident corresponding to $5.85e^{-05}$ kg solid/kg solvent. Furthermore, Fig.10.7 shows that there is a predicted shift to the right in the CSD and increase in the particle size with an increase in the mean residence time and is as expected within an MSMPR crystallizer even though a decrease in the growth rate is observed and confirms the behaviour of an MSMPR crystallization process.

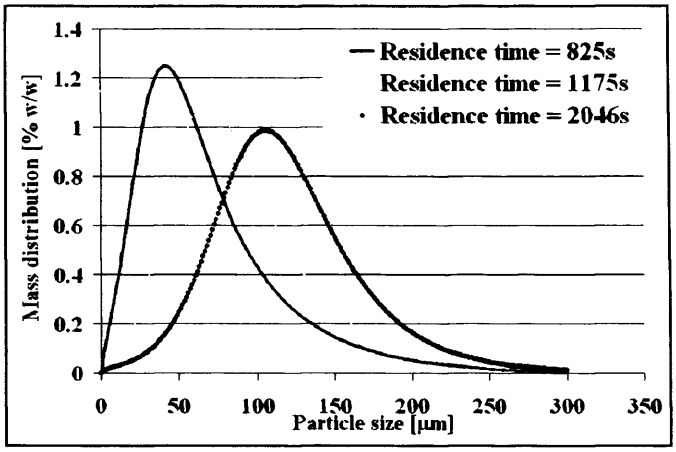

***Figure 10.8: Predicted** shift in crystal size distribution due to increase in mean residence time.*

10.5 LABORATORY SCALE BATCH COOLING CRYSTALLIZER WITH SIZE-DEPENDENT GROWTH AND TOTAL NUCLEATION

A batch crystallizer operating in forced cooling mode to produce organic fine chemical crystals from an aqueous organic solution is described in this section. A compartmental modelling approach is not applied to this system as the crystallizer is well mixed and therefore a lumped description should suffice in this case.

10.5.1 MODELLING EQUATIONS

Batch cooling crystallization models thus far only considered a 'lumped' description of the process system, whereby crystallization and hydrodynamic phenomena are not separated and taken into account. The batch crystallizer is therefore treated as a well-mixed MSMPR crystallizer. In this case the particle population balance based on a constant volume batch crystallizer is as follows,

$$\frac{\partial n(L,t)}{\partial t} + \frac{\partial (G(L,t)n(L,t))}{\partial L} = 0 \qquad [10.23]$$

The mass balance describing the solute phase concentration in the batch crystallizer given as,

$$\frac{\partial C_L(t)}{\partial t} = -k_v \rho_s \left[\int_0^\infty \frac{\partial (n(L,t)G(L,t))}{\partial L} L^3 dL + \int_o^\infty \phi^+_{n,nuc}(L,t) L^3 dL \right] \qquad [10.24]$$

The bulk solution temperature can be evaluated from an enthalpy balance as follows,

$$\rho_s V(t) C_p(t) \frac{\partial T_b}{\partial t} = -F(t) A \left(T_b - T_c(t) \right) + 3\rho_s k_v \Delta H_C \int_o^\infty G(L,t) n(L,t) L^2 dL + \rho_s k_v \Delta H_c \int_o^\infty \phi^+_{n,nuc}(L,t) L^3 dL \qquad [10.25]$$

A sample gPROMS source code for a batch cooling suspension crystallizer using a lumped description consisting of a single compartment is shown in Appendix F. Laboratory scale batch cooling crystallizations were carried out using a 0.06 kg solute per kg solvent solution. The initial supersaturated solution at 60 °C was cooled to 10 °C using a linear cooling profile of 0.5 °C min^{-1}. The crystallization kinetics developed from the steady state MSMPR cooling crystallizations were transferred to the batch cooling crystallization for the organic fine chemical under investigation. Fig.10.9 shows the predicted and experimental mass crystal size distributions, whereby the predicted crystal size distribution is underestimated with an overestimated mean particle size. Nucleation events in unseeded batch crystallizations occur at different levels of supersaturation due to the variable metastable zone width, which depends on the cooling, agitation rate, thermodynamics and impurity levels. Another crucial reason for the under prediction of the CSD is that the crystallization kinetic data developed from MSMPR crystallizations have been used to model batch processes. This is a direct result of kinetics having been developed at steady state conditions (constant supersaturation levels) whereas batch processes are transient in nature and the supersaturation is variable with time. The size-dependent growth model developed using Mydlarz and Jones (1993) three parameter exponential model is therefore not suitable for modelling batch cooling crystallization processes. In addition, implementation of a linear cooling profile results in primary nucleation events once the supersolubility limit is exceeded. From MSMPR crystallizations, the contribution of primary nucleation towards the total nucleation kinetic model may

not be significant. In batch cooling crystallizations, where linear cooling profiles are used, primary nucleation events will dominate. However, if a high seed concentration in the batch crystallization is used (to deplete the supersaturation generated as a result of cooling), the supersolubility limit can be avoided and hence primary nucleation is negligible with a linear cooling profile. In this case, secondary nucleation will dominate and therefore the nucleation kinetic model from the MSMPR crystallization will be assumed to be more valid. The model proposed by Jones (2002), should be suitable for developing growth kinetics from steady state MSMPR crystallizations which are transferable to batch crystallization processes.

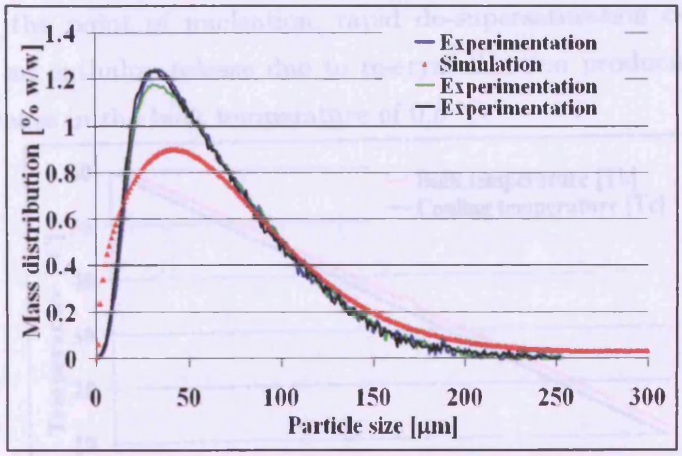

Figure 10.9: *Simulated and experimental mass distributions for laboratory scale 0.5l unseeded batch cooling suspension crystallization.*

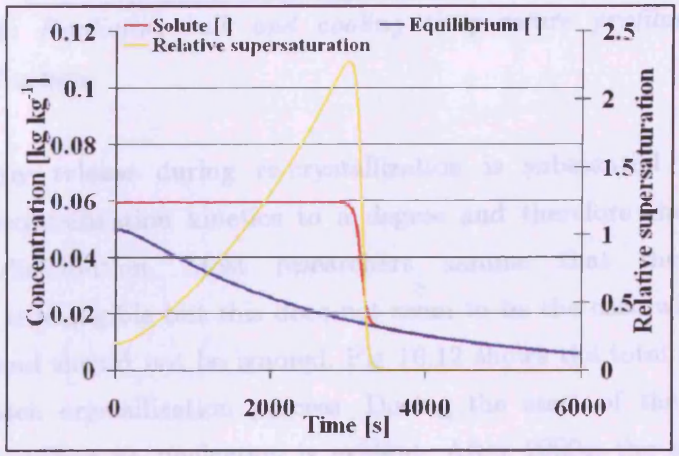

Figure 10.10: *Predicted solute and equilibrium solute concentration profiles including the relative supersaturation profile during unseeded uncontrolled conventional batch cooling suspension crystallization.*

Fig.10.9 also shows that during linear cooling batch cooling crystallizations, which are unseeded, the primary nucleation rate is variable during different experiments resulting in inconsistent particle size distributions. Fig.10.10 shows the generation of supersaturation during cooling. At the onset of primary nucleation and crystal growth, a rapid de-supersaturation occurs. A relative supersaturation spike is produced as a result of linear cooling followed by a rapid decrease as a result of nucleation and crystal growth. Fig.10.11 shows that there is a predicted 1.5 °C discrepancy between the bulk and coolant water temperature based on using an estimated heat transfer coefficient from the Nusselt number correlation. At the point of nucleation, rapid de-supersaturation occurs and also corresponds to an enthalpy release due to re-crystallization producing a small but substantial increase in the bulk temperature of 0.8 °C.

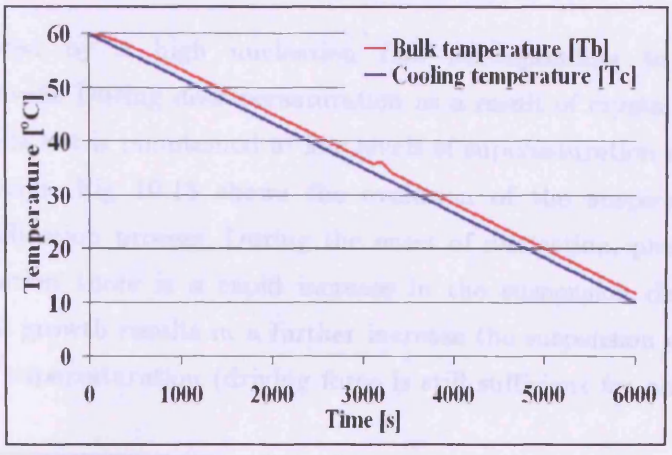

Figure 10.11: *Predictive bulk and cooling temperature profiles during batch cooling crystallization.*

The enthalpy release during re-crystallization is substantial and this may influence the crystallization kinetics to a degree and therefore the final product crystal size distribution. Most researchers assume that the enthalpy of crystallization is negligible but this does not seem to be the case with this organic fine chemical and should not be ignored. Fig 10.12 shows the total nucleation rate during the batch crystallization process. During the start of the batch cooling crystallization process no nucleation is evident. After 2000s, the onset and early stages of nucleation is predicted and is similar to the nucleation process that occurs in reality.

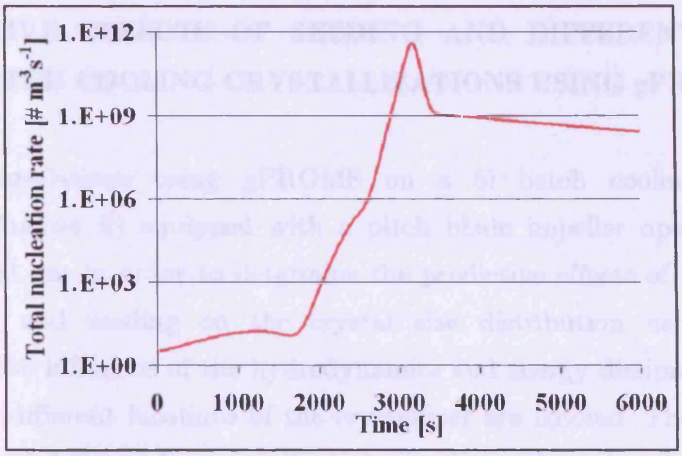

Figure 10.12: *Predicted nucleation rate profile during batch cooling crystallization process.*

This is followed by a high nucleation rate corresponding to a peak in supersaturation levels. During de-supersaturation as a result of crystal growth, the nucleation rate falls but is maintained at low levels of supersaturation as a result of secondary nucleation. Fig 10.13 shows the evolution of the suspension density during the crystallization process. During the onset of nucleation, predicted at 35 °C and crystallization there is a rapid increase in the suspension density. After nucleation, crystal growth results in a further increase the suspension density even at lower levels of supersaturation (driving force is still sufficient for an increase in the yield).

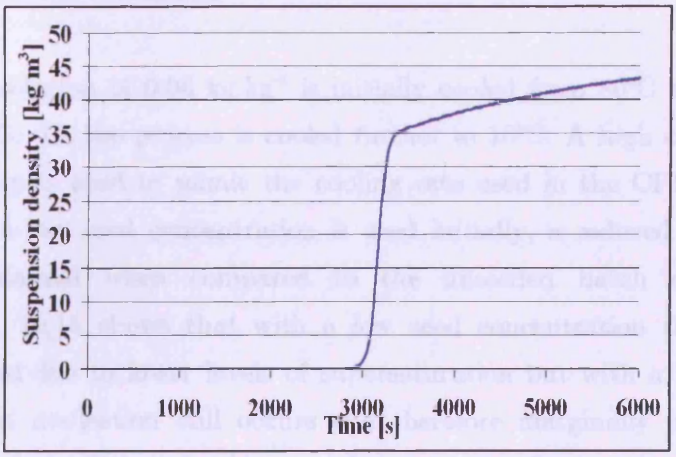

Figure 10.13: *Evolution of the suspension density predicted during the unseeded uncontrolled batch cooling crystallization process.*

10.6 PREDICTIVE EFFECTS OF SEEDING AND DIFFERENT COOLING MODES IN BATCH COOLING CRYSTALLIZATIONS USING gPROMS

Predictive simulations using gPROMS on a 5l batch cooling crystallizer (described in Chapter 8) equipped with a pitch blade impeller operating at 300 rpm were carried out in order to determine the predictive effects of linear cooling, natural cooling and seeding on the crystal size distribution using a lumped description i.e. the influence of the hydrodynamics and energy dissipation including heat transfer in different locations of the crystallizer are ignored. The use of a flat blade impeller and different linear cooling rates is also evaluated and predicted.

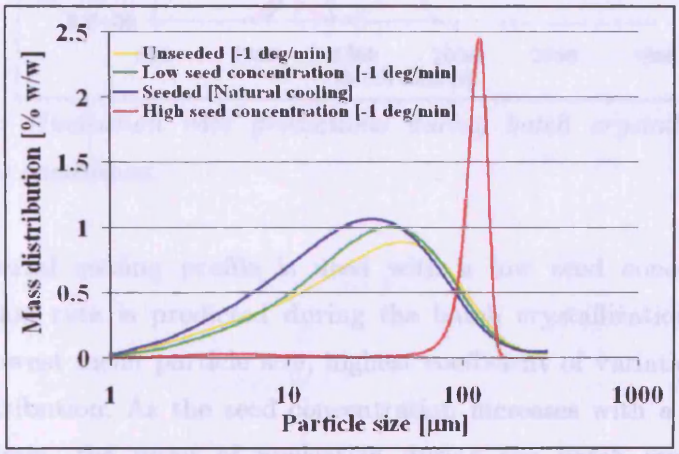

Figure 10.14: *Crystal size distributions predicted during batch crystallizations using different process conditions.*

A saturated solution of 0.06 $kg.kg^{-1}$ is initially cooled from 80°C to 60°C. Once equilibrated at 60 °C, the process is cooled further to 10°C. A high cooling rate of rate of –1 °C/min is used to mimic the cooling rate used in the CFD simulations (Chapter 8). If a low seed concentration is used initially, a reduced coefficient of variation is obtained when compared to the unseeded batch crystallization (Fig.10.14). Fig. 10.15 shows that with a low seed concentration the nucleation rate is suppressed due to lower levels of supersaturation but with a linear cooling profile significant nucleation still occurs and therefore marginally better control over particle size is predicted. A wide crystal size distribution is still predicted with a lower mean particle size when using a low seed concentration. However, if a high seed concentration (seed size 5-10 μm) is used, the nucleation rate is suppressed

significantly and therefore the coefficient of variation is significantly reduced giving rise to a tight distribution with an increased mean particle size.

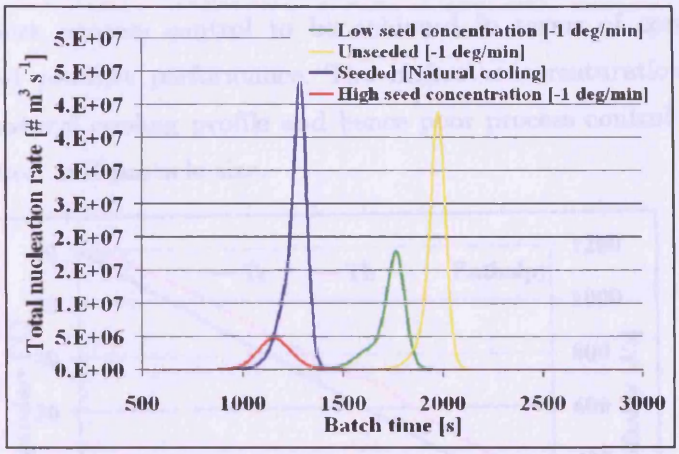

Figure 10.15: *Nucleation rate predictions during batch crystallizations using different process conditions.*

When a natural cooling profile is used with a low seed concentration, the highest nucleation rate is predicted during the batch crystallization process and results in the lowest mean particle size, highest coefficient of variation and widest crystal size distribution. As the seed concentration increases with a linear cooling rate of −1 °C/min, the onset of nucleation during the batch crystallization is predicted sooner. These predictions require validation through experimentation but seem to be consistent with those expected to be obtained experimentally.

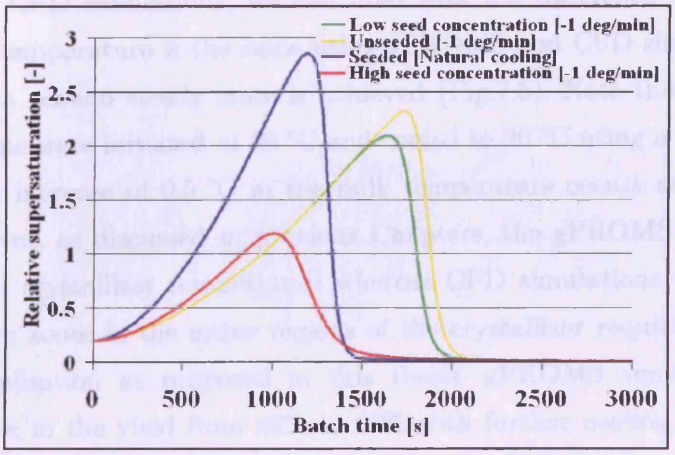

Figure. 10.16: *Relative supersaturation profiles predicted using different process conditions.*

Fig.10.16 shows the predicted supersaturation profiles using different process conditions. As the seed concentration is increased from low to high, the supersaturation levels at which the batch crystallizer is operating at is reduced. This allows for more process control to be achieved in terms of control of the nucleation rate and product performance. The highest supersaturation levels are predicted with a natural cooling profile and hence poor process control is achieved in terms of nucleation and particle size.

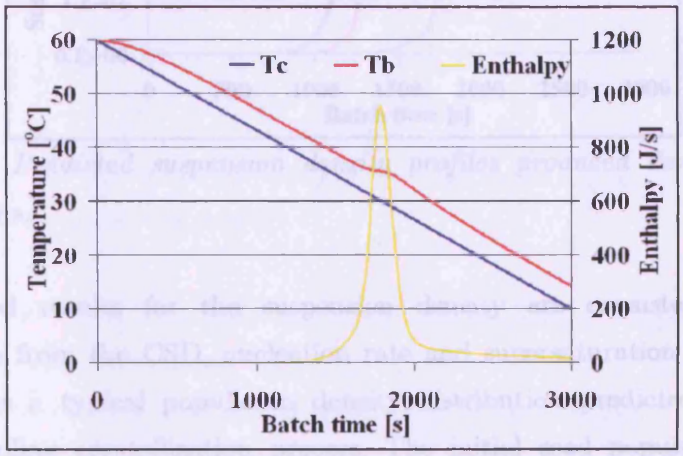

***Figure 10.17**: Temperature distribution and enthalpy release during nucleation (unseeded uncontrolled batch crystallization).*

Fig.10.17 shows the cooling and bulk temperature predictions in the 5l batch crystallizer including the enthalpy release profile predicted as a result of nucleation. From CFD simulations, we can infer that the difference between the bulk and coolant temperature is the same using gPROMS and CFD simulations on the 5l scale once a pseudo steady state is achieved (Fig.7.5). Note that CFD heat transfer simulations were initiated at 80 °C and cooled to 20 °C using a cooling rate of –1 °C/min. An increase of 0.5 °C in the bulk temperature occurs as a result of nucleation. However, as discussed in previous Chapters, the gPROMS simulations assume a uniform crystallizer temperature whereas CFD simulations indicate the presence of cooling zones in the upper regions of the crystallizer requiring the need for compartmentalisation as proposed in this thesis. gPROMS simulations also predict an increase in the yield from 83% to 87% with further cooling to 0°C (low seed concentration with linear cooling), with no change in the crystal size distribution (results not shown).

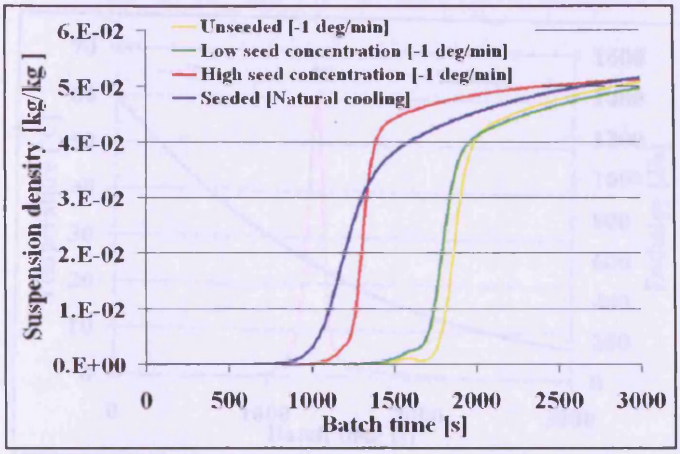

Figure 10.18: *Predicted suspension density profiles produced during different process conditions.*

The predicted results for the suspension density are consistent with the predicted results from the CSD, nucleation rate and supersaturation profiles. Fig. 10.19 also shows a typical population density distribution predicted during the entire batch cooling crystallization process. The initial seed population density distribution [low seed concentration using a linear cooling profile) is shown at time equal to zero. Seed particle sizes up to 10 μm are considered. Once nucleation occurs and subsequent crystal growth a population density distribution with size-dependent growth is predicted as observed in Fig.10.19. Fig.10.18 shows the suspension density for different conditions used.

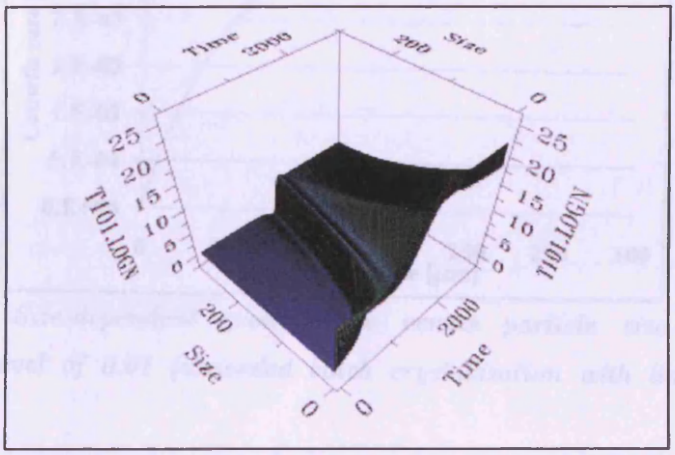

Figure 10.19: *Population density distribution evolution predicted using gPROMS for a low seed concentration using a linear cooling rate.*

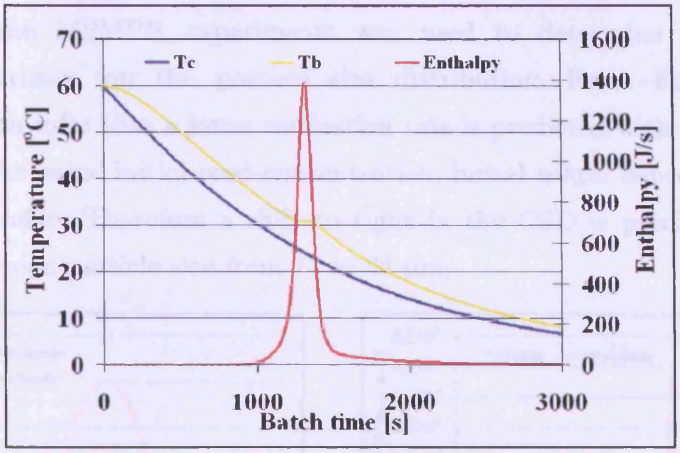

Figure 10.20: *Cooling and bulk temperature profiles predicted including enthalpy release using a natural cooling profile.*

Fig.10.20 shows the cooling and bulk temperature profiles predicted including enthalpy release using a natural cooling profile and Fig.10.21 shows a typical growth rate versus particle size plot at a supersaturation level of 0.01. From the Fig. 10.21 we can clearly see that growth becomes independent at approximately 200 μm and a very low growth rate is evident at such low levels of supersaturation.

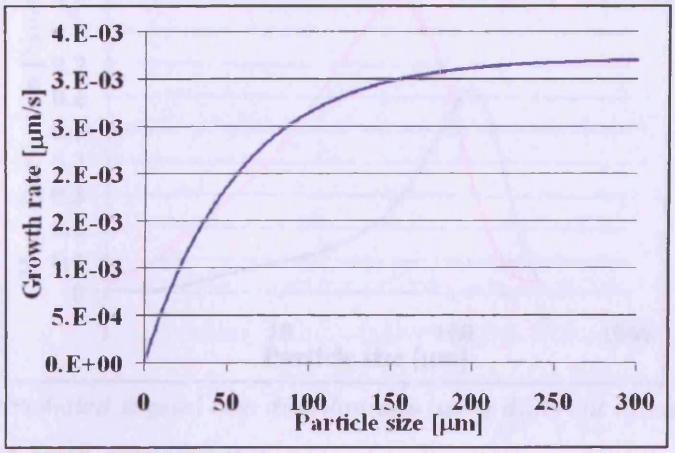

Figure 10.21: *Size-dependent growth rate versus particle size plot at a supersaturation level of 0.01 (unseeded batch crystallization with linear cooling rate).*

In a gPROMS simulation the nucleation rate model developed for a flat blade impeller from the MSMPR experiments was used to determine the effect of impeller configuration on the particle size distribution. From Fig.10.22a and Fig.10.22b we can infer that a lower nucleation rate is predicted with the flat blade impeller using the same initial seed concentration, initial solute concentration and linear cooling profile. Therefore a shift to right in the CSD is predicted with an increase in the mean particle size from 77 to 94 μm.

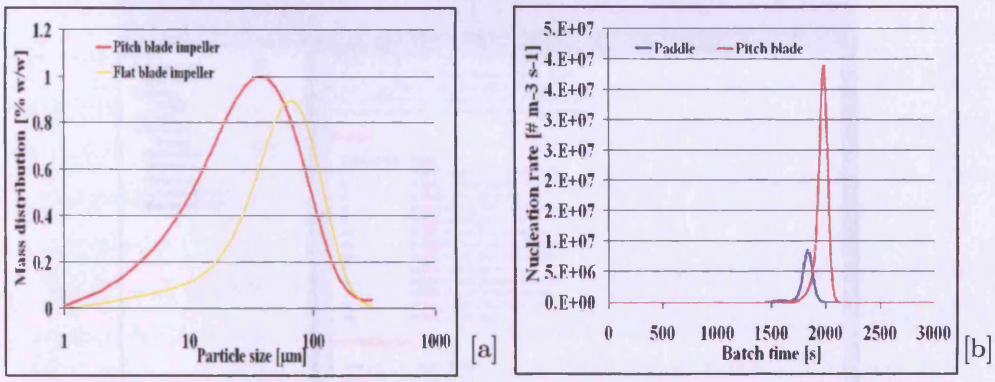

Figure 10.22: *[a] Predicted crystal size distribution [b] Predicted nucleation rate profile.*

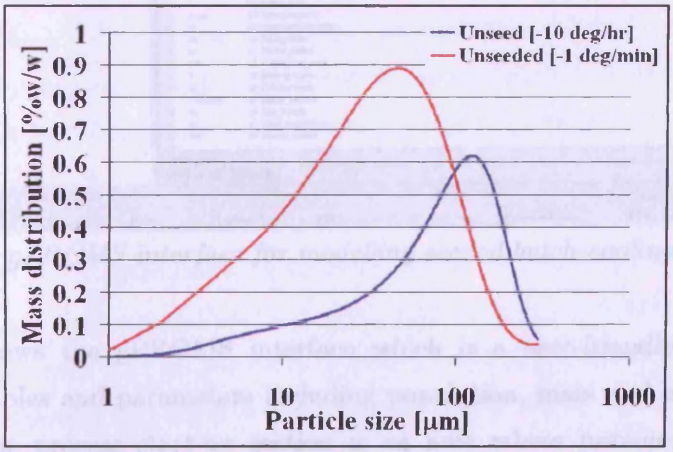

Figure 10.23: *Predicted crystal size distributions using different linear cooling rates for unseeded batch crystallization.*

Using a slower linear cooling rate of –10 °C hr^{-1} results in the predicted formation of particles with a mean particle size of 134 μm compared to 77 μm with

a fast linear cooling ramp of −1 °C min^{-1} for the unseeded batch cooling crystallization process (Fig.10.23).

Finally scale-up gPROMS simulations using a single compartment do not take into account the local conditions that exist within a crystallizer including the influence of scale on the hydrodynamics. Therefore similar CSD and product performances are predicted upon scale-up i.e. from 1-25l scales.

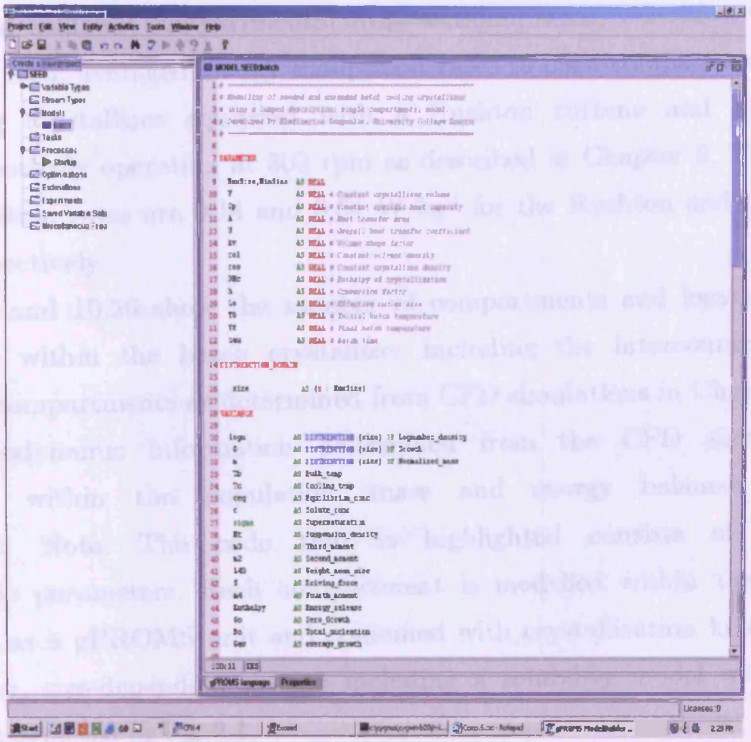

Figure 10.24: *gPROMS interface for modelling seeded batch-cooling crystallizer.*

Fig.10.24 shows the gPROMS interface which is a user-friendly environment where the variables and parameters including population, mass and energy balance are defined. The process start-up section is an area where parameter values are implemented and initial boundary conditions for the conservation equations defined. The gPROMS simulation can be run from this section for the entire batch duration. For higher-level models such as implementation of the batch cooling compartmental modelling framework, streams are used to link one compartment to another and the simulation started within the start-up environment. More user

information about gPROMS and modelling of particulate systems can be found at www.psenterprise.com [Process Systems Enterprise Ltd].

10.7 gPROMS COMPARTMENTAL MODELLING

Tables 10.2-10.5 list hydrodynamic information estimated from predictive CFD simulations based on the crystallizer physical dimensions and includes compartmental volumes, compartmental cross-sectional areas, velocities, volumetric flowrates and local averaged energy dissipation rates in each compartment for a 5l batch cooling crystallizer equipped with a Rushton turbine and pitch blade impeller respectively operating at 300 rpm as described in Chapter 8. The average energy dissipation rates are 0.14 and 0.04 W kg^{-1} for the Rushton and pitch blade impellers respectively.

Fig. 10.25 and 10.26 show the number of compartments and location of each compartment within the batch crystallizer including the interconnecting flows between the compartments as determined from CFD simulations in Chapter 9.

The hydrodynamic information determined from the CFD simulations is implemented within the population, mass and energy balances for each compartment. Note: The code that is highlighted consists of the CFD hydrodynamic parameters. Each compartment is modelled within the gPROMS environment as a gPROMS unit and combined with crystallization kinetic models for nucleation, size-dependent growth including a solubility model with physical properties as depicted in Fig 9.1

A sample gPROMS source code describing the first compartmental unit for the batch cooling suspension crystallizer equipped with a Rushton turbine impeller can be found in Appendix I.1. In addition to this source an abstract containing the source code describing the sixth compartment, which contains a size-dependent classification function within the population balance can be found in Appendix I.2. Note only the equations describing the population balance with the classification function are shown in this section.

Compartment No.	Volume Fraction [-]	Compartment Volume [L]	Average Volume Energy Dissipation [W/kg]	Normalized Energy dissipation [$\varepsilon_{loc}/\varepsilon_{av}$]
1	0.01	0.05	0.025	0.19
2	0.1	0.48	0.500	3.70
3	0.08	0.41	0.050	0.38
4	0.04	0.21	0.025	0.19
5	0.05	0.23	0.025	0.19
6	0.02	0.1	0.025	0.19
7	0.07	0.37	0.025	0.19
8	0.39	1.95	0.025	0.19
9	0.24	1.20	0.025	0.19

Table 10.2: *Compartment- number, volume & local energy dissipation rate [Rushton].*

Stream No	Velocity [m/s]	Cross-Sectional Area [m^2]	Vol. Flowrate FV[L/s]
1	0.21	2.39e-04	0.05
2	0.95	1.20e-03	1.14
3	0.28	2.07e-03	0.58
4	0.21	1.43e-03	0.30
5	0.28	9.34e-04	0.26
6	0.21	6.24e-04	0.13
7	0.14	9.34e-04	0.13
8	0.14	6.43e-04	0.09
9	0.14	2.14e-04	0.03
10	0.34	2.65e-04	0.01
11	0.21	1.43e-04	0.03
12	0.07	8.29e-04	0.58
13	0.07	8.29e-03	0.58
14	0.14	7.14e-05	0.01
15	0.14	6.21e-03	0.87

Table 10.3: *Streams connecting compartments with velocity, cross-sectional area and volumetric flowrates listed [Rushton turbine operating at 300 rpm].*

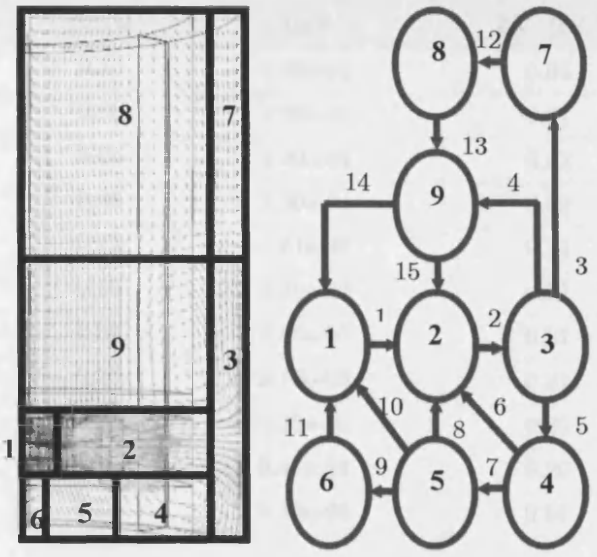

Figure 10.25: *Location of the compartments [a] Interconnecting flow diagram showing streams and compartment numbers [Rushton turbine].*

Compartment No.	Volume Fraction [-]	Compartment Volume [L]	Average Volume Energy Dissipation [W/kg]	Normalized Energy dissipation [$\varepsilon_{loc}/\varepsilon_{av}$]
1	0.08	0.41	0.070	1.84
2	0.07	0.34	0.100	2.63
3	0.22	1.08	0.070	1.84
4	0.11	0.53	0.015	0.39
5	0.01	0.04	0.100	0.26
6	0.03	0.16	0.005	0.13
7	0.49	2.45	0.005	0.13

Table 10.4: *Compartment- number, volume & local energy dissipation rate [Pitch].*

Stream No	Velocity [m/s]	Cross-Sectional Area [m^2]	Vol. Flowrate FV [L/s]
1	0.13	2.39e-04	0.03
2	0.60	1.20e-03	0.21
3	0.05	3.00e-04	0.02
4	0.05	3.00e-04	0.02
5	0.13	1.61e-03	0.21
6	0.15	3.40e-03	0.51
7	0.03	8.40e-03	0.21
8	0.05	2.10e-03	0.21
9	0.21	7.28e-05	0.02
10	0.21	9.47e-04	0.20
11	0.15	3.40e-03	0.51

Table 10.4: *Streams connecting compartments with velocity, cross-sectional area and volumetric flowrates listed [Pitch blade impeller operating at 300 rpm].*

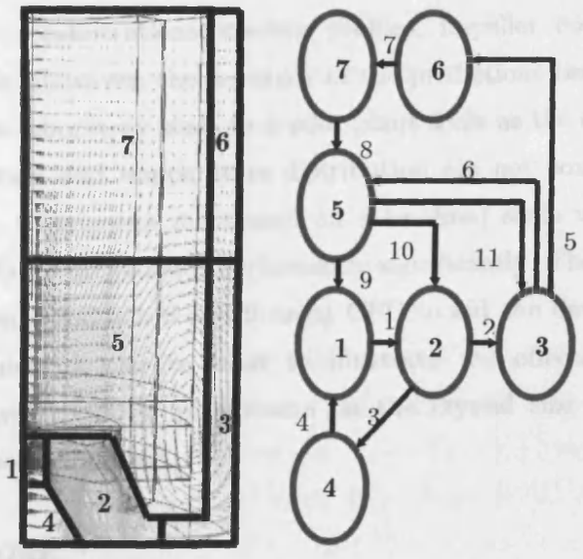

[a] [b]

Figure 10.26: *Location of the compartments [a] Interconnecting flow diagram showing streams and compartment numbers [Pitch blade impeller].*

For size-dependent classification modelling, the MinSize is estimated to be 50μm. This was based on predictive CFD simulations carried out using different monodisperse particle sizes up to 300 μm. CFD predictions showed that a suspension was uniformly mixed for particle sizes up to 50 μm (results not shown in Fig.8.17). Fig. 8.17 shows the solids distribution for different monodisperse particle sizes to include 100 μm, 200 μm and 300 μm using a fixed solids concentration. This suggests that particles less than 50 μm are not subject to classification effects within the batch cooling crystallizer. The extent of classification also depends on the liquid velocity leaving a source compartment and entering a target compartment. As the agitator speed increases the need for a classification function is also eliminated.

10.8 CONCLUSIONS

The gPROMS simulations based on a single compartment using a lumped description gives a good indication of the crystallization behaviour on a laboratory scale for a continuous MSMPR crystallizer and batch cooling crystallizer based on using different seed concentrations, cooling profiles, impeller configurations and mean residence times. However, the accuracy of the predictions becomes important upon scale-up from a laboratory scale to a pilot plant scale as the effects of mixing, local energy dissipation and temperature distribution are not considered as all of these hydrodynamic phenomena mentioned on a localized scale will influence the crystal size distribution and product performance significantly. The compartmental model developed from Chapters 8 and 9 using CFD to aid the development of the compartmental framework can be used to illustrate the effects of taking into account localised hydrodynamic phenomena on the crystal size distribution and product performance as discussed.

10.9 FURTHER WORK

Firstly, validation experiments will be necessary in order to confirm the results obtained on a 0.5l batch cooling crystallizer scale. The parameters that need to be monitored on-line include the supersaturation levels using ATR-UV/FTIR

spectroscopy and the turbidity, such that the supersaturation and suspension density profiles predicted using gPROMS and then compared to experimentation. Furthermore, experimentation to determine the CSD on a 1l, 5l and 25l scale based on the CFD crystallizer configurations used in Chapter 7 and 8 will be necessary using the process and operating conditions that were implemented during the gPROMS simulations.

In this thesis, the foundations for the novel predictive compartmental modelling framework has been developed and implemented within the gPROMS environment. The key milestones achieved are in the development of key process engineering information on a laboratory scale, which is critical for the predictive scale-up of organic crystallization processes. This includes kinetics, physical properties and thermodynamics. CFD is also used to develop the novel compartmental modelling framework for seeded batch cooling suspension crystallization processes and finally the effects of mixing and heat transfer upon scale-up were also investigated. However, to achieve a fully working predictive compartmental model for seeded batch cooling crystallizers, this will require further development work, which could not be carried out within the time frame available. In the next section, a detailed methodology for further work to be carried out in order to link up the individual gPROMS compartments, which have been fully coded as described in Appendix I.1. and I.2 will be discussed.

The individual gPROMS compartments consist of conservation equations for mass, energy and the population of particles and need to be defined in the process start-up section using a high level programming approach within the gPROMS environment. This will require that the parameters such as physical properties, compartmental volume, volumetric flowrates and energy dissipation rates be defined (as listed in Appendix I.1) for each individual gPROMS compartment within the process start-up section of gPROMS. The source code has been colour coded to indicate the parameters that are implemented from CFD simulations. The compartmental volume is indicated in green, the interconnecting flowrates based on the flow velocities and cross-sectional areas in yellow and finally the local energy dissipation rates in red.

The critical programming function within gPROMS will involve linking the compartments via streams within each individual gPROMS compartment. The code for the STREAMS section has been omitted in Appendix I.1.

The streams define the input and output of crystal population, concentration and temperature from the source compartments which are the fifth, sixth and ninth respectively and the exiting compartment, which is the first compartment. The code from the streams section of each individual gPROMS compartment must then be linked to the start-up section whereby each gPROMS unit is defined in terms of setting and assigning values for parameters, initial boundary conditions and batch time over which the simulation is to run.

Within each compartment in the process start-up section, the initial boundary conditions are defined with respect to the initial solute concentration, initial crystal size distribution and initial temperature.

Based on the predictive CFD simulations using seed particles, a uniform particle size distribution of seed particles is assumed within the batch cooling crystallizer and hence within each individual gPROMS compartment. Furthermore, the initial solute concentration within each gPROMS compartment will also be assumed to be uniform within the crystallizer although this may not be the case in reality within a batch cooling crystallizer particularly on a 1500l pilot scale used at GlaxoSmithKline pharmaceuticals. CFD predictive simulations have shown that there are also cooling zones evident during cooling. The cooling zones correspond to compartments 7 and 6 for a Rushton turbine and pitch blade impeller respectively. In these compartments a predicted temperature difference of approximately 0.2°C and 0.4 °C exists when compared to the other compartments. Therefore this will be taken into account when specifying the initial boundary conditions for the temperature within each gPROMS compartment.

The gPROMS compartmental modelling aspect presented does not consider the implementation of the attrition rate model developed in Chapter 6 within the population balance for each individual gPROMS compartment. Furthermore, since the compartmental modelling framework presented in Chapter 9 is generic for suspension crystallization processes, an agglomeration model can also be introduced

within the population balance for organic fine chemicals exhibiting size-dependent or independent agglomeration. This will have the effect of increasing the complexity of the compartmental model within gPROMS.

Recommendations

This section highlights areas that merit a closer examination for further research and development based on the results presented in this thesis.

It is recommended that there be a continued drive and investment in the development of a design or 'predictive' and robust scale-up tool, which allows interfacing between heuristic and rigorous models and additionally guides the user through a process design procedure within an expert environment. This will necessitate the design, development and supply of a reliable and robust generic crystallization software package. Urban and Liberis (1999) at Process Systems Enterprise Ltd using gPROMS have made an important step in this direction with respect to combining heuristics and rigorous predictive models by developing a hybrid gPROMS/CFD interface for dynamic isothermal draft tube crystallizers. The interface is based on viscosity and density properties (mother liquor) being implemented within the CFD environment to mimic the dynamic crystallization process is modeled producing an output result with respect to refinement in the mean time averaged flow rates and local volume energy dissipation rates at different time intervals. In addition to this approach being recommended, it is also proposed that a heat transfer coefficient model as a function of temperature be developed through experimentation for different crystallizer designs and impeller configurations. The drawback associated with this method (Urban and Liberis, 1999) is that the compartmental modelling framework is only based on a 'single-phase' only and does include the effects of the solid phase particles on the development of the compartmental modelling framework. The density difference between the solid and liquid phase and hence the need for a classification function is ignored as a homogeneous liquid taking account of the presence of solid indirectly through a suitable adjustment of the transport properties of the bulk fluid is used. This is necessarily applicable to organic fine chemicals with moderate solubility characteristics and low bulk densities. CFD simulations in this research predicted that with the crystallization system studied, the impeller frequency and particle size influences the incorporation of a classification function even for dilute suspensions. The compartmental modelling framework presented in this thesis

does allow for the use of a generic classification function. Other aspects of the crystallisation process-modelling framework that require further attention are related to physical properties and hydrodynamics. With respect to the hydrodynamics, it is recommended to explore the use of automatic zoning techniques (Bezzo et al., 2004) for setting up compartmental models, as the current procedure for constructing these models is largely heuristic. In the future, as computational technology improves and process modelling and CFD packages evolve and converge, the choice between a compartmental modelling and CFD approach with the full population balance should be reconsidered. The effect of suspension density and particle size on the velocity profiles has to be modeled and implemented within the compartmental modelling framework. The compartmental volumes in reality will change as a result of particle growth and settling effects, particularly in the upper region where it is possible that a clear mother liquor region will develop as the seed particles grow. This will be especially prominent in high solids contents systems with large particle sizes. The effect of temperature on the mother liquor viscosity, density and specific heat capacity must be also evaluated because these physical properties influence the crystallization process performance and kinetics (growth) significantly.

Further improvements will be necessary in terms of developing reliable crystallization kinetic models from first principles. The Gahn kinetic model (Gahn and Mersmann, 1999a and1999b) is the most advanced as it is based on both material and physical properties to model crystal attrition, nucleation and growth. The crystallization kinetic models developed in this research are mostly empirical and determined from a laboratory scale MSMPR crystallizer. A major limitation is that the kinetics for growth determined in this research cannot reliably be transferred from a continuous to a batch process. It is therefore suggested to develop crystallization kinetics for growth rate dispersion and primary nucleation through batch cooling crystallization experiments. The growth rate dispersion implies that each crystal has its own intrinsic growth rate and is related to the internal strain of a crystal. Additionally, the effects of seeding and seed concentration on the batch crystallization could be valuable for process development and implementation within the compartmental modelling framework. The effects of temperature on the growth rate coefficient and determination of the activation energy will be necessary. Furthermore, the type of cooling regime

employed will affect not only the rate of nucleation but also the type of nucleation i.e. primary or secondary nucleation. The development of optimal cooling profiles (Jones, 1973) to maintain constant supersaturation levels eliminates the need for a primary nucleation model and hence secondary nucleation is expected to dominate. This can be achieved using ATR-UV spectroscopy (in-situ) by design of a control strategy using a feedback control loop whereby the temperature of a crystallizer is altered to control the supersaturation levels within a batch crystallizer.

The CFD simulations predicting mean time averaged flow rates, local energy dissipation rates including temperature and solid distributions must all be validated through experimentation and further development and optimisation of the models implemented within the CFD environment is necessary.

The effects of impurities (solvent or foreign compounds) on the solubility characteristics and crystallization kinetics must also be taken into account within the compartmental modelling framework. The reason for this is that if the feed impurity concentration from different batches (synthetic step) used in the final purification step is variable this will influence the crystal size distribution, product performance due to different nucleation and growth kinetics. The purity of the particles (Appendix H) can also be affected as a result of incorporation of impurities within the unit cell.

Finally the predictive compartment simulation model must be validated extensively. Once this important milestone is achieved process design and optimisation investigations will need to be performed. This should result in substantial operational and economic benefits. For instance, the need for dry milling may be eliminated within the manufacturing stage prior to formulation. In addition, for the ability of the model to predict the variation of key process conditions in localised areas that affect the crystallization kinetics over the entire batch process it may also be useful in locating areas in the crystallizer where local conditions could favour the formation of different crystal forms (crystal habit/polymorphism) or encrustation. The problematic regions can be identified and the hybrid model used to determine the best operating policy for the crystallizers.

References

Al-Rashed, M.H., and Jones, A.G., (1999). CFD modelling of gas-liquid reactive precipitation. *Chem. Eng. Sci.,* 54, **21**, 4770-4784.

Abegg, C.F., Stevens, J.D., and Larson, M.A., (1968). Crystal Size Distributions in Continuous Crystallizers when Growth Rate is Size-dependent. *AIChE J.*, **14(1)**, 118-122.

Allen, T. (1981). *Particle Size Measurement.* 3rd edition. Chapman and Hall.

Alexopoulos, A.H., Maggiorios, D., and Kiparissides, C., (2002). CFD analysis of turbulence non-homogeneity in mixing vessels: A two-compartment model. *Chem. Eng. Sci., 57,* **10**, 1735-1752.

Austin, L., Shoji, V., Jindal, V., Savage, K. and Kimpel, R. (1976). Some results on the description of size reduction as a rate process in various mills. *Ind. Eng. Chem. Process Des. Dev.*, **15**, 187-196.

Baldyga, J. and Bourne, J.R. (1992). Interactions between mixing on various scales in a stirred tank reactor. *Chem. Eng. Sci.*, **47**, 1839-1848.

Barrett, P., Glennon, B. and O'Sullivan, B. (2002). Solubility Curve and Metastable Zone Width Using Lasentec FBRM and PVM. *Lasentec Technical Paper.*

Barrett, P., and Glennon. B., (1999). In-line FBRM monitoring of particle size in dilute agitated suspensions. *Part. Sys. Charact.,* **16(5)**, 207-211.

Barton, P.I. and Pantelides, C.C., (1994). The modelling of combined discrete/continuous processes. *AIChE J.*, **40**, 966-979.

Bamforth, A.W. (1965). *Industrial crystallization*. Leonard Hill, UK.

Beiny, D.H.M. and Mullin, J.W., (1987). Solubilities of higher normal alkanes in m-xylene, *J. Chem. Eng. Data*, **32**, 9-10.

Bennett, R.C. (1984). Crystallization from solution. In D.W. Green and J.O. Maloney (Ed.), *Perry's Chemical Engineer's Handbook*, 6th ed., McGraw- Hill, New York, USA, chapter 19, pp. 25-40.

Bennett, R.C. (1993). Crystallizer selection and design. In A.S. Myerson (Ed.), *Handbook of Industrial Crystallization*, Butterworth-Heinemann, Boston, USA.

Berglund, K.A., (1980). Summary of recent research on growth rate dispersion of contact nuclei. *Chem. Eng. Commun.* **41**, 357-360.

Berglund, K.A. and Larson, M.A., (1984). Modeling of growth rate dispersion of citric acid monohydrate in continuous crystallizers. *AIChE J.*, **30**, 280–287.

Bermingham, S.K., (2003). A design procedure and predictive models for solution crystallization applications. PhD thesis. Delft University. The Netherlands.

Bermingham, S.K., Kramer, H.J.M., van Rosmalen, G.M., (1998). Towards on-scale crystallizer design using compartmental models, *Computers Chem. Eng.*, **22**, S355-362.

Berry, D.A. and Ng, K.M., (1997). Synthesis of reactive crystallization processes. *AIChE J.*, **43**, 1737-1750.

Berthoud, A., (1912). Theorie de la formation des faces d'un crystal. *Journal de Chemique Physique*, **10**, 624-635.

Bezzo, F., Macchietto, S., Pantelides, C.C., (2004). A general methodology for hybrid multizonal/CFD models: Part I. Theoretical framework. *Computers Chem. Eng.*, **28**, 4, 501-511.

Bezzo, F., Macchietto, S., Pantelides, C.C., (2004). A general methodology for hybrid multizonal/CFD models: Part II. Automatic zoning. *Computers Chem. Eng.*, **28**, 4, 513-525.

Bisio, A. and Kabel, R.L., (1985). *Scale-up of Chemical Processes: Conversion from Laboratory Scale Tests to successful Commercial Size Design.* Wiley, New York.

Bransom, S.H., (1960). Factors in the design of continuous crystallizers, *Brit. Chem. Eng.*, **5**, 838-844.

Brucato, A., Grisafi, F. and Montante, G., (1998). Particle drag coefficients in turbulent fluids, *Chem. Eng. Sci.*, **53**, 3295-3314.

Brucato, A., Ciofalo, M., Grisafi, F and Micale, G., (1998). Numerical prediction of flow fields in baffled stirred vessels: A comparison of alternative modelling approaches. *Chem. Eng. Sci.*, **53**, 3653-3684.

Brucato, A., Ciofalo, M., Grisfali, F. and Tocco, R., (2000). On the simulation of stirred tank reactors via computational fluid dynamics. *Chem Eng. Sci.*, **55**, 291-302.

Buckley, H.E., (1952). *Crystal growth*, Chapman and Hall, London.

Burton, W.K., Cabrera, N. and Frank, F.C., (1951). The growth of crystals and the equilibrium structure of their surfaces. Royal Society of London *Philosophical transactions,* **A243,** 299-358.

Carreta, M.K. and Liebel, J.M., (2000). *Crystal Size Distribution Control during Batch Cooling Crystallization*, Lasentec Technical Papers.

Canning, T.F., and Randolph, A.D., (1967). Some Aspects of Crystallization Theory: Systems that Violate McCabe's ΔL law, *AIChE J.*, **13**, 5-13.

Chatfield, C. and Collins A.J., (1980). Introduction to Multivariate Analysis, Chapman & Hall, London, New York, ISBN 0-412-16040-4.

Chen, M.R., and Larson, M.A., (1985). Crystallization Kinetics of Calcium Nitrate Tetrahydrate from MSMPR crystallizer. *Chem. Eng. Sci.*, **40** (7), 1267-1294.

Chernov, A.A., (1989). Formation of crystals in solution. *Contemporary Physics,* **30**, 251-276.

Clift, R., Grace, J.R., and Weber, M.E., (1978). Bubbles, Drops and Particles, (*Academic Press, London*).

Daudey, P.J., van Rosmalen, G.M. and de Jong, E.I., (1990). Secondary nucleation kinetics of ammonium sulphate in a CMSMPR crystallizer, *J. Crystal Growth,* **99,** 1076-1081.

Daudey, P.J., Brouwer, D.B., and Wienk, B.G., (1993). A simple two-zone model of an NaCl evaporator for the analysis of the spatial distribution of crystals and the supersaturation measured from CSDs, in: J.Ulrich, O.S.L. Bruinsma (Eds.), Proc. D+BIWIV Int. Workshop Ins. Cryst. 18-26.

De Jong, E.J., (1984). The one or the other. In S.J. Jancic and E.J. de Jong (Ed.), *Industrial Crystallization 84*, Elsevier Science Publishers B.V., Amsterdam, The Netherlands, p. 177-184.

Derdour, L., Feroutte, G., Peul, F., and Ceurin, P., (2003). Real-time evaluation of concentration of impurities during organic solution crystallization. *Powder Technology,* **129**, 1-7.

Douglas, J.M., (1985). A hierarchical decision procedure for process synthesis. *AIChE J.*, **31**, 353-362.

Dunuwila, D.D., Caroll, L.B. and Berglund, K.A., (1994). An investigation of the applicability of attenuated total reflection infrared spectroscopy for measurement of solubility and supersaturation of aqueous citric acid solutions. *J. Crystal Growth,* **137**, 561–568.

Dunuwila, D., (1996a). An investigation of the feasibility of using in situ ATR FTIR spectroscopy in the measurement of crystallization phenomena for research and development of batch crystallization processes. *Dissertation*, Michigan State University, Department of Chemical Engineering.

Dunuwila, D., & Berglund, K. A., (1996b). ATR FTIR spectroscopy for *in situ* analysis of crystallization. *Proceedings of the 13th symposium on industrial crystallization*, Toulouse.

Dunuwila, D. and Berglund, K.A., (1997). ATR FTIR spectroscopy for *in situ* measurement of supersaturation. *J. Crystal Growth*, **179**, 185–193.

Dye, S.R. and Ng, K.M., (1995). Fractional crystallization: design alternatives and tradeoffs. *AIChE J.*, **41**, 2427-2438.

Eek, R.A., Dijkstra, S., van Rosmalen, G.M., (1993). Dynamic modeling of suspension crystallizers, using experimental process data. *AIChE J.*, **41**(3), 1-14.

Gahn, C. and Mersmann, A., (1997). Theoretical prediction and experimental determination of attrition rates. *Trans IChemE.*, **75(A)**, 125-131.

Gahn, C. and Mersmann, A., (1999a). Brittle fracture in crystallisation processes. Part A. Attrition and abrasion of brittle solids. *Chem Eng. Sci.*, **54**, 1273-1282.

Gahn, C. and Mersmann, A., (1999b). Brittle fracture in crystallisation processes. Part B. Growth of fragments and scale-up of suspension crystallizers. *Chem Eng. Sci.*, **54**, 1283-1292.

Garside, J., Mullin, J.W., and Sha, S.N., (1974). Growth and dissolution kinetics of Potassium Sulphate Crystals in an agitated vessel. *Ind. Eng. Chem. Fundam.* **13**, 299-305.

Garside, J., Philips, A.V., and Shah, M.B., (1976). On Size-dependent Crystal Growth, *Ind. Eng. Chem. Fundam.*, **15**(3), 230-233.

Garside, J. and Larson, M.A., (1978). Direct observation of secondary nuclei production. *J. Crystal Growth*, **43**, 694-704.

Garside, J and Jancic, S.J., (1979). Measurement and scale-up of secondary nuclei production for the potash alum-water system. *AIChE J.*, **25** (6), 948-958.

Garside, J. and Davey, R.J., (1980). Secondary contact nucleation: kinetics, growth and scale-up. *Chem. Eng. Commun.*, **4**, 393-424.

Geladi, P., (1988). Notes on the history and nature of partial least squares (PLS) modelling. *J. Chemometrics.* **2**, 231-240.

Gerla, J.H., Kramer, H.J.M., Van Rosmalen, G.M., Scarlett, B., (1993). First approach of the implementation of hydrodynamics in the modeling of industrial crystallizers, in: Rojkowski, Z.H. (Ed.), *Proc. 12th Symp. Ind. Cryst.* 4-29-4-34.

Groen, H and Roberts K.J., (1999). Proceedings of the Fifth International Workshop on the Crystal Growth of Organic Materials (CGOM-5); *IChemE,* Cambridge, UK, ISBN 0 85295 4247.

Groen, H., Borissova, A. and Roberts. K.J., (2003). In-process ATR-FTIR spectroscopy for closed loop supersaturation control of a batch crystallizer producing monosodium glutamate crystals of defined size. *Ind. Eng. Chem. Res.* **42(1)**, 198-206.

Groen, H. and Roberts. K.J., (2004). An examination of the crystallization of urea from supersaturated aqueous-methanol solution using in-process ATR-FTIR spectroscopy. *Cryst. Growth Des.* **4**, 929.

Grootscholten, P.A.M., and Jancic, S.J., (1984). In S.J. Jancic and E.J. de Jong (Ed.), *Industrial Crystallization 84*, Elsevier Science Publishers B.V., Amsterdam, The Netherlands.

Halfon, A., and Kaliaguine, S., (1976). Alumina trihydrate crystallisation. Part 2. A model of agglomeration. *Can. J. Chem. Engng.* **54**, 168-172.

Halfon, A., and Kaliaguine, S., (1976). Alumina trihydrate crystallisation. Part 1. Secondary nucleation and growth rate kinetics. *Can. J. Chem. Engng.* **54**, 168-172.

Harnby, N., Edwards, M. F., Nienow, A. W., (1992). Mixing in the Process Industries. 2ND Edition. Butterworth-Heinemann.

Hinze, J.O., (1975). Turbulence, 2nd Edition., McGraw-Hill, New York.

Hlozny, L., Sato, A., Kubota, N., (1992). On-line measurement of supersaturation during batch cooling crystallization of ammonium alum *J. Chem. Eng. Jpn.* **5**, 604-606.

Höskuldsson, A., (1988). PLS regression models *J. Chemometrics,* **2,** 211-228.

Ilievski, D., (2001). Development of a Constant Supersaturation, Semi-batch Crystallizer and its Application to Investigating Crystal Agglomeration. *J. Crystal Growth,* **233**, 846-862.

Jager, J., de Wolf, S., Kramer, H.J.M., Scarlett, B., and de Jong, E.J., (1991). The effect of the scale of operation on CSD dynamics in evaporative crystallizers. *AIChE J.*, **37**, 182-192.

Janse, A.H., and E.J. de Jong., (1976). The occurrence of growth rate dispersion and its Consequences, in *Industrial Crystallization,* J.W. Mullin, Ed., Plenum, New York, 145.

Jaworski, Z., and Nienow, A.W., (2003). CFD modelling of continuous precipitation of barium sulphate in a stirred tank. *Chem. Eng. J.,* **2-3**, 167-174.

Jennings, K. H., Hardy, M. M. J. and Wilkinson, M. J., (2000). *Microsc. Microanal.* 6 (Suppl. 2 Proceedings) 996-997, Microscopy Society of America.

Jones, A.G., (1974). Optimal operation of a batch cooling crystallizer. *Chem. Eng. Sci.*, **29**, 1075-1087.

Jones, A.G. and Mullin, J.W., (1974). Programmed Cooling Crystallization of Potassium Sulphate Solutions. *Chem. Eng. Sci.*, **29**, 105-118.

Jones, A.G., (1972). Programmed Cooling Crystallization of Potassium Sulphate Solutions. *PhD thesis,* University College London, UK.

Jones, A.G., Budz, J., and Mullin, J.W., (1986). Crystallization kinetics of potassium sulphate in an MSMPR agitated vessel. *AIChE J.*, **32**(12), 2002-2009.

Jones, C.M. and Larson, M.A., (1999). Stochastic modelling and control of particle size in crystallization of pharmaceutical. University of Wisconsin.

Jones, C.M., (2002). Using Discrete Distributions to Analyze CSD data from MSMPR Crystallizers. *AIChE J.*, **48** (7) 1448-1456.

Kossel, W., (1934). Zur Energetik von Oberflachenvorgangen. *Annalen der Physik*, **21.**

Kramer, H.J.M., O'Meadhra, R.S., Neumann, A.M. and van Rosmalen, G.M., (1996). Scale-up of ammonium sulphate crystallization in a DTB crystallizer. *Industrial Crystallization 1996*, Toulouse, 619-625.

Kramer, H.J.M., Dijkstra, J.W., Verheijden, P.J.T and van Rosmalen, G.M., (2000). Modeling of industrial crystallizers for control and design purposes. *Powder Technology*, **108**, 185-191.

Kramer, H.J.M., Bermingham, S.K. and van Rosmalen, G.M., (1999). Design of industrial crystallizers for a given product quality. *J. Crystal Growth*, **198/199**, 729-737.

Kuipers, J.A.M. and Swaaij, W.P.M., (1997). Application of computational fluid dynamics to chemical reaction engineering. *Reviews in Chem. Eng.*, **13**, 1-110.

Kumar, S. and Ramkrishna, D., (1996a). On the solution of population balance by discretization I. A fixed pivot technique, *Chem. Eng. Sci.*, **51**, 1311-1332.

Kumar, S and Ramkrishna, D., (1996b). On the solution of population balance by discretization II. A fixed pivot technique, *Chem. Eng. Sci.*, **51**, 1333-1342.

Lane, G.L. and Schwarz, M.P., (1999). CFD Modelling of gas-liquid flow in stirred tank, *Chemeca* '99, Newcastle, Australia.

Lapidus, L. and Pinder, G.F., (1982). *Numerical solution of partial differential equations in science and engineering*, Wiley, New York, USA.

Launder, B.E. and Spalding, D.B., (1974). The numerical computation of turbulent flows. *Computer Methods in Applied Mechanics and Engineering*, **3**, 269-289.

Lewiner, F., Klein, J.P., Puel, F., Conesa, F. and Fevotte, G., (2001). On-line ATR-FTIR measurement during solution crystallization process. Calibration and applications on three solute/solvent systems. *Chem. Eng. Sci.,* **56**(6), *2069-2084.*

Lewis, B., (1980). Nucleation and growth theory. *In Crystal growth,* 2nd edition., B.R. Pamplin (ed). Pergamon Press, Oxford, 23-63.

Liiri, M., Koiranen, Tuomas, A., and Aittamaa, J., (2002). Secondary nucleation due to crystal-impeller and crystal-vessel collisions by population balances in CFD-modelling. *J. Crystal Growth*, **237-239**, 2188-2193.

Magelli, F., Fajner, D., Nocentini, M., and Pasquali, G., (1990). Solid distribution in vessels stirred with multiple impellers. *Chem. Eng. Sci.*, **45**, 615-625.

Manninen, M. and Syräjnen, J., (1998). Modelling turbulent flow in stirred tanks. *CFX Update*, **16,** 10-11.

Mazarotta, B., (1992). Abrasion and breakage phenomena in agitated crystal suspensions. *Chem. Eng. Sci.*, **47** (12), 3105-3111.

McCabe, W.L., (1929). Crystal growth in aqueous solutions. *Ind. Eng. Chem.*, **21**, 112-129.

Mersmann, A. (1995). Fundamentals of Crystallization. In A. Mersmann (Ed.), *Crystallization Technology Handbook*, Marcel Dekker, New York, USA. pp. 1-78.

Mersmann, A. (1988). Design of crystallizers. *Chem. Eng. Process.*, **23**, 213-228.

Micale, G., Montante G., Magelli, F. and Brucato, A., (2001). Experiments and CFD predictions of solid particle distribution in a vessel agitated with four pitch blade turbines, *Trans IChemE*, **79**, (A8), 1005-1010.

Micale, G., Montante G., Magelli, F. and Brucato, A., (2000). CFD simulation of particle distribution in a multi-impeller high aspect ratio stirred vessel, *10th European conference on mixing.* 125-132, Delft, The Netherlands.

Micale, G., Ciofalo, M., Grisfali, F., Magelli, F. and Micale, G., (1997). On the simulation of solid particle distribution in multi-impeller agitated tanks via Computational fluid dynamics, *AIDIC Conference series*, **2.**

Micale, G., Montante, G., Grisafi, F., Brucato, A., and Godfrey, J., (2000). CFD simulation of particle distribution in stirred vessels. *Trans IChemE,* **78**,435-444.

Miller, S.M. and Rawlings, J.B. (1994). Model identification and control strategies for batch cooling crystallizers. *AIChE. J.* **40(8)**, 1312-1327.

Misra, C. and White, E.T., (1976). Kinetics of Crystallization of Aluminium Trihydroxide from Seeded Caustic Aluminate Solutions. *Chem. Eng. Prog. Symp. Ser,* **67**, 53-65.

Mohameed, H.A, Abu-Jdayil, B., Khateeb, M.A., 2002, Effect of cooling rate on unseeded batch crystallization of KCL, *Chem. Eng. Proc.*, 41, 297-302.

Melikhov, I.V., and Berliner, L.B., 1981, Simulation of batch crystallization, *Chem. Eng. Sci.*, 36, 1021-1034

Momonaga, M., Yazawa, H. and Kagara, K., (1992). Reactive crystallization of methyl α–methoxyimino acetoacetate. *J. Chem. Eng. of Japan*, **25**, 237-242.

Montante, G., Lee, K.C., Brucato, A., and Yianneskis, M., (2001). Experiments and predictions of the transition of the flow pattern with impeller clearance in stirred tanks. *Computers and Chemical Engineering*, 25, 729-735.

Montante, G., Micale, G., Magelli, F. and Brucato, A., (2001). Experiments and CFD predictions of solid particle size distribution in a vessel agitated with four pitch blade turbines, *Trans IChemE*, **79** (A8), 1005-1010.

Mullin, J.W., (1993), *Crystallization*, 3rd. Edition, Butterworth-Heinemann, Oxford.

Mullin, J.W. and Raven, K.D., (1961a). Nucleation in agitated solutions. *Nature*, **190**, 251.

Mullin, J.W. and Raven, K.D., (1961b). Influence of mechanical agitation on the nucleation of some aqueous salt solutions. *Nature*, **195**, 35-36.

Mullin, J.W. (1972). *Crystallization*, 2nd Edition. Butterworth, London.

Mydlarz, J., and Jones, A.G., (1990). On modelling the size-dependent growth rate of potassium sulphate in an MSMPR crystallizer. *Chem. Eng. Comm.*, **90**, 47-56.

Mydlarz, J., and Jones, A.G., (1989). On numerical computation of size-dependent crystal growth rates. *Computers Chem. Eng.* **13**, (8), 959-965.

Mydlarz, J., and Jones, A.G., (1993). On the estimation of size-dependent crystal growth rate functions in MSMPR crystallizers. *Chem. Eng. J.*, **53**, 125-135.

Nývlt, J. (1994). Solid–Liquid Equilibria, Elsevier, Amsterdam.

Oh, M. (1995). *Modelling and simulation of combined lumped and distributed processes.* PhD Thesis, Imperial College London, UK.

Oh, M and Pantelides, C.C., (1996). A modelling and simulation language for combined lumped and distributed parameter systems. *Computers Chem. Eng.* **20**, (6-7), 611-633.

O'Hara, M and Reid, R.C., (1973). Modeling crystal growth rates from aqueous solution, Prentice-Hall.

O'Meadhra, R., Peutz, M.M.V., Kramer, H.J.M., Van der Heijden, A.E.D.M and Van Rosmalen, G.M., (1993). The role of attrition in the crystallization of ammonium sulphate, in: Rojkowski, Z.H. (Ed.), *Proc. 12th Symp. Ind. Cryst.* 4-29-4-34.

O'Meadra, R., (1995). Modelling of the kinetics of Suspension Crystallizers. ISBN 90-407-1190-9. Delft University Press.

Ostwald, W., (1897). Studien uber die Bildung und Umwandlung fester Korper. *Z. Phys. Chem.* **22:** 289-330.

Ottens, E.P.K., and de Jong, E.J., (1973). A model for secondary nucleation in a stirred vessel crystallizer. *Ind. Eng. Chem. Fundamentals*, **12**, 179-184.

Patience, D.B. (2002). Crystal Engineering through Particle Size and Shape Monitoring, Modelling and Control. PhD thesis, University of Wisconsin-Madison.

Patience, D.B., Dell' Orco, P., Rawlings, J.B. (2004). Optimal operation of a seeded pharmaceutical crystallization with growth rate dispersion. *Org. Proc. Res. Des.* 8(4), 609-615.

Ploß, R., Tengler, T. and Mersmann, A., (1976). Scale-up of MSMPR crystallizers. *Ger. Chem. Eng*, **1**, 42-48.

Ploβ , R., T. Tengler, A. Mersmann (1989). A new model of the effect of stirring intensity on the rate of secondary nucleation. *Chem. Eng. Technol.*, **12**, 137-146.

Pratola, F., Simons, S.J.R. and Jones, A.G., (2002). "Measurements of agglomerative crystallization forces: a microscopic study on potash alum crystals". In *Industrial Crystallization,* 15-18 September 2002, Sorrento, Italy. *Chemical Engineering Transactions*, **1**, 389-394.

Qian, R., Chen, Z., Ni, H., Fan, Z. and Cai, F., (1987). Crystallization kinetics of potassium chloride from brine and scale-up criterion. *AIChE. J.*, **33**, 1690-1697.

Qui, Y., and Rasmuson, A.C., (1994). Estimation of crystallization kinetics from batch cooling experiments. *AIChE. J.* **40**(5), 799-812.

Rajagopal, S., Ng, K.M. and Douglas, J.M., (1992). A hierarchical procedure for the conceptual design of solids processes. *Computers Chem. Eng.*, **16**, 675-689.

Ranade, V.V. (1997). An efficient computational model for simulating flow in stirred vessels: a case of Rushton turbine. *Chem. Eng. Sci.*, **52**, 4473-4484.

Randolph, A.D. (1969). Effect of crystal breakage on CSD in mixed suspension crystallizer. *Ind. Engng. Chem. Fundam.* 8(1), 53-58.

Randolph, A.D. and Larson, M.A. *Theory of Particulate Processes.* 2nd Edition., Academic Press, New York (1988).

Randolph, A.D., and Cise, M.D., (1972). Nucleation kinetics of the Potassium Sulphate-Water System. *AIChE J.*, **18(4)**, 798-807.

Rigopoulos, S., and Jones, A.G., (2003). A hybrid CFD-reaction engineering framework for multiphase reactor modelling: basic concept and application to bubble column reactors, *Chem. Eng. Sci.,* **58**, 3077-3089.

Ristic, R.I., Sherwood, J.N., and Shripathi, T., (1990). Strain variation in the (100) growth sectors of Potash Alum single-crystals and its relationship to growth-rate dispersion. *J. Crystal Growth.*, **102**, 245-248.

Rodi, W., (1984). Turbulence models and their Applications in Hydraulics- a State of the Art Review. 2nd Edition. *International Association for Hydraulic Research (IAHR),* 92.

Rohani, S., and Bourne, J.R., 1990, Self-tuning control of crystal size distribution in a cooling batch crystallizer, *Chemical Engineering Science*, 45, 12, 3457-3466.

Rojkowski., Z.H., (1993). Crystal growth rate models and similarity of population balances for size-dependent growth rate and for constant growth rate dispersion. *Chem. Eng. Sci.*, **48** (8), 1475-1485.

Rossiter, A.P. and Douglas, J.M., (1986). Design and optimisation of solids processes. I: A hierarchical decision procedure for process synthesis of solids systems. *Chem. Eng. Res. Des.*, **64**, 175-183.

Rousseaux, J.M., Vial, C., Muhr, H., and Plasari, E., (2001). CFD modelling of precipitation in the sliding-surface mixing device. *Chem. Eng. Sci.,* **56**, (4), 1677-1685.

Sha, Z., Oinas, P., Louhi-Kultanen, M., Yang, G. and Palosaari, S., (2001). Application of CFD simulation to suspension crystallization—factors affecting size-dependent classification, *Powder Technology*, **121**, (1), 20-25.

Sha, Z.L., Hatakka, H., Louhi-Kultanen, M., and Palosaari, S., (1996). Crystallization kinetics of potassium sulphate in an MSMPR stirred crystallizer. *J. Crystal Growth*, **166**, 1105-1110.

Sikdar, S.K., (1977). Size-dependent growth rate from curved *Ln n (L)* vs. *L* Steady state data. *Ind. Engng Chem. Fundam.* **16**(3), 390-341.

Stickland-Constable, R.F., (1968). Kinetics and Mechanism of crystallization, Academic Press, London.

Sung, C.Y., Estrin, J., and Youngquist, G.R., (1973). Secondary nucleation of magnesium sulphate by fluid shear. *AIChE J.*, **19(3)**, 957-962.

Synoweic, P., Jones, A.G., and Shamlou, P.A., (1993). Crystal break-up in dilute turbulently agitated suspensions. *Chem Eng. Sci.* **48**, 3495-3495.

Tanrikulu, S. Ü., Bulutchu, A.N., and Özkar, S., (2000). Crystallization kinetics of ammonium perchlorate in MSMPR crystallizer. *J. Crystal Growth*, **208**, 533-540.

ten Cate, A., Bermingham, S.B., Derksen, J.J and Kramer, H.M.J., (2000). Compartmental modelling of an 1100L DTB crystallizer based on Large Eddy flow simulation. *10th European conference on mixing*, 255-264,Delft, The Netherlands.

Togkalidou, T., Fujiwara, M., Patel, S., and Braatz, R.D., (2001). Solute concentration prediction using chemometrics and ATR-FTIR spectroscopy. *J. Crystal Growth*, **231**(4), 534-543.

Ulrich, J., (1989). *Crystal Res. Technol.* **24**, 249.

Urban, Z., and Liberis, L., (1999). Hybrid gPROMS-CFD modelling of an industrial scale crystalliser with rigorous crystal nucleation and growth kinetics and a full population balance. *Chemputers*, Dusseldorf, Germany.

Van der Heijden, A.E.D.M., Van der Eerden, J.P., (1992). Growth rate dispersion: The role of lattice strain. *J. Crystal Growth* **118**, 14-26.

Versteeg, H.K. and Malalasekera, W., (1995). An introduction to Computational Fluid Dynamics. *The finite volume method.* 1st edition. Longman Group.

Villadsen, J., (1997). Putting structure into chemical engineering. *Chem. Eng. Sci.*, **52**, 2857-2864.

Wadell, H., (1932). Volume, shape and roundness of rock particles. *J.Geology*, **40**, 443-451.

Wang, S., and Mersmann, A., (1992). Initial size dependent growth rate dispersion of attrition fragments and secondary nuclei, *Chemical Engineering Science*, **47** (6), 1365-1371.

Wei, H., and Garside, J., (1997). Application of CFD modelling to precipitation systems, Chem. Eng. Res. Des. 75, (A2), 219-227.

Wells, A.F. (1946). Crystal growth. *Annual reports on the progress of Chemistry.* The Chemical society, London, **43**, 62-87.

White, E.T., Bendig, L.L., and Larson, M.A., (1976). *AIChE Symposium Series*, **72** 41, 1976.

Westhoff, G.M. (2002). *Design and analysis of suspension crystallisers – Aspects of crystallisation kinetics and product quality.* PhD Thesis, Delft University of Technology, The Netherlands.

Wojcik, J.A. and Jones, A.G., (1998). Particle Disruption of precipitated $CaCO_3$ crystal agglomerates in turbulently agitated suspensions. *Chem. Eng. Sci.*, **53**, (5) 1097-1101.

Wold, S., Antti, H., Lindgren, F. and Öhman, J., (1998). Orthogonal signal correction of near-infrared spectra. *Chemometrics Intell. Lab. Syst.* **44**, 175-185.

Wood-Kaczmar, M.W. (2002). The use of FBRM in Mixed Suspension Mixed Product Removal (MSMPR) Continuous Crystallization for the on-line measurement of Growth Kinetics, Lasentec Users Forum, Charleston, SC.

Wood-Kaczmar, M.W. (2003). Personal Communication. Pilot plant data on an organic fine chemical produced at GlaxoSmithKline pharmaceuticals.

Yang, G., Louhi-Kultanen, M. and Kallas, J., (2002). The CFD simulation of programmed batch cooling crystallization. *Chem. Eng. Trans.*, **1**, 83-88.

Zacher, U., and Mersmann, A., (1995). The influence of internal crystal perfection on growth rate dispersion in a continuous suspension crystallizer. *J. Crystal Growth*, **147**, 172-180.

Zauner, R. (1999). *Scale-up of precipitation processes.* PhD thesis, University College London, UK.

Zauner, R., and Jones, A.G., (2000). Determination of nucleation, growth, agglomeration and disruption kinetics from experimental precipitation data: the calcium oxalate system. *Chem. Eng. Sci.*, **55**, 4219-4232.

Zauner, R., and Jones, A.G. (2002). On the influence of mixing on crystal precipitation processes-application of the segregated feed model, *Chem. Eng. Sci.*, **57** (5), 821-831.

Zumstein, R.C., and Rousseau, R.W., (1987). Growth rate dispersion by initial growth rate distributions and growth rate fluctuations. *AIChE .J*, **33**, 121-129.

Zwietering, Th. N. (1958). Suspending of solid particles in liquid by agitation. *Chem. Eng. Sci.*, 8, 244-253.

Nomenclature

LIST OF SYMBOLS

A	heat transfer area, [m^2]
A_T	total crystal surface area, [m^2]
a	surface area of crystal, [m^2]
a_0, a_1, a_2	constants
a, b, c	constants
B°	nucleation rate, [# $m^{-3}.s^{-1}$]
B_{TOT}	total nucleation rate, [# $m^{-3}.s^{-1}$]
B	birth term, [-]
B_N	nucleation rate, [# $m^{-3}.s^{-1}$]
C	impeller off-bottom clearance, [m]
C	solute concentration, [g g^{-1} solvent, %w/w]
C*	equilibrium saturation concentration, [g g^{-1} solvent, %w/w)]
C_o	initial concentration, [g g^{-1} solvent, %w/w]
C_p	specific heat capacity, [kJ. $kg^{-1}.k^{-1}$]
C_O	modified drag coefficient
C_D	drag coefficient, [-]
Cv	coefficient of variation based on number mean size, [%]
D_G	growth rate diffusivity, [$m^2.s^{-1}$]
d_p	particle diameter, [m]
d_w	depth to width ratio, [-]
d_v	volume mean size, [m^3]
d_s	surface area mean size, [m^3]
D, d	impeller diameter, [m]
d_t	tank diameter, [m]
D	death term
E	activation energy, [kJ mol^{-1}]
F	heat transfer coefficient, [$W.m^{-2}.K^{-1}$]
Fl	flow number [-]

NOMENCLATURE

e	void fraction, [-]
g	gravitational acceleration, [m.s^{-2}]
g	overall growth rate kinetic order, [-]
G	growth rate, [m.s^{-1}]
h	impeller clearance, [m]
H	tank height, [m]
i j, k	nucleation rate orders
i_{max}	number of meshes
k_v	volume shape factor, [-]
k_g,k_g'	growth rate coefficient, [m.s^{-1}]
k_b, k_n	nucleation rate coefficient, [#./[m^3.s(m/s)^i(kg/m^3)^j(rev/s)^k]or [# m^{-3}.s^{-1}]
k_a	surface area shape factor, [-]
L	characteristic crystal size, [m]
L_o	critical nuclei size, [m]
L_{32}	surface area mean particle size, [μm]
L_{43}	volume mean particle size, [μm]
L_{10}	number mean particle size, [μm]
L_M	Malvern equivalent spherical particle size, [μm]
L_o	effective crystal size, [μm]
l_w	length to width ratio, [-]
M	torque, [N m^{-1}]
M_T	suspension density, [kg.m^{-3}]
m_j, m_i	jth and ith moment of distribution
m_l	liquid mass flowrate [kg s^{-1}]
n	supersaturation order
N	impeller rotational speed, [s^{-1}]
N(L)	cumulative number of oversize particles, [# m^{-3}]
n (L)	population density at crystal size, L, [# m^{-4}]
N_T	total number of crystals, [#]
N_o	crystal number of the nuclei size, [#]
N_s	seed crystal number, [#]
N	number of crystals, [#]

n_o	nuclei population density, [# $m^{-3}.m^{-1}$]
n_o	crystal density of the nuclei size, [#. m^{-1}]
P	power input [W]
Po	power number [-]
q	flowrate per unit time [kg s^{-1} or m^3 s^{-1}]
q_e	exit flowrate per unit time [kg s^{-1} or m^3 s^{-1}]
q_f	feed flowrate per unit time [kg s^{-1} or m^3 s^{-1}]
Q	volumetric flowrate, [m^3 s^{-1}]
Q_p	product volumetric flowrate, [m^3 s^{-1}]
R = 8.314	ideal gas constant, (kJ mol^{-1} K^{-1})
R_G	mass growth rate [kg s^{-1}]
s	impeller dependent proportionality constant, [-]
S	absolute supersaturation, [-]
Sc	source term
t	time, [s]
T	tank diameter, [m]
T	temperature, [° C]
T_M	melting (fusion) temperature [° C]
u_t	particle terminal settling velocity, [m s^{-1}]
V	crystallization volume, [m^3]
v	volume of crystal, [m^3]
V	volume or compartmental volume [m^3]
X	solids mass fraction, [-]
X	mole fraction, [-]
U	overall heat transfer coefficient, [W. m^{-2}. K^{-1}]
U	velocity vector, [$m^3.s^{-1}$]
U_h	hindered settling velocity, [$m.s^{-1}$]
Z	tank diameter, [m]

Greek letters

δ	dirac function
β_d	disruption rate, [s^{-1}]

NOMENCLATURE

B_a	agglomeration kernel
ρ	fluid density, [kg m^{-3}]
ρ_L	liquid density, [kg m^{-3}]
ρ_S	solid density, [kg m^{-3}]
ρ_f	feed slurry density, [kg m^{-3}]
ρ_c	crystalline density, [kg m^{-3}]
ϕ	solid concentration, [kg.kg^{-1}]
ϕv	volumetric flowrate [m^3 s^{-1}]
ϕ_m	mass flowrate [kg s^{-1}]
ε	power input, [W kg^{-1}]
Δc	concentration driving force [g g^{-1}, % w/w]
Θ	equilibrium saturation temperature [° C/K]
$\Delta\Theta_{max}$	maximum allowable undercooling [° C/K]
$\Delta\Theta_c$	undercooling rate [° C/K]
σ	relative supersaturation, [-]
ΔH_d	enthalpy of dissolution, [kJ mol^{-1}]
ΔS_d	entropy of dissolution, [kJ mol^{-1}]
ΔH_c	enthalpy of crystallization, [kJ mol^{-1}]
Δc	supersaturation (concentration driving force), [kg.kg^{-1}]
ε	power input per unit volume, [W kg^{-1}]
τ	mean residence time, [s]
σ_L^2	variance [-]
ΔM	mass fraction of solid, [-]
ΔL	difference between particle size classes (L_i-L), [m]
ψ	sphericity, [-]
σ_L	standard deviation
η	viscosity, [Pa.s^{-1}]
μ	viscosity, [Pa.s^{-1}]
β_{agg}	agglomeration kernel
β_{dis}	disruption kernel
λ	kolmogorov turbulent scale, [μm]
λ	thermal conductivity [$W.m^{-1}.K^{-1}$]
ν	kinematic viscosity, [$Ns.m.kg^{-1}$]

Subscripts

a	agglomeration
e	effective size independent
av	average
s	solid
agg	agglomeration
dis	disruption
p	particle
o	initial
f	final
s	solution
w	wall
c	cooling
i	impeller
b	bulk
s	solution

Dimensionless

Nu	Nusselt number, $Nu = kd_t/\lambda$
Po	Power number, $P_O = P/\rho N^3 d^5$
Pr	Prandtl number, $P_\rho = \mu C_p/\lambda$
Re	Reynolds number, $Re = \rho N d^2/\mu$

Acknowledgments

The author would like to thank GlaxoSmithKline pharmaceuticals for allowing part of this research to be carried out at the research and development facilities at Stevenage, United Kingdom.

Appendix

A. FORTRAN SOURCE CODE FOR DISRUPTION AND AGGLOMERATION

```
**********************************************************************
Fortran 90 code enabling the determination of agglomeration and
disruption kernels for attrition experiments carried out using different
specific power inputs.
**********************************************************************

C     ...SIZE DEPENDENT AGGREGATION AND DISRUPTION..
C     ...PARAMERERS..
      INTEGER         N, LIW, LW, M
      PARAMETER       (N=2,LIW=N+2,LW=N*(N-1)/2+12*N,M=253)
C     ..Arrays
      DOUBLE PRECISION T(M,N),T1(M),Y(M),Y1(M)
      INTEGER         NOUT,NIN,NOUT1
      PARAMETER       (NOUT1=6,NIN=5,NOUT=10)
      CHARACTER TITLE*80
C     .. Local Scalars ..
      DOUBLE PRECISION F,TAU,DL,G,BN,D,DD,SUM,SUMN,SUU,SU
     *,BA1,BA,BA2,BN2,BN1,SQ,BD1,BD2
      INTEGER         IBOUND, IFAIL, J,I,K
C     ...COMMON BLOCKS...
      COMMON          Y,T
C     .. Local Arrays ..
      DOUBLE PRECISION BL(N), BU(N), W(LW), X(N)
      INTEGER         IW(6)
C     .. External Subroutines ..
      EXTERNAL        E04JAF
C     .. Executable Statements ..
      X(1) = 1.0D-15
      X(2) = 1.0D-1
      IBOUND = 2

      OPEN(NIN,FILE='D:/terry/scale-up/data/old.TXT',STATUS='OLD')
      OPEN(NOUT,FILE='D:/terry/scale-up/data/RES.TXT',STATUS='UNKNOWN')
      READ(NIN,*)TITLE
C     ..tau - residence time DL-delta L
      READ(NIN,*)TAU,DL,BN,G
```

```
      WRITE(NOUT,FMT=99995)TITLE
      WRITE(NOUT,*)'START'
      WRITE(NOUT,FMT=99996)X(1),X(2)
C     ..Observations of PSD T1(I)=SIZE Y1(I)=NUMBER
C     ..(I=1,2,...,M)
      DO 20 I=1,M
        READ(NIN,FMT=*)T1(I),Y1(I)
   20 CONTINUE
C     ..Y(I)- value of N(I)/tau - Discretised PBE
C     ..Sum of all particles
      SUMN=0.D0
      SUU=0.D0
      SU=0.D0
      DO 22 I=1,M
        Y(I)=Y1(I)/TAU
        SUMN=SUMN+Y1(I)
        SU=SU+Y1(I)**3
        SUU=SUU+Y1(I)*(T1(I)+T1(1))**3
   22 CONTINUE
      Y(1)=Y(1)-BN
C     ...Sum of all growth terms T(I,3) is 0
C     T(1,3)=-Y1(1)/DL
C     T(M,3)=Y1(M-1)DL
C     ..To the first class come primary disrupted particles
C     ..from the 2nd class
C     ..but there is no disruption in the class
      T(M,2)=-Y1(M)*T1(M)**5
      T(1,2)=T(M,2)
C     ..In the last class the number of decreases by
C     ..virtue of disruption death
      DO 23 I=2,M-1
      T(I,2)=Y1(I+1)*T1(I+1)**5-Y1(I)*T1(I)**5
C     ..The difference between birth and death by disruption
C     T(I,3)=(Y1(I-1)-Y1(I))/DL
C     ..The difference between birth and death by growth
   23 CONTINUE
C******************AGGLOMERATION TERM**************
C                    BIRTH
      T(1,1)=-0.5*Y1(1)*Y1(1)
      DO 26 K=2,M
      SUM=0.D0
       DO 25 I=1,M-1
        DO 24 J=I,M-1
         IF(T1(I)**3+T1(J)**3.LT.(T1(K)+0.5*DL)**3.AND.
```

```
     *     T1(I)**3+T1(J)**3.GT.(T1(K)-0.5*DL)**3) THEN
            DD=Y1(I)*Y1(J)*(T1(I)+T1(J))**3
            SUM=SUM+DD
            T(I,1)=T(I,1)-DD
            IF(I.NE.J)T(J,1)=T(J,1)-DD
          END IF
  24    CONTINUE
  25   CONTINUE
       T(K,1)=T(K,1)+SUM
  26  CONTINUE
C     ..Dividing primary particles into subsequent classes
      DO 30 I=1,M-1
       D=(T1(I+1)**3-T1(I)**3)**(1./3.)
       DO 29 J=1,M-1
        IF(D.GE.T1(J)-0.5*DL.AND.D.LT.T1(J)+0.5*DL)
     *  T(J,2)=T(J,2)+Y1(I+1)
  29   CONTINUE
  30  CONTINUE
      IFAIL = 1
      CALL E04JAF(N,IBOUND,BL,BU,X,F,IW,LIW,W,LW,IFAIL)
C     SINCE IFAIL WAS SET TO 1 BEFORE ENTERING E04JAF, IT IS
C     ESSENTIAL TO TEST WHETHER IFAIL IS NON-ZERO ON EXIT
      IF (IFAIL.NE.0) WRITE (NOUT,FMT=99998) IFAIL
      IF (IFAIL.NE.1) THEN
        WRITE (NOUT,FMT=99997) F
        WRITE (NOUT,FMT=99996) (X(J),J=1,N)
      END IF
      WRITE(NOUT,FMT=*)'Bn= ',BN,'   G= ',G
      BA1=((1/TAU+X(2))*Y1(M))*2./T(M,1)/T1(M)**3
      BA=(Y1(74)/TAU-X(2)*T(74,2))/T(74,1)/T1(74)**3
      BA2=(BN+X(2)*Y1(2)-Y1(1)/TAU)/Y1(1)/SUU/T1(1)**3
      BN2=Y(1)+T(1,1)*X(1)-T(1,2)*X(2)
      BN1=SUMN/TAU
      SQ=SQRT(F/(M-1))
      WRITE(NOUT,FMT=*)'Ba1= ',BA2,'  Balast= ',BA1,
     *                 '              ',' Ba20= ',BA

          WRITE(NOUT,FMT=*)'Nt = ',SUMN,'  BN1= ',BN1
C     WRITE(NOUT,FMT=*)'Bd1= ',BD1,'  Bd2 = ',BD2
      WRITE(NOUT,FMT=*)'Sq = ',SQ
      WRITE(NOUT1,FMT=*)'GOT¢W'
      STOP
C     END OF KIN.FOR MAIN PROGRAM
99999 FORMAT (' KIN.FOR PROGRAM RESULTS',/1X)
```

```
99998 FORMAT (//' ERROR EXIT TYPE',I3,' - SEE ROUTINE DOCUMENT')
99997 FORMAT (//' FUNCTION VALUE ON EXIT IS ',D12.4)
99996 FORMAT (' AT THE POINT',2D12.4,/)
99995 FORMAT (' Results of ',A80)
      END
C
      SUBROUTINE FUNCT1(N,XC,FC)
C     FUNCTION EVALUATION ROUTINE FOR KIN.FOR PROGRAM -
C     THIS ROUTINE MUST BE CALLED FUNCT1
C     .. Scalar Arguments ..
      DOUBLE PRECISION  FC
      INTEGER           N,M,NIJ,I
                        PARAMETER(NIJ=2,M=198)
C     .. Array Arguments ..
      COMMON Y,T
      DOUBLE PRECISION  XC(N),T(M,NIJ),Y(M)
C     .. Local Scalars ..
      DOUBLE PRECISION  X1, X2
C     .. Executable Statements ..
      X1 = XC(1)
      X2 = XC(2)
      FC=0.0D0
      DO 20 I=1,M
      FC = FC+(X1*T(I,1)+X2*T(I,2)-Y(I))**2
   20 CONTINUE
      RETURN
C     END OF FUNCTION EVALUATION ROUTINE
      END
```

B. CFD SOURCE CODE FOR MODELLING MIXING AND HEAT TRANSFER

B.1 CFX source file for two-phase systems

The following is a sample CFX source file used for modelling two-phase suspensions with a monodisperse particle size in batch crystallizers. For more information on the format of CFX source files, one should consult the CFX manual (AEA Technology).

APPENDIX

```
/*****************************************************/
/*TURBULENT FLOW                                     */
/*MULTIPLE FRAMES OF REFERENCE                       */
/*MULTI-PHASE SIMULATION USING MF MODEL              */
/*MODEL INCLUDES DRAG COEFFICIENT TERM               */
/*ELEFTHERIOS KOUGOULOS                              */
/*UNIVERSITY COLLEGE LONDON, LONDON, UK              */
/*24/06/2003                                         */
/*****************************************************/

/*General settings*********************************/

>>CFX4
#CALC
        DENL = 800;  # Solvent density
        VISL = 0.00235; # Solvent viscosity
        DENS = 1400; # Solid density
        VISS = 0.00235; # Solid viscosity: assumed to be that of solvent
        BDIA = 2.0000E-04; # Particle diameter
        VF2 = 0.05; # Volume fraction of solid phase
        VF1 = 1-VF2;
        RESOR = 1.0E-011;
#ENDCALC
>>SET LIMITS
  TOTAL INTEGER WORK SPACE 120000000
  TOTAL CHARACTER WORK SPACE 100000
  TOTAL REAL WORK SPACE 100000000
>>OPTIONS
  THREE DIMENSIONS
  CYLINDRICAL COORDINATES
  AXIS INCLUDED
  TURBULENT FLOW
  STEADY STATE
  ISOTHERMAL FLOW
  INCOMPRESSIBLE FLOW
  BUOYANT FLOW
  NUMBER OF PHASES 2
```

APPENDIX

```
  ROTATING COORDINATES
  UNMATCHED GRIDS
  USER SCALAR EQUATIONS 4
>>USER FORTRAN
  USRINT
  USRGRD
  USRTRN
  USRSRC
  USRCVG
>>VARIABLE NAMES
  K 'TKE'
  USER SCALAR1 'MFR U VELOCITY'
  USER SCALAR2 'MFR V VELOCITY'
  USER SCALAR3 'MFR W VELOCITY'
  USER SCALAR4 'MFR SPEED'

/* Define the grid**********************************/

>>MODEL TOPOLOGY
  >>CYCLIC CONNECTIONS
    Z CYCLES PER REVOLUTION 4  # Pitch blade impeller
  >>GLUE PATCHES FOR UNMATCHED GRIDS
    FIRST PATCH NAMES 'PER_A'
    SECOND PATCH NAMES 'PER_B'
    FROZEN ROTOR
  >>GLUE PATCHES FOR UNMATCHED GRIDS
    FIRST PATCH NAMES 'PER1_IMP1'
    SECOND PATCH NAMES 'PER2_IMP1'
    FROZEN ROTOR
  >>GLUE PATCHES FOR UNMATCHED GRIDS
    FIRST PATCH NAMES 'TOP_IMP1'
    SECOND PATCH NAMES 'INT_TOP_1'
    FROZEN ROTOR
  >>GLUE PATCHES FOR UNMATCHED GRIDS
    FIRST PATCH NAMES 'BOTTOM_IMP1'
    SECOND PATCH NAMES 'INT_BOTTOM_1'
    FROZEN ROTOR
```

```
  >>GLUE PATCHES FOR UNMATCHED GRIDS
    FIRST PATCH NAMES 'OUTER_IMP1'
    SECOND PATCH NAMES 'INT_OUTER_1'
    FROZEN ROTOR

/* Multiphase model data************************/
>>MODEL DATA
  >>TITLE
    PROBLEM TITLE 'TEST 1'
  >>SET INITIAL GUESS
    >>SET CONSTANT GUESS
        PHASE NAME 'PHASE1'
      VOLUME FRACTION #VF1
    >>SET CONSTANT GUESS
      PHASE NAME 'PHASE2'
        VOLUME FRACTION #VF2
   >>PHYSICAL PROPERTIES
     >>FLUID PARAMETERS
         PHASE NAME 'PHASE1'
         DENSITY #DENL
         VISCOSITY #VISL
     >>FLUID PARAMETERS
         PHASE NAME 'PHASE2'
         DENSITY #DENS
         VISCOSITY #VISS
     >>MULTIPHASE PARAMETERS
         >>PHASE DESCRIPTION
          PHASE NAME 'PHASE1'
          LIQUID
          CONTINUOUS
       >>PHASE DESCRIPTION
         PHASE NAME 'PHASE2'
         SOLID
         DISPERSE
         MEAN DIAMETER #BDIA
        >>MULTIPHASE MODELS
         >>MOMENTUM
```

```
          INTER PHASE TRANSFER
        >>TURBULENCE
          HOMOGENEOUS
  >>INTER PHASE TRANSFER MODELS
      >>MOMENTUM
        FIRST PHASE NAME 'PHASE1'
        SECOND PHASE NAME 'PHASE2'
       >>MIXTURE MODEL
         DRAG COEFFICIENT 19.59 # (Brucato, 1998)
         INTERFACE LENGTH SCALE 1.200e-04
  >>BUOYANCY PARAMETERS
      ALL PHASES
      GRAVITY VECTOR -9.81 0.0 0.0
      BUOYANCY REFERENCE DENSITY #DENL

/*************************************************/

/* Turbulence model*********************************/

  >>TURBULENCE PARAMETERS
      >>TURBULENCE MODEL
        PHASE NAME 'PHASE1'
        TURBULENCE MODEL 'K-EPSILON'
      >>TURBULENCE MODEL
        PHASE NAME 'PHASE2'
        TURBULENCE MODEL 'K-EPSILON'
      >>TURBULENT PRANDTL NUMBER
        PHASE NAME 'PHASE2'
        VOLUME FRACTION 0.8
/*************************************************/

      >>ROTATING COORDINATES PARAMETERS
        PATCH NAME 'ALLBLOCKS_IMP1'
        OMEGA -65.44984694978736 0.0 0.0
        POSITION VECTOR ON ROTATING AXIS 0.0 0.0 0.0

/* Solver options*********************************/
```

APPENDIX

```
 >>SOLVER DATA
  >>DEFERRED CORRECTION
   K START 3000
   K END   3001
   EPSILON START 3000
   EPSILON END   3001
      >>PROGRAM CONTROL
        MAXIMUM NUMBER OF ITERATIONS 3000
        MASS SOURCE TOLERANCE #RESOR
  >>UNDER RELAXATION FACTORS
        U VELOCITY 3.0000E-01
        V VELOCITY 3.0000E-01
        W VELOCITY 3.0000E-01
        PRESSURE 1.0000E+00
        TKE 5.0000E-01
        EPSILON 5.0000E-01
     VOLUME FRACTION 3.0000E-01

/* Boundary conditions*******************************/

 >>MODEL BOUNDARY CONDITIONS
  >>WALL BOUNDARIES
   PATCH NAME 'TOP'
   TAUX 0.0
   TAUY 0.0
   TAUZ 0.0
  >>WALL BOUNDARIES
   PATCH NAME 'SHAFT'
   ANGULAR VELOCITY -65.44984694978736 0.0 0.0

/* Output files*************************************/

 >>OUTPUT OPTIONS
  >>DUMP FILE OPTIONS
   FINAL SOLUTION
   ALL REAL DATA
```

```
   >>PRINT OPTIONS
   >>WHAT
     NO VARIABLES
     NO GEOMETRIC INFORMATION
     PRINT TOTALS FOR EACH PATCH
     /* NO WALL PRINTING */
   >>WHEN
   >>WHERE
/*****************************************************/

 >>STOP
```

B.2 CFX source file

The following is a sample CFX source file used for modelling heat transfer in batch cooling crystallizer vessels based on estimation of a liquid side heat transfer coefficient and manual implementation of a linear cooling profile. The heat transfer simulations utilise the steady state hydrodynamic information produced from solvent phase CFD simulations.

```
/*****************************************************/
/*HEAT TRANSFER                                      */
/*ESTIMATED HEAT TRANSFER COEFFICIENT WITH           */
/*LINEAR COOLING PROFILE IMPLEMENTED                 */
/*ELEFTHERIOS KOUGOULOS                              */
/*UNIVERSITY COLLEGE LONDON, LONDON, UK              */
/*24/06/2003                                         */
/*****************************************************/

/*General settings*************************************/

>>CFX4
  >>SET LIMITS
    TOTAL CHARACTER WORK SPACE 20000
  >>OPTIONS
```

```
   THREE DIMENSIONS
   CYLINDRICAL COORDINATES
   AXIS INCLUDED
   TURBULENT FLOW
   HEAT TRANSFER
   TRANSIENT FLOW
   ROTATING COORDINATES
   UNMATCHED GRIDS
   USER SCALAR EQUATIONS 4
  >>USER FORTRAN
   USRINT
   USRGRD
   USRTRN
   USRSRC
   USRCVG
  >>VARIABLE NAMES
   K 'TKE'
   USER SCALAR1 'MFR U VELOCITY'
   USER SCALAR2 'MFR V VELOCITY'
   USER SCALAR3 'MFR W VELOCITY'
   USER SCALAR4 'MFR SPEED'

/* Define the grid**********************************/

>>MODEL TOPOLOGY
  >>CYCLIC CONNECTIONS
   Z CYCLES PER REVOLUTION 2 # Rushton turbine
  >>GLUE PATCHES FOR UNMATCHED GRIDS
   FIRST PATCH NAMES 'PER_A'
   SECOND PATCH NAMES 'PER_B'
   FROZEN ROTOR
  >>GLUE PATCHES FOR UNMATCHED GRIDS
   FIRST PATCH NAMES 'PER1_IMP1'
   SECOND PATCH NAMES 'PER2_IMP1'
   FROZEN ROTOR
  >>GLUE PATCHES FOR UNMATCHED GRIDS
   FIRST PATCH NAMES 'TOP_IMP1'
```

```
   SECOND PATCH NAMES 'INT_TOP_1'
   FROZEN ROTOR
  >>GLUE PATCHES FOR UNMATCHED GRIDS
   FIRST PATCH NAMES 'BOTTOM_IMP1'
   SECOND PATCH NAMES 'INT_BOTTOM_1'
   FROZEN ROTOR
  >>GLUE PATCHES FOR UNMATCHED GRIDS
   FIRST PATCH NAMES 'OUTER_IMP1'
   SECOND PATCH NAMES 'INT_OUTER_1'
   FROZEN ROTOR

/* Model data and properties*************************/

>>MODEL DATA
  >>TITLE
   PROBLEM TITLE 'ADVANCED EXAMPLE3'
  >>SET INITIAL GUESS
   >>INPUT FROM FILE
        READ DUMP FILE
        LAST DATA GROUP
   >>SELECT VARIABLES FROM FILE
        ALL RELEVANT DATA

  >>PHYSICAL PROPERTIES
   >>FLUID PARAMETERS
    DENSITY 800.0
    VISCOSITY 0.00235
   >>HEAT TRANSFER PARAMETERS
    THERMAL CONDUCTIVITY 0.2
    FLUID SPECIFIC HEAT 2900

/************************************************/
   >>TRANSIENT PARAMETERS
    >>FIXED TIME STEPPING
     TIME STEPS 120*0.5

/************************************************/
```

```
   >>ROTATING COORDINATES PARAMETERS
     PATCH NAME 'ALLBLOCKS_IMP1'
     OMEGA -21.048670779051612 0.0 0.0
     POSITION VECTOR ON ROTATING AXIS 0.0 0.0 0.0

/* Solver options*************************************/

>>SOLVER DATA
  >>DEFERRED CORRECTION
    K START 1000
    K END   1001
    EPSILON START 1000
    EPSILON END   1001
  >>PROGRAM CONTROL
    MAXIMUM NUMBER OF ITERATIONS 30
    ITERATIONS OF HYDRODYNAMIC EQUATIONS 0
    MASS SOURCE TOLERANCE 1.E-11

/* Boundary conditions*******************************/
>>MODEL BOUNDARY CONDITIONS
  >>WALL BOUNDARIES
    PATCH NAME 'TOP'
    TAUX 0.0
    TAUY 0.0
    TAUZ 0.0
  >>WALL BOUNDARIES
    PATCH NAME 'DEFAULT_WALL'
    TEMPERATURE ABC 682.0 1.0 240746.0
  >>WALL BOUNDARIES
    PATCH NAME 'SHAFT'
    ANGULAR VELOCITY -21.048670779051612 0.0 0.0

/* Output file options*******************************/
>>OUTPUT OPTIONS
  >>DUMP FILE OPTIONS
    FINAL SOLUTION
    ALL REAL DATA
```

APPENDIX

```
 >>PRINT OPTIONS
  >>WHAT
   NO VARIABLES
   NO GEOMETRIC INFORMATION
   PRINT TOTALS FOR EACH PATCH
  >>WHEN
  >>WHERE

/*************************************************/
>>STOP
```

C. COMPARTMENTAL POPULATION, MASS AND ENERGY BALANCE DERIVATIONS

C.1 COMPARTMENTAL POPULATION BALANCE DERIVATION

For a complete description of the crystal size distribution (CSD) in a continuously operated crystallizer (MSMPR compartment) it is required that the nucleation and growth rates are quantified and to apply the three conservation laws of mass, energy and crystal population. The mathematical model used to describe this is known as the population balance. The importance of a population balance is that it accounts for all the particles in a system and formed the basis of pioneering work that was carried out by Randolph and Larson (1962,1988). Randolph and Larson investigated in detail the modelling of crystal distributions using population balances and developed the mixed-suspension mixed-product removal (MSMPR) model for continuous crystallizers. The population balance is a statement of continuity for particulate systems. It follows the change in the CSD as particles are born, die, grow and leave the control volume.

The deterministic population balance was derived as a conservation equation for the number of particles in a population $n(z,t)$, where z is a vector of variables that includes three spatial coordinates, x, and internal coordinates, y that describe the state of the particles, such as quality and intrinsic growth rate. If we consider,

the subregion of particle phase space, Ω, and $d\Omega$ is an infinitesimal volume in the particle space phase, then the total number of particles per unit volume of the crystallizer is as follows,

$$\int_{\Omega} n(z,t)d\Omega \qquad [1.1]$$

The general form of a population balance for particles in the fixed subregion of phase space is,

$$\text{Accumulation} = \text{Input} - \text{Output} + \text{Net generation} \qquad [1.2]$$

The derivative of equation [0.0], will depend on the rates of birth, B and death, D, in Ω and is stated as follows:

$$\frac{d}{dt}\int_{\Omega} n(z,t)d\Omega = \int_{\Omega}(B-D).d\Omega \qquad [1.3]$$

Using the Liebnitz formula (in three dimensions), the left hand side of equation [0.0], may be expanded to a volume or surface integral, and then the divergence theorem is used to convert the surface integral to a volume integral as follows,

$$\begin{aligned}\frac{d}{dt}\int_{\Omega} n(z,t)d\Omega &= \int_{\Omega}\frac{\partial n(z,t)}{\partial t}.d\Omega + \int_{\Sigma}(n.v).n(z,t).d\Sigma \\ &= \int_{\Omega}\left[\frac{\partial n(z,t)}{\partial t} + (\nabla.n(z,t).v)\right].d\Omega\end{aligned} \qquad [1.4]$$

Recalling that z is partitioned into internal y or L, and external coordinates, $\mathbf{x}$, or x, y, and z.

$$z = \begin{bmatrix} x \\ y \end{bmatrix} = \begin{bmatrix} x \\ y \\ z \\ L \end{bmatrix} \qquad [1.5]$$

The velocity ($\mathbf{v}$) is defined as the vector of the sum of the external coordinates, v_x, v_y, v_z (Cartesian components of fluid velocities) and the internal velocities, v_L (particle growth rate).

APPENDIX

$$v = v_{ext} + v_{\text{int}} = \begin{bmatrix} v_x \\ v_y \\ v_z \\ v_L \end{bmatrix} \qquad [1.6]$$

Substituting the right hand side of equation [0.0], into equation [0.0], allows the population balance to be described as follows,

$$\int_{\Omega} \left[\frac{\partial n(z,t)}{\partial t} + (\nabla . n(z,t).v) - (B - D) \right] . d\Omega = 0 \qquad [1.7]$$

Since the region Ω is arbitrary, the integrand must vanish identically. Thus the population balance is given as follows:

$$\frac{\partial n(z,t)}{\partial t} + (\nabla . n(z,t).v) - (B - D) = 0 \qquad [1.8]$$

Equation [0.0] is a number continuity equation in particle phase space and when it is combined with both mass and energy balances, particle number formation kinetics can be completely described. Equation [0.0] can be further simplified for well-mixed systems such that $f(z,t)$, B and D have no spatial dependence. Equation [0.0] can also be integrated over the entire crystallizer volume to give,

$$\int_{V} \left[\frac{\partial n(z,t)}{\partial t} + (\nabla . n(z,t).v_{\text{int}} + \nabla . n(z,t).v_{ext}) - (B - D) \right] . dV = 0 \qquad [1.9]$$

Assuming the system is well mixed $f(z,t)$, B and D are all functions of internal coordinates so,

$$n(z,t) = n(y,t) = n(L,t) \qquad [1.10]$$

The volume integral in equation [0.0] can be expressed as a surface integral using the divergence theorem as follows,

$$\int_{v} (\nabla . n(L,t).v_{ext}) . dV = \int_{S} v_n . n(L,t) dS \qquad [1.11]$$

The S term may be considered as a sum of three components $S = S_k + S_s + S_e$ where S_k is the surface area where flow in and out of the volume occurs, S_s is the free surface of liquid in the vessel and S_e is the total solid-fluid interface.

APPENDIX

$$\int_{S_k} v_n.n(L,t)dS = \frac{\omega_{exit}}{\rho_{exit}}.n_{exit}(L,t) - \frac{\omega_{feed}}{\rho_{feed}}.n_{feed}(L,t) = \sum_k Q_k n_k$$

$$\int_{S_e} v_N.n(L,t)dS + \int_{S_s} v_N.n(L,t)dS = n(L,t).\frac{dV}{dt} \quad [1.12]$$

where dV/dt is the total rate of change of solids free volume. Integration of equation [0.0], over V and substitution into equation [0.0] and [0.0] for the external velocity terms produces,

$$V.\left(\frac{\partial n(L,t)}{dt} + (\nabla.v_L.n(L,t)) - (B-D)\right) = -\left[\frac{\omega_{exit}}{\rho_{exit}}.n_e(L,t) - \frac{\omega_{feed}}{\rho_{feed}}.n_{feed}(L,t)\right] - n(L,t).\frac{dV}{dt} \quad [1.13]$$

Equation [0.0] can describe both batch and continuous crystallizers with appropriate values for $\frac{\omega}{\rho} = Q$, specification of the internal variables and functional forms of $v_L, n(L,t)$, B and D and supply the initial and boundary conditions. Additional length co-ordinates, crystal shape, purity, intrinsic growth and size-dependent growth can be included. If breakage and agglomeration terms are ignored and nuclei appear at a small size range, L_o then equation [0.0] becomes,

$$V.\frac{\partial n(L,t)}{\partial t} + V.\frac{\partial[G(L,t).n(L,t)]}{\partial L} - V.[B.\delta(L-L_0)] + n(L,t).\frac{dV}{dt} = -|Q_e n_e(L,t) - Q_f n_f(L,t)| \quad [1.14]$$

Where $G = v_L = dL/dt$ is the crystal growth rate, B is the nucleation rate density, and $\delta(L-L_0)$ is the Dirac delta function acting at L_o. Equation [0.0] can be integrated over L_0^- and L_0^+ to show that nucleation can be removed and be specified as a boundary condition, and assuming a constant volume system, produces equation [0.0],

$$\frac{\partial n(L,t)}{\partial t} + \frac{\partial[G(L,t).n(L,t)]}{\partial L} = -\frac{|q_e n_e(L,t) - q_f n_f(L,t)|}{V}, \quad [1.15]$$

APPENDIX

with the boundary condition $$n(L_o,t)=\frac{B}{G\big|_{L_0}} \qquad [1.16]$$

The population balance described above can be often simplified using the MSMPR assumption in which, there is a uniform environment for growth, nucleation, birth and death, resulting in the following macrodistributed population balance,

$$\frac{\partial n(L,t)}{\partial t}+\frac{n(L,t)}{\tau}=-\frac{\partial\left(G(L).n(L,t)\right)}{\partial L}+B^0.\delta(L-L_0)+B-D \qquad [1.17]$$

Birth and death from a size range can occur by agglomeration and breakage and is given by,

$$B_{agg}+B_{dis}=\frac{L^2}{2}\int_0^L\frac{\beta_{agg}(L_u,L_v).n(L_u).n(L_v).dL_u}{L_v^{\,2}}+$$

$$\int_{L_v}^{\infty}\beta_{dis}(L_u,L_v).S'(L_u,L_v)n(L_u)n(L_v)dL_u$$

$$D_{agg}-D_{dis}=\quad n(L,t).\int_0^{\infty}\beta_{agg}(L_u,L_v).n(L_u).dL_u+\beta_{dis}(L_u,L_v).n(L) \qquad [1.18]$$

Using a moment transformation of the population balance, the dimensionality of the population balance can be reduced to that of transport equations. Moment transformation allows the population balance to be solved more easily but the distribution of the variables with the particle size is lost.

In a crystallization process yield and purity of extreme importance including the size range of the final product. Hence emphasis has been place on controlling the CSD, which forms the basis of design and operation of crystallization processes (McCabe and Smith, 1976).

The CSD is expressed as a population number or mass distribution. The population distribution shows the number of crystals at each size distributed over the size domain.

APPENDIX

Both distributions are related and affect crystallization processes. The crystal population density, n (number of crystals per unit size per unit volume of system) is a function of the characteristic crystal dimension, L defined by,

$$\underset{\Delta L \to 0}{Lim} \frac{\Delta N}{\Delta L} = \frac{dN}{dL} = n(L) \qquad [1.19]$$

where ΔN is the number of crystals in the size range ΔL per unit volume in a size range from L to $L+\Delta L$. Since n is based on the system volume, the volume must be defined in order to have a meaningful population density function. The number of crystals in the size range L_i to L_{i+1} is given by,

$$N_i = \int_{L_i}^{L_{i+1}} n dL \approx n_i (L_{i+1} - L_i) \qquad [1.20]$$

C.3 COMPARTMENTAL ENERGY BALANCE

From first principles the enthalpy balance can be given as follows,

$$\overbrace{\frac{dE}{dt}}^{\text{rate of accumulation of energy}} + \overbrace{\sum_{h=1}^{NI} \phi_{E,in,k}}^{\text{rate of total energy in by convection}} - \overbrace{\sum_{l=1}^{NO} \phi_{E,out,k}}^{\text{rate of total energy out by convection}} - \overbrace{\phi_{E,v,out}}^{\text{rate of energy out by convection via vapour}} + \overbrace{\hat{Q}}^{\text{net rate of addition}} - \overbrace{\hat{W}_s}^{\text{net rate of shaft work}}$$

$$- \overbrace{\hat{W}_{vo}}^{\text{net rate of work due to volume change}} + \overbrace{\sum_{h=1}^{NI} \phi_{m,in,k} \cdot \frac{P_{in,k}}{\rho_{in,k}}}^{\text{work needed to introduce inlet streams}} - \overbrace{\sum_{l=1}^{NI} \phi_{m,out,l} \cdot \frac{P_{out,l}}{\rho_{out,l}}}^{\text{work needed to introduce inlet streams}} - \overbrace{\phi_{v,out,k}}^{\text{work needed to remove vapour streams}} \qquad [3.1]$$

Initial condition:

$$E(t=0) = E_O \qquad [3.2]$$

$$E = U + E_K + E_P \qquad [3.3]$$

$$\phi_E = \phi_m . (\hat{U} + \hat{E}_K + \hat{E}_P) \qquad [3.4]$$

For crystallisation processes, kinetic energy, potential energy and shaft work can usually be neglected, thus reducing the above equation to the following,

APPENDIX

$$\sum_{h=1}^{NI} \phi_{m,in,k} \cdot \left(\frac{P_{in,k}}{\rho_{in,k}} + \hat{U}_{in,k} \right) - \sum_{h=1}^{NI} \phi_{m,out,l} \cdot \left(\frac{P_{out,l}}{\rho_{out,l}} + \hat{U}_{out,k} \right) - \phi_{v,out,k} \left(\frac{P_{V,out}}{\rho_{V,out}} + \hat{U}_{V,k} \right) + Q - W_{VO} \qquad [3.5]$$

The sum of internal energy and work due to the entrance and exit of mass is the enthalpy,

$$\hat{H} = \hat{U} + P\hat{V} = \hat{U} + \frac{P}{\rho} \qquad [3.6]$$

$$\phi_H = \phi_m . H \qquad [3.7]$$

$$\frac{dU}{dt} = \sum_{h=1}^{NI} \phi_{H,k} - \sum_{l=1}^{NI} \phi_{H,l} - \phi_{H,V,out} + Q - W_{vo} \qquad [3.8]$$

$$\frac{d(H - PV)}{dt} = \frac{dH}{dt} - \frac{dPV}{dt} = \sum_{h=1}^{NI} \phi_{H,k} - \sum_{l=1}^{NI} \phi_{H,l} - \phi_{H,V,out} + Q - W_{vo} \qquad [3.9]$$

and as,

$$\frac{dPV}{dt} = W_{vo} \qquad [3.10]$$

Equation [ ] reduces to the enthalpy balance as is frequently used in most engineering applications,

$$\frac{dH}{dt} = \sum_{h=1}^{NI} \phi_{H,k} - \sum_{l=1}^{NI} \phi_{H,l} - \phi_{H,V,out} + Q \qquad [3.11]$$

Initial condition:

$$H(t=0) = H_o \qquad [3.12]$$

C.2 COMPARTMENTAL MASS BALANCE

Mass balance for liquid component i

$$\overbrace{\frac{dm_{L,i}}{dt}}^{\text{mass rate of accumulation}} + \overbrace{\sum_{h=1}^{NI} \phi_{m,L,i,in,k} - \sum_{l=1}^{NO} \phi_{m,L,i,out,l} - \phi_{m,V,out}}^{\text{mass rates in and out via convection}} + \overbrace{M_i \sum_{P=1}^{NR_L} \upsilon_{L,p,i} . r_p}^{\text{mass production rate due to liquid phase reactions}} + \overbrace{M_i \sum_{g=1}^{NP_g} \upsilon_{S,q,i} \left[\phi_{mol,nuc,q} + \phi_{mol,grow,q} - \phi_{mol,dis,q} \right]}^{\text{interphase mass flux due to crystal growth and nucleation including dissolution at the critical nuclei size}} \qquad [2.1]$$

Initial condition:

$$n_{L,i}(t=0) = n_{L,i,0} \qquad [2.2]$$

APPENDIX

D. THERMODYNAMICS AND PHYSICAL PROPERTIES

Most of the physical property data required for the compartmental modelling framework of the organic fine chemical alcohol-water system as a function of temperature and concentration is unavailable. Material property data with unknown constants are presented such that they can be evaluated in future development research.

SOLUBILITY

$$C^{*}[T(t)] = 3.69e^{-02} - 1.77e^{-03}T + 3.35e^{-05}T^{2} \qquad 0^{O}C \le T \le 80^{O}C \quad [kg\,solute/kg\,solvent]$$

DENSITY

Organic fine chemical solid phase,

$$\rho_{S} = a - bT \qquad 0^{O}C \le T \le 80^{O}C \qquad 0 \le C_{API} \le 10 \ wt\% \quad [kg/m^{3}]$$

Saturated crystal free mother liquor density,

$$\rho_{L} = a_{O} + a_{1}C_{API} + a_{2}C_{API}^{2} + a_{3}C_{API}^{3} + a_{4}T + a_{5}T^{2} + a_{6}T^{3} \quad [kg/m^{3}]$$
$$0^{O}C \le T \le 80^{O}C \qquad 0 \le C_{API} \le 10 \quad wt\%$$

SPECIFIC HEAT CAPACITY

Organic fine chemical solid phase,

$$C_{ps} = a + bT \qquad 0^{O}C \le T \le 80^{O}C \quad [kJ/kg.K]$$

Saturated crystal free mother liquor density,

$$C_{pL} = a + bC_{API} + cT + dT^{2} + eT^{3} \quad 0^{O}C \le T \le 80^{O}C \quad [kJ/kg.K]$$

VISCOSITY

Saturated crystal free mother liquor viscosity,

$$\eta_{L} = 10^{a+bc_{api}+cc_{api}^{2}+dT+eT^{2}fT^{3}}$$

APPENDIX

E. MSMPR CRYSTALLIZER gPROMS SOURCE CODE

```
#*****************************************************************#
# gPROMS source code for a laboratory scale continuous            #
# MSMPR crystallizer                                              #
# Eleftherios Kougoulos                                           #
# University College London 18-07-2004 [Copyright 2004]           #
#*****************************************************************#

#*****************************************************************#
#Declarations
#*****************************************************************#

DECLARE
 TYPE
   solute_concentration          UNIT= kg/kg
   suspension_density            UNIT= kg/m3
   supersaturation               UNIT= kg/kg or [-]
   mean_residence_time           UNIT= s
   mass_flow_rate                UNIT= kg/s
   crystallizer_temperature      UNIT= °C
   second_moment                 UNIT= m-1
   third_moment                  UNIT= [-]
   fourth_moment                 UNIT= m
   total_nucleation_rate         UNIT= #/m3/s
   growth_zero_size                    UNIT= m/s
   average_growth_rate           UNIT= m/s
END # Declare

#*****************************************************************#
# Model description of MSMPR crystallizer
#*****************************************************************#
PARAMETER
   MaxSize              AS REAL # crystal size limit
   rol, ros         AS REAL # solvent, solid density
   V                AS REAL # crystallizer volume
   kv               AS REAL # volumetric shape factor
   eploc            AS REAL # energy dissipation rate

DISTRIBUTION_DOMAIN
   size AS (0: MaxSize)

VARIABLE
logn                        AS DISTRIBUTION (size) OF lognumber_density
```

APPENDIX

```
G                    AS DISTRIBUTION (size) OF growth_rate
C, Cin, Ceq, cc      AS solute_concentration
Mt                   AS suspension_density
sigma, sigm          AS supersaturation
tau                  AS mean_residence_time
W                    AS mass_flow_rate
temp                 AS crystallizer_temperature
m2                   AS second_moment
m3                   AS third_moment
m4                   AS fourth_moment
L43                  AS volume_mean_size
m                    AS DISTRIBUTION (size) OF mass_distribution
Bo                   AS total_nucleation_rate
Go                   AS growth_zero_size
Gav                  AS average_growth_rate

BOUNDARY
# Modelling total nucleation (primary and secondary)
  logn(0) = log (Bo/Go);
# No secondary or primary nucleation
# logn(0) = 0;

EQUATION

# Definition of Total nucleation rate (Kougoulos et al.,
# 2004) based on different impeller types

# Pitch blade impeller nucleation definition
   Bo = 4.9e9 * Mt^1.57 * sigma^2.64;
# Flat blade impeller nucleation definition
# Bo = 1.98e9 * Mt^1.64 * sigma^2.93;
# Pitch blade impeller (energy dissipation rate included)
# Bo = 1e19 * Gav^1.2 * Mt^1.5 * eploc^0.15;

# Growth rate at zero particle size (Abegg et al., 1968)
  Go = 3e-04 * sigma;

# Total mass balance on solute
   V * rol * $cc = W * (cin - cc);

# Definition of combined concentration
   cc = c + Mt / rol;

# Definition of suspension density
   Mt = 1e-18 * ros * kv * INTEGRAL (L: =0: MaxSize; L^3 * EXP
   (logn (L)));
```

APPENDIX

```
# Definition of the average growth rate (Kougoulos et al. 2004)
# Gav = 1.26e-08 * sigma^1.26;

# Crystal population balance
   FOR L: = 0|+ TO MaxSize DO
   $logn (L) + G (L) * PARTIAL (logn (L), size) + PARTIAL (G (L), size) + 1/tau  =  0;

END
# Mean Residence time
   tau = V * rol /W;

# Definition for the moments of the distribution
   m2 = INTEGRAL (L: =0 : MaxSize; L^2 * EXP (logn(L)));
   m3 = INTEGRAL (L: =0 : MaxSize; L^3 * EXP (logn(L)));
   m4 = INTEGRAL (L: =0 : MaxSize; L^4 * EXP (logn(L)));

# Volume mean diameter
   L43 = m4/m3;

# Supersaturation conditions
   IF c < ceq + 1E-6 THEN
   sigm = 1E-6;
   ELSE
   sigm = c - ceq;
   END

# Definition of relative supersaturation
   sigma = sigm/ceq;

# Crystal growth rate correlation (Kougoulos et al. 2004)

  FOR L: = 0 TO MaxSize DO
  G (L) = 0.0313 * sigma * (1-exp (-17400 * 1e-6 * (L + 0.1)));

END

# Equilibrium solubility concentration
    ceq = 0.0035 * exp (0.0443 * temp);

# Definition of the crystal size distribution
   FOR L: = 0 TO MaxSize DO
   m(L) = ((exp(logn(L))* 1 * (L * 1e-6)^3 * ros * kv)/Mt) * 100;
   END
```

APPENDIX

```
#*****************************************************************#
# PROCESS START UP                                                #
#*****************************************************************#

UNIT

P AS MSMPR Crystallizer

SET
WITHIN P DO

MaxSize   := 300;
rol       := 800;
ros       := 1400;
V         := 5.5e-04;
kv        := 1.6;
eploc     := 0.12;
size      := [bfdm, 1,252];

END

ASSIGN

WITHIN P DO
cin     := 0.0371;  # kg/kg
temp    := 30.0;    # oC
W       := 5.3e-04; # kg/s
END

INITIAL
WITHIN P DO

# Initial solute concentration within MSMPR crystallizer
  c = 0;

# Definition for seed distribution
FOR L := 0|+ TO MaxSize DO
logn(L) = 0;

END
END

SCHEDULE

# MSMPR crystallizer simulated for ten residence times
CONTINUE FOR 8250
```

APPENDIX

F. BATCH CRYSTALLIZER gPROMS SOURCE CODE

```
#*****************************************************************#
# gPROMS source code for seeded and unseeded batch cooling        #
# crystallizers using a lumped description                        #
# Eleftherios Kougoulos                                           #
# University College London 21-07-2004 [Copyright 2004]           #
#*****************************************************************#

#*****************************************************************#
# Model description of batch crystallizer                         #
#*****************************************************************#

PARAMETER

  MaxSize, MinSize      AS REAL
  V                     AS REAL # Constant crystallizer working volume
  Cp                    AS REAL # Constant specific heat capacity
  A                     AS REAL # Heat transfer area
  U                     AS REAL # Overall heat transfer coefficient
  kv                    AS REAL # Volume shape factor
  rol                   AS REAL # Constant solvent density
  ros                   AS REAL # Constant crystalline density
  DHc                   AS REAL # Enthalpy of crystallization
  h                     AS REAL # Conversion factor
  Lo                    AS REAL # Effective nuclei size
  T0                    AS REAL # Initial batch temperature
  Tf                    AS REAL # Final batch temperature
  tau                   AS REAL # Batch time
  eploc                 AS REAL # Energy dissipation rate

DISTRIBUTION_DOMAIN

  size          AS (0 : MaxSize)

VARIABLE

  logn                  AS DISTRIBUTION (size) OF Lognumber_density
  G                     AS DISTRIBUTION (size) OF Growth
  m                     AS DISTRIBUTION (size) OF Normalized_mass
  Tb                    AS Bulk_temperature
  Tc                    AS Cooling_temperature
  ceq                   AS Equilibrium_concentration
  c                     AS Solute_concentration
```

APPENDIX

```
sigma          AS Supersaturation
Mt             AS Suspension_density
m3             AS Third_moment
m2             AS Second_moment
L43            AS Weight_mean_size
S              AS Driving_force
m4             AS Fourth_moment
Enthalpy       AS Energy_release
Go             AS Zero_Growth
Bo             AS Total_nucleation
Gav            AS average_growth

BOUNDARY

# Modelling of primary and secondary nucleation is as follows,
   logn(0) = log (Bo/Go);
# If no secondary or primary nucleation occurs then,
# logn(0) = 0;

EQUATION

# Total nucleation rate (Kougoulos et al., 2004)
# Pitch blade impeller nucleation definition
# Bo = 4.9e9 * Mt^1.65 * sigma^2.64;
# Flat blade impeller nucleation definition
# Bo = 1.98e9 * Mt^1.64 * sigma^2.93;

  Bo = 1e19 * Gav^1.2 * Mt^1.5 * eploc ^0.15;

# Growth rate at zero particle size (Abegg et al., 1968)

 Go = 3e-04 * sigma;

# Solute concentration balance on solid and liquid phase

  $c = (-3 * kv * ros * m2  * 1e-18) - (ros * kv * Bo * Lo^3) ;
  m2 = INTEGRAL (L :=0 : MaxSize; L^2 * G(L) * EXP(logn(L)));

# Population balance with size-dependent growth

FOR L:= 0|+ TO MaxSize DO

$logn(L) + G(L) * PARTIAL(logn(L),size) + logn(L) * PARTIAL (G(L), size) = 0;

END
```

APPENDIX

```
# Energy balance containing enthalpy release and nucleation term
 rol * V * Cp * $Tb = -U * A * (Tb - Tc) + Enthalpy + (ros * kv *  DHc * h * Bo * Lo^3);

 Enthalpy = 3 * DHc * h * ros * kv  * m2;

#*****************************************************************#
# Implementation of cooling profile                              #
#*****************************************************************#

# Linear cooling profile
 $Tc = -(T0-Tf)/tau;  #constant cooling rate

# Natural cooling profile
# $Tb = -(1/tau)* log((T0-0)/(Tf-0))*(Tb-0);

# Suspension density
 Mt = ros * kv * m3 * 1e-18;

# Definition of the third moment
 m3 =  INTEGRAL (L :=0 : MaxSize; L^3 * EXP (logn(L)));
 m4 =  INTEGRAL (L :=0 : MaxSize; L^4 * EXP (logn(L)));

# Equilibrium concentration
 ceq = (0.0035 * EXP (0.0443 * Tb)) * rol;
# Supersaturation
 sigma = (c-ceq)/ceq;
 S = c/ceq;

# Size-dependent crystal growth rate

FOR L:= 0 TO MaxSize DO
G(L) = 0.0313 * sigma * (1-exp(-17400 * 1e-06 * (L + 0.1)));
END

# Average crystal growth
 Gav = 1.26e-08 * sigma^1.26;

# Volume mean diameter
 L43 = m4/m3;

# Definition of the crystal size distribution

FOR L := 0 TO MaxSize DO
m(L) = ((exp(logn(L))* 1 * (L * 1e-6)^3 * ros * kv)/Mt) * 100;
END
```

APPENDIX

```
#*********************************************************************#
# PROCESS START UP                                                    #
#*********************************************************************#

UNIT

T101 AS BATCH CRYSTALLIZER

SET

T101.rol := 800;                    # kg/m3
T101.ros := 1400;                   # kg/m3
T101.V := 5.5e-04;                  # m3
T101.Cp := 2900;                    # J/kg/oC
T101.A := 8.8e-03;                  # m2
T101.U := 750;                      # W/m2/oC
T101.kv := 1.6;
T101.size := [bfdm,1,300];
T101.MaxSize := 300;                # µm
T101.MinSize := 10;                 # µm
T101.DHc: = 8.6e3;                  # J/kg
T101.h := 1e3;
T101.Lo := 1e-06;                   # m
T101.T0 := 60;                      # °C
T101.Tf := 10;                      # °C
T101.tau := 6000;                   #  s
T101.eploc: = 0.25;                 # W/kg

INITIAL

T101.Tc = 60;                       # oC
T101.Tb = 60;                       # oC
T101.c = 48;                        # kg/m3 converted to kg solute/ kg solvent

WITHIN T101 DO

# Initial seed size distribution
# FOR L:= 0|+ TO MinSize DO

# logn(L) = log (3.25e5 * exp (-0.022 * L));

# END

# FOR L:= MinSize|+ TO MaxSize DO

  FOR L:= 0|+ TO MaxSize DO
```

```
 Logn(L) = 0;

END
  END

SOLUTIONPARAMETERS
REPORTINGINTERVAL := 30; #Output file produced in 30s intervals

SCHEDULE
CONTINUE FOR 6000
```

APPENDIX

G. CFD DATA AND OPERATING CONDITIONS INCLUDING LIQUID SIDE HEAT TRANSFER COEFFICIENTS

		Rushton Turbine impeller				Pitch blade impeller			
Size [L]	**Heat transfer area [m^2]**	**Speed [rpm]**	**Power [W]**	**Heat transfer coefficient [W m^{-2} K^{-1}]**	**Modified drag coefficient**	**Speed [rpm]**	**Power [W]**	**Heat transfer coefficient [W m^{-2} K^{-1}]**	**Modified drag coefficient**
1	0.30	300	0.09	848	19.66	460	0.09	1156	19.66
5	0.11	289	0.47	784	19.58	450	0.49	1054	19.58
25	0.04	201	2.18	656	19.58	313	2.32	881	19.58

Table G.1: Operating conditions used in CFD simulations based on scale-up with constant power input per unit mass [0.12 W kg^{-1}] using a 5% v/v dilute suspension with a modified drag coefficient based on a particle size of 200 μm.

Speed [Rpm]	**Reynolds number**	**Power [W]**	**Power per unit mass [W kg^{-1}]**	**Kolmogorov scale [m]**	**CD_0**	**Heat coefficient [W m^{-2} K^{-1}]**
300	7191	0.52	0.13	1.17e-04	19.58	682
400	9588	1.23	0.32	9.43e-05	19.66	826
500	11985	2.41	0.62	7.89e-05	19.77	958

Table G.2: Operating conditions used in CFD simulations based on a 5l batch cooling crystallizer equipped with a Rushton turbine impeller using a 5% v/v dilute suspension using a modified drag coefficient based on a particle size of 200 μm.

Speed [Rpm]	Reynolds number	Power [W]	Power per unit mass [W kg^{-1}]	Kolmogorov scale [m]	CD_0	Heat coefficient [W m^{-2} K^{-1}]
300	7191	0.15	0.04	1.61e-04	19.53	505
400	9588	0.35	0.09	1.29e-04	19.56	611
500	11985	0.68	0.18	1.09e-04	19.60	710

Table G.3: Operating conditions used in CFD simulations based on a 5l batch cooling crystallizer equipped with a pitch blade impeller using a 5% v/v dilute suspension using a modified drag coefficient based on a particle size of 200 μm.

Particle size [μm]	Drag coefficient	Modified Drag Coefficient	Rep
3	2000	2000	1.6e-05
100	35.3	35.3	0.34
200	19.5	19.6	0.69
300	15.3	15.5	1.37

Table G.3: Particle size, drag coefficient and particle Reynolds number relationships.

H. CRYSTAL PURITY

If crystals are grown at relatively low rates and under constant conditions, normally purities of about 99.5 to 99.8 percent can be achieved in one process step. Under certain conditions, the purity may be significantly lower due to one or more of the following mechanisms,

I. Inclusion of mother liquor in the lattice
II. Entrapment of mother liquor in cracks, processes and agglomerates
III. Incorporation of impurities in the crystal lattice
IV. Adsorption of impurities or solvent on crystal surfaces.

APPENDIX

Impurities are undesirable for one or more of the following reasons: they increase the caking tendency, may lead to further reactions, incorrect chemical composition. The latter is a serious concern in pharmaceutical applications.

Mother liquor inclusions

The inclusion of mother liquor by the crystal lattice is strongly dependent on the Supersaturation level. At supersaturation levels where growth instabilities occur, mother liquor inclusions are almost unavoidable. For instance, at high supersaturation levels macrosteps may be formed on the crystal surface.
When macrosteps are present, overhangs can be formed that lead to mother liquor inclusions. These inclusions are therefore aligned along the outer crystal faces At even higher supersaturation levels, the edges and corners of the crystals start exhibiting higher growth rates than the centers of the faces because, for geometric reasons, they suffer less from mass transfer limitation. Under such circumstances hopper crystals, which have more inclusions than crystals with flat faces, can be formed.

Another cause for the formation of liquor inclusions is attrition of crystals due to collisions with other crystals; pump blades or other equipment surfaces. Above a certain size, which depends on the material strength and the collision energies, the edges and in particular the corners of the crystals exhibit micro-attrition affects. If a crystal that has undergone micro-attrition and is in a supersaturated region, the edges and corners will 'heal' as a result of crystal growth. During this healing, mother liquor is included because the growth layers propagating along two faces no longer fit perfectly. This phenomenon of solvent inclusions towards the corners of the crystals beyond a certain crystal size as well as the occurrence of other inclusions can easily be visualized under a microscope when the crystals are embedded in a non-dissolving liquid with the same refractive index: only the boundaries of the crystals and the mother liquor inclusions show up.

Incorporation of impurities in the crystal lattice

As a crystalline material has a very rigid structure, incorporation of impurities by occupation of crystal lattice positions that are normally occupied by the growth units will only occur if the impurity fits reasonably well into the lattice.

I.1 gPROMS COMPARTMENTAL SOURCE CODE

```
# ==========================================#
# Compartmental modelling of a gPROMS 5l batch crystallizer equipped  #
# with a Rushton turbine impeller                                     #
# University College London, Eleftherios Kougoulos                    #
# 01/09/2004                                                          #
# MODEL: Compartment 1                                                #
# ==========================================#

PARAMETER

 MaxSize,MinSize          AS REAL
 [redacted]               AS REAL # Compartmental volume
 CP                       AS REAL # Constant specific heat capacity
 A1                       AS REAL # Heat transfer area
 U1                       AS REAL # Overall heat transfer coefficient
 kv                       AS REAL # Volume shape factor
 rol                      AS REAL # Constant solvent density
 ros                      AS REAL # Constant crystalline density
 DHc                      AS REAL # Enthalpy of crystallization
 h                        AS REAL # Conversion factor
 Lo                       AS REAL # Critical nuclei size
 T0                       AS REAL # Initial batch temperature
 Tf                       AS REAL # Final batch temperature
 tau                      AS REAL # Batch time
 FV14,FV10,FV1,FV11       AS REAL # Volumetric flowrates as determined from CFD simulations: Fig.11.1

DISTRIBUTION_DOMAIN

 size          AS (0 : MaxSize)

STREAMS

VARIABLE

 logn1,logn9,logn6,logn5  AS DISTRIBUTION (size) OF Lognumber_density
 G1                       AS DISTRIBUTION (size) OF Growth
 m1                       AS DISTRIBUTION (size) OF Normalized_Mass
 T1,T5,T6,T9              AS Compartment_Temperature
 TC1                      AS Cooling_Temperature
 CEQ1                     AS Equilibrium_Conc
 C1,C9,C5,C6              AS Solute_Concentration
 SUP1                     AS Supersaturation
```

MT1	AS Suspension_density
m3	AS Third_moment
m2	AS Second_moment
L43	AS Volume_mean_size
S1	AS Driving_force
m4	AS Fourth_moment
Enthalpy	AS Energy_release # Re-crystallization
G01	AS Zero_Growth
BN1	AS Total_nucleation
GAV1	AS Average_growth
[redacted]	AS Enery_Dissipation_Rate # Determined from CFD simulations: Table 11.1

BOUNDARY

Modelling of primary and secondary nucleation is as follows,

logn1(0) = log (BN1/G01);

If no secondary or primary nucleation occurs then,

logn1(0) = 0;

EQUATION

Total nucleation rate (Kougoulos et al., 2005)

BN1 = 1e19 * GAV1^1.2 * MT1^1.5 * [redacted]^0.2;

Growth rate at zero particle size (Abegg et al., 1968)

G01 = 3e-04 * SUP1;

Solute concentration balance with interconnecting flows between compartments

[redacted]* $C1 = ((FV14*C9) + (FV10 * C6) + (FV11 * C5)) -(FV1 * C1) - (kv * ros * [redacted] * m2 * 1e-18) - (kv * ros * [redacted] * BN1* Lo^3);

m2 = INTEGRAL (L :=0 : MaxSize; L^2 * G(L) * EXP(logn1(L)));

Population balance with size-dependent growth and total nucleation

FOR L:= 0|+ TO MaxSize DO

$(logn1(L)) + (G1(L)*PARTIAL(logn1(L),size) + PARTIAL (G1(L), size))* [redacted] * EXP(logn1(L))=(FV14 *EXP(logn9(L))) + (FV10 *EXP(logn5(L))) + (FV11 * EXP(logn6(L)))-((FV1 * EXP(logn1(L)))) + (EXP(log(BN1)) * [redacted]);

END

```
# Energy balance containing enthalpy release and nucleation term
rol * [redacted] * CP * $T1= CP * ((FV14 * C1* T9)+ (FV10 * C5 * T5) + (FV11 * C6 * T6)) - (FV1 * C1 * T1) -(U1
* A1 * (T1-TC1)) +(3 * ros * kv * DHc * m2 * h) + (ros * kv * DHc * BN1 * Lo^3 * h);

#*****************************************************************#
# Implementation of cooling profile                               #
#*****************************************************************#

# Linear cooling profile
 $TC1 = -(T0-Tf)/tau;  #constant cooling rate

# Natural cooling profile
# $TC1 = -(1/tau)* log((T0-0)/(Tf-0))*(T1-0);

# Suspension density
 MT1= ros * kv * m3 * 1e-18;

# Definition of the third moment
 m3 =  INTEGRAL (L :=0 : MaxSize; L^3 * EXP (logn1(L)));
 m4 =  INTEGRAL (L :=0 : MaxSize; L^4 * EXP (logn1(L)));

# Equilibrium concentration
 CEQ1 = (0.0035 * EXP (0.0443 * T1)) * rol;

# Supersaturation
 SUP1 = (C1-CEQ)/(CEQ);
 S1 = (C1/CEQ);

# Size-dependent crystal growth rate
 FOR L:= 0 TO MaxSize DO
 G1(L) = 0.0313 * SUP1 * (1-exp(-17400 * 1e-06 * (L + 0.1)));
 END

# Average crystal growth
 GAV1 = 1.26e-08 * SUP1^1.26 * 1e-06;

# Volume mean diameter
 L43 = m4/m3;

# Definition of the crystal size distribution
FOR L := 0 TO MaxSize DO
M1(L) = ((EXP(logn1(L))* 1 * (L * 1e-06)^3 * ros * kv)/MT1) * 100;
END
```

I.2 gPROMS COMPARTMENTAL SOURCE CODE

```
EQUATION

# Population balance with size-dependent growth, total nucleation and size-dependent classification

FOR L:= 0|+ TO MaxSize DO

[redacted] * $EXP(logn6(L)) + (G6(L) *PARTIAL(logn6(L),size) + PARTIAL (G6(L), size)) * [redacted]* EXP(logn6(L)) =
(FV9* EXP (logn5(L)))-((FV11 * EXP(logn6(L))*hout(L)) + (EXP(log(BN6)) * [redacted]);

END
# Size-dependent classification function modelling equations described in [9.33] and [9.34]

FOR L: MinSize TO MaxSize DO
hout(L) = (Uslip(L)/FV9) + ((MT1out/MT1) * 1/rol);
END
FOR L: MinSize TO MaxSize DO
Uslip (L) = ((-B(L) + (B(L)^2+ ((A*C(L))^2))^0.5)/C(L))^2;
END

A = a1^0.5;

FOR L: MinSize TO MaxSize DO
B(L) = 0.5 * (a2(L) * a4(L))^0.5;
END
FOR L: MinSize TO MaxSize DO
C(L) = (a2(L) * a3(L))^0.5;
END

a1 = g * ((ros-rol)/(ros + rol));

FOR L: MinSize TO MaxSize DO
a2(L) = 0.75 * ((1+(1+(MT1/rol))^0.33)/((ros + rol) * L^2* (MT1/rol));
END
FOR L: MinSize TO MaxSize DO
a3(L)= 0.63 * (L*rol)^0.5;
END
FOR L: MinSize TO MaxSize DO
a4(L) = 4.8 * (il) *exp(0.83 * ((1-(MT1/rol))/(MT1/rol)));
END
```

Personal Acknowledgements

Firstly, I would like to thank my academic supervisor, Professor Alan Jones for his invaluable advise in the field of crystallization and providing me with the vision to overcome some challenging aspects of this research work. My academic supervisor at GlaxoSmithKline pharmaceuticals, Kaz Wood-Kaczmar who trained me and taught me the skills of a process development chemist of which I have further developed working at Accentus plc as a Senior Chemical Engineer and now at Pfizer Ltd. The time spent at GlaxoSmithKline was a tremendous experience and I would like to thank Kaz for the patience he had with me during my industrial placements. I would also like to thank Julian Perfect for the stimulating conversations we had about UCL while preparing, loading and visualising crystals under an SEM and Martin Vale, who I nearly drove mad with my constant visits to the computer laboratory to solve endless problems with CFD etc. Bill, Lars and Parathy all provided me with plenty of laughter to get through the day in the crystallization laboratory. During my many late nights at UCL, Marcello Murru would regularly come and join me in the office and kept me awake with his passion for life and explaining to me how nothing seems to go right for him. I wish him well and every success in the future. My partner, Bhupinder, was especially a part of my research work and would encourage me through trying times and was always there for me. Finally, a special thanks to my mum Georgina, who stood by me every step of the way during extremely difficult times and for providing me with the bulk of the financial support to see me overcome this huge challenge over the three years over which this research work has been carried out.

Curriculum Vitae

1997-2001	**M. Eng Chemical with Biochemical Engineering, UCL, London**
2001-2004	**Ph. D Chemical Engineering, UCL, London**
2004-2005	**Senior Chemical Engineer, AEA technology (Accentus), Harwell**
2005-Present	**Process Development Chemist, Pfizer, Sandwich, UK**

List of Publications

1. D.R. Thompson, E. Kougoulos, M. Wood-Kazcmar and A.G. Jones. Solute concentration measurement of an important organic compound using ATR-UV spectroscopy (2005). *Journal of Crystal Growth.* Volume 276, **1-2**, 230-236.

2. E. Kougoulos, M. Wood-Kazcmar and A.G. Jones. Modelling particle disruption of an organic fine chemical compound using Lasentec focussed beam reflectance monitoring (FBRM) in agitated suspensions (2005). *Powder Technology*, **155**, 153-158.

3. Z. Guo, M. Zhang, H. Li, J. Wang and E. Kougoulos. Effect of ultrasound on anti-solvent crystallization process (2005). *Journal of Crystal Growth.* Volume 273, **3-4**, 555-563.

4. E. Kougoulos, A.G. Jones, K.H. Jennings, M. W. Wood-Kaczmar. Use of Focused Beam Reflectance Measurement (FBRM) and Process Video Imaging (PVI) in a modified mixed suspension mixed product removal (MSMPR) cooling crystallizer (2005). *Journal of Crystal Growth.* Volume 273, **3-4**, 529-534.

5. E. Kougoulos, A.G. Jones, M. W. Wood-Kaczmar. Estimation of crystallization kinetics for an organic fine chemical using a modified continuous cooling mixed suspension mixed product removal (MSMPR) crystallizer (2005). *Journal of Crystal Growth.* Volume 273, **3-4**, 520-528.

6. E. Kougoulos, A.G. Jones, M. W. Wood-Kaczmar. CFD modelling of mixing and heat transfer in batch cooling crystallizers: Aiding the development of a novel predictive compartmental model (2005). Trans IChemE, Part A, January 2005, *Chemical Engineering Research and Design*, **83** (A1), 30-37.

7. Kougoulos, E., A.G. Jones and Kaz. Wood-Kaczmar. 'Scale-Up of Organic Crystallization Process'. In AIChE National Meeting, Recent Developments in Crystallization and Evaporation. San Francisco, CA, USA, 16-21 November 2003, (New York: AIChE), Paper 310B.